Kinetic theory of stellar self-gravitating systems

Mathieu Roule

Sorbonne Université

École Doctorale 127 – Astronomie et Astrophysique d'Ile-de-France

Institut d'Astrophysique de Paris

Théorie cinétique des systèmes stellaires autogravitants

par

Mathieu Roule

Thèse de doctorat en Astronomie et Astrophysique

Directeur de thèse : **Jean-Baptiste Fouvry**
Co-directeur de thèse : **Christophe Pichon**

présentée et soutenue publiquement le 23 Septembre 2024

devant un jury composé de

M. Michael Joyce	Sorbonne Université, Paris	Président
M. Julien Barré	Institut Denis Poisson, Orléans	Rapporteur
M. John Magorrian	Oxford University, UK	Rapporteur
Mme Elena D'Onghia	University of Wisconsin–Madison, USA	Examinatrice
Mme Kathryn V. Johnston	Columbia University, USA	Examinatrice
M. Pierre-Henri Chavanis	Laboratoire de Physique Théorique, Toulouse	Membre invité

Institut d'Astrophysique de Paris
UMR 7095 – CNRS – Sorbonne Université

« *Ce qui est difficile, c'est la partie pédalo,*
c'est pas la partie canard. »
Hubert

Remerciements

Je souhaite avant tout remercier mes encadrants de thèse, Jean-Baptiste et Christophe. Votre soutien, votre disponibilité permanente et nos échanges scientifiques ont été des sources de motivation et d'inspiration tout au long de cette belle aventure. Je vous suis infiniment reconnaissant pour ces trois années et demi, et pour tout ce que j'ai appris à vos côtés.

Je tiens également à remercier chaleureusement les membres de mon jury : Julien Barré et John Magorrian, pour votre relecture attentive, vos commentaires constructifs qui ont grandement amélioré ce manuscrit ; ainsi qu'Elena D'Onghia, Kathryn Johnston et Michael Joyce, pour vos questions pertinentes et vos suggestions lors de la soutenance.

Merci Pierre-Henri pour toutes les discussions enrichissantes sur Zoom ou autour d'un café à Toulouse. Merci Mike, cela a été un immense plaisir de travailler avec toi sur nos projets communs. Plus généralement, je remercie Alex, Anna-Lisa, Anwar, Bruno, Chris, Dimitri, Douglas, Eugene, Eunhee, John, Jordan, Kerwann, Martin, Pierre, Robbie, Simon P., Simon R., Sofia, Sven, et toutes les personnes qui constituent l'environnement scientifique de cette thèse. Merci pour l'atmosphère de travail agréable et stimulante que vous avez participé à créer collectivement autour du projet Ségal, et pour les discussions passionantes tant scientifiques que personnelles.

Un grand merci aux personnes qui, dans l'ombre, assurent le bon fonctionnement de tout ce qui entoure la recherche : l'école doctorale, les équipes techniques et administratives du laboratoire et du restaurant d'entreprise. Merci particulièrement à Frédéric Daigne, Thierry Fouchet, Jacqueline Plancy, Sandy Artero, Valérie Bona, Isabelle Coursimault, Christophe Gobet, Lionel Provost, Stéphane Rouberol et Cyril Hachet, pour votre aide précieuse et votre disponibilité.

Merci à tous les doctorants, post-doctorants et membres permanents du laboratoire, pour les discussions, les pauses-cafés, les repas partagés, les parties de jeux de société, et pour l'ambiance conviviale que vous avez su instaurer à l'IAP. Merci à Pierre, pour les parties de ping-pong, de squash, et les bons plans parisiens, à Marion pour les pancakes, à Hugo, pour les pauses du vendredi en souvenir des profiterolles, à Clément, pour les discussions lunaires, à Louise, de les avoir longuement supportées (mais pas pour les règles du dutch), à Ira, pour le sauvetage de chemise, à Sofia, pour les potins, à Eunhee, de reprendre le flambeau, à Patrick, pour le parapente, à Axel, Chi An, Denis, Emilie, Emma, Marie, Simon et avec une pensée pour Tianxiang, pour ces trois années partagées. Merci à Cyril et Florence pour le suivi attentionné de ma thèse.

Merci également à mes amis de plus longue date, pour tous les moments de détente et de partage. À Chloé, Guillaume, Ju et Raph, pour ces douzes dernières années et celles à venir, à Isam, pour les discussions scientifiques jusqu'au Frioul, à Olivier et à Elian, d'amener un peu de soleil du Sud à Paris, à Simon, pour ton énergie débordante et communicative, à Pablo, pour ces trois années de colocation en respectant le principe d'exclusion de Pauli presque sûrement, donc à Charlotte aussi, et pour les heureuses superpositions, à Bastien et Alexane, pour les brunchs, les soirées jeux à Toulouse et les émotions fortes devant les Bleus, à Axel et Philippine, pour les visites californiennes, à Maxime et Amaury, du Canada à Paris, les girouettes auront bien tourné, et à tous ceux dont je recroise plus rarement le chemin mais toujours avec joie : Pierre, Robin, Adel, Cédric, Walid, Margaux et Lucas, Tarek et Léa, Antoine, Rind, Nathan, Arthur, Bastien, Clara, Cyprien, Eric, François, Thomas, Sirine...

Merci Manon pour ton amour, les week-ends hors du temps et tous les petits moments de vie partagés le long de ce chemin qui nous emmène vers de belles contrées bleues. Merci à Yves, Virginie, Charline, Cédric et aux familles Billy et Jarry pour les joyeux week-ends en Anjou.

Enfin, je ne saurais conclure ces remerciements sans adresser un mot tout particulier à ma famille. Merci à mes oncles, tantes, cousins et cousines, en particulier à Christine, Marie-Joëlle et Nabil pour les repas parisiens. Merci mémé pour les histoires, les rires et de toujours me laisser gagner au Scrabble. Merci grand-frère pour tes sages conseils, de PES aux études, et de construire avec Léa un avenir de grandes joies familiales. Merci grande-soeur pour ta profonde gentillesse et ton soutien, et de construire avec Nicolas un foyer de douceur et de calme où se ressourcer.
Merci Papa, merci Maman, pour tout.

Plagiarism statement

I hereby declare that

- the results presented in this thesis are the fruit of my personal work,
- I am the author of all the following except when stated explicitly,
- I did not use third-party sources or results without clearly citing and referencing them according to the recommended bibliographic rules.

23rd September 2024 Mathieu Roule

Résumé

Les systèmes stellaires, tels que les galaxies et les amas globulaires, sont des systèmes complexes où les étoiles sont liées par le champ gravitationnel qu'elles contribuent à créer collectivement. L'étude de ces systèmes est particulièrement intéressante car la gravité est une force attractive à longue portée qui tend à former des structures inhomogènes sujettes à de forts comportements collectifs (bras spiraux, barres). Au cours des cinq dernières décennies, les simulations numériques ont fourni des informations inestimables sur la formation et l'évolution des galaxies sur des temps cosmiques. En parallèle, les développements de la théorie cinétique offrent un cadre théorique remarquable pour comprendre les résultats statistiques de ces processus d'évolution non linéaires.

L'état de l'art actuel de la théorie cinétique des systèmes stellaires isolés est l'équation inhomogène de Balescu–Lenard. Elle décrit l'évolution à long terme d'un système auto-gravitant sous l'effet des interactions résonantes entre fluctuations internes (bruit de Poisson), tout en tenant compte de leur dynamique collective. Ce formalisme est particulièrement important car il capture de manière perturbative le réarrangement non linéaire des orbites. Cette thèse aborde plusieurs questions clés sur l'évolution des systèmes stellaires isolés : Comment les interactions résonantes et les effets collectifs influencent-ils leur évolution à long terme ? Dans quelles conditions ces effets augmentent-ils ou diminuent-ils la diffusion orbitale ? Quelles sont les limites des théories cinétiques actuelles pour prédire l'évolution des systèmes auto-gravitants ?

Pour aborder ces questions, je considère deux systèmes : un modèle unidimensionnel imitant le mouvement vertical des étoiles dans un disque galactique et un disque (infiniment) mince décrivant leur mouvement dans le plan. Je reprends la notion de susceptibilité gravitationnelle qui joue un rôle fondamental dans la compréhension de leur évolution. En fonction de leur configuration, qu'ils soient dynamiquement froids (disque mince) ou chauds (unidimensionnel), je montre que les systèmes stellaires réagissent différemment aux perturbations. J'analyse cette susceptibilité en utilisant le formalisme de la matrice de polarisation. Cette méthode générique me permet de sonder la présence de modes instables ou faiblement amortis dans différents disques. Je discute de la difficulté intrinsèque d'analyser les fréquences propres des systèmes stellaires stables ainsi que les comportements spécifiques qu'ils présentent, tels que l'amortissement algébrique de Landau.

En confrontant les prédictions théoriques de l'équation de Balescu–Lenard aux simulations numériques, je montre que la théorie cinétique capture quantitativement l'évolution moyenne à long terme des systèmes stellaires. Les effets collectifs jouent cependant un rôle très différent dans les deux systèmes envisagés. Dans le modèle unidimensionnel, ils rigidifient le système contre les perturbations, entraînant une diffusion plus faible. Cette géométrie souffre également d'un quasi-blocage cinétique : le réarrangement orbital est fortement retardé car les résonances dominantes ne transfèrent pas efficacement l'énergie entre les différentes régions. En étudiant des configurations encore plus contraintes pour lesquelles les rencontres à deux corps ne prédisent aucune évolution, je fournis une borne supérieure pour le temps typique de relaxation. Grâce aux effets collectifs, les interactions à trois corps entraînent nécessairement une évolution. A contrario, les modes faiblement amortis amplifient les fluctuations dans les disques froids. Cela pousse le système à évoluer vers un état instable rapidement. À la transition de phase, l'évolution dépend de plus en plus des conditions initiales, une caractéristique qui dépasse la portée actuelle de la théorie cinétique.

Abstract

Stellar systems, such as galaxies and globular clusters, are fascinating yet complex many-body systems in which stars are bound together by their collective gravitational field. The analytical study of these systems is particularly challenging because gravity is a long-range attractive force which tends to form inhomogeneous structures prone to impressive collective behaviours such as spiral arms and bars. In the last five decades, numerical simulations have provided invaluable insights in the formation and evolution of galaxies over cosmic times. As a complementary approach, developments in kinetic theory offer a theoretical framework to understand the statistical outcome of these non-linear evolution processes.

The current state-of-the-art kinetic theory of isolated stellar systems is the inhomogeneous Balescu–Lenard equation. It describes the long-term evolution of a self-gravitating system under the effect of resonant interactions between noise-driven fluctuations while accounting for their collective dynamics. Such a formalism is particularly valuable because it captures perturbatively the non-linear reshuffling of orbits. This thesis addresses several key questions on the fate of isolated stellar systems: How do resonant interactions and collective effects influence their long-term evolution? Under what conditions do these effects enhance or dampen orbital diffusion? What are the limitations of current kinetic theories in predicting the evolution of self-gravitating systems?

To tackle these questions, I consider side-by-side two different self-gravitating systems: a one-dimensional model mimicking the vertical motion of stars in a galactic disc and a razor-thin disc describing their in-plane motion. At the heart of this investigation is the role of the susceptibility of self-gravitating systems. Depending on their configuration, whether they are centrifugally (razor-thin) or pressure (one-dimensional) supported, I show that stellar systems exhibit different responses to perturbations. I analyse this susceptibility using the polarisation matrix formalism. This generic method allows me to probe the presence of growing modes in unstable discs as well as weakly damped modes in stable ones. I discuss the intrinsic difficulty of analysing the natural frequencies of stable stellar systems as well as the specific behaviours they exhibit such as algebraic Landau damping.

Confronting theoretical predictions from the Balescu–Lenard equation to numerical simulations, I show that kinetic theory quantitatively captures the average long-term evolution of stellar systems. Collective effects play a very different role in the two studied systems. On the one hand, they stiffen the one-dimensional system against perturbations, leading to a slower diffusion rate. This geometry also suffers from a quasi-kinetic blocking: orbital reshuffling is delayed because dominant resonances do not efficiently transfer energy between different regions. Studying even more contrived configurations for which two-body encounters predict exactly no evolution, I provide an upper limit for the typical relaxation time. Thanks to collective effects, three-body interactions can always drive a relaxation. On the other hand, weakly damped modes (swing) amplify the fluctuations in cold discs. It ultimately urges the system to evolve towards an unstable state. At phase transition, the pathway increasingly depends on the initial conditions, a feature that lies beyond the reach of current kinetic theory.

Contents

Chapter 1

Introduction

This thesis delves into the intricate long-term evolution of mass ensembles, bound together by the force of gravity: this is the celebrated N–body problem. Studying the evolution of such a system with many bodies, $N \gg 1$, is the realm of stellar dynamics (Binney & Tremaine, 2008). It encompasses a wide range of astrophysical systems of various sizes and masses, from clusters of stars orbiting Sagittarius A*, the super-massive black hole at the centre of our Galaxy, to the Milky Way itself, its dark matter halo and networks of galaxies' clusters.

Their study is both challenging and particularly interesting because gravity is an attractive long-range force. Thus, stellar systems typically form inhomogeneous structures and their evolution fundamentally is a collective story. Stars in a globular cluster or a galaxy do not move in straight lines. They orbit around the system's centre of mass. But contrary to planetary systems, this motion is not dictated by a single massive central object. It is the result of the collective gravitational potential generated by all the stars in the system. As such, stars cannot be considered as test particles tracing an externally imposed potential. These collective interactions can play a major role in the response of the system to external perturbations and in its long-term evolution.

N–body dynamics typically focuses on the physics of gravity while losing track of other physical phenomena such as hydrodynamics, stellar formation and evolution, etc. This is motivated by the fact that it is most often the dominant force. Before diving into the details of stellar dynamics, let me first introduce this thesis in its broader astrophysical context.

1.1 Astrophysical context

Large-scale structures and cosmology

Galaxies are not isolated objects. Instead, they form vast and intricate patterns known as large-scale structures. These structures include clusters, filaments, walls and voids, composing a cosmic web that spans the Universe. This organisation influences how galaxies rotate, interact, and evolve together. Observations from missions like the Sloan Digital Sky Survey (SDSS) have provided detailed maps that reveal the filamentary patterns connecting galaxy clusters, as illustrated in figure 1.1.

The current understanding of the formation and evolution of these structures is based on the Λ–Cold Dark Matter (Λ–CDM) model (Peebles, 1980; Blumenthal et al., 1984; Springel et al., 2006). The early universe contained small quantum density fluctuations, which were stretched during the inflationary epoch (Guth, 1981) and imprinted in the cosmic microwave background (CMB) (Planck Collaboration, 2020). These fluctuations served as the seeds for all future structure formation. As the universe expanded, the density fluctuations grew under the influence of gravity, predominantly driven by dark matter due to its significant mass fraction ($\sim$85% of the total matter content). Over billions of years, these regions of higher density attracted more matter, both dark and baryonic,

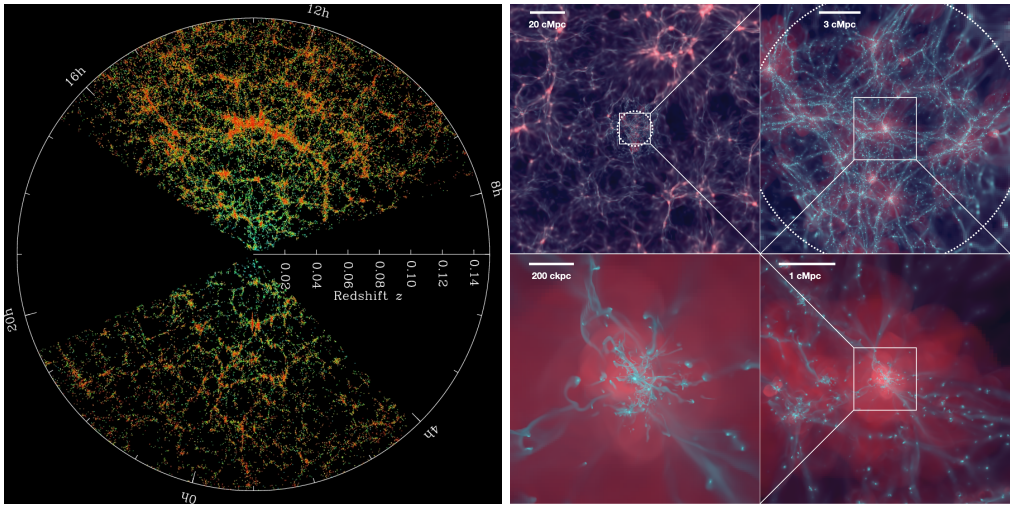

Figure 1.1: *Left:* Map of the galaxies in the nearby Universe from the Sloan Digital Sky Survey (SDSS). Galaxies are not uniformly distributed but form a cosmic web of clusters, filaments, walls, and voids. *Right:* Figure from Dubois et al. (2021). Four successive zooms (clockwise) in a Λ–CDM cosmological hydrodynamical simulation from the NewHorizon project. Such a simulation probes the intricate processes involved in the formation of galaxies in their anisotropic cosmic environment.

leading to the formation of the cosmic web of structures observed today (Frenk & White, 2012).

Galaxy formation and evolution

While dark matter solely interacts through gravity, baryonic matter shocks and cools, forming stars and galaxies as it flows in the potential wells created by dark matter overdensities. In this paradigm, galaxies form through the hierarchical assembly of smaller structures. In regions of higher dark matter density, massive galaxies form and evolve rapidly, often leading to the early creation of elliptical galaxies through major merger events. These violent processes trigger an intense activity of the super-massive black holes, the so-called active galactic nuclei (AGN) feedback. It ultimately quenches the galaxy from its reservoir of cold gas, preventing later star formation and leading to the formation of red and dead elliptical galaxies (Silk & Rees, 1998) as illustrated in figure 1.2.

Figure 1.2: Illustration of the two main types of galaxies in the Hubble sequence. *Left:* Elliptical galaxy, characterised by its spheroidal shape, old stars and absence of cold gas (NGC4621, Messier 59). *Right:* Spiral galaxy, characterised by its rotating spiral arms and flat disc (NGC5457, Messier 101). Credit: NASA/ESA Hubble Space Telescope.

Conversely, in less dense regions, the slower coherent accretion of cold gas allows for the extended formation of disk galaxies. In these thin structures, stars form from corotating gas on nearly circular

orbits. Their velocity dispersion is low compared to their typical rotational velocity. Such a system is said to be dynamically cold. As a result, flat galaxies are quite susceptible to quasi spontaneous morphological restructuring: they generically display grand design spiral arms and sometimes a central bar. These beautiful patterns, illustrated in figure 1.2, are the result of the collective dynamics of the stars. This is to be contrasted to mostly pressure-supported elliptical galaxies which cannot rely on rotational free energy to evolve.

The realm of galaxy formation and evolution involves various physical phenomena happening on a wide range of scales and interacting non-linearly with one another. Consequently, the field mostly relies on numerical simulations to understand the complex interplay of these processes. Despite their (many) successes, these simulations face significant challenges (Vogelsberger et al., 2020). They are limited by computational power, which constrains their resolution and the complexity of the physical models they can accurately simulate. The processes on sub-grid scales, such as star formation and black hole accretion, must be treated with phenomenological prescriptions that approximate the unresolved physics. These limitations, coupled with their intrinsically non-linear nature, introduce uncertainties that can affect the predictive power and accuracy of the simulations (Scannapieco et al., 2012). As a complementary approach, it is therefore of interest to develop a generic theoretical framework that can explain the long-term gravity-driven evolution of these systems, relying on a deterministic perturbative approach. Such a framework could provide insights into the underlying physics of these systems and help interpret and test the results and limitations of numerical simulations.

1.2 Stellar dynamics

With this perspective in mind, let me focus on stellar dynamics, an area of astrophysics that provides essential theoretical tools for understanding the evolution of gravitationally bound systems. Stellar dynamics applies principles of statistical mechanics to describe how galaxies, globular clusters, and other self-gravitating systems evolve under their own gravitational influence. By modelling a galaxy or any similar system as a collection of N identical point particles of mass m, it lays the groundwork for a quantitative analysis that bridges theory with the computational models discussed earlier. I postpone to chapter 8 the discussion on the limitations of such assumptions. Let me now introduce the basic tools and equations used in the kinetic theory of inhomogeneous stellar systems, which are crucial for capturing the essence of these complex dynamical phenomena.

1.2.1 Hamiltonian dynamics

The only considered force is Newtonian gravity. This force is conservative, and I therefore make extensive use of Hamiltonian dynamics. I refer to Goldstein (1950); Arnold (1978) for a detailed introduction to this topic.

The configuration of a conservative system with d_f degrees of freedom is fully characterised by its $2d_f$ canonical phase-space coordinates, $\mathbf{w} = (\mathbf{q}, \mathbf{p})$. The system's motion then follows Hamilton's equations

$$\frac{\mathrm{d}\mathbf{q}}{\mathrm{d}t} = \frac{\partial H}{\partial \mathbf{p}}, \quad \frac{\mathrm{d}\mathbf{p}}{\mathrm{d}t} = -\frac{\partial H}{\partial \mathbf{q}}, \tag{1.1}$$

where $H = H(\mathbf{q}, \mathbf{p}, t)$ is the system's Hamiltonian.

This generic set of $2d_f$ equations is valid for both a single particle moving in an external potential field and a system of particles interacting through a pairwise potential. In the former case, the phase-space coordinates, $\mathbf{w}$, simply is a $2d$ vector where d is the dimension of the physical space. In the later case, the phase-space coordinates of the system are a $2dN$ vector, $\mathbf{w} = (\mathbf{q}_1, \ldots, \mathbf{q}_N, \mathbf{q}_1, \ldots, \mathbf{q}_N)$, with N the number of particles.

Hamilton's equations (1.1) can be written under the short form

$$\frac{\mathrm{d}\mathbf{w}}{\mathrm{d}t} = [\mathbf{w}, H(\mathbf{w}, t)], \tag{1.2}$$

where $[\cdot,\cdot]$ stands for the Poisson bracket

$$[f(\mathbf{w}), g(\mathbf{w})] \equiv \frac{\partial f}{\partial \mathbf{q}} \cdot \frac{\partial g}{\partial \mathbf{p}} - \frac{\partial f}{\partial \mathbf{p}} \cdot \frac{\partial g}{\partial \mathbf{q}}. \tag{1.3}$$

A cornerstone of Hamiltonian mechanics is the concept of canonical transformations, which are changes of the phase-space coordinates that preserve the form of Hamilton's equations. A transformation from the original canonical coordinates $(\mathbf{q}, \mathbf{p})$ to new coordinates $\mathbf{W} = (\mathbf{Q}, \mathbf{P})$ is canonical if it conserves the form of the Poisson bracket, i.e.,

$$[\mathbf{W}_i, \mathbf{W}_j] = [\mathbf{w}_i, \mathbf{w}_j] = J_{ij}, \quad \text{with } \mathbf{J} = \begin{pmatrix} \mathbf{0} & \mathbf{I} \\ -\mathbf{I} & \mathbf{0} \end{pmatrix}. \tag{1.4}$$

This property ensures that the equations of motion retain their canonical form (equations 1.1 and 1.2) under transformation. The symplectic properties of these transformations notably imply that the volume in phase space is conserved, i.e., $\mathrm{d}\mathbf{Q}\mathrm{d}\mathbf{P} = \mathrm{d}\mathbf{q}\mathrm{d}\mathbf{p}$. Canonical transformations thus serve as a bridge connecting various representations of a physical system, facilitating the exploration of its dynamics from multiple perspectives while maintaining the core physical laws dictated by the Hamiltonian structure.

The canonical momenta are usually proportional to the mass of the particles. However, the gravitational acceleration is independent of the mass of the particle (equivalence principle). In what follows, I mainly work with specific momenta, i.e., momentum per unit mass. The typical phase-space coordinates therefore are $\mathbf{w} = (\mathbf{x}, \mathbf{v})$ with $\mathbf{x}$ the position and $\mathbf{v}$ the velocity of the particle. The canonical form of Hamilton's equations (1.1) still holds using the specific (i.e., per unit mass) Hamiltonian, abusively denoted H.

1.2.2 N–body evolution

At any given time, a system of N identical particles can be exactly described by its Klimontovich distribution function (DF)

$$F_\mathrm{d}(\mathbf{w}, t) = \sum_{i=1}^{N} m\, \delta_\mathrm{D}[\mathbf{w} - \mathbf{w}_i(t)]. \tag{1.5}$$

where δ_D stands for the Dirac δ-function, $\mathbf{w}_i(t)$ for the phase space location of the i-th particle at time t and $m = M_\mathrm{tot}/N$ its individual mass with M_tot the system's total mass.

The instantaneous potential induced by this DF of masses is

$$\psi_\mathrm{d}(\mathbf{w}, t) = \sum_{i=1}^{N} m\, U[\mathbf{w}, \mathbf{w}_i(t)] = \int \mathrm{d}\mathbf{w}' F_\mathrm{d}(\mathbf{w}', t)\, U(\mathbf{w}, \mathbf{w}'), \tag{1.6}$$

with $U(\mathbf{w}, \mathbf{w}')$ the considered (specific) pairwise interaction potential. For usual self-gravitating systems, one has

$$U(\mathbf{w}, \mathbf{w}') = \frac{-G}{\|\mathbf{x} - \mathbf{x}'\|}. \tag{1.7}$$

Taking the partial derivative w.r.t. time of equation (1.5), one can show that the dynamics of the discrete DF in phase space is exactly given by the Klimontovich equation (Klimontovich, 1967)

$$\boxed{\frac{\partial F_\mathrm{d}}{\partial t} + [F_\mathrm{d}, H_\mathrm{d}] = 0,} \tag{1.8}$$

where H_d stands for the discrete (specific) Hamiltonian of the system

$$H_\mathrm{d}(\mathbf{w},t) = \tfrac{1}{2}\mathbf{v}^2 + \psi_\mathrm{d}(\mathbf{w},t). \tag{1.9}$$

Importantly, the Klimontovich equation (1.8) is equivalent to the $2dN$ Hamilton's equations (1.2) or the dN Newton's equations. It exactly describes the evolution of the N–body system and summarises it as a continuity equation in phase space. In practice, this equation is not directly solvable. First, because it is quadratic in the DF, as the Hamiltonian, H_d, linearly depends on F_d through equation (1.6). Second, difficulties arise from the fact that the DF, F_d, and the Hamiltonian, H_d, are highly discontinuous.

1.2.3 Mean-field distribution

The discrete quantities introduced in the previous section are actively fluctuating and difficult to handle. However, when considering a large number of particles, $N \gg 1$, one can introduce a mean-field approximation. Seeing these discrete functions as a realisation of a stochastic process, the (smooth) mean DF and mean Hamiltonian read

$$F(\mathbf{w},t) = \langle F_\mathrm{d}(\mathbf{w},t)\rangle, \quad H(\mathbf{w},t) = \langle H_\mathrm{d}(\mathbf{w},t)\rangle, \tag{1.10}$$

where $\langle\cdot\rangle$ stands for the expectation of the stochastic process, i.e., the average over realisations (while only varying the initial conditions). These realisations correspond, in this thesis, to different initial conditions independently sampled from the same (mean-field) distribution. The greater the number of particles N, the closer to these mean functions. This is illustrated in figure 1.3 for a 1D system, where I represent the discrete and the mean-field density together with the cumulative density to understand the proximity between the two functions. Using the linearity of

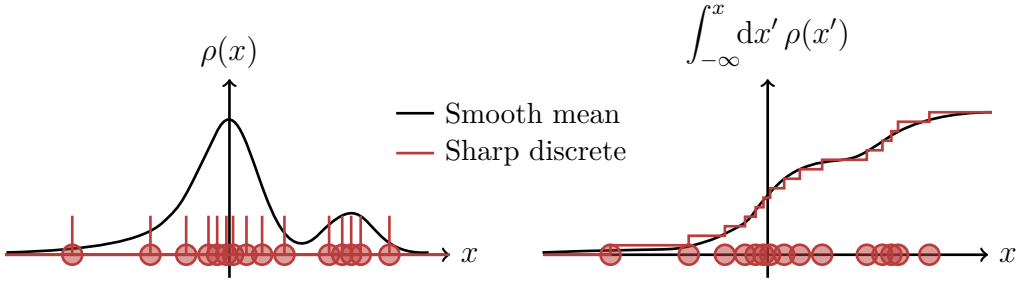

Figure 1.3: Illustration of the discrete vs the smooth density and cumulative density functions in a 1D system. For a large number of particles, $N \gg 1$, the instantaneous discrete density is well approximated by the smooth mean-field density.

the expectation in equations (1.6) and (1.9), one similarly has $H(\mathbf{w},t) = \mathbf{v}^2/2 + \psi(\mathbf{w},t)$. Here, the mean-field potential, $\psi = \langle\psi_\mathrm{d}\rangle$, follows from equation (1.6) and reads

$$\psi(\mathbf{w},t) = \int \mathrm{d}\mathbf{w}'\, F(\mathbf{w}',t)\, U(\mathbf{w},\mathbf{w}'). \tag{1.11}$$

This smooth potential is a particularly good approximation of the discrete potential because gravity is a long-range force. Phrased differently, the orbits of stars in a galaxy are predominantly influenced by the collective gravitational potential of the entire galaxy rather than by the immediate interactions with nearby stars. This is in sharp contrast with the motion of molecules in a gas which is primarily driven by violent and short-lived interactions with their nearest neighbours.

1.2.4 Perturbative expansion

The initial N–body (discrete) system can then be seen as fluctuations (Poisson shot noise, scaling as $1/\sqrt{N}$) on top of the mean-field functions introduced in equation (1.10), yielding the perturbative expansions

$$F_\mathrm{d} = F + \delta f, \quad \psi_\mathrm{d} = \psi + \delta\psi, \quad H_\mathrm{d} = H + \delta\psi. \tag{1.12}$$

Substituting these expansions in the Klimontovich equation (1.8), the mean-field DF and the fluctuations evolve through time following the coupled equations

$$\frac{\partial F}{\partial t} + [F, H] = -\langle[\delta f, \delta\psi]\rangle, \tag{1.13a}$$

$$\frac{\partial \delta f}{\partial t} + [\delta f, H] + [F, \delta\psi] + [\delta f, \delta\psi] - \langle[\delta f, \delta\psi]\rangle = 0, \tag{1.13b}$$

where I assumed $\langle\delta f\rangle = \langle\delta\psi\rangle = 0$. These equations represent a perturbative expansion approach to understanding the dynamics of a gravitational N–body system. Each equation and term within these equations play a specific role in capturing the evolution of the system as I shall now detail.

1.2.5 Violent relaxation

The first equation (1.13a) describes the evolution of the mean-field DF, F. At the lowest order, it is driven by the Poisson bracket of the mean-field DF and the mean-field Hamiltonian, H, on the l.h.s. of the equation. When this term is non-zero, the mean-field evolution is approximately described by the Vlasov–Poisson equations (Vlasov, 1968)

$$\frac{\partial F}{\partial t} + [F, H] = 0, \tag{1.14a}$$

$$H(\mathbf{w}, t) = \tfrac{1}{2}\mathbf{v}^2 + \int \mathrm{d}\mathbf{w}' F(\mathbf{w}', t)\, U(\mathbf{w}, \mathbf{w}'). \tag{1.14b}$$

It captures the *violent collisionless relaxation* of an out-of-equilibrium system (Lynden-Bell, 1967). This is the typical equation at play to describe the merger of two galaxies, as illustrated in figure 1.4. The fast dynamics is driven by significant changes in the gravitational potential due to

Figure 1.4: Illustration of the merger of two galaxies. The fast dynamics are driven by significant changes in the gravitational potential due to the rearrangement of mass, as the system seeks a new equilibrium configuration. This phase of violent relaxation is captured by the coupled Vlasov–Poisson equations (1.14). Credit: NASA/ESA Hubble Space Telescope.

the rearrangement of mass, as the system seeks a new equilibrium configuration. As visible in the coupled Vlasov–Poisson equations (1.14), violent relaxation involves highly non-linear changes in

the system's properties and therefore is specifically challenging to understand. Very few analytical results have been obtained (see, e.g., Chavanis, 2006b, for a review) and the full understanding of the outcome of this phase remains an open question and an active field of research (Ewart et al., 2022; Chavanis, 2022; Teles et al., 2023; Worrakitpoonpon, 2024). At the end of this short and violent phase, the system reaches a so-called quasi-stationary state (QSS) such that

$$[F, H] = 0. \tag{1.15}$$

Importantly, this mean-field equilibrium is usually not the thermodynamical equilibrium of the system. In fact, there is no such a thing as a thermal equilibrium for 2D and 3D self-gravitating systems, i.e., there is no state of maximum entropy (Campa et al., 2014). A QSS is an equilibrium state of the collisionless dynamics. It physically reflects the fact that the system locks itself: it cannot exchange angular momentum internally. If the system was perfectly isolated and did not experience any noise, it would remain in this state indefinitely. The existence of such a state is a direct consequence of the long-range nature of the gravitational force (Gabrielli et al., 2010). In practice, the system will still evolve under the effect of internal or external fluctuations as captured by the r.h.s. of equation (1.13a). However, this evolution happens on timescales much longer than the ones of violent relaxation. This is the regime of secular or long-term evolution in which I am interested in this thesis.

The mean-field equilibrium reached at the end of violent relaxation is typically much more symmetric than the initial conditions. Equation (1.15) states that the equilibrium DF, F, is constant along the flow generated by the Hamiltonian, H. As a consequence, this DF and its associated Hamiltonian, $H = H[F]$, are only functions of the integrals of motion (Jeans' theorem).

1.2.6 Angle-action variables

For *integrable* systems, the number of independent integrals of motion (invariants) is, at least, equal to the dimension of the system's physical space, d. In such a case, useful sets of canonical coordinates are angles-actions variables $(\boldsymbol{\theta}, \mathbf{J})$. They are defined such that the actions, $\mathbf{J}$, are isolating integrals of motion and the angles, $\boldsymbol{\theta}$, are 2π-periodic. Following equation (3.195) of Binney & Tremaine (2008), the actions of an orbit are given by the circulation of the momenta $\mathbf{p}$ along the orbital torus (Poincaré invariants)

$$J_i \equiv \frac{1}{2\pi} \oint \mathrm{d}q_i \, p_i, \tag{1.16}$$

where the integration contour runs along the orbit. Within its angle-action system of coordinates, an equilibrium Hamiltonian is independent of the angles, i.e., $H = H(\mathbf{J})$. Therefore, Hamilton's equations (1.1) take the simple form

$$\frac{\mathrm{d}\boldsymbol{\theta}}{\mathrm{d}t} = \frac{\partial H}{\partial \mathbf{J}} = \boldsymbol{\Omega}(\mathbf{J}), \quad \frac{\mathrm{d}\mathbf{J}}{\mathrm{d}t} = -\frac{\partial H}{\partial \boldsymbol{\theta}} = \mathbf{0}, \tag{1.17}$$

with $\boldsymbol{\Omega}(\mathbf{J})$ the orbital frequencies. Trajectories become particularly simple, since

$$\boldsymbol{\theta}(t) = \boldsymbol{\theta}_0 + \boldsymbol{\Omega}(\mathbf{J})\, t, \quad \mathbf{J}(t) = \mathbf{J}_0, \tag{1.18}$$

and the orbits, while intricate in the initial configuration space, are formally straight lines in angle-action space.

To illustrate the angle-action coordinates, I represent in figure 1.5 the change of coordinates from position-velocity to angle-action in the simple case of a harmonic oscillator. In such a case, orbits are concentric circles in the position-velocity coordinates and straight lines in the angle-action ones. Furthermore, the action can be computed as a simple function of the circle's "radius". Using the action definition (1.16), one can easily show that $J \propto r^2$ where r is the "radius" of the orbit in the (x, v)-plane.

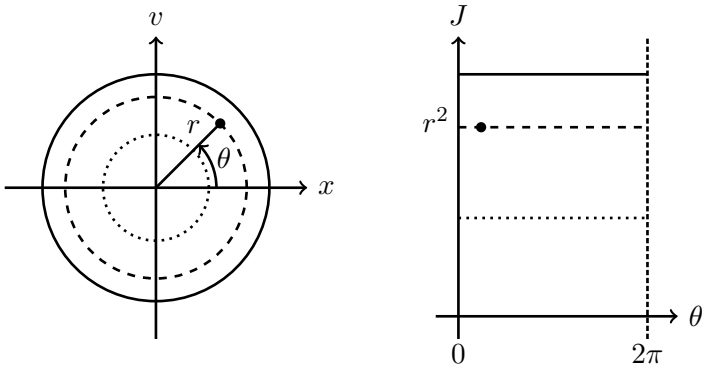

Figure 1.5: Schematic illustration of the change from position-velocity to angle-action coordinates for a harmonic oscillator. Importantly, within these new canonical coordinates, the trajectories become straight lines.

1.2.7 Secular evolution

Let me now assume the system has undergone violent relaxation and reached a QSS where the mean-field DF, as well as its associated (integrable) Hamiltonian, are only functions of the actions. Using the canonical angle-actions variables and the equilibrium property (equation 1.15), the evolution equations equation (1.13), together with the Poisson equation (1.6), form a closed set of equations. Using a quasi-linear approximation, i.e., assuming small fluctuations and neglecting the second-order contributions in their evolution, the set of equations reads

$$\frac{\partial F(\mathbf{J})}{\partial t} = -\langle [\delta f, \delta\psi] \rangle, \tag{1.19a}$$

$$\frac{\partial \delta f}{\partial t} + \boldsymbol{\Omega}(\mathbf{J}) \cdot \frac{\partial \delta f}{\partial \boldsymbol{\theta}} - \frac{\partial F}{\partial \mathbf{J}} \cdot \frac{\partial \delta\psi}{\partial \boldsymbol{\theta}} = 0, \tag{1.19b}$$

$$\delta\psi(\mathbf{w}, t) = \int \mathrm{d}\mathbf{w}' \, \delta f(\mathbf{w}', t) \, U(\mathbf{w}, \mathbf{w}'). \tag{1.19c}$$

The first equation (1.19a) describes the slow evolution of the mean-field DF under the small correlated effects of fluctuations. This is the regime of the secular evolution where stars diffuse away from their initial orbits while evolving in a quasi-stationary smooth potential imposed by long-range interactions. The bracket $\langle \cdot \rangle$ stands for the expectation of the stochastic process, i.e., the average over realisations. Together with the perturbative expansion equation (1.12), ensemble averaging is a necessary step to capture analytically some on the non-linear effects of the fluctuations on the mean-field evolution. Providing an expression for the r.h.s. of equation (1.19a), i.e., a collision operator, is the main goal of kinetic theory.

For example, such an equation captures how stars in the Milky Way undergo a so-called secular heating (Binney & Lacey, 1988; Johnston et al., 2017): the youngest stars in the solar neighbourhood have smaller velocity dispersions ($\sim 10\,\mathrm{km.s^{-1}}$) than the older population I stars ($\sim 40\,\mathrm{km.s^{-1}}$). This heating is well understood as the result of stochastic scatterings. These stochastic perturbations could naturally arise from local encounters with massive complexes such as giant molecular clouds (Spitzer & Schwarzschild, 1951). However, another source of significant fluctuations could be transient spiral arms. My thesis focuses on the effects of such global perturbations on the long-term evolution of stellar systems. Of course, these internal perturbations are not the only source of gravitational stochasticity in real galaxies who recurrently undergo minor mergers and are impacted by the turbulence of gas flows, supernovae and AGN feedback. The efficiency of these

various heating mechanisms can be strongly enhanced when exciting natural dynamical frequencies of the disc.

1.2.8 Collective effects

The ability to enhance fluctuations at specific frequencies is captured by the second and third equations (1.19b) and (1.19c). The second describes the fast (linearised) evolution of the fluctuations. The first term, $\boldsymbol{\Omega}(\mathbf{J})\cdot\partial\delta f/\partial\boldsymbol{\theta}$, solely captures the effect of differential rotation or *phase mixing*. Fluctuations are advected along the mean-field orbits at different rates/frequencies. They quickly get sheared, yielding in finer and finer structures. This process is illustrated in figure 1.6. The Gaia

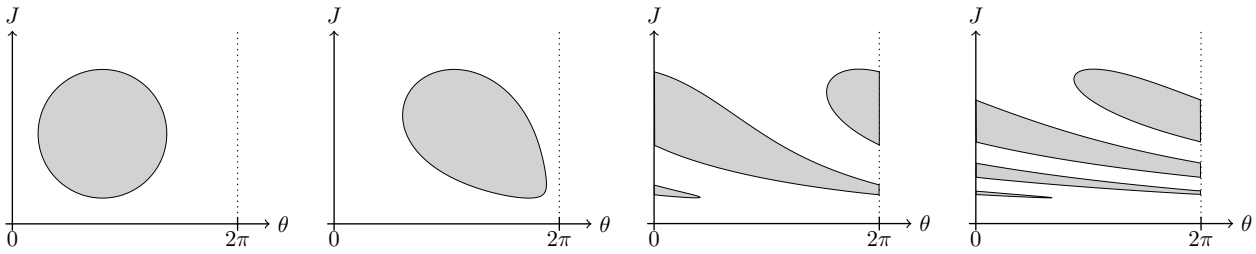

Figure 1.6: Figure from Fouvry (2017). Illustration of the phase mixing process in angle-action space. Fluctuations (grey blob) are advected along the (unperturbed) mean-field orbits at different rates/frequencies. The differential rotation quickly shears the fluctuations until they wash out.

snail (Antoja et al., 2018; Hunt et al., 2022; Tremaine et al., 2023) and stellar streams (Johnston et al., 1995; Bonaca & Price-Whelan, 2024) are typical examples of ongoing phase mixing in the Milky Way.

The second term in the evolution equation (1.19b), $\partial F/\partial\mathbf{J}\cdot\partial\delta\psi/\partial\boldsymbol{\theta}$, together with the third equation (1.19c), captures how the density fluctuations are impacted by the potential fluctuations they generate. These are the so-called *collective effects* induced by self-gravity.

The impact of collective effects on the secular evolution of stellar systems is the main focus of my thesis. In dynamically cold systems such as galactic discs, these effects can be particularly strong. Swing amplification (Toomre, 1981) is a typical example: a small perturbation can be amplified by a few orders of magnitude even in a stable system. The colder the system, the stronger the amplification. These cold systems are centrifugally supported and have a low velocity dispersion compared to their typical rotational velocity. The corresponding kinetic energy offers a large reservoir of free energy that can be used to redistribute the angular momentum in the system through collective behaviours such as spiral structures (Lynden-Bell & Kalnajs, 1972). Conversely, dynamically hot systems such as globular clusters or elliptical galaxies are pressure supported and have a high velocity dispersion compared to their typical rotational velocity. In such systems, collective effects are usually expected to be weak: perturbations induce wakes which do not (strongly) self-amplify.

1.2.9 Kinetic theory

Kinetic theory aims to describe perturbatively the weakly non-linear evolution of many-body systems over secular timescales. This endeavour is timely given the wealth of data available across cosmic time (Gaia, SDSS, JWST, Euclid...). The main goal of kinetic theory is to provide a collision operator, i.e., an expression for the r.h.s. of equation (1.19a) so as to write

$$\frac{\partial F(\mathbf{J},t)}{\partial t} = \mathcal{C}[F](\mathbf{J}). \tag{1.20}$$

In parallel of similar developments in plasma physics (Landau, 1936), the first kinetic theories of stellar systems were developed by Jeans (1929) and Chandrasekhar (1942, 1943). These theories

are based on the assumption that the system is (locally) homogeneous and that relaxation is driven by two-body deflections. As such, they do not take collective effects into account. This is further discussed in chapter 5 and I refer to Chavanis (2013a,c, 2024) for a thorough historical account of kinetic theories of plasmas and stellar systems. Here, I just outline four major axes of differences that distinguish the different flavours of theories, highlighting key conceptual and methodological distinctions.

Local deflections vs resonant encounters The first conceptual difference is whether relaxation is driven by local deflections (Chandrasekhar, 1942) or resonant encounters (Landau, 1936). Chandrasekhar's theory focuses on local scatterings where the cumulative effect of many small-angle gravitational deflections between stars leads to a gradual relaxation of the system. In contrast, theories inspired by Landau's approach emphasise resonant encounters, where the interactions between stars at resonant velocity (homogeneous) or frequencies (inhomogeneous) drive the relaxation process. For homogeneous systems, these two approaches are equivalent (Chavanis, 2013a). Yet, in resonant formulations, emphasis is placed on global, low-order resonances, while high-order resonances corresponding to local deflections are most often truncated. If relaxation is mostly driven by local deflections, the Chandrasekhar theory provides a much more efficient way to compute the collision operator.

Homogeneity The second axis concerns whether the system and encounters are treated as homogeneous or if spatial inhomogeneity is taken into account. In classical kinetic theories, such as those developed by Chandrasekhar and those directly transposed from plasmas, the system is often approximated as homogeneous, assuming a uniform distribution of stars. However, more advanced theories incorporate spatial inhomogeneity, i.e., a non-constant mean-field density, by using angle-actions variables. Intermediate approaches consider homogeneous (local) encounters but averaged over the particle's orbital phase which take into account the spatial inhomogeneity of the system (see, e.g., Tep et al., 2022, and references therein).

External vs internal fluctuations The fluctuations which drives the relaxation can be considered as external or internal. In Fokker–Planck approaches (Chandrasekhar, 1942; Binney & Lacey, 1988; Weinberg, 2001), fluctuations are treated as external perturbations, simplifying somewhat the analysis. Conversely, the Landau and Balescu–Lenard theories consider the effect of internal shot-noise-driven fluctuations. This internal perspective provides a self-consistent understanding of the collective dynamics and self-driven long-term evolution of the system (Landau, 1936; Balescu, 1960; Lenard, 1960).

Collective effects Finally, the impact of self-gravity on the stochastic scattering of orbits is particularly difficult to take into account and took some time to be properly addressed. For plasmas, it led to the development of the Balescu–Lenard equation (Balescu, 1960; Lenard, 1960). In this case, collective effects tend to screen the interactions beyond the Debye length. It regularises the long-range divergence in the Landau equation. For self-gravitating systems, the impact of collective effects is much more diverse. Among these contributions let me point out the seminal work of Weinberg (1993) who showed the importance of self-gravity in the secular evolution of (homogeneous) stellar systems (see also Magorrian, 2021), and Pichon & Aubert (2006) in inhomogeneous systems.

It is only recently that a fully self-consistent internally-driven kinetic theory taking both spatial inhomogeneity and self-gravity into account has been achieved (Heyvaerts, 2010; Chavanis, 2012; Fouvry & Bar-Or, 2018; Hamilton, 2021). It led to the derivation of the *inhomogeneous Balescu–Lenard equation*. This equation describes the long-term evolution of stable stellar systems under the collisional resonant contributions of internal fluctuations dressed by collective effects. Since its

derivation, this equation has been successfully applied to various systems such as razor-thin discs (Fouvry et al., 2015), the Hamiltonian mean-field (HMF) model (Benetti & Marcos, 2017), galactic nuclei (Fouvry & Bar-Or, 2018) and the one-dimensional model (Roule et al., 2022). It is at the hearth of this thesis and is further discussed in chapters 5 and 6.

1.3 Overview

In this thesis, I aim to quantify the impact of collective effects on secular orbital diffusion in self-gravitating systems. I address the following questions: *What is the relationship between damped modes and orbital diffusion in galactic discs? When do collective effects enhance or dampen the long-term orbital reshuffling in self-gravitating systems? What kind of systems are least subject to orbital diffusions? What are the limitations of the current state-of-the-art kinetic theory?*

In chapter 2, I introduce the self-gravitating systems I am interested in, namely the one-dimensional model and the razor-thin disc. For each model, I present the corresponding angle-action variables along with the mean-field equilibria I consider in chapters 4 and 6.

Chapter 3 develops the necessary tools to study the linear response of a stellar system, i.e., how to solve equations (1.19b) and (1.19c) together. I notably pinpoint the specificities of inhomogeneous systems and the difficulties they raise. I also present a new method to take gravitational softening into account in the linear theory.

In chapter 4, I apply the method presented in chapter 3 to the models of chapter 2. I illustrate its versatility and its ability to capture instabilities as well as weakly damped modes. I discuss the convergence of this generic method and its limitations. Using numerical simulations, I also study the impact of gravitational softening on instabilities in razor-thin discs.

Chapter 5 presents the most advanced kinetic theories developed to study the secular evolution of self-gravitating systems, i.e., to solve equation (1.19a). I give some insights on the derivation of the corresponding inhomogeneous Balescu–Lenard equation to highlight the underlying assumptions and discuss their limitations. This theory is also compared to the historic Chandrasekhar theory of two-body relaxation.

In chapter 6, I apply the kinetic theories from chapter 5 to the models presented in chapter 2 and compare my predictions to numerical simulations. I show that collective effects can have very diverse consequences on the secular evolution of self-gravitating systems. Neglecting them can lead to significant overestimation as well as underestimation of the relaxation rate. Conversely, taking them into account, the Balescu–Lenard equation is able to capture qualitatively and quantitatively the (average) secular evolution. I also discuss the limitations of this state-of-the-art theory, specifically for marginally stable systems.

In chapter 7, I study systems for which two-body encounters drive no relaxation. These systems are said to undergo a kinetic blocking. In this case, a kinetic equation has recently been derived to take into account the effect of three-body encounters while neglecting collective effects (Fouvry et al., 2019a, 2020; Fouvry, 2022). This equation can also be blocked for specific systems. Yet, I show that collective effects prevent three-body encounters from being unable to drive any relaxation.

Finally, chapter 8 summarises the main results of this thesis and discusses the perspectives they open.

Chapter 2

Mean-field models

Let me present the self-gravitating systems I studied during my PhD, namely the one-dimensional model and the razor-thin disc. For each model, I detail the explicit expressions for the mappings between different constants of motion, in particular the actions and frequencies. Finally, I present the analytical quasi-stationary state (QSS) I considered for each model.

2.1 The models

2.1.1 One-dimensional or "sheet" model

One-dimensional gravity is a toy model equivalent to aligned uniformly dense parallel planes in 3D attracting one another. It was first introduced by Spitzer (1942) and Camm (1950) to explain the vertical evolution of a self-gravitating disc of stars. Its simplicity allowed for an extensive numerical investigation of both its violent relaxation (see, e.g., Hohl & Campbell, 1968; Reidl & Miller, 1988; Teles et al., 2011) and its slow (collisional) evolution towards thermodynamical equilibrium (see, e.g., Wright et al., 1982; Yawn & Miller, 1997; Joyce & Worrakitpoonpon, 2010; Roule et al., 2022; Souza & Rocha Filho, 2023).

Similarly to infinite charged planes in electrostatics, the gravitational force created by one plane over another one does not depend on their respective separation, but only on their relative position (right or left). This model is illustrated in figure 2.1. It can be interpreted as particles embedded

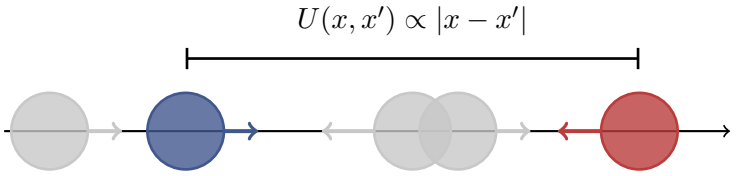

Figure 2.1: Illustration of the sheet model: particles are free to move on a line, interacting through a gravitational force proportional to the distance between them. As such, they can interpenetrate without merging and are in fact infinitely small (Dirac δ-functions).

on a line. On top of their usual (specific) kinetic energy, $\frac{1}{2}v^2$, particles are acting on one another through the interaction potential

$$U(x, x') = G\,|x - x'|, \tag{2.1}$$

with G the gravitational constant. In that limit, I also emphasise that there are no collisions between the particles: they can interpenetrate one another without colliding.

This interaction potential corresponds to the generalisation of Newton's gravity law to the one-dimensional case as equation (2.1) is naturally associated with the Poisson equation

$$\Delta\psi = 2G\rho, \tag{2.2}$$

where the prefactor 2 comes from the surface of the 1-sphere, $\{-1, 1\}$ (the analogue of 4π for the 3-sphere in the usual 3D-Poisson equation). In figure 2.2, I illustrate the density, the force and the potential fields induced by one particle in the sheet model. The 1D gravitational potential

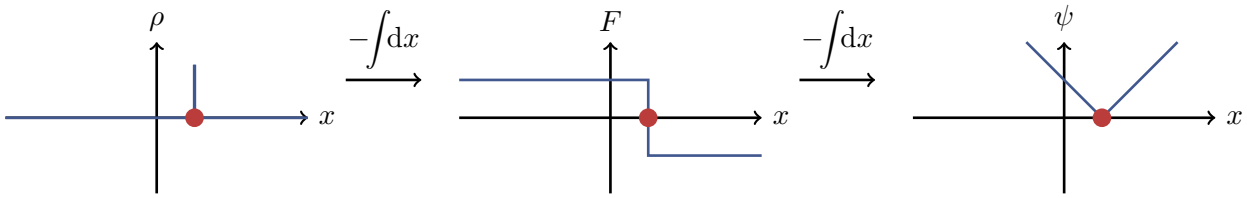

Figure 2.2: Illustration of the density (Dirac δ-function), the force field (Heaviside function) and the potential field (absolute value) induced by one particle in the sheet model.

differs from its 3D counterpart in two main respects: (i) it is unbounded at large separation, hence all particles are trapped (i.e., no escapers are possible); (ii) it is finite at zero separation allowing particles to cross one another.

Numerous simplifications arise from the one-dimensional assumption, both for N–body simulations and for analytical and computational developments of the corresponding kinetic theory. This system will be investigated in detail in sections 4.1 and 6.1.

2.1.2 Razor-thin disc

Turning my interest to the in-plane motion of stars in a flat galaxy, I now consider a razor-thin disc of stars. In this configuration, the motion of the stars is confined to the same (infinitely thin) plane, but stars do interact through the usual $3D$ Newtonian gravity. The pairwise interaction potential then is

$$U(\mathbf{r}, \mathbf{r}') = \frac{-G}{\|\mathbf{r} - \mathbf{r}'\|}, \tag{2.3}$$

with G the strength of the interaction and $\|\mathbf{r}-\mathbf{r}'\|^2 = r^2 + r'^2 - 2rr'\cos(\phi-\phi')$, using the polar coordinates $\mathbf{r} = (r, \phi)$.

Within an axisymmetric configuration, the typical motion of (bounded) stars are rosette-like orbits, illustrated in figure 2.3. Stars oscillate between two extreme radii, the pericentre r_p and

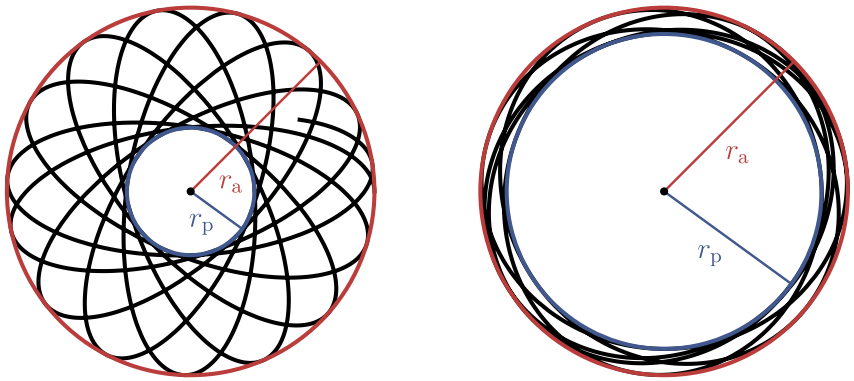

Figure 2.3: Inspired by Hamilton & Fouvry (2024). Illustration of the rosette-like orbits of stars in the galactic plane and in globular clusters. Typical orbits in galactic discs are nearly circular (right). Orbits in globular clusters are more eccentric (left).

the apocentre r_a. When the potential is dominated by the central mass, the motion reduces to the well-known Keplerian orbits. In a realistic galactic disc, most stars lie on nearly circular orbits, with small eccentricities (Binney & Tremaine, 2008).

2.2 Orbital constants

In this section, I detail the explicit expressions for the mappings between different constants of motion in the one-dimensional model and the razor-thin disc, in particular the actions and frequencies. As the mean-field motion of self-gravitating systems is naturally described in angle-action coordinates (equation 1.18), accurately computing these quantities is the first necessary step towards describing their (long-term) dynamics.

2.2.1 One-dimensional model

I consider a mean-field equilibrium associated with a symmetric potential $\psi(-x)=\psi(x)$. Given that this potential is unbounded (following equation 2.1), all particles are trapped, and therefore librate around the position $x=0$. As such, an orbit of energy E may be solely characterised by its apocentre, r_a, i.e., the maximum radius reached during the particle's libration. It is defined through

$$\psi(r_\mathrm{a}) = E. \tag{2.4}$$

Following equation (1.16), the action of a particle is defined by the integral of the momentum, $v=\pm\sqrt{2[E-\psi(x)]}$, during one full radial oscillation. Paying careful attention to the prefactors, it reads

$$\begin{aligned} J &= \frac{1}{\pi}\int_{-r_\mathrm{a}}^{r_\mathrm{a}} \mathrm{d}x\, \sqrt{2[E-\psi(x)]} \\ &= \frac{2\sqrt{2}}{\pi}\int_{0}^{r_\mathrm{a}} \mathrm{d}x\, \sqrt{\psi(r_\mathrm{a})-\psi(x)}. \end{aligned} \tag{2.5}$$

The associated frequency, Ω, naturally follows from $\Omega=\partial H/\partial J$ (equation 1.17), so that

$$\begin{aligned} \frac{1}{\Omega} &= \frac{1}{\pi}\int_{-r_\mathrm{a}}^{r_\mathrm{a}} \frac{\mathrm{d}x}{\sqrt{2[E-\psi(x)]}} \\ &= \frac{\sqrt{2}}{\pi}\int_{0}^{r_\mathrm{a}} \frac{\mathrm{d}x}{\sqrt{\psi(r_\mathrm{a})-\psi(x)}}. \end{aligned} \tag{2.6}$$

However, the integration in this equation should not be performed as such, because its integrand diverges like $1/\sqrt{x}$ at the edge of the domain $x=r_\mathrm{a}$. It is therefore more appropriate to perform a change of variables, $x=r_\mathrm{a}f(w)$, towards an effective anomaly, $-1\leq w\leq 1$, that allows for explicit mappings, and cures the edge divergences. To do so, the mapping function, f, should satisfy $f(\pm1)=\pm1$ and $f'(\pm1)=0$. In practice, I use Hénon's mapping function (Hénon, 1971)

$$f(w) = \frac{1}{2}\left(3w - w^3\right), \tag{2.7}$$

and the frequency integral equation (2.6) becomes

$$\frac{1}{\Omega} = \frac{\sqrt{2}}{\pi}\int_{0}^{1} \mathrm{d}w\, \Theta_{r_\mathrm{a}}(w), \tag{2.8}$$

where I introduced the angle gradient (w.r.t. the Hénon anomaly)

$$\Theta_{r_\mathrm{a}}(w) = \frac{r_\mathrm{a}f'(w)}{\sqrt{\psi(r_\mathrm{a})-\psi[r_\mathrm{a}f(w)]}}. \tag{2.9}$$

To address the arising 0/0 limit in this quantity, I use a second-order Taylor expansion in $w\to\pm1$. Computing the frequency from equation (2.8) then requires a numerical integration of the (regularised) integrand Θ_{r_a}. I perform this integral using the Simpson's 1/3 rule with K_mf integration

nodes. The angle gradients, $\Theta_{r_\mathrm{a}}(w)$, are smooth functions of the anomaly w, so that the integration scheme quickly converges. I typically use $K_\mathrm{mf}=100$.

Finally, the canonical angle, θ, associated with the action, J, from equation (2.5) follows from equation (37) of Tremaine & Weinberg (1984). It reads

$$\theta = \int_{\mathcal{C}} \mathrm{d}x' \, \frac{\Omega}{\sqrt{2[E-\psi(x')]}}, \tag{2.10}$$

where $\mathcal{C}$ is the contour going from $x'=-r_\mathrm{a}$ up to the current position $x'=x(\theta)$ along the radial oscillation. Therefore, the angle mapping is such that

$$x(\theta=0) = -r_\mathrm{a},\ x(\tfrac{\pi}{2}) = 0,\ x(\pi) = r_\mathrm{a},\ x(\tfrac{3\pi}{2}) = 0. \tag{2.11}$$

2.2.2 Razor-thin discs

Let me now consider razor-thin discs. Assuming central symmetry, i.e., $\psi=\psi(r)$, natural isolating integrals of motion are energy E and angular momentum L defined as

$$E = \frac{1}{2}\dot{r}^2 + \psi_\mathrm{eff}(r,L), \quad L = r^2\dot{\phi}, \tag{2.12}$$

with the polar coordinates, (r,ϕ). In equation (2.12), I introduced the effective potential

$$\psi_\mathrm{eff}(r,L) = \psi(r) + \frac{L^2}{2r^2}. \tag{2.13}$$

Given an angular momentum, L, this effective potential sets the radial motion of the particle. It is illustrated in figure 2.4. Stars oscillate radially between the pericentre, r_p, and the apocentre, r_a,

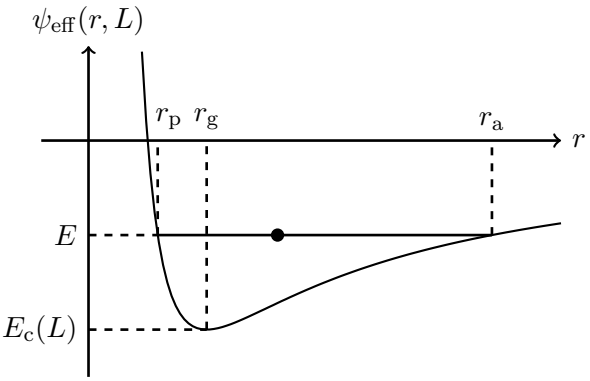

Figure 2.4: Illustration of the effective potential, ψ_eff, from equation (2.13). Bounded orbits ($E<0$) oscillate between the pericentre r_p and the apocentre r_a. Circular orbits correspond to the minimum of the effective potential. They are equivalently defined by their angular momentum, L, circular energy, E_c, or guiding radius, r_g.

defined as the root of the equation $E=\psi_\mathrm{eff}(r)$. These constants of motion are defined independently of the mean-field potential, ψ, and are therefore good representative variables for the (bounded) orbits. From them, one can straightforwardly obtain the energy and angular momentum as

$$E = \frac{r_\mathrm{a}^2\psi(r_\mathrm{a}) - r_\mathrm{p}^2\psi(r_\mathrm{p})}{r_\mathrm{a}^2 - r_\mathrm{p}^2}, \quad L = \sqrt{\frac{2\,[\psi(r_\mathrm{a}) - \psi(r_\mathrm{p})]}{r_\mathrm{p}^{-2} - r_\mathrm{a}^{-2}}}. \tag{2.14}$$

Following equation (1.16), the natural actions variables $\mathbf{J}=(J_r, J_\phi)$ are given by (Lynden-Bell & Kalnajs, 1972)

$$J_r = \frac{1}{\pi}\int_{r_\mathrm{p}}^{r_\mathrm{a}} \mathrm{d}r\, v_r = \frac{1}{\pi}\int_{r_\mathrm{p}}^{r_\mathrm{a}} \mathrm{d}r \sqrt{2[E-\psi_\mathrm{eff}(r,L)]}, \tag{2.15a}$$

$$J_\phi = L. \tag{2.15b}$$

The radial action, J_r, encodes the eccentricity of the orbit and is such that $J_r=0$ corresponds to circular orbits. The associated frequencies, $(\Omega_r,\Omega_\phi)=\partial H/\partial\mathbf{J}$, are obtained through the dimensionless frequency ratios (Tremaine & Weinberg, 1984)

$$\frac{1}{\alpha}=\frac{\Omega_0}{\Omega_r}=\frac{\Omega_0}{\pi}\int_{r_\mathrm{p}}^{r_\mathrm{a}}\frac{\mathrm{d}r}{\sqrt{2[E-\psi_\mathrm{eff}(r,L)]}}, \tag{2.16a}$$

$$\beta=\frac{\Omega_\phi}{\Omega_r}=\frac{L}{\pi}\int_{r_\mathrm{p}}^{r_\mathrm{a}}\frac{\mathrm{d}r}{r^2\sqrt{2[E-\psi_\mathrm{eff}(r,L)]}}, \tag{2.16b}$$

where Ω_0 is a natural frequency scale, typically the maximal radial frequency at the system's centre (when it exists). In figure 2.5, I illustrate the typical mappings between the pericentre and apocentre, the energy and angular momentum, and these dimensionless frequency ratios.

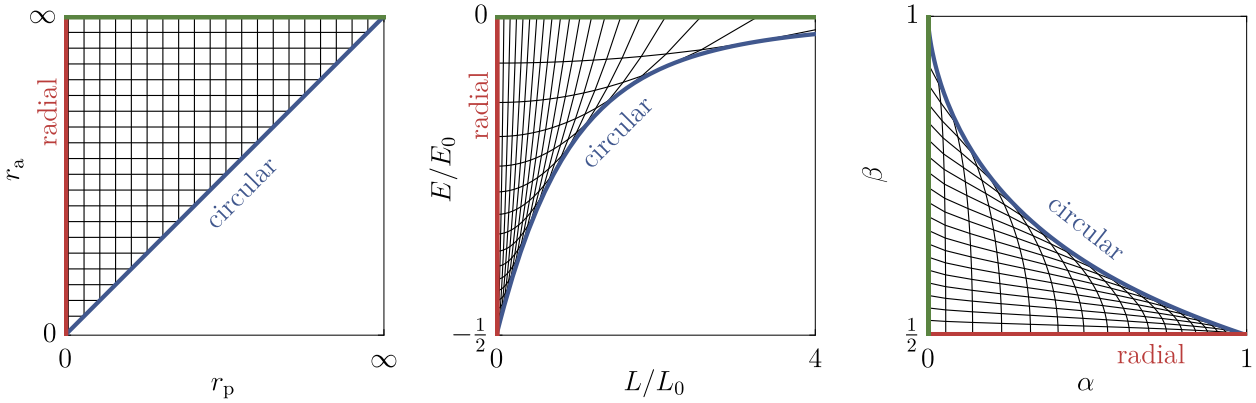

Figure 2.5: Illustration of the typical mappings between orbital constants in razor-thin discs with cored potential. The pericentre and apocentre (left), are mapped to energy and angular momentum (middle) from equation (2.14), and to the dimensionless frequency ratios (right) from equation (2.16). The red lines represent the radial orbits, while the blue lines represent the circular orbits and the green lines the infinitely far (yet bounded) orbits.

Similarly to equation (2.6), the integrals in equation (2.16) should be performed with care, as they diverge at the edges of the domain $r\to r_\mathrm{p/a}$. Using the same approach, I use the change of variables $r(w)=a[1+ef(w)]$ with $f(w)$ the Hénon mapping function (equation 2.7) and where I introduced the effective semi-major axis and eccentricity

$$a=\frac{r_\mathrm{a}+r_\mathrm{p}}{2},\quad e=\frac{r_\mathrm{a}-r_\mathrm{p}}{r_\mathrm{a}+r_\mathrm{p}}. \tag{2.17}$$

Once again, using this anomaly, the frequency integrand

$$\Theta(w)=\frac{aef'(w)}{\sqrt{2[E-\psi_\mathrm{eff}(r[w],L)]}}, \tag{2.18}$$

is no longer divergent and equations (2.16) simply read

$$\frac{1}{\alpha}=\frac{\Omega_0}{\pi}\int_{-1}^{1}\mathrm{d}w\,\Theta(w), \tag{2.19a}$$

$$\beta=\frac{L}{\pi}\int_{-1}^{1}\mathrm{d}w\,\frac{\Theta(w)}{r^2(w)}. \tag{2.19b}$$

Some examples of these frequency integrands, $w\mapsto\Theta(w)$, are illustrated in figure 2.6. Importantly, they are smooth and bounded functions of the anomaly w. Close to $w\to\pm1$, the integrands are interpolated to cure the arising 0/0 limit. Furthermore, for too small values of the effective semi-major axis, a, and/or eccentricities, e, close to 0 (circular orbits) or 1 (radial), their computation

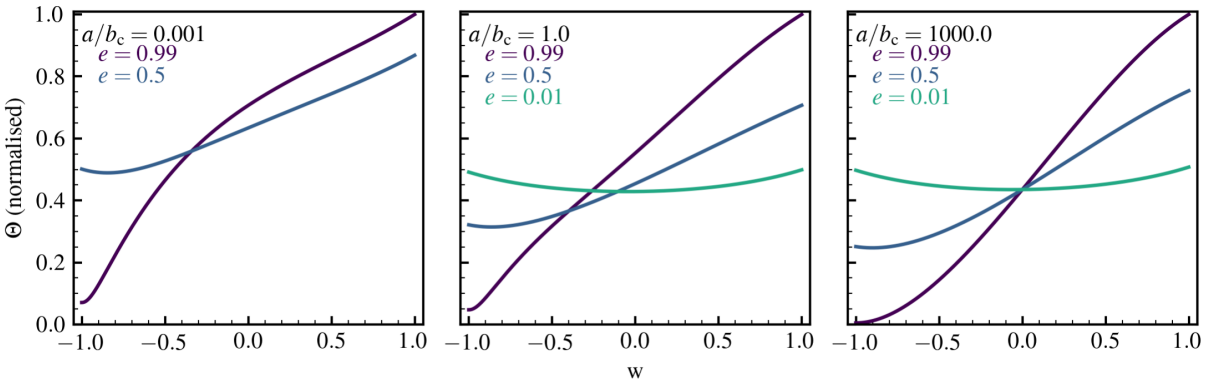

Figure 2.6: Figure from the cosigned article Petersen et al. (2024). Example of $\Theta(w)$ (equation 2.18) for different effective semi-major axes and eccentricities (a, e) (equation 2.17) in the isochrone potential (Hénon, 1959), $\psi(r) = -GM/(b_c + \sqrt{r^2 + b_c^2})$. The angle gradient is normalised to $\Theta(w=1)=1$, and semi-major axes with b_c, the potential scale radius. The range of w runs from -1 (pericentre) to 1 (apocentre). The curves are smooth and straightforward to integrate via low-order schemes. The line for $a/b_c = 0.001$ and $e = 0.01$ is not shown because it corresponds to an orbit for which interpolation is used to compute the frequency ratios (equation 2.16).

may fail. In these cases, I determine the frequency ratios from equation (2.16) through interpolation. For circular orbits, the frequency ratios follow from the epicyclic frequencies. They read

$$\alpha_c(r) = \frac{1}{\Omega_0}\sqrt{\psi''(r) + 3\frac{\psi'(r)}{r}}, \quad \beta_c(r) = \frac{\sqrt{\psi'(r)/r}}{\Omega_0\,\alpha_c(r)}. \tag{2.20}$$

From the frequency ratios, the radial and azimuthal frequencies are readily obtained through the mappings

$$\alpha = \Omega_r/\Omega_0, \quad \beta = \Omega_\phi/\Omega_r; \tag{2.21a}$$

$$\Omega_r = \alpha\Omega_0, \quad \Omega_\phi = \alpha\beta\Omega_0. \tag{2.21b}$$

Finally, the canonical angles, $\boldsymbol{\theta}$, associated with the action, $\mathbf{J}$, from equation (2.15) follows from equation (37) of Tremaine & Weinberg (1984). It reads

$$\theta_r[w] = \Omega_r \int_{-1}^{w} \mathrm{d}w'\,\Theta(w'), \tag{2.22a}$$

$$(\theta_\phi - \phi)[w] = \int_{-1}^{w} \mathrm{d}w' \left[\Omega_\phi - \frac{L}{r(w')^2}\right]\Theta(w'). \tag{2.22b}$$

2.3 Quasi-stationary states

2.3.1 One-dimensional model

This section is adapted from Roule et al. (2022).

For the one-dimensional model (section 2.1.1), I consider two explicit quasi-stationary distributions: (i) the global thermodynamical equilibrium; and (ii) a more peaked QSS, analogue of the 2D Plummer sphere (Plummer, 1911), as I now detail.

Thermodynamical equilibrium

Unlike their 3D analogues (unless confined in a box with repulsive walls – Padmanabhan, 1990; Miller & Youngkins, 1998; Chavanis, 2006a), 1D self-gravitating systems have a well-defined maximum entropy equilibrium state. Under the constraints of fixed total mass and energy, its density

follows (Spitzer, 1942; Camm, 1950; Rybicki, 1971; Joyce & Worrakitpoonpon, 2010)

$$\rho(x) = \frac{M_{\rm tot}}{2\Lambda}\,\mathrm{sech}^2(x/\Lambda)\,, \tag{2.23}$$

with Λ the system's characteristic length. The associated potential is given by

$$\psi(x) = E_0 \log\left[2\cosh\left(x/\Lambda\right)\right], \tag{2.24}$$

with $E_0 = GM_{\rm tot}\Lambda$ the characteristic (specific) energy, while its distribution function (DF) reads

$$F(E) = \frac{2M_{\rm tot}}{\sqrt{\pi}\sigma\Lambda}\,\exp(-2E/E_0)\,, \tag{2.25}$$

with $\sigma = \sqrt{GM_{\rm tot}\Lambda}$ the characteristic velocity. I emphasise that the DF from equation (2.25) cannot further relax by design. Naturally, this does not prevent individual particles from undergoing themselves a diffusion as detailed in chapter 6.

Plummer quasi-stationary equilibrium

I also investigate an equilibrium stemming from polytropes (Eddington, 1916; Hénon, 1973; Horedt, 2004). More precisely, by analogy with the 3D Plummer sphere (Plummer, 1911), I consider the 1D density

$$\rho(x) = \frac{M_{\rm tot}}{2\alpha}\left[1 + (x/\alpha)^2\right]^{-3/2}, \tag{2.26}$$

where $\alpha = 2\Lambda/\pi$ ensures that this distribution has the same energy as equation (2.23). The associated DF follows the power law distribution

$$F(E) = \frac{15\,G^3\,M_{\rm tot}^4\,\alpha^2}{32\sqrt{2}}\,E^{-7/2}. \tag{2.27}$$

This DF was obtained through Eddington's inversion formulae (appendix 2.A). In figure 2.7, I illustrate the density and frequency profiles of these two states. While the thermodynamical equi-

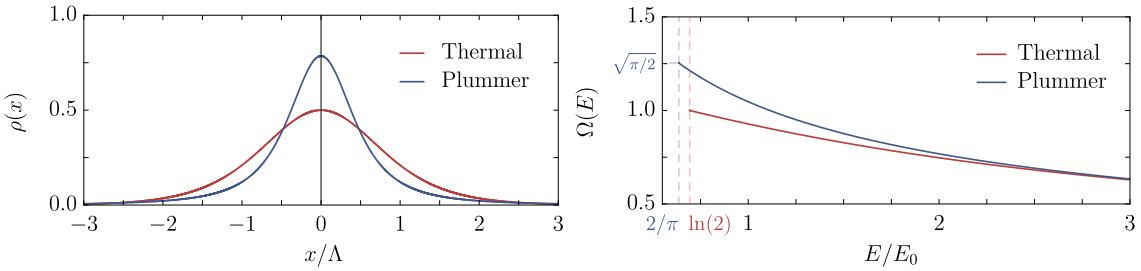

Figure 2.7: Figure from Roule et al. (2022). *Left:* Density profiles of the thermal and Plummer equilibria. The Plummer equilibrium has a sharper core. *Right:* Corresponding frequency profiles. The range of available frequencies is wider for the Plummer equilibrium. The vertical dashed lines represent the minimal (central) energy in each equilibrium.

librium has a strong core and few particles in the tails (only $\sim 10^{-9} M_{\rm tot}$ outside $[-10\Lambda, 10\Lambda]$), the Plummer distribution has a sharper core and much wider tails ($\sim 10^{-3} M_{\rm tot}$ outside $[-10\Lambda, 10\Lambda]$). The Plummer denser core widens its frequency profile, allowing in turn for more resonances. At high energies, both frequency profiles decrease like $1/\sqrt{E}$. This is the expected "Keplerian" behaviour for a one-dimensional system. For a particle at very large energy, it is as if all the mass was concentrated at the origin, leading to a potential $\psi(x) \propto |x|$. Injecting this form in equation (2.6), one can retrieve the expected behaviour.

Polytropes quasi-stationary equilibria

The "Plummer" equilibrium presented in the previous paragraph corresponds to a particular case of a broader class of equilibria called polytropes (see Horedt, 2004, for a review on their use in astrophysics). Polytropes are hydrostatic equilibria between pressure and gravitational forces which satisfy a so-called polytropic relation of the form

$$P = K\,\rho^{1+1/n}, \tag{2.28}$$

between the pressure, P, and the density, ρ. As detailed in appendix 2.B, polytropes have exact analytical solutions in 3 different cases: $n = 0$ ($\rho = \text{cst}$), $n = 1$ and $n = \frac{d+2}{d-2}$ (Horedt, 2004).

The Plummer equilibrium corresponds to this last analytical case. One could also be interested in the second one, $n=1$. This solution has density

$$\rho(x) = \frac{M_{\rm tot}\pi}{4\alpha}\cos\left(\frac{\pi}{2}\frac{x}{\alpha}\right)\mathbb{1}_{|x|<\alpha}, \tag{2.29}$$

It has the same total energy as the thermodynamical equilibrium if $\alpha=2\Lambda$. It is difficult to predict and measure the long-term evolution of this model due to the rough cut-off in density and the diverging gradient of the associated DF,

$$F(E) = \frac{\pi\sqrt{2}M_{\rm tot}}{8\alpha\sqrt{GM_{\rm tot}\alpha}}\sqrt{1-\frac{E}{GM_{\rm tot}\alpha}}\,\mathbb{1}_{1-\frac{2}{\pi}\leq E/GM_{\rm tot}\alpha\leq 1}. \tag{2.30}$$

Furthermore, as this model has a more prominent core than the thermal equilibrium, its frequency profile is flattened. This can lead to a particularly slow relaxation towards the thermodynamical equilibrium. This is discussed further in section 6.1.2. All in all, it makes both theoretical predictions and measurements in N–body experiments too challenging. I did not investigate further the model from equation (2.29).

2.3.2 Razor-thin discs

I will mainly focus on one model of discs, namely tapered Mestel discs. These discs' dynamics have been extensively studied (e.g., Zang, 1976; Toomre, 1981; Evans & Read, 1998b; Sellwood & Evans, 2001; Sellwood, 2012; Fouvry et al., 2015). They are not perfectly representative of observed galactic profiles whose radial surface-brightness are better fitted by one (Freeman, 1970; Elmegreen et al., 2005) or two (Pohlen & Trujillo, 2006) exponential profiles, mainly depending on their Hubble type.[1] However, they offer a well-documented test case for the study of these dynamically cold systems, with a flat rotation curve.

Mestel disc

A razor-thin Mestel disc has constant circular velocity, $v_{\rm c}=\sqrt{r\partial\psi/\partial r}=V_0$, mimicking the (relatively) flat rotation curve of the Milky Way (Eilers et al., 2019). The associated potential is

$$\psi(r) = V_0^2\ln(r/R_0), \tag{2.31}$$

with R_0 an arbitrary length scale. It requires a surface density

$$\Sigma(r) = \frac{V_0^2}{2\pi G r} = \Sigma_0\frac{R_0}{r}, \tag{2.32}$$

[1] While going from surface-brightness to surface-density is no easy task, the Milky Way is well captured by a single exponential density profile (Bovy & Rix, 2013).

with $\Sigma_0 = V_0^2/2\pi G R_0$. In such a disc, any (centred) annulus of radial size $\mathrm{d}r$ contains the same mass $\mathrm{d}M = V_0^2 \mathrm{d}r/G$. Mestel discs therefore have infinite mass.

The orbital frequencies of this profile diverge at the centre. To cure this divergence, I truncate the Mestel potential, so that equation (2.31) becomes

$$\psi(r) = V_0^2 \ \ln\left(\sqrt{\left(\frac{r}{R_0}\right)^2 + \varepsilon^2}\right), \tag{2.33}$$

with $\varepsilon \ll 1$. This truncation introduces a scale length in this scale-invariant disc and breaks the self-consistency between the distribution function and the potential. In practice, I performed such a softening for numerical reasons, and ensured that the cut-off was small enough not to affect the disc's dynamical properties. However, it could also be physically motivated as the rotation curve of real galaxies is not perfectly flat and decreases in the central regions (Rubin et al., 1980). In this case, one would probably want to set an observationally-motivated value for the cut-off.

A compatible DF for a (non-truncated) Mestel disc is given by

$$F(E, L) = C \, L^q \, \mathrm{e}^{-E/\sigma^2}, \tag{2.34}$$

where σ is the radial velocity dispersion and

$$q = \left(\frac{V_0}{\sigma}\right)^2 - 1, \quad C = \frac{V_0^2}{2^{q/2+1}\pi^{3/2} \, G \, \Gamma[(q+1)/2] \, \sigma^{q+2} R_0^{q+1}}, \tag{2.35}$$

respectively the power index, which measures the degree to which the disk is centrifugally supported, and the normalisation constant (equation 4.163 in Binney & Tremaine, 2008).

Taper and active fraction

In order to deal with the singularity at the centre and the infinite mass of this disc, I follow Evans & Read (1998b) and introduce an inner and an outer tapering in the distribution equation (2.34). These tapers do not affect the mean-field potential. Once again, it breaks the self-consistency between the DF and the potential, but in fact allows for a more realistic description. The total potential can be interpreted as generated by (i) an inert bulge in the centre,[2] (ii) an inert halo (which dominates in the outer region) and (iii) the self-gravitating disc. In addition, I can also vary the overall amplitude of the DF with a constant prefactor, ξ, called the active fraction. This free parameter allows me to control the relative importance of the self-gravitating disc to the total potential. It is a proxy for the relative masses of the disc and the dark matter halo (which I assume to be gravitationally inert).

Importantly, the tapered Mestel disc (or Zang disc) is therefore to be thought as a multi-component (bulge, disc, halo) system in which the disc is much more responsive to any perturbation than the other components. This will be justified in chapter 5 by the geometry and dynamical temperatures of the different components. Probing the (coupled) evolution of a true, self-consistent, multi-component system would be particularly interesting but is beyond the scope of this thesis. All in all, the DF is given by

$$F(E, L) = \xi \, C \, L^q \, \mathrm{e}^{-E/\sigma^2} \, T_{\mathrm{in}}(L) \, T_{\mathrm{out}}(L). \tag{2.36}$$

In this equation the inner and outer tapers act on the angular momentum only. All central, distant and radial orbits are suppressed by the tapers. They read

$$T_{\mathrm{in}}(L) = \frac{L^\nu}{(R_{\mathrm{in}} V_0)^\nu + L^\nu}, \quad T_{\mathrm{out}}(L) = \frac{(R_{\mathrm{out}} V_0)^\mu}{(R_{\mathrm{out}} V_0)^\mu + L^\mu}. \tag{2.37}$$

[2] Note that discs with too sharp inner taper (indices $\nu > 2$ in equation 2.37) do not admit spherical bulges whose volume densities are everywhere non-negative (see appendix B in Zang, 1976).

The sharpness of the inner (resp. outer) taper is controlled by the power index ν (resp. μ) while its location is set by the radius $R_{\rm in}$ (resp. $R_{\rm out}$). The exact set of parameters are given in appendix 2.C.

Appendices

2.A Eddington's inversion

I now detail the construction of a self-consistent distribution function given a density profile for a $1D$ integrable system. This follows the Eddington's inversion, as given in section 4.3.1 of Binney & Tremaine (2008).

Let me consider a system whose mean-field density is given by $\rho=\rho(r)$, with $r=|x|$, and the associated potential $\psi=\psi(r)$. I assume that the potential is a monotonically increasing function of radius, and similarly the density is monotonically decreasing. I suppose that the system is in mean-field equilibrium, so that $F=F(E)$, with $E=\frac{1}{2}v^2+\psi(r)$. By definition, the density satisfies the self-consistency relation

$$\begin{aligned}\rho(r) =& \int_{-\infty}^{+\infty} \mathrm{d}v\, F(x,v)\\ =& \int_{-\infty}^{+\infty} \mathrm{d}v\, F\big[\tfrac{1}{2}v^2+\psi(r)\big]\\ =& \,2\int_{0}^{+\infty} \mathrm{d}v\, F\big[\tfrac{1}{2}v^2+\psi(r)\big]. \end{aligned} \tag{2.38}$$

Performing the change of variable $\mathrm{d}E=v\mathrm{d}v$, I can write

$$\rho(r) = 2\int_{\psi}^{+\infty} \mathrm{d}E\, \frac{F(E)}{\sqrt{2(E-\psi)}}, \tag{2.39}$$

where I introduced the shortened notation $\psi=\psi(r)$. Since $\psi=\psi(r)$ is a monotonic function of r, one can regard the density ρ as a function of ψ rather than r. I then rewrite equation (2.39) as the self-consistent relation

$$\frac{1}{\sqrt{2}}\,\rho(\psi) = \int_{\psi}^{+\infty} \mathrm{d}E\, \frac{F(E)}{\sqrt{E-\psi}}. \tag{2.40}$$

This takes the form of an Abel integral equation which can be explicitly inverted. Following equation (B.72) of Binney & Tremaine (2008), it reads

$$\begin{aligned}F(E) =& -\frac{1}{\pi\sqrt{2}}\frac{\mathrm{d}}{\mathrm{d}E}\int_{E}^{+\infty} \mathrm{d}\psi\, \frac{\rho(\psi)}{\sqrt{\psi-E}}\\ =& -\frac{1}{\pi\sqrt{2}}\int_{E}^{+\infty} \mathrm{d}\psi\, \frac{\mathrm{d}\rho/\mathrm{d}\psi}{\sqrt{\psi-E}}\\ =& \,\frac{\sqrt{2}}{\pi}\int_{E}^{+\infty} \mathrm{d}\psi\, \sqrt{\psi-E}\,\frac{\mathrm{d}^2\rho}{\mathrm{d}\psi^2}. \end{aligned} \tag{2.41}$$

Using Poisson equation (1.19c), the potential associated to the Plummer quasi-stationary state from equation (2.26) reads

$$\psi(x) = GM_{\mathrm{tot}}\alpha\left[1+(x/\alpha)^2\right]^{1/2}. \tag{2.42}$$

The density then is a simple function of the potential and reads

$$\rho(\psi) = \frac{M_{\mathrm{tot}}}{2\alpha}\left(\frac{\psi}{GM_{\mathrm{tot}}\alpha}\right)^{-3}. \tag{2.43}$$

From this expression and Edington's inversion equation (2.41), one can retrieve the distribution function of the Plummer model given in equation (2.27).

2.B Polytropes

Considering spherically-symmetric systems, the equilibrium between pressure and gravitational forces can be written as

$$\begin{aligned}\Delta P =& \frac{1}{r^{d-1}}\frac{\mathrm{d}}{\mathrm{d}r}\left[r^{d-1}\frac{\mathrm{d}P}{\mathrm{d}r}\right]\\ =& \,\mathcal{S}_d(1)\,G\,\rho(r), \end{aligned} \tag{2.44}$$

where $\mathcal{S}_d(1)$ is the surface of the d-dimensional unit-sphere (2 in 1D, 2π in 2D, 4π in 3D). Assuming a polytropic relation between pressure and density (equation 2.28), one can

Distribution function name	Active fraction ξ	Power index q	Inner taper		Outer taper[3]	
			$R_{\rm in}$	ν	$R_{\rm out}$	μ
Zang $\nu=...$	1	6	1	...	11.5	5
Toomre[4]	0.5	11.4	1	4	11.5	5

Table 2.1: Values of the parameters for the razor-thin discs explored in this thesis (equations 2.36–2.37).

find a set of particular solutions of the hydrostatic equilibrium. Using this relation in the change of variables $\rho=\rho_0\,\theta^n$ (equation 2.28 implies $P=P_0\,\theta^{n+1}$) and $r=\alpha\xi$ with $\alpha=\sqrt{|n+1|P_0/(\mathcal{S}_d(1)G\rho_0^2)}$, one can retrieve the Lane–Emden equation (see, e.g., equation 2.1.14 in Horedt, 2004)

$$\frac{1}{\xi^{d-1}}\frac{\mathrm{d}}{\mathrm{d}\xi}\left(\xi^{d-1}\frac{\mathrm{d}\theta}{\mathrm{d}\xi}\right)=\theta''+(d-1)\frac{\theta'}{\xi}=\pm\theta^n.$$

This equation has exact analytical solutions in 3 different cases: $n=0$ ($\rho=$cst), $n=1$ and $n=\frac{d+2}{d-2}$ (Horedt, 2004).

2.C Discs parameters

In table 2.1, I summarise the (default) parameters of the discs considered in this thesis.[3]

These values are mainly chosen to match the literature and ease comparison (Zang, 1976; Evans & Read, 1998b; Sellwood & Evans, 2001; Sellwood, 2012; Fouvry et al., 2015). For all Zang and Toomre[4] discs, I use $G=R_0=V_0=1$ and $\varepsilon=10^{-5}$ for the potential truncation (equation 2.33).

[3] There is no outer taper in the original works of Zang (1976) and Toomre (1981). It was later introduced by Evans & Read (1998b) and shown to weakly alter the dynamical properties of the disc (i.e., the unstable mode frequencies and growth rates), provided the cut-out is sufficiently sharp and far enough from the populated regions. This taper is necessary for N–body simulations, as the non-tapered disc has infinite (active) mass. The values used in this thesis are those from Sellwood (2012) and Fouvry et al. (2015).

[4] The power index q (equation 2.35) in Fouvry et al. (2015) slightly differs from Sellwood (2012). In all computations in this thesis, I used the value from Fouvry et al. (2015). In practice, it only changes the velocity dispersion and the stability Toomre number Q (Toomre, 1964) by 0.1%. I checked that it does not alter the predictions. However, one should rather use Sellwood (2012)'s value ($q=11.44$) which relies on a simple motivation: having nominal Toomre $Q=1.5$.

Chapter 3

Linear response of stellar self-gravitating systems

Let me now explore the stability of a given quasi-stationary state (QSS) w.r.t. small perturbations. This is the subject of linear response theory, which I develop in this chapter. I first introduce the general formalism here, before applying it to specific systems in the following chapter 4.

The first two sections of this chapter are inspired by Hamilton & Fouvry (2024).

3.1 Gravitational susceptibility

Given a mean-field distribution, F, the evolution of perturbations follows equation (1.13b). Considering sufficiently small perturbations, one can linearise this equation, yielding equation (1.19b) that I recall here for convenience:

$$\frac{\partial \delta f}{\partial t} + \boldsymbol{\Omega}(\mathbf{J}) \cdot \frac{\partial \delta f}{\partial \boldsymbol{\theta}} - \frac{\partial F}{\partial \mathbf{J}} \cdot \frac{\partial \delta \psi}{\partial \boldsymbol{\theta}} = 0. \qquad \text{(recall 1.19b)}$$

This is known as the *linearised collisionless Boltzmann equation*. Together with the Poisson equation (1.19c), this equation describes the (linear) self-consistent evolution of a perturbation δf in the potential perturbation it generates, $\delta\psi$. While these perturbations implicitly depend on angles, actions and time, the mean-field distribution, $F(J)$, is assumed to be time and angles independent. The underlying assumptions are that (i) the perturbations are sufficiently small, (ii) the mean-field distribution function (DF) is phase mixed, and (iii) the mean-field DF evolves on a timescale much longer than the perturbations' timescale. In the following subsection, I study this evolution equation using Fourier decomposition w.r.t. angles and Laplace transform w.r.t. time. This study leads me to introduce the gravitational susceptibility of the system. Rather than focusing on the evolution of a given perturbation, this susceptibility generically captures the propensity of the system to amplify or damp perturbations at any given frequency. The linear response theory developed in this chapter assumes that there are only internal perturbations and no externally-imposed perturbations. Phrased differently, I am mainly interested in the nature/stability of collective effects, i.e., in the homogeneous[1] solutions of the (linear) differential equations.

3.1.1 Angle Fourier decomposition

The angles, $\boldsymbol{\theta}$, being 2π-periodic, the perturbations can naturally be expanded in a Fourier series

$$g(\boldsymbol{\theta}, \mathbf{J}, t) = \sum_{\mathbf{k}} g_{\mathbf{k}}(\mathbf{J}, t)\, \mathrm{e}^{\mathrm{i}\mathbf{k}\cdot\boldsymbol{\theta}}, \tag{3.1}$$

[1] Here homogeneous relates to the differential equation (no source term) not to the spatial homogeneity of the system.

with $\mathbf{k}\in\mathbb{Z}^d$ and the Fourier coefficients

$$g_{\mathbf{k}}(\mathbf{J},t) = \frac{1}{(2\pi)^d}\int \mathrm{d}\boldsymbol{\theta}\, \mathrm{e}^{-\mathrm{i}\mathbf{k}\cdot\boldsymbol{\theta}}\, g(\boldsymbol{\theta},\mathbf{J},t). \tag{3.2}$$

Similarly, one can decompose the (action-dependent) interaction potential in a Fourier series

$$U(\boldsymbol{\theta},\mathbf{J},\boldsymbol{\theta}',\mathbf{J}') = \sum_{\mathbf{k},\mathbf{k}'} U_{\mathbf{k}\mathbf{k}'}(\mathbf{J},\mathbf{J}')\, \mathrm{e}^{\mathrm{i}(\mathbf{k}\cdot\boldsymbol{\theta}-\mathbf{k}'\cdot\boldsymbol{\theta}')}. \tag{3.3}$$

In this equation, the Fourier coefficients

$$U_{\mathbf{k}\mathbf{k}'}(\mathbf{J},\mathbf{J}') = \frac{1}{(2\pi)^{2d}}\int \mathrm{d}\boldsymbol{\theta}\mathrm{d}\boldsymbol{\theta}'\, \mathrm{e}^{-\mathrm{i}(\mathbf{k}\cdot\boldsymbol{\theta}-\mathbf{k}'\cdot\boldsymbol{\theta}')}\, U(\boldsymbol{\theta},\mathbf{J},\boldsymbol{\theta}',\mathbf{J}'), \tag{3.4}$$

represent the bare coupling harmonic coefficients between orbits $\mathbf{J}$ and $\mathbf{J}'$ at resonance numbers $\mathbf{k}$ and $\mathbf{k}'$ (Pichon, 1994). The dependence of these coefficients on the orbital actions is at odds with their plasma equivalent. It highlights that, for inhomogeneous systems, the interaction between particles, i.e., the Poisson equation (1.19c), and their (mean-field) motion are not "diagonal" in the same coordinate systems. In homogeneous plasmas, these coupling coefficients, as well as the interaction potential, U, are independent of the particles' velocities. This difference makes linear response computations more intricate in the inhomogeneous self-gravitating case.

For each angular Fourier mode, the system of coupled equations to solve finally reads

$$\frac{\partial \delta f_{\mathbf{k}}}{\partial t} + \mathrm{i}\mathbf{k}\cdot\boldsymbol{\Omega}\, \delta f_{\mathbf{k}} - \mathrm{i}\mathbf{k}\cdot\frac{\partial F}{\partial \mathbf{J}}\delta\psi_{\mathbf{k}} = 0, \tag{3.5a}$$

$$\delta\psi_{\mathbf{k}}(\mathbf{J},t) = (2\pi)^d \sum_{\mathbf{k}'}\int \mathrm{d}\mathbf{J}'\, \delta f_{\mathbf{k}'}(\mathbf{J}',t)\, U_{\mathbf{k}\mathbf{k}'}(\mathbf{J},\mathbf{J}'). \tag{3.5b}$$

In equation (3.5a), the fluctuations implicitly depend on the actions and time. Similarly, the dependence of frequencies on actions is implicit, i.e., $\boldsymbol{\Omega}=\boldsymbol{\Omega}(\mathbf{J})$.

3.1.2 Time Laplace transform

Equations (3.5), together with initial conditions given by the Fourier coefficients of the initial perturbation, $\delta f_{\mathbf{k}}(\mathbf{J},0)$, constitute an initial value problem. It can be solved using Laplace transform,

$$\widetilde{g}(\mathbf{J},\omega) = \int_0^{+\infty} \mathrm{d}t\, \mathrm{e}^{\mathrm{i}\omega t}\, g(\mathbf{J},t). \tag{3.6}$$

With this convention, the Laplace transform is defined for $\mathrm{Im}(\omega)>0$ sufficiently large, i.e., such that the integral converges at $t\to\infty$. If the function g is (purely) exponentially growing at a rate $\gamma>0$, its Laplace transform would have a singularity at $\omega=\mathrm{i}\gamma$. Conversely, if the function g is bounded, its Laplace transform is well-defined for $\mathrm{Im}(\omega)>0$. After rearranging, the Laplace transform of the linearised evolution equations (3.5a) reads

$$\delta\widetilde{f}_{\mathbf{k}}(\mathbf{J},\omega) = \underbrace{\frac{\overbrace{\delta f_{\mathbf{k}}(\mathbf{J},0)}^{\text{initial conditions}}}{\mathrm{i}(\mathbf{k}\cdot\boldsymbol{\Omega}-\omega)}}_{\text{phase mixing}} + \underbrace{\frac{\mathbf{k}\cdot\partial F/\partial\mathbf{J}}{\mathbf{k}\cdot\boldsymbol{\Omega}-\omega}\,\delta\widetilde{\psi}_{\mathbf{k}}(\mathbf{J},\omega)}_{\text{collective effects}}. \tag{3.7}$$

The first term in the r.h.s. of this equation corresponds to the phase mixing of initial fluctuations, i.e., their shearing along unperturbed orbits dictated by the mean-field potential (figure 1.6). Taking only this effect into account, the time-evolution of the perturbations simply reads

$$\delta f_{\mathbf{k}}(\mathbf{J},t) = \delta f_{\mathbf{k}}(\mathbf{J},0)\, \mathrm{e}^{-\mathrm{i}\mathbf{k}\cdot\boldsymbol{\Omega}t}. \tag{3.8}$$

The second term in the r.h.s. of equation (3.7) accounts for collective effects. It relates the evolution of the DF perturbations to the potential perturbations they induce (coupled through Poisson equation 1.19c). Accounting for this effect is the main focus of this chapter.

3.1.3 Gravitational dressing

Neglecting collective effects in equation (3.7) leads to the simple phase mixing of the fluctuations. Using Poisson equation (3.5b) (whose Laplace transform is obtained through the substitution $t \to \omega$, since the equation is linear), the corresponding *bare* potential fluctuations then read

$$\delta\widetilde{\psi}^{\rm b}_{\mathbf{k}}(\mathbf{J},\omega) = (2\pi)^d \sum_{\mathbf{k}'} \int \mathrm{d}\mathbf{J}' \, \frac{\delta f_{\mathbf{k}'}(\mathbf{J}',0)}{\mathrm{i}(\mathbf{k}'\cdot\boldsymbol{\Omega}' - \omega)} U_{\mathbf{k}\mathbf{k}'}(\mathbf{J},\mathbf{J}'), \tag{3.9}$$

where $\boldsymbol{\Omega}' \equiv \boldsymbol{\Omega}(\mathbf{J}')$. Once again, it corresponds to the potential fluctuations generated by the initial density perturbations simply orbiting in the mean-field potential, i.e., phase mixing.

Similarly, from equation (3.7) and Poisson equation (3.5b), the *dressed* potential fluctuations satisfy the self-consistency relation

$$\delta\widetilde{\psi}_{\mathbf{k}}(\mathbf{J},\omega) = \delta\widetilde{\psi}^{\rm b}_{\mathbf{k}}(\mathbf{J},\omega) + (2\pi)^d \sum_{\mathbf{k}'} \int \mathrm{d}\mathbf{J}' \, \frac{\mathbf{k}'\cdot\partial F/\partial \mathbf{J}'}{\mathbf{k}'\cdot\boldsymbol{\Omega}' - \omega} \, U_{\mathbf{k}\mathbf{k}'}(\mathbf{J},\mathbf{J}') \, \delta\widetilde{\psi}_{\mathbf{k}'}(\mathbf{J}',\omega) \tag{3.10}$$

Linearly accounting for the self-interaction of the fluctuations, i.e., collective effects, one can search for solution of equation (3.10) under a form similar to equation (3.9)

$$\delta\widetilde{\psi}_{\mathbf{k}}(\mathbf{J},\omega) = (2\pi)^d \sum_{\mathbf{k}'} \int \mathrm{d}\mathbf{J}' \, \underbrace{U^{\rm d}_{\mathbf{k}\mathbf{k}'}(\mathbf{J},\mathbf{J}',\omega)}_{\text{dressed coupling}} \, \frac{\delta f_{\mathbf{k}'}(\mathbf{J}',0)}{\mathrm{i}(\mathbf{k}'\cdot\boldsymbol{\Omega}' - \omega)}. \tag{3.11}$$

This is the Rostoker's superposition principle (Rostoker, 1964). It is as if particles were independently evolving along their mean-field orbits, but their effective mass was modified by the wake they create in the system (see, e.g., Hamilton, 2021). The bare Newtonian interaction potential is replaced by a dressed, frequency-dependent, interaction potential. Injecting equation (3.11) in equation (3.10) shows that such dressed coupling coefficients satisfy the self-consistency relation

$$U^{\rm d}_{\mathbf{k}\mathbf{k}'}(\mathbf{J},\mathbf{J}',\omega) = U_{\mathbf{k}\mathbf{k}'}(\mathbf{J},\mathbf{J}') + (2\pi)^d \sum_{\mathbf{k}''} \int \mathrm{d}\mathbf{J}'' \, \frac{\mathbf{k}''\cdot\partial F/\partial \mathbf{J}''}{\mathbf{k}''\cdot\boldsymbol{\Omega}'' - \omega} \, U_{\mathbf{k}\mathbf{k}''}(\mathbf{J},\mathbf{J}'') \, U^{\rm d}_{\mathbf{k}''\mathbf{k}'}(\mathbf{J}'',\mathbf{J}',\omega). \tag{3.12}$$

The interaction between two orbits $\mathbf{J}$ and $\mathbf{J}'$ is dressed by the interaction with the (background) orbits $\mathbf{J}''$. The dressing is particularly effective for orbits $\mathbf{J}''$ at resonance with the (complex) frequency ω, as captured by the resonant denominator in the integral.

This dependence on the frequency ω is a key difference between the bare and dressed coupling coefficients. It implies that gravitational dressing is a non-local and time-dependent effect. Contrary to their bare counterparts, the effective/dressed coupling between two orbits is not a simple function of their respective position. It takes time to build up, depends on their relative motion and also involves the overall distribution of stars.

In practice, the integral in equation (3.12) would diverge for purely real frequencies, i.e., for $\mathrm{Im}(\omega) = 0$. Given the definition of the Laplace transform equation (3.6), equation (3.12) is in fact only valid for $\mathrm{Im}(\omega) > 0$ large enough. It needs to be regularised for neutral and damped frequencies, i.e., for $\mathrm{Im}(\omega) = 0$ and $\mathrm{Im}(\omega) < 0$. Indeed, Laplace-transformed quantities are defined for $\mathrm{Im}(\omega)$ sufficiently large, i.e., above any pole. Here the resonant denominator induces a pole on the real axis on which the integral is performed. The continuation of equation (3.12) to the whole complex plane is further discussed in section 3.3.

Dyson equation The dressed coupling coefficients from equation (3.12) account for collective effects in the dynamics of perturbations. Forgetting about the details in this equation, it simply reads formally

$$U^{\rm d}(\omega) = U^{\rm b} + \mathbf{M}(\omega) \, U^{\rm d}(\omega), \tag{3.13}$$

where the superscript b (resp. d) stands for the bare (resp. dressed) coupling coefficients and $\mathsf{M}(\omega)$ is a polarisation operator.[2] More precisely, it is interesting to note that equation (3.12) is a Dyson equation. Roughly denoting the coordinates $1=\{\mathbf{k}_1,\mathbf{J}_1\}$, $2=\{\mathbf{k}_2,\mathbf{J}_2\}$ and so on, and assuming summation over repeated indices, it reads

$$U^{\rm d}_{12}(\omega) = U_{12}(\omega) + U_{13}(\omega)\mathbf{\Sigma}^{34}(\omega)U^{\rm d}_{42}(\omega), \tag{3.14}$$

where U is a constant function of the frequency ω. In equation (3.14), I have introduced the *self-energy*

$$\mathbf{\Sigma}^{34}(\omega) = (2\pi)^d\delta_{\rm D}(\mathbf{J}_3-\mathbf{J}_4)\delta^{\mathbf{k}_3}_{\mathbf{k}_4}\frac{\mathbf{k}_3\cdot\partial F/\partial\mathbf{J}_3}{\mathbf{k}_3\cdot\mathbf{\Omega}(\mathbf{J}_3)-\omega}. \tag{3.15}$$

It heuristically captures the effective "mass" of the two interacting orbits dressed by their effect on the mean-field [hidden in the mapping $\mathbf{J}\mapsto\mathbf{\Omega}(\mathbf{J})$ and the DF, F]. This quantity captures the shielding of interactions above the Debye length in plasma physics (Nicholson, 1992). As in quantum many-body systems, this effective mass is the result of the interaction between the particles and their mean-field environment (Nelson & Tremaine, 1999). Such a rewriting could prove valuable to study the non-linear perturbative effects from equation (1.13b) and derive the associated dressing (see, e.g., section 6.5.2 in Krommes, 2002).

As the pairwise interaction potential in equation (3.13), the potential fluctuations from equation (3.10) can be schematically expressed as

$$\delta\widetilde{\psi}(\omega) = \delta\widetilde{\psi}^{\rm b}(\omega) + \mathsf{M}(\omega)\,\delta\widetilde{\psi}(\omega), \tag{3.16}$$

where the bare fluctuations follow from equation (3.9). All in all, the self-consistent fluctuations read

$$\delta\widetilde{\psi}(\omega) = \mathsf{N}(\omega)\,\delta\widetilde{\psi}^{\rm b}(\omega), \tag{3.17}$$

where I introduced the gravitational susceptibility

$$\mathsf{N}(\omega) = \left[\mathsf{I}-\mathsf{M}(\omega)\right]^{-1}, \tag{3.18}$$

with I the identity operator. This susceptibility quantifies the propensity of the system to amplify or weaken perturbations. It captures the stiffness of collective effects at a given frequency ω.

3.1.4 Response to external perturbations

To clarify the respective roles of polarisation and susceptibility (as defined in the previous section), let me shortly discuss the response of the system to an external perturbation, $\delta\widetilde{\psi}_{\rm ext}(\omega)$. If the system was composed of independent (massless) test particles following the mean-field potential, the response to this perturbation would be a simple polarisation of test particles around it. It corresponds to the bare response of the system. The induced perturbations would then (schematically) read

$$\delta\widetilde{\psi}^{\rm b}(\omega) = \mathsf{M}(\omega)\,\delta\widetilde{\psi}_{\rm ext}(\omega). \tag{3.19}$$

Hence, $\mathsf{M}(\omega)$ is called the polarisation operator. Conversely, when considering a system of live (massive) particles collectively creating the mean-field in which they evolve, the induced perturbation has to be self-consistent. One then has the self-consistency relation

$$\delta\widetilde{\psi}(\omega) = \mathsf{M}(\omega)\left[\delta\widetilde{\psi}(\omega)+\delta\widetilde{\psi}_{\rm ext}(\omega)\right]. \tag{3.20}$$

[2] Sometimes called linear response function (e.g., Hamilton & Fouvry, 2024).

Seen differently, in such a case, the bare induced perturbation creates its own polarisation, which itself creates its own and so on. Dropping the dependencies w.r.t. the frequency ω, one then have

$$\begin{aligned}\delta\widetilde{\psi} &= \mathbf{M}\delta\widetilde{\psi}_{\rm ext} + \mathbf{M}\left(\mathbf{M}\delta\widetilde{\psi}_{\rm ext}\right) + \mathbf{M}\left[\mathbf{M}\left(\mathbf{M}\delta\widetilde{\psi}_{\rm ext}\right)\right] + ... \\ &= (\mathbf{I} + \mathbf{M} + \mathbf{M}^2 + ...)\mathbf{M}\delta\widetilde{\psi}_{\rm ext} \\ &= (\mathbf{I} - \mathbf{M})^{-1}\mathbf{M}\delta\widetilde{\psi}_{\rm ext} \\ &= \mathbf{N}\,\delta\widetilde{\psi}^{\rm b}, \end{aligned} \tag{3.21}$$

where $\mathbf{N}$ is the susceptibility operator introduced in equation (3.18). In the bare limit, the perturbation still induces a polarisation of the bath particles. However, there is no back-reaction of this polarisation on itself. Neglecting collective effects then amounts to setting $\mathbf{N}(\omega)\to\mathbf{I}$ [but not $\mathbf{M}(\omega)=\mathbf{0}$].

3.1.5 Gravitational modes

For some particular (complex) frequencies, the gravitational "permittivity", $\mathbf{I}-\mathbf{M}(\omega)$, might not be invertible. At such a frequency $\omega_{\rm M}=\Omega_{\rm M}+{\rm i}\gamma_{\rm M}$, the gravitational susceptibility from equation (3.18) is not properly defined. There is a specific perturbation (eigenvector) which is spontaneously supported by the (mean-field) system. This perturbation can either grow ($\gamma_{\rm M}>0$) or decay ($\gamma_{\rm M}<0$) exponentially, or steadily oscillate ($\gamma_{\rm M}=0$). In that sense, it is a mode of the system. Probing these modes proves particularly difficult in the context of inhomogeneous self-gravitating systems (see, e.g., Hamilton & Fouvry, 2024, and references therein). Indeed, the dispersion relation,

$$\det\left[\mathbf{I} - \mathbf{M}(\omega)\right] = 0, \tag{3.22}$$

involves linear operators instead of scalar quantities as in, e.g., homogeneous systems (see, e.g., Weinberg, 1993; Magorrian, 2021).

Of course, perturbations cannot grow (if they do) indefinitely in the (true) physical system. At some point, the underlying assumptions behind the linearisation of the collisionless Boltzmann equation (1.13b) do not hold, and the mode saturates because of non-linear effects (see, e.g., Laughlin et al., 1997; Hamilton, 2024).

Damped "modes"

The nature of damped solutions of equation (3.22) is a complicated question. Indeed, the gravitational dressing definition (equation 3.12) only stands in the upper-half complex plane, i.e., for $\mathrm{Im}(\omega)>0$. The dispersion relation (equation 3.22) is defined for neutral and damped frequency through analytical continuation (section 3.3.2). The associated solutions are not genuine modes and should rather be called Landau-damped disturbance (section 5.3.3 in Binney & Tremaine, 2008). I refer to, e.g., section 5.2.4 in Binney & Tremaine (2008) and Polyachenko et al. (2021) for a detailed discussion on the subject. These questions are deeply connected to the nature of Landau damping whose precise understanding is still at stake and far beyond the scope of this thesis (see, e.g., Mouhot & Villani, 2011). However, we shall see that these disturbances play a crucial role in the response of stellar systems and their long-term evolution (section 6.2.3). For simplicity, I will abusively refer to them as modes in the following. Note that inhomogeneous self-gravitating systems can also support algebraically decaying fluctuations (Barré et al., 2011; Barré & Yamaguchi, 2013). This is further discussed in section 3.3.3.

3.2 Kalnajs' matrix method

3.2.1 Bi-orthogonal bases

An effective way to compute the gravitational susceptibility is to use the matrix method developed by Kalnajs (1971–1977). This method is based on the expansion of fluctuations in a basis of potential-density pairs, $(\psi^{(p)}, \rho^{(p)})$, that are solutions of the Poisson equation

$$\psi^{(p)}(\mathbf{w}) = \int \mathrm{d}\mathbf{w}' \, \rho^{(p)}(\mathbf{w}') \, U(\mathbf{w}, \mathbf{w}'). \tag{3.23}$$

When properly normalised, these pairs of potential-density basis functions can be made to be bi-orthonormal, i.e., to satisfy

$$\int \mathrm{d}\mathbf{w} \, \psi^{(p)}(\mathbf{w}) \, \rho^{(q)*}(\mathbf{w}) = -\delta_{pq}. \tag{3.24}$$

In this orthogonality condition, the negative sign follows from the attractive nature of the gravitational potential. Let me stress that, given the absence of (physical) dimension in the r.h.s. of equation (3.24), the potential and density basis functions are not physical potentials and densities. Such a basis is effectively used to transform the bare interaction potential into a pseudo-separable form (Hernquist & Ostriker, 1992)

$$U(\mathbf{w}, \mathbf{w}') = -\sum_p \psi^{(p)}(\mathbf{w}) \, \psi^{(p)*}(\mathbf{w}'). \tag{3.25}$$

The basis elements are eigenfunctions of the Poisson equation, i.e., they diagonalise the interaction potential. Equation (3.25) is the corresponding expansion of the pairwise interaction potential (i.e., the Green's function of the Poisson equation) in these eigenfunctions. If properly ordered (in decreasing order of eigenvalues), the expansion converges rapidly and the high-order functions represent smaller and smaller scales (Weinberg, 1999). Truncating the basis then effectively amounts to softening the interaction potential at small scales. However, the exact shape of this softening is not straightforward and does not (generically) correspond to the softening used in numerical simulations (see, e.g., section 2.5 in Dootson, 2023). When using a non-biorthogonal basis, one should be particularly careful with the effect of truncation on the representation of the interaction potential.

Finally, equation (3.25) proves particularly useful when designing new basis functions (e.g., in section 4.1.1). From this equation, it is also clear that the bare coupling coefficients from equation (3.4) can be expressed in terms of the basis functions as

$$U_{\mathbf{k}\mathbf{k}'}(\mathbf{J}, \mathbf{J}') = -\sum_p \psi^{(p)}_{\mathbf{k}}(\mathbf{J}) \, \psi^{(p)*}_{\mathbf{k}'}(\mathbf{J}'), \tag{3.26}$$

with

$$\psi^{(p)}_{\mathbf{k}}(\mathbf{J}) \equiv \frac{1}{(2\pi)^d} \int \mathrm{d}\boldsymbol{\theta} \, \mathrm{e}^{-\mathrm{i}\mathbf{k}\cdot\boldsymbol{\theta}} \psi^{(p)}(\mathbf{w}), \tag{3.27}$$

the angle-Fourier transform of the bi-orthogonal basis elements.

3.2.2 Polarisation matrix

Having expanded the perturbations in a basis of potential-density pairs, the linear response is captured by the polarisation matrix, $\mathbf{M}(\omega)$ (see, e.g., equation 5.94 in Binney & Tremaine, 2008) whose elements generically read

$$M_{pq}(\omega) = -(2\pi)^d \sum_{\mathbf{k}\in\mathbb{Z}^d} \int \mathrm{d}\mathbf{J} \, \frac{\mathbf{k}\cdot\partial F/\partial \mathbf{J}}{\mathbf{k}\cdot\boldsymbol{\Omega}(\mathbf{J}) - \omega} \, \psi^{(p)*}_{\mathbf{k}}(\mathbf{J}) \, \psi^{(q)}_{\mathbf{k}}(\mathbf{J}), \tag{3.28}$$

with the angle-Fourier transform of the bi-orthogonal basis elements introduced in equation (3.27). The polarisation matrix defined in equation (3.28) is the (infinite) matrix representation of the linear operator $\mathbf{M}(\omega)$ from equation (3.16) within the basis of potential-density pairs. As for the coupling coefficients definition (equation 3.12), the polarisation matrix definition (equation 3.28) is only valid for $\mathrm{Im}(\omega)>0$. Its continuation to the whole complex plane is further discussed in section 3.3.

If the DF abruptly vanishes at the boundary, its gradient is a Dirac-δ function. It might notably happen when the actions' support is (semi-)finite. In this case, one might need to add the contribution from boundary integrals in equation (3.28) (Jalali & Hunter, 2005). There are no such a contribution in the models studied in this thesis. However, one should be careful when applying equation (3.28) to systems presenting such a discontinuity.

3.2.3 Dressed coupling coefficients

I now have at my disposal a practical way to compute the linear response of integrable self-gravitating systems. The associated susceptibility matrix, $\mathbf{N}$, is obtained through equation (3.18), to be understood as a manipulation of matrices instead of linear operators, i.e., $\mathbf{N}=[\mathbf{I}-\mathbf{M}(\omega)]^{-1}$. Given this susceptibility matrix, the *dressed* (i.e., accounting for collective effects) coupling coefficients from equation (3.12) effectively read (see, e.g., equation 35 in Heyvaerts, 2010)

$$\boxed{U^{\mathrm{d}}_{\mathbf{k}\mathbf{k}'}(\mathbf{J},\mathbf{J}',\omega) = -\sum_{p,q} \psi^{(p)}_{\mathbf{k}}(\mathbf{J})\, N_{pq}(\omega)\, \psi^{(q)*}_{\mathbf{k}'}(\mathbf{J}').} \tag{3.29}$$

Obtaining these dressed coupling coefficients is an important step towards understanding the long term evolution of self-gravitating systems. Indeed, they capture how two stars resonantly interact with each other while they collectively participate in shaping the galaxy's gravitational potential.

3.2.4 Softened gravity bases

In N–body simulations, the pairwise interaction potential, $U(\mathbf{w},\mathbf{w}')$, is usually softened to avoid singularities at small scales. This softening is commonly done using a Plummer kernel (Aarseth, 1963; Dehnen, 2001)

$$U_\varepsilon(\mathbf{r},\mathbf{r}') = -\frac{G}{\sqrt{\varepsilon^2+\|\mathbf{r}-\mathbf{r}'\|^2}}, \tag{3.30}$$

with ε the softening length. Such a regularisation has known consequences on the dynamics of the system (e.g., Miller, 1971; Salo & Laurikainen, 2000; Polyachenko, 2013). In particular, it can affect the pattern speed and growth rate of modes in simulations of unstable systems (Sellwood & Evans, 2001; De Rijcke et al., 2019b). Taking this softening into account in the linear response calculations would ease the comparison between numerical simulations and theoretical predictions. Yet, usual basis elements are constructed for the non-softened potential, i.e., the genuine Newtonian interaction. In this section, I present a new method to efficiently construct a bi-orthogonal basis for a softened gravity from a bi-orthogonal basis for the usual Poisson kernel.

Let me search for these basis elements under the form

$$\psi^{(p)}_\varepsilon(\mathbf{w}) = \sum_q A_{pq}\, \psi^{(q)}(\mathbf{w}), \quad \rho^{(p)}_\varepsilon(\mathbf{w}) = \sum_q B_{pq}\, \rho^{(q)}(\mathbf{w}), \tag{3.31}$$

where the (fixed) two matrices $\mathbf{A}$ and $\mathbf{B}$ are to be determined. Denoting $U_\varepsilon(\mathbf{w},\mathbf{w}')$, the softened (pairwise) interaction potential, the relevant quantity to consider is the bi-product matrix

$$C_{pq} = -\int \mathrm{d}\mathbf{w}\mathrm{d}\mathbf{w}' \rho^{(p)}(\mathbf{w})\, U_\varepsilon(\mathbf{w},\mathbf{w}')\, \rho^{(q)*}(\mathbf{w}'), \tag{3.32}$$

which reduces to the identity matrix for the non-softened interaction potential $U_{\varepsilon=0}$. This matrix is Hermitian, i.e., $C_{pq}=C^*_{qp}$, because the interaction kernel, $U_\varepsilon(\mathbf{w},\mathbf{w}')$ is real and symmetric. As such, one has $\mathbf{C}=\mathbf{C}^\dagger$, with $\mathbf{C}^\dagger$ the conjugate transpose.

I then want to impose the softened Poisson equation (3.23), substituting $U\to U_\varepsilon$, as well as the bi-orthonormality of the softened basis elements (equation 3.24). Together, these constraints read (see appendix 3.A for the details)

$$\mathbf{B}\,\mathbf{C}=\mathbf{A}, \tag{3.33a}$$

$$\mathbf{B}\,\mathbf{C}\,\mathbf{B}^\dagger=\mathbf{I}. \tag{3.33b}$$

Assuming that $\mathbf{C}$ is definite positive,[3] one can construct its Cholesky decomposition as

$$\mathbf{C}=\mathbf{L}\,\mathbf{L}^\dagger, \tag{3.34}$$

where $\mathbf{L}$ is a lower triangular matrix. With this decomposition, the matrices

$$\mathbf{A}=\mathbf{L}^\dagger,\quad \mathbf{B}=\mathbf{L}^{-1}, \tag{3.35}$$

do satisfy the constraints equation (3.33). In practice, since the polarisation matrix equation (3.28) only involves the potential basis element, one only needs to compute the matrix $\mathbf{A}$.

Finally, the softened matrix, $\mathbf{M}_\varepsilon(\omega)$, can be obtained from the non-softened one, $\mathbf{M}_0(\omega)$, using (appendix 3.A)

$$\begin{aligned}\mathbf{M}_\varepsilon &= \mathbf{A}^*\,\mathbf{M}_0\,\mathbf{A}^{\mathrm{T}}\\ &= \mathbf{L}^{\mathrm{T}}\,\mathbf{M}_0\,\mathbf{L}^*,\end{aligned} \tag{3.36}$$

where $\mathbf{L}^{\mathrm{T}}$ stands for the matrix transpose. To conclude, in order to compute the softened response matrix, it suffices to: (i) compute once the matrix $\mathbf{C}$ (equation 3.32) for the considered softening length ε (and softening kernel); (ii) compute its Cholesky decomposition, i.e., the matrix $\mathbf{L}$ (equation 3.34); (iii) compute the non-softened matrix, $\mathbf{M}_0$, as usual ; (iv) compute the softened matrix, $\mathbf{M}_\varepsilon$, via a simple matrix contraction (equation 3.36) *a posteriori*. The actual implementation of this method is left for future work. In appendix 6.B.2, I provide some analytical expressions which might prove useful for the razor-thin disc.

3.3 Hilbert transform

3.3.1 Resonant coordinates

A difficult part in the computation of equation (3.28) is the resonant denominator, $1/(\mathbf{k}\cdot\boldsymbol{\Omega}-\omega)$. To handle it properly, one can first align the resonant denominator by a change of variables, $\mathbf{J}\to(u,...)$, with $u\propto\mathbf{k}\cdot\boldsymbol{\Omega}$ (Vauterin & Dejonghe, 1996; Fouvry & Prunet, 2022). One may already see that peculiar things should happen when this mapping is not bijective, i.e., when $\mathbf{J}\mapsto\mathbf{k}\cdot\boldsymbol{\Omega}(\mathbf{J})$ reaches an extremum. On such an orbit, a star does not leave the resonance (at first order) even pulled/pushed away of its orbit by resonant torquing. Indeed, the Jacobian $\partial(\mathbf{k}\cdot\boldsymbol{\Omega})/\partial\mathbf{J}$ involves the so-called donkey parameter (Lynden-Bell, 1979; Pichon, 1994), a measure of the inverse moment of inertia which may vanish for some specific orbits.

Within this resonant coordinate system, equation (3.28) takes the generic form of a Hilbert transform (more precisely a sum of Hilbert transforms)

$$\widehat{g}(\omega)=\int\mathrm{d}u\,\frac{g(u)}{u-\omega}. \tag{3.37}$$

[3] This is guaranteed for ε small enough. Indeed, one has $\mathbf{C}\to\mathbf{I}$ when $\varepsilon\to0$, and positive-definite matrices form an open set.

Once again, this definition holds in the upper-half of the complex plane, i.e., for $\mathrm{Im}(\omega)>0$ (see also section 3.3.2). In equation (3.37), the integration boundaries are purposely left unspecified. The resonant coordinate, u, most often has a finite support because orbital frequencies are typically bounded in galactic discs (in contrast to velocities in plasmas). It can also be interpreted as considering functions g with cut-offs at the domain boundaries. Such a discontinuity requires additional care when continuing the definition to damped frequencies, $\mathrm{Im}(\omega)<0$ (section 3.3.3). In practice, the polarisation matrix takes the form

$$\mathbf{M}(\omega) = \sum_{\mathbf{k}\in\mathbb{Z}^d} \int \mathrm{d}u \, \frac{\mathbf{G}_{\mathbf{k}}(u)}{u - \varpi_{\mathbf{k}}(\omega)} = \sum_{\mathbf{k}} \widehat{\mathbf{G}}_{\mathbf{k}}[\varpi_{\mathbf{k}}(\omega)], \tag{3.38}$$

where the matrices of functions, $\mathbf{G}_{\mathbf{k}}$, the resonant frequencies, $\varpi_{\mathbf{k}}(\omega)$, and the resonant coordinates, $(u, ...)$, are tailored to each system. This is detailed in Petersen et al. (2024) which I cosigned. I refer to section 4.1.2 and section 4.2.2 for the definition of these quantities in the one-dimensional model and razor-thin discs, respectively. As we shall see in the next section, the polarisation matrix should be computed differently for damped frequencies than it is for growing frequencies. One therefore needs to be particularly careful with the resonant frequencies $\varpi_{\mathbf{k}}(\omega)$. I make sure that they share the same imaginary part as ω to avoid any practical issue in this continuation.

3.3.2 Landau's prescription

Given the definition of the Laplace transform equation (3.6), the transformed quantities are defined for $\mathrm{Im}(\omega)$ sufficiently large, i.e., above any pole. The resonant integral equations (3.12), (3.28) and (3.37) are therefore only valid for $\mathrm{Im}(\omega)>0$. Similarly, the inversion formula

$$g(\mathbf{J}, t) = \frac{1}{2\pi} \int_{\mathcal{B}} \mathrm{d}\omega \, \mathrm{e}^{-\mathrm{i}\omega t} \, \widetilde{g}(\mathbf{J}, \omega), \tag{3.39}$$

holds when the Bromwich contour, $\mathcal{B}$, is taken sufficiently high in the complex plane, i.e., above any singularity of $\widetilde{g}(\mathbf{J}, \omega)$. However, this inversion would be easier to perform by bringing the contour down in the complex plane so that the exponential prefactor $\mathrm{e}^{-\mathrm{i}\omega t}$ is as damped as possible. Doing so, only the contributions from the singularities of $\widetilde{g}(\mathbf{J}, \omega)$ would remain (see, e.g., equation 5.9), streamlining the integral computation in equation (3.39). For this integral to be unchanged, the Laplace transform $\widetilde{g}(\mathbf{J}, \omega)$, need to be analytically continued below its dominant singularity, so that $\widetilde{g}$ can be evaluated for any complex value of ω.

Specifically considering the case of the resonant integral equation (3.37), this analytic continuation is done through Landau's prescription (e.g., §5.2.4 in Binney & Tremaine, 2008) which generically reads

$$\boxed{\int_{\mathcal{L}} \mathrm{d}u \, \frac{G(u)}{u - \omega} = \begin{cases} \displaystyle\int_{-\infty}^{+\infty} \mathrm{d}u \, \frac{G(u)}{u - \omega} & \text{if } \mathrm{Im}(\omega) > 0, \\ \mathcal{P}\displaystyle\int_{-\infty}^{+\infty} \mathrm{d}u \, \frac{G(u)}{u - \omega} + \mathrm{i}\pi G(\omega) & \text{if } \mathrm{Im}(\omega) = 0, \\ \displaystyle\int_{-\infty}^{+\infty} \mathrm{d}u \, \frac{G(u)}{u - \omega} + 2\mathrm{i}\pi G(\omega) & \text{if } \mathrm{Im}(\omega) < 0, \end{cases}} \tag{3.40}$$

where $\mathcal{P}$ stands for Cauchy's principal value. This prescription is illustrated in figure 3.1. The integration contour along the (real) u coordinates needs to snatch the ballistic pole $u=\omega$ coming from above, i.e., from $\mathrm{Im}(\omega)>0$. This is done by adding a contribution from the residue at the pole, or half the residue for real ω.

For equation (3.40) to be unambiguously defined, the function G needs to be analytic on the whole real axis (and its power series should have an infinite radius of convergence). In the context

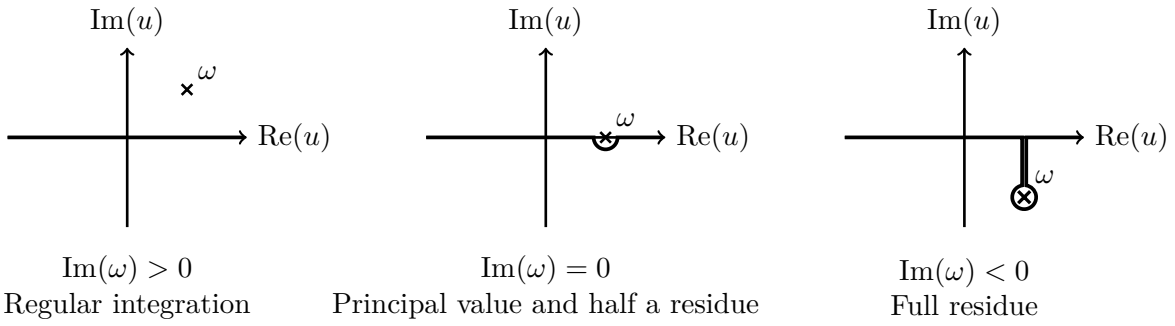

Figure 3.1: Illustration of Landau's prescription (equation 3.40) for the analytical continuation of the polarisation function (equation 3.28) from growing (left) to neutral (middle) and damped (right) frequencies. The integration contour along the real axis needs to snatch the ballistic pole $u=\omega$ coming from above, i.e., from $\mathrm{Im}(\omega)>0$. This is done by adding a contribution from the residue at the pole, or half the residue for real ω.

of homogeneous systems such as plasmas where u is a proxy for the (unbounded) velocity, this is usually the case. With self-gravitating systems, we are not so lucky for two main reasons. First, the numerator G in the integral equation (3.38) is, in general, not known analytically and involves expensive numerical computations. Hence, evaluating the residue $G(\omega)$ for non-real values of ω can prove particularly challenging. Second, the integral is not carried over unbounded velocities but over frequencies that can be of finite extent. It can also be interpreted as using (non-analytic) G functions with cut-offs at the domain boundaries.

3.3.3 Frequency support and branch cuts

Landau's prescription (equation 3.40) is well-posed when the integrand function G is analytic on the whole real axis. When considering inhomogeneous self-gravitating systems, the integral in equation (3.38) is performed over the resonant coordinate, $u\propto\mathbf{k}\cdot\mathbf{\Omega}$, which (usually) has a finite support. In this case, one can generally recast the integration domain as $u\in[-1,1]$ in equation (3.37). Following Landau's prescription (equation 3.40), I need to continue the integral

$$\int_{-1}^{1}\mathrm{d}u\,\frac{G(u)}{u-\omega} \tag{3.41}$$

from the upper-half complex plane to the whole complex plane. One can already spot an issue: at $\omega=\pm1$, if $G(\pm1)\neq0$ the integral is divergent and cannot be regularised using a principal value. At these points, such that $\varpi_{\mathbf{k}}(\omega)=\pm1$, the continuation of the polarisation matrix equation (3.38) has logarithmic singularities.

Building upon Robinson (1990), Fouvry & Prunet (2022) (hereafter FP22) proposed a way to generically handle the continuation of the polarisation matrix (equation 3.38) to the whole complex plane for such a system with (i) a finite frequency support and (ii) analytically unknown integrand functions, G.

Finite support

The first step is to choose a continuation for the Hilbert transform equation (3.37) with a finite integration domain $u\in[-1,1]$. It reads

$$\int\limits_{\mathcal{L}}^{1}\mathrm{d}u\,\frac{G(u)}{u-\omega}=\begin{cases}\displaystyle\int_{-1}^{1}\mathrm{d}u\,\frac{G(u)}{u-\omega} & \text{if } \mathrm{Im}(\omega)>0,\\ \displaystyle\mathcal{P}\int_{-1}^{1}\mathrm{d}u\,\frac{G(u)}{u-\omega}+\mathrm{i}\pi H(\omega)G(\omega) & \text{if } \mathrm{Im}(\omega)=0,\\ \displaystyle\int_{-1}^{1}\mathrm{d}u\,\frac{G(u)}{u-\omega}+2\mathrm{i}\pi H[\mathrm{Re}(\omega)]G(\omega) & \text{if } \mathrm{Im}(\omega)<0.\end{cases} \tag{3.42}$$

In this expression, I introduced the Heaviside (rectangular) function

$$H(x) = \begin{cases} 0 & \text{if } |x| > 1, \\ \frac{1}{2} & \text{if } x = \pm 1, \\ 1 & \text{if } -1 < x < 1. \end{cases} \tag{3.43}$$

This may appear to be a complete redundancy of Landau's prescription (equation 3.40), yet it is not. Indeed, here, the continuation is not uniquely defined (Barré et al., 2010). Similarly to the complex logarithm, it has multiple branches. With the choice from equation (3.42), one introduces vertical branch cuts at $\omega = \pm 1$, as illustrated in figure 3.2.

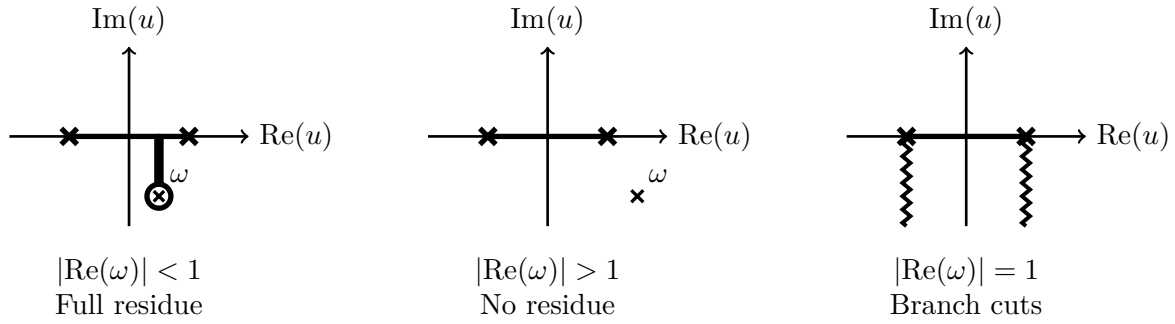

Figure 3.2: Illustration of the branch cuts in the continuation of finite Hilbert transform equation (3.42) for the analytical continuation of the polarisation function (equation 3.28). For frequencies below the integration interval, the integration contour snatches the ballistic pole as if it was coming straight from above. The residue at the pole is then added to the integral. Outside the integration interval, the ballistic pole does not cross the contour. No residue contribution is added. In this case the continuation is not unique. The chosen branch of the function has vertical branch cuts at $\omega = \pm 1$.

This does not mean that the continuation is spurious. The branch cuts have physical origins. Indeed, Barré et al. (2011) showed that these branch cuts result in the algebraic (asymptotic) decay of perturbations in the Hamiltonian mean-field (HMF) model. Only considering damped poles, one would have incorrectly predicted an exponential decay of the perturbations (Landau damping), $\delta\phi(t) \to \mathrm{e}^{\gamma_{\mathrm{M}} t}$ with $\gamma_{\mathrm{M}} < 0$ the smallest damping rate. However, in Barré et al. (2011)'s experiments, the perturbations first undergo a transient exponential decay before switching to an asymptotic algebraic decay, $\delta\phi(t) \to t^{\beta}$ with $\beta < 0$. This is illustrated in figure 3.3 (adapted from Barré et al., 2015). Interestingly, this phenomenon is also observed in the relaxation of other physical systems such as two-dimensional Bose superfluids (see, e.g., Duval & Cherroret, 2024). Barré & Yamaguchi (2013) extended the analysis from the inhomogeneous HMF model to razor-thin discs and spherical globular clusters and pointed out three types of singularities. These different types lead to various algebraic decay rates.

These singularities are present in the polarisation matrix, $\mathbf{M}$, from equation (3.38). Contrary to the Landau damped modes, they do not necessarily involve collective effects through the gravitational susceptibility, $\mathbf{N}$, from equation (3.18). One might indeed expect an algebraic decay to happen, even in the bare response to external perturbations (equation 3.19). Without involving external perturbations, such singularities could also be imprinted in the bare response to initial conditions in equation (3.9).

Unknown integrand functions

I now have at my disposal a prescription to continue the resonant integral equation (3.38) to the whole complex plane. Given this prescription (equation 3.42), I still need to define $G(\omega)$ for complex ω and intricate functions G. Following FP22, I do so by approximating the integrand functions, G,

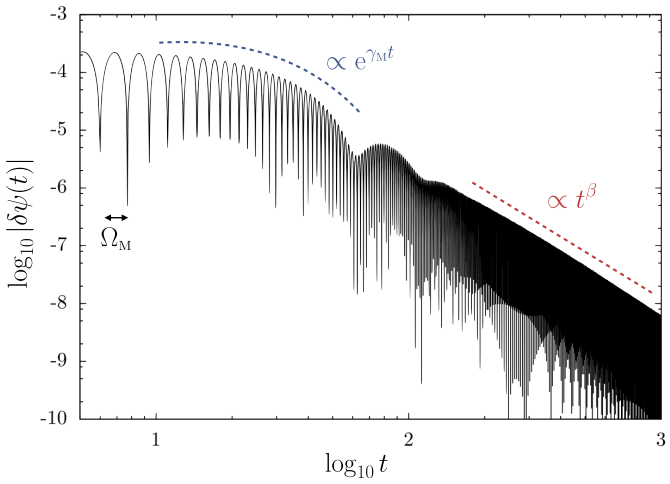

Figure 3.3: Figure adapted from Barré et al. (2015), with additional annotations. Illustration of the asymptotic algebraic damping of perturbations in the inhomogeneous HMF model. The perturbations first undergo a transient exponential decay at rate $\gamma_M < 0$ given by the least damped Landau mode. It then switches to an asymptotic algebraic decay with rate $\beta \approx 3$ as predicted from Barré et al. (2011). Both the mean-field distribution and the perturbations are smooth quantities. This phenomenon is due to the finite range of available frequencies in the inhomogeneous system.

using Legendre polynomials

$$G(u) \approx \sum_{j=0}^{K_u^{\mathrm{d}}} a_j P_j(u). \tag{3.44}$$

Given the range $u \in [-1, 1]$, these polynomials are a natural choice of analytical basis functions. In equation (3.44), the expansion coefficients can be efficiently computed using Gauss–Legendre quadrature. It reads

$$a_j = \frac{1}{c_j} \sum_{i=0}^{K_u^{\mathrm{q}}} w_i \, G(u_i) \, P_j(u_i), \tag{3.45}$$

with w_i the weights and u_i the abscissas of the Gauss–Legendre quadrature (see, e.g., Press et al., 2007), and c_j the normalisation constants of the Legendre polynomials. In practice, the number of points for the quadrature, K_u^{q}, and the number of Legendre polynomials for the decomposition, K_u^{d}, could be equal. Yet, for convergence purpose, I found that the number of quadrature points should be taken as large as possible while the number of Legendre polynomials should be chosen wisely (section 4.1.4).

By linearity of equation (3.42) (w.r.t. the integrand function G), the polarisation matrix can be approximated as

$$\widehat{G}(\omega) \approx \sum_{j=0}^{K_u^{\mathrm{d}}} a_j D_j(\omega), \tag{3.46}$$

where D_j is the finite Hilbert transform of the Legendre polynomials, P_j. They read (FP22)

$$D_j(\omega) = \begin{cases} Q_j(\omega) & \text{if } \mathrm{Im}(\omega) > 0, \\ Q_j(\omega) + \mathrm{i}\pi P_j(\omega) H(\omega) & \text{if } \mathrm{Im}(\omega) = 0, \\ Q_j(\omega) + 2\mathrm{i}\pi P_j(\omega) H(\mathrm{Re}[\omega]) & \text{if } \mathrm{Im}(\omega) < 0, \end{cases} \tag{3.47}$$

where H is the Heaviside function from equation (3.43) and Q_i are (almost) Legendre polynomials of the second kind. Importantly, they can be evaluated using stable recurrence relations (see appendix D FP22).

The corresponding first function, $D_0(\omega)$, is illustrated in figure 3.4. This function is smooth in

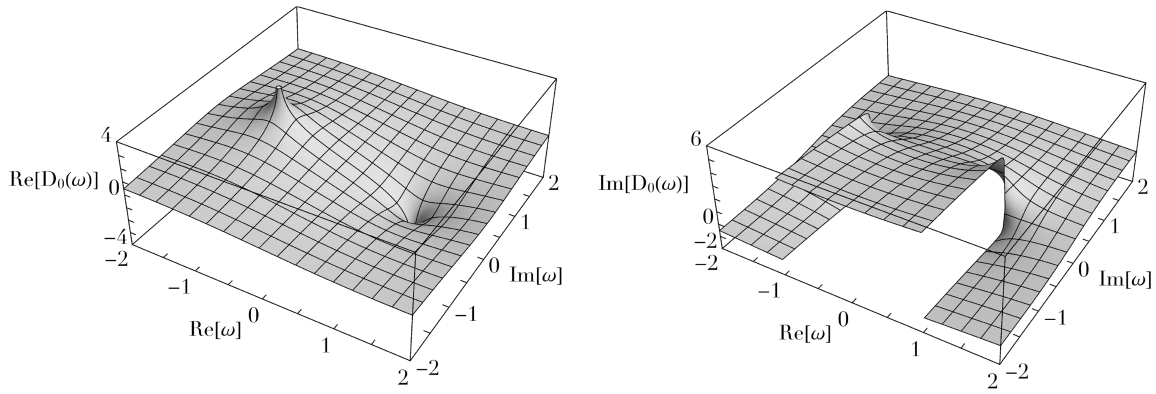

Figure 3.4: Figure from Fouvry & Prunet (2022). Illustration of the complex function $D_0(\omega)$ in equation (3.46). This function is smooth is the upper-half complex plane, $\mathrm{Im}(\omega)>0$, and has branch point singularities at $\omega=\pm1$ in its real part (left). The associated branch cuts are straight vertical lines starting at the singularities and extending down in the lower-half complex plane in its imaginary part (right).

the upper-half plane, $\mathrm{Im}(\omega)>0$, and has logarithmic singularities at $\omega=\pm1$. The associated branch cuts are straight vertical lines starting at the singularities and extending down in the lower-half complex plane. The real part of the D_i functions is symmetric w.r.t. the real axis. The difference between growing and damped frequencies is captured in the imaginary part of these functions. This imaginary part is significantly larger in the lower-half plane. Therefore, in this region, the computation of the polarisation matrix from equation (3.46) involves drastic cancellations, leading to numerical saturation (section 4.1.4).

3.4 Other methods

In this chapter, I focused on the method I used to compute the linear response of stellar systems. Importantly, this method straightforwardly allows me to incorporate the gravitational susceptibility in the coupling between interacting orbits, as described in equation (3.12). These coupling coefficients are crucial to study the long-term evolution of stellar systems (chapter 5). Other similar methods have been implemented to compute the linear response of self-gravitating systems. Let me briefly review some of them.

Without resonant coordinates The polarisation matrix from equation (3.28) can be computed directly for growing frequencies, $\mathrm{Im}(\omega)>0$, without the use of resonant coordinates or any analytical continuation. This has notably been performed by Weinberg (1989); Palmer (1994); Saha (1991); Rozier et al. (2019) for spherical systems and by Pichon & Cannon (1997); Jalali & Hunter (2005); Fouvry et al. (2015) for razor-thin discs. The integral might then be performed in various spaces of orbital constants (pericentre and apocentre radii, energy and angular momentum, actions, etc.) using a simple change of variables.

"Eigenmodes" methods These methods do not solve the linearised collisionless Boltzmann equation (1.19b) as an initial value problem but rather look for normal modes as solutions of the form $\delta\psi(\mathbf{w})\,\mathrm{e}^{\mathrm{i}\omega t}$ (see, e.g., Vauterin & Dejonghe, 1996; Polyachenko, 2005; Jalali, 2007; De Rijcke & Voulis, 2016). These two approaches are in practice very similar. Vauterin & Dejonghe (1996) was in fact the first put the matrix equation (3.28) under the form of a Hilbert transform (equation 3.37) using a change of variable similar to the one presented in section 3.3. Their work was followed by De Rijcke & Voulis (2016) and implemented in the code `pystab`. The only fundamental difference

between the two approaches is the status of damped frequencies, $\mathrm{Im}(\omega)<0$. Such frequencies are discarded in the eigenmodes methods. In this approach, stable systems are expected to have a continuous spectrum of oscillatory modes known as Van Kampen modes (Van Kampen, 1955; Case, 1959; Polyachenko et al., 2021; Lau & Binney, 2021). In the method I presented, one gives a meaning to the response at damped frequencies through analytical continuation and Landau's prescription (section 3.3.2). Among the eigenmodes methods, some of them allow one to compute all the unstable modes at once (Polyachenko, 2005; Jalali, 2007, 2010) but require large matrix inversions. A comparison between these methods is presented in Omurkanov & Polyachenko (2014).

Time evolution The linear response can also be computed by evolving the perturbations in time (see, e.g., Murali, 1999; Pichon & Aubert, 2006; Rozier et al., 2022; Magorrian, 2021; Dootson, 2023). Using a basis of potential-density pairs (equation 3.23), the internal and external perturbations are expanded as

$$\delta\psi(\mathbf{w},t)=\sum_p a_p(t)\,\psi^p(\mathbf{w}),\quad \delta\psi_{\rm ext}(\mathbf{w},t)=\sum_p b_p(t)\,\psi^p(\mathbf{w}). \tag{3.48}$$

The time evolution of the fluctuations' coefficients is then given by a Volterra-type integral equation (see, e.g., Rozier et al., 2022)

$$\mathbf{a}(t)=\int_0^t \mathrm{d}t'\,\mathbf{M}(t-t')\,\left[\mathbf{a}(t')+\mathbf{b}(t')\right], \tag{3.49}$$

where the time polarisation matrix,

$$M_{pq}(t)=-i(2\pi)^d\sum_{\mathbf{k}}\int \mathrm{d}\mathbf{J}\,\mathbf{k}\cdot\frac{\partial F}{\partial \mathbf{J}}\,\psi^{(p)*}_{\mathbf{k}}(\mathbf{J})\,\psi^{(q)}_{\mathbf{k}}(\mathbf{J}), \tag{3.50}$$

can be obtained by taking the inverse Laplace transform of equation (3.28). This is a dual approach to the method I detailed in this chapter. It is particularly suited for the study of the transient response to external perturbations, such as the Large Magellanic Cloud perturbing the Milky Way halo. This method is also interesting when aiming to couple the external perturbations to the internal response of the system, for instance, to study how a satellite sinks under the effect of dynamical friction. This is achieved by updating $\mathbf{b}(t)$ to the drag induced by $\mathbf{a}(t)$.

Analytical continuation using rational function The first *generic* method to probe damped frequencies was proposed by Weinberg (1994) while studying spherical systems. He used the value of the dispersion relation (equation 3.22) on a grid of unstable frequencies to fit a rational function (Padé approximant)

$$\det[\mathbf{I}-\mathbf{M}(\omega)]=\frac{N(\omega)}{D(\omega)}, \tag{3.51}$$

with N and D two polynomials. This rational function was then evaluated at damped frequencies and Weinberg (1994) showed the existence of weakly damped modes in stable King's spheres. His results were later confirmed by Heggie et al. (2020) using numerical simulations. However, the main drawbacks of this method is that (i) the choice of the interpolation grid is arbitrary and should be made carefully (Weinberg, 1994; Fouvry & Prunet, 2022) and (ii) it does not explicitly take into account the presence of branch cuts (section 3.3.3). Yet, one could adapt the method and enforce the presence of physically motivated branch cuts in the fitted function.

Semi-analytic results for specific models Beyond these other generic methods some very important results have been obtained with tailored methods for specific models.

Zang (1976) designed a method for the Mestel discs (section 2.1.2). This method was generalised to other power-law discs by Evans & Read (1998a). Both methods take advantage of the self-similarity of orbits within these specific potentials. Using logarithmic spirals as (continuous) basis elements, they reduced the stability analysis to a single Fredholm integral equation of the form

$$A(\beta) = \int_{-\infty}^{+\infty} \mathrm{d}\alpha \, S(\alpha, \beta; \omega) A(\alpha), \tag{3.52}$$

where A stands for the decomposition of the perturbations in the basis of logarithmic spirals and S is a coupling kernel that depends on the frequency. This is detailed in Evans & Read (1998a). For the fully self-similar disc, this kernel weakly depends on the frequency and needs to be computed only once. Such a disc is either stable or has a continuum of modes. For tapered discs,[4] the equation is more involved and needs to be solved for each frequency. Interestingly, Zang (1976) was able to predict the location of some damped modes in his model as well as the presence of branch cuts and their relation to the algebraic decay of perturbations.

Finally, Olivetti (2011) extensively investigated damped modes and branch cuts in the (thermal) equilibria of the HMF model for which he derived appropriate analytical expressions.

[4] The taper functions from equation (2.37) were actually introduced to get analytical expressions for some intermediate integrals (namely equation 3.44 in Zang, 1976).

Appendices

3.A Softened bases

In this appendix, I detail the computations of section 3.2.4 for the polarisation matrix of softened gravitational potential.

For a given index p of the softened basis (equation 3.31), the Poisson equation (3.23) reads

$$\sum_{p'}\int \mathrm{d}\mathbf{w}'\, U_\varepsilon(\mathbf{w},\mathbf{w}')B_{pp'}\rho^{(p')}(\mathbf{w}') = \sum_{p'} A_{pp'}\psi^{(p')}(\mathbf{w}). \quad (3.53)$$

Multiplying both sides of this equation with $\int \mathrm{d}\mathbf{w}\,\rho^{(q)*}(\mathbf{w})$, I obtain

$$\sum_{p'} B_{pp'}\int \mathrm{d}\mathbf{w}\mathrm{d}\mathbf{w}'\, U_\varepsilon(\mathbf{w},\mathbf{w}')\rho^{(p')}(\mathbf{w}')\,\rho^{(q)*}(\mathbf{w}) = \sum_{p'} A_{pp'}\int \mathrm{d}\mathbf{w}\,\psi^{(p')}(\mathbf{w})\,\rho^{(q)*}(\mathbf{w}), \quad (3.54)$$

which gives

$$\sum_{p'} B_{pp'}C_{p'q} = A_{pq}, \quad (3.55)$$

using the definition of the cross-product matrix C (equation 3.32) and the bi-orthonormality of the non-softened basis (equation 3.24). Overall, this gives the first constraint in equation (3.33a).

Then, the bi-orthonormality equation (3.24) imposes

$$\begin{aligned}\delta_{pq} &= -\int \mathrm{d}\mathbf{w}\,\psi_\varepsilon^{(p)}(\mathbf{w})\,\rho_\varepsilon^{(q)*}(\mathbf{w}) \\ &= -\int \mathrm{d}\mathbf{w}\mathrm{d}\mathbf{w}'\, U_\varepsilon(\mathbf{w},\mathbf{w}')\,\rho_\varepsilon^{(p)}(\mathbf{w}')\,\rho_\varepsilon^{(q)*}(\mathbf{w}) \\ &= -\int \mathrm{d}\mathbf{w}\mathrm{d}\mathbf{w}'\, U_\varepsilon(\mathbf{w},\mathbf{w}')\,\rho_\varepsilon^{(p)}(\mathbf{w})\,\rho_\varepsilon^{(q)*}(\mathbf{w}') \\ &= -\sum_{p',q'}\int \mathrm{d}\mathbf{w}\mathrm{d}\mathbf{w}'\, U_\varepsilon(\mathbf{w},\mathbf{w}')B_{pp'}\rho^{(p')}(\mathbf{w}) \times B^*_{qq'}\rho^{(q')*}(\mathbf{w}') \\ &= \sum_{p',q'} B_{pp'}C_{p'q'}B^*_{qq'}, \end{aligned} \quad (3.56)$$

where I used, once again the definition of the cross-product matrix C (equation 3.32). Overall, this gives the second constraint in equation (3.33b).

Finally, the element (p,q) of the response matrix for the softened interaction is of the form

$$\begin{aligned} M^\varepsilon_{pq} &\propto \psi_\varepsilon^{(p)*}\,\psi_\varepsilon^{(q)} \\ &= \sum_{p',q'} A^*_{pp'}\,\psi^{(p')*}\,A_{qq'}\,\psi^{(q)} \\ &= \sum_{p',q'} A^*_{pp'}\,M_{p'q'}\,A_{qq'}. \end{aligned} \quad (3.57)$$

As a result, the softened matrix, $\mathsf{M}_\varepsilon(\omega)$, is readily computed from the non-softened one, $\mathsf{M}(\omega)$, following equation (3.36).

Chapter 4

Linear response – Applications

In this chapter, I explore the applications of the linear response theory presented in chapter 3 to the various systems detailed in chapter 2. For each particular system, I first start by detailing the necessary ingredients to compute the polarisation matrix from equation (3.28), namely the basis elements and the resonant coordinates. I then illustrate the susceptibility of the system to particular (complex) frequencies and discuss the physical implications. The results presented in this chapter are mainly based on the published article Roule et al. (2022) and my work in Petersen et al. (2024), hereafter PR+24.

4.1 One-dimensional model

4.1.1 Bi-orthogonal basis

To construct basis elements for the one-dimensional model, I substituted the interaction potential, $U(x,x')=G\,|x-x'|$, with its periodisation into a triangle wave of period $2L$ as represented in figure 4.1.

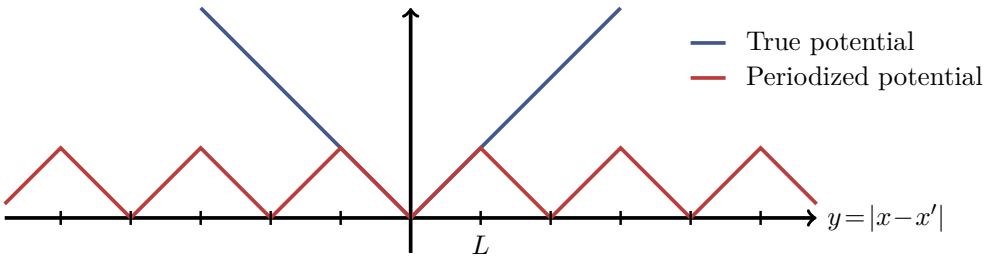

Figure 4.1: Illustration of the periodisation of the interaction potential (equation 4.1) used to construct the bi-orthogonal basis for the one-dimensional model.

Owing to the separability trigonometric identity $\cos(a-b)=\cos(a)\cos(b)+\sin(a)\sin(b)$, the periodised potential from equation (2.1) reads

$$U_{\text{per}}(x,x') = -\frac{4GL}{\pi^2}\sum_{\substack{p\ \text{odd}\\ p>0}}\frac{1}{p^2}\left[\cos\left(p\pi\frac{x}{L}\right)\cos\left(p\pi\frac{x'}{L}\right)+\sin\left(p\pi\frac{x}{L}\right)\sin\left(p\pi\frac{x'}{L}\right)\right], \tag{4.1}$$

where I dropped the constant ($p=0$) term. Following equation (3.25), some natural basis elements then are

$$\psi^{(p)}_{\text{even}}(x) = \frac{2\sqrt{GL}}{(2p+1)\,\pi}\cos\left[(2p+1)\pi\frac{x}{L}\right], \tag{4.2}$$

with $p \geq 0$, and their odd counterpart $\psi^{(p)}_{\text{odd}}$ via $\cos \to \sin$. Following the Poisson equation (2.2), the associated "densities" are

$$\rho^{(p)}_{\text{even}}(x) = \frac{-\pi^2 (2p+1)^2}{2GL^2} \psi^{(p)}_{\text{even}}(x), \tag{4.3}$$

and equivalently for the odd ones. One can check that this basis complies with the integral Poisson equation (3.23) for the periodised interaction potential (offset for the mean potential to be zero) as well as the orthonormalisation constraint (equation 3.24), in which the integral is performed over one $2L$-period.

The main benefit of periodisation is its numerical simplicity. Its main drawback is that it introduces a superfluous characteristic length, L. This could lead to unexpected behaviours at low frequencies (high energies) introducing a new circulation regime whereas the true interaction potential can only allow for librations. As such, on these large scales, one may expect some artefacts bearing similarities with the Hamiltonian mean-field (HMF) model with its two regimes, libration and circulation and its separatrix (Dauxois et al., 2002). To prevent this periodisation length from affecting my predictions, a simple solution is to take L sufficiently large so that, effectively, no particles exist at such a high circulation energy.

From the fact that the Fourier expansion converges the slowest at the triangle wave extrema, one can already predict that our basis will be less representative (as it is truncated) at small separations. This is not a fundamental issue as collective effects do not involve arbitrarily small scales (Weinberg, 1993). In addition, the effect of small-scale undressed interactions can be resolved back from the (bare) multiple approach (appendix 6.B).

In Roule et al. (2022), I used a periodisation length $L = 10\Lambda$ (resp. $L = 100\Lambda$) and 256 (resp. 1024) basis elements for thermal (resp. Plummer) computations. Indeed, since the Plummer equilibrium density has wider tails (see figure 2.7), a larger L is required which, in turn, requires more basis elements to reach a sufficient resolution. In section 4.1.4, I discuss the relevance of such a large number of basis elements. Fortunately, it did not alter the results because the convergence issues only affect the high-order basis elements which are irrelevant to collective effects.

Remark In practice, the basis construction from equation (4.2) involves two separate parts: the cosine and sine elements. There is no interaction between the two groups of elements. Indeed, their Fourier transform cancel at opposite parity in the resonance number k and the polarisation matrix definition equation (3.28) involves only products of Fourier-transformed basis elements with the same resonance number. I therefore naturally distinguish these two components and refer to them as the cosine and the sine polarisation matrices. The full polarisation matrix can be thought as diagonal by block, one block being the cosine and the other one the sine polarisation matrix.

4.1.2 Resonant coordinates

For this one-dimensional model, designing resonant coordinates as defined in section 3.3.1 proves particularly simple. Indeed, the extremal resonant frequencies weakly depend on the considered resonance and no other variables need to be defined (in 1D, the resonance "line" is a single point).

In practice, I only want to perform the integral in equation (3.38) over trapped orbits, i.e., orbits with $\Omega < \Omega_L$, where Ω_L is the smallest frequency captured by the periodised potential. The (truncated) resonant frequency domain $[k\Omega_0, k\Omega_L]$ – with $\Omega_0 = \Omega(J_0)$, $\Omega_L = \Omega(J_L)$, $J_0 = J(r_\text{a} = 0)$ and $J_L = J(r_\text{a} = L)$ – is remapped to $[-1, 1]$ via

$$u = \text{Sign}(k) \frac{\Omega(J) - \Sigma_\Omega}{\Delta_\Omega}, \tag{4.4}$$

where $\Sigma_\Omega = \frac{1}{2}(\Omega_0 + \Omega_L)$ and $\Delta_\Omega = \frac{1}{2}(\Omega_0 - \Omega_L)$. The associated numerators and resonant frequencies

in equation (3.38) are then given by

$$G_k^{pq}(u) = 2\pi\,\mathrm{Sign}(k)\left|\frac{\mathrm{d}J}{\mathrm{d}\Omega}\right|\frac{\partial F}{\partial J}\psi_k^{(p)*}(J)\,\psi_k^{(q)}(J), \tag{4.5a}$$

$$\varpi_k(\omega) = \frac{\omega}{|k|\Delta_\Omega} - \mathrm{Sign}(k)\frac{\Sigma_\Omega}{\Delta_\Omega}, \tag{4.5b}$$

where the action J implicitly depends on the resonant coordinate u through equation (4.4). In practice, the Jacobian involved in equation (4.5a) is computed as

$$\frac{\mathrm{d}J}{\mathrm{d}\Omega} = \frac{\mathrm{d}J}{\mathrm{d}E}\frac{\mathrm{d}E}{\mathrm{d}r_\mathrm{a}}\frac{\mathrm{d}r_\mathrm{a}}{\mathrm{d}J} = \frac{\psi'(r_\mathrm{a})}{\Omega}\left(\frac{\mathrm{d}\Omega}{\mathrm{d}r_\mathrm{a}}\right)^{-1}, \tag{4.6}$$

where the last term is computed via finite differences.

In figure 4.2, I illustrate some functions $u\mapsto G(u)$ from equation (4.5a) for the thermal equilibrium. The higher the element index, the more oscillatory the function. The function $G_k^{pq}(u)$ heuristically oscillates $p+q$ times on the interval $[-1,1]$. The number of oscillations weakly varies with the resonance number k. In the right panel of this figure, I analyse the maximal value of these functions as a function of the basis element p and the resonance number k. At fixed resonance number, k, the strongest function is such that $p=k$, but the larger the resonance number the weaker the functions. One may then expect that the polarisation matrix will be dominated by its low order elements and that the sum over the resonances in equation (3.38) can be safely truncated to a few terms.

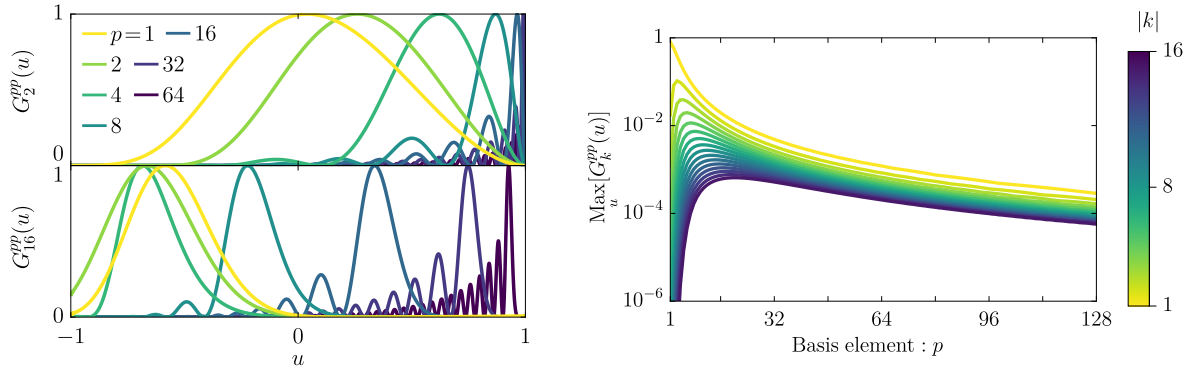

Figure 4.2: Typical polarisation matrix integrands, G_k^{pq}, from equation (4.5a) for the thermal equilibria. *Left:* Few normalised elements $p=q\in\{1,2,4,...,64\}$ as a function of the resonance coordinate u for $k=2$ (top) and $k=16$ (bottom) respectively. The higher the basis element, the more oscillatory the function. Increasing the resonance number k does not significantly change the number of oscillations but shifts the functions. *Right:* Maximal value of G_k^{pp} as a function of the basis element p and the resonance number k. The parity of k sets the considered basis elements (cosine or sine, see equation 4.7). The higher the resonance number or the basis element, the smaller the amplitude of the function. Consequently, the matrices elements should be dominated by the low order elements and the sum over the resonances can be truncated to a few terms.

Basis Fourier transform

Given the convention from equation (2.11), the Fourier transform of the basis elements involved in equation (4.5a) reads

$$\psi_k^{(p)}(J) = \frac{1}{\pi}\int_0^\pi \mathrm{d}\theta\,\psi^{(p)}(x[\theta,J])\cos(k\theta). \tag{4.7}$$

It vanishes for the cosine basis elements from equation (4.2) for odd resonance number, k, and conversely for the sine basis elements. This stems from the fact that (i) $x(\pi-\theta)=-x(\theta)$ (equation 2.11), and (ii) $\cos[k(\pi-\theta)]=(-1)^k\cos(k\theta)$. The integrals on $[0,\frac{\pi}{2}]$ and $[\frac{\pi}{2},\pi]$ compensate each

other for k and basis elements ($\cos$ / $\sin$ not p) of opposite parity. Consequently, there is no ambiguity in the definition of G_k^{pq}. The parity of k sets the basis elements I am considering in the r.h.s. of equation (4.5a). For the same reasons, the bare coupling coefficients, $U_{kk'}$, and the dressed ones, $U^{\mathrm{d}}_{kk'}$, (equations 3.26 and 3.29 respectively) vanish for k, k' of different parity.

The integration from equation (4.7) cannot be performed w.r.t. the angle θ because it would require to invert the mapping $x \mapsto \theta(x)$ from equation (2.10). To compute this integral, I naturally perform the same change of variables as for the frequency computation (equation 2.7). Similarly, the integration is performed w.r.t. the Hénon anomaly (and not the position x) to cure numerical divergences. One is left with two integrals that must be performed simultaneously

$$\psi_k^{(p)}(J) = \frac{1}{\pi}\int_{-1}^{1} \mathrm{d}w \, \frac{\mathrm{d}\theta}{\mathrm{d}w} \, \psi^{(p)}(x[w]) \, \cos(k\,\theta[w]), \tag{4.8a}$$

$$\theta[w] = \int_{-1}^{w} \mathrm{d}w' \, \frac{\mathrm{d}\theta}{\mathrm{d}w'}, \tag{4.8b}$$

where $\mathrm{d}\theta/\mathrm{d}w = \Omega(r_\mathrm{a})\Theta(w)/\sqrt{2}$ with $\Theta(w)$ defined in equation (2.9). Although the integrals from equations (4.8) seem nested, they can be evaluated via the single integral of a 2-vector (see, e.g., appendix B in Rozier et al., 2019). In practice, I use a fourth-order Runge-Kutta (RK4) scheme with 10^3 steps for $w \in [-1, 1]$.

4.1.3 Susceptibility

The polarisation matrix from equation (3.28) involves a sum over the resonances k. Benefiting from the rapid decay of the coupling coefficients, the sum over k can be safely truncated to $|k| \leq k_{\max}$. In practice, $k_{\max} = 10$ proves quite sufficient.

In figure 4.3, I illustrate the determinant of the susceptibility matrix $\mathbf{N}$, from equation (3.18), for the thermal and Plummer equilibria (section 2.3.1), along real frequencies. The frequency $\Omega_0 = \sqrt{GM_{\mathrm{tot}}/\Lambda}$ is the (maximum) orbital frequency in the system's centre ($\Omega_0 = \sqrt{GM_{\mathrm{tot}}/\alpha}$ for the Plummer equilibrium). Because the system possesses this finite maximum frequency, Ω_0, its linear

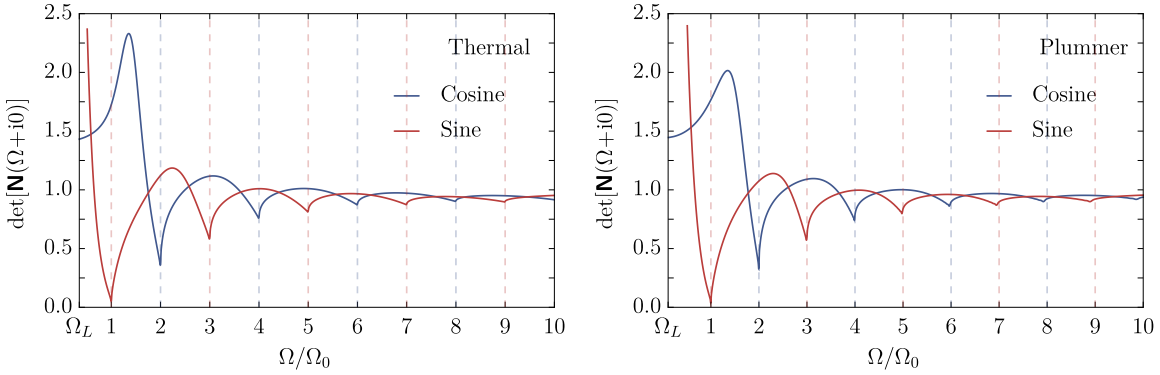

Figure 4.3: Figure from Roule et al. (2022). Determinant of the susceptibility matrix, $\mathbf{N}(\omega)$, as a function of the real frequency Ω/Ω_0 for the even (cosine) and odd (sine) basis elements (section 4.1.1) for both the thermal (left) and Plummer (right) equilibria. Here, Ω_0 is the maximum frequency in the system's centre, while $\Omega_L \simeq 0.35\,\Omega_0$ (resp. $\Omega_L \simeq 0.11\,\Omega_0$) is the smallest frequency captured by the periodised potential with $L = 10\,\Lambda$ (resp. $100\,\Lambda$). Collective effects become negligible at small separation (high frequencies). Conversely, they induce a striking damping for frequencies $\Omega \sim \Omega_0$.

response shows clear signatures at every (resonant) multiple of this frequency. Nonetheless, the collective amplification remains limited, i.e., $\det(\mathbf{N})$ is never much larger than unity.[1] Conversely,

[1] This is not completely true. In figure 4.3, the determinant of the sine susceptibility matrix blows up at low frequencies for both Plummer and thermal equilibria, but it concerns unpopulated regions, $x > L$. This might be related to the periodisation of the basis elements and the associated truncation in the considered frequency domain.

collective effects significantly damp the contribution of the odd resonances $k\Omega \sim \Omega_0$, i.e., the lowest order resonances in the most populated regions.

Both thermal and Plummer equilibria are stable. Accordingly, I did not find any singularity of the susceptibility in the upper-half plane of complex frequencies.[2] I also looked for damped modes (in the lower half-plane) but did not find any either. In this region, the linear response computation requires a careful analytical continuation (section 3.3.2). As illustrated in figure 4.4, such a continuation quickly suffers from numerical saturation. It is to be expected as this opera-

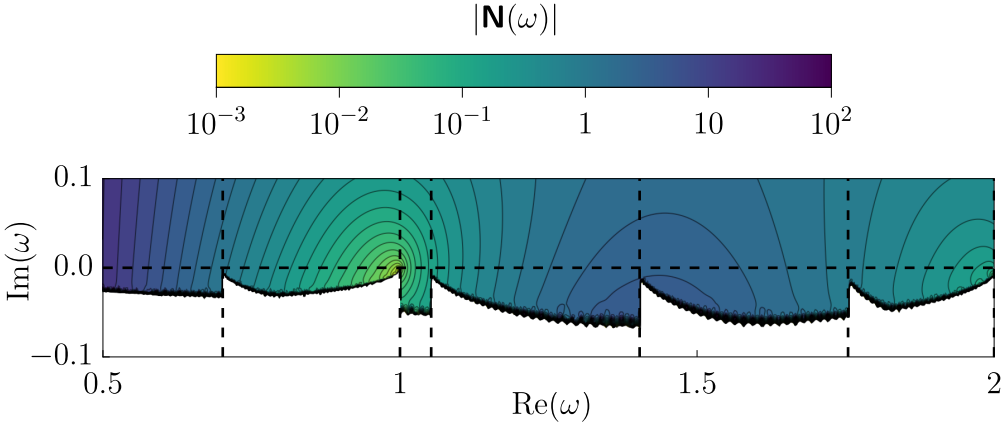

Figure 4.4: Determinant of the (total) susceptibility matrix, $\mathbf{N}(\omega)$, from equation (3.18) for the one-dimensional thermal equilibrium for damped frequencies $\mathrm{Im}(\omega) < 0$ (both the cosine and sine part of the basis are included). Landau's prescription (section 3.3.2) is applied to the polarisation matrix to analytically continue the computation in the lower half-plane. As discussed in section 3.3.3, branch cuts (vertical dashed lines) appear every $k\Omega_L$ and $k\Omega_0$ due to the finite frequency support, $[\Omega_L, \Omega_0] \simeq [0.35, 1]$. The ability to probe damped frequencies remains limited. The analytical continuation quickly saturates and no damped mode is found within the converged regions.

tion is an ill-conditioned numerical problem (Trefethen, 2023). Probing more damped frequencies would require a finer treatment of this continuation. In practice, the response functions $u \mapsto G(u)$ from equation (4.5a) are expanded over Legendre polynomials via Gauss–Legendre quadrature (section 3.3.3). The higher the number of polynomials, the more accurate the function representation but the more difficult the analytical continuation. As I shall now discuss, the contribution from high-order polynomials is enhanced by numerical noise and should be regularised to achieve a better continuation.

4.1.4 Heuristic on convergence and numerical saturation

The numerical computation of the polarisation matrix (equation 3.28) involves a significant number of parameters. I divide the parameters into two categories: (i) the ones that could be taken as large as the computational resources allow and (ii) the ones that should be chosen with care. The dummy parameters are the number of integration points used to perform the various integrals, namely

- K_{mf}, for the integration of the mean-field quantities (action and frequency equations 2.5 and 2.6): typically 32 points proves sufficient.
- K_{ft}, for the Fourier transform of basis elements (equation 3.27): should be taken at least twice as large as the number of basis elements (+ the maximal resonance number) to avoid aliasing.
- K_u^{q}, for the Gauss–Legendre quadrature used to decompose the G functions from equation (4.5a) on Legendre polynomials (equation 3.45): should be taken at least eight times

[2] A better diagnostic than visual inspection of a limited range of (growing) frequency would be to use Nyquist's diagrams (see, e.g., section 2.3 in Pichon & Cannon, 1997).

as large as the number of basis elements to avoid aliasing. Indeed, as illustrated in figure 4.2, the $u \mapsto G_k^{pq}(u)$ function typically oscillates $p+q$ times over the interval $[-1, 1]$. However, these oscillations are highly clustered on one side of the interval.

- $k_{\max}$, the number of resonances over which the sum in equation (3.28) is performed: typically 10 resonances prove sufficient. However, using too few resonances may quickly lead to non-converged results (offsets in the mode's location in figure 4.11), independently of the method used to compute the polarisation matrix and both for growing and damped frequencies. This was already pointed out by Zang (1976); Pichon & Cannon (1997); Evans & Read (1998b). As mentioned in appendix C2 of PR+24, the false weakly damped $\ell = 1$ mode reported by FP22 in the isochrone model is a good example of this issue.

The critical parameters are (i) the number of basis elements, (ii) the number of Legendre polynomials used to approximate the G functions. To discuss their appropriate choice, let me first describe the origin of the saturation in figure 4.4.

The integrands G (equation 4.5a) are not analytical known. However, to compute the polarisation matrix for damped frequencies, $\mathrm{Im}(\omega) < 0$, one needs to evaluate the functions G at complex values of $u = \omega$, as required by Landau's prescription in equation (3.40). To do so, using FP22's method, I approximated the integrands G by their projection over Legendre polynomials,

$$G(u) \simeq \sum_{j=0}^{K_u^{\mathrm{q}}} a_j P_j(u). \qquad \text{(recall 3.44)}$$

In the left panel of figure 4.5, I illustrate the typical $j \mapsto a_j$ series for different resonances k and basis elements p, q. Note that these coefficients have been evaluated through Gauss–Legendre quadrature (equation 3.45) with $K_u^{\mathrm{q}} = 1024$ points, i.e., more than the number of represented coefficients. The coefficients a_j decay for small j but eventually saturate. For small basis index p, q (yellow), the coefficients a_j decay faster. It was to be expected as the G functions are less oscillatory for small p, q (figure 4.2). Let me stress that, forgetting about the saturation, these coefficients should decrease more than exponentially. However, the larger the basis index p, q, the later the decay and the flatter the initial slope.

In the right panel (adapted from PR+24), I illustrate the behaviour of the polarisation matrix computations from equation (3.46). For damped frequencies, the sum in this equation runs over exponentially increasing quantities $D_j(\omega)$. This exponential growth is due to the evaluation of the Legendre polynomials at complex frequencies. From here, there is two distinct cause of numerical instabilities.

Low order basis elements

For low order basis elements, the exponential growth of the $j \mapsto |D_j(\omega)|$ series is compensated by the decay of the coefficients a_j. However, as these coefficients saturate (figure 4.5), the sum in equation (3.46) becomes ultimately divergent when performed over too many Legendre polynomials. The right panel of figure 4.5 perfectly illustrates this behaviour. To prevent this divergence, one should (adaptively) regularise the $j \mapsto a_j$ series. This could be done by truncating the series at the saturation point.

High order basis elements

For high order basis elements, $p, q \gg 1$, at low j, the coefficients a_j decay as

$$|a_j| \propto \exp\left(-\beta_p j\right), \tag{4.9}$$

where $\beta_p > 0$ is a decreasing function of p, q. On the other hand, the $D_j(\omega)$ functions grow as

$$|D_j(\omega)| \propto \exp\left(\beta_\omega j\right), \tag{4.10}$$

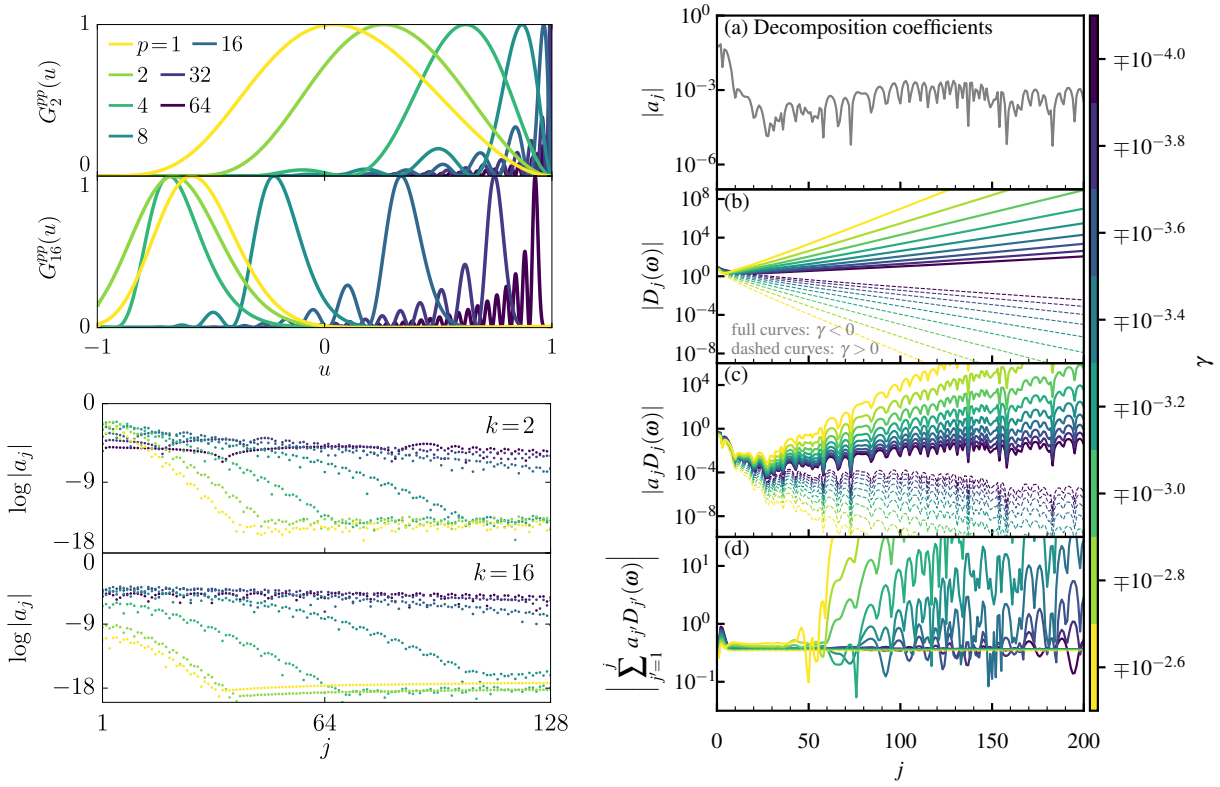

Figure 4.5: *Left:* Typical decomposition series $j \mapsto a_j$ (bottom) of the integrand functions G_k^{pq} (top) over Legendre polynomials using Gauss–Legendre quadrature (equation 3.45) for the one-dimensional model. *Right:* Figure adapted from PR+24. Convergence of the finite Hilbert Transform method presented in section 3.3.3 and extensively used in this thesis. Panel (a) shows the considered coefficients a_j. They correspond to computations for a spherical globular cluster but present the same behaviour as the one-dimensional model (left panel). They decay for small j, but they eventually saturate. Panel (b) shows that, for damped frequencies, the quantity $D_j(\omega)$ in equation (3.46) increases exponentially as a function of j (plain curves). Conversely, for unstable frequencies (dashed curves show the corresponding calculation for $-\gamma$), it decays exponentially. This difference stems from the fact that, for damped frequencies, one has to evaluate the Legendre polynomials $P_j(\omega)$, for complex frequencies. This is the result of residue contribution in Landau's prescription (equation 3.40). Panel (c) shows the individual components of a_jD_j as a function of j. For j large enough, this product does not decay anymore. Finally, panel (d) shows the cumulative sum in equation (3.46) as function of j. For γ sufficiently close to the real frequency line, the sum is convergent. However, as $\mathrm{Im}[\omega]$ becomes more negative, the sum begins to diverge for smaller and smaller j. In contrast to the solid lines which show the damped frequencies (i.e., $\gamma<0$), the dashed lines – which show the unstable frequencies (i.e., $\gamma>0$) – are always convergent.

where $\beta_\omega > 0$ is a growing function of $|\gamma| = |\mathrm{Im}(\omega)|$. For $|\gamma|$ too large, the sum $\sum a_j D_j(\omega)$ involves exponentially growing terms. Let me stress that this growth is only true in norm and for low j. In practice, the a_j coefficients (i) are oscillating between negative and positive values and (ii) should ultimately decay more than exponentially.

While mathematically well-posed, such a behaviour is difficult to handle numerically. This is the reason why, to probe damped frequencies, one should try to keep the number of basis elements as low as possible, though this might be in tension with the requirement to resolve the corresponding shape of the mode. As illustrated in figure 4.6, the larger the number of basis elements, the higher the saturation line. Yet, if one is only interested in growing modes, the number of basis elements can be taken as large as possible (as long as they can be safely evaluated). Indeed, in this case, the Hilbert transform $D_j(\omega)$ from equation (3.46) does not involve the Legendre polynomials (of the first kind), P_j, but only the Legendre functions of the second kind, Q_j. As illustrated by dashed lines in the right panel of figure 4.5, these functions decay exponentially for large j.

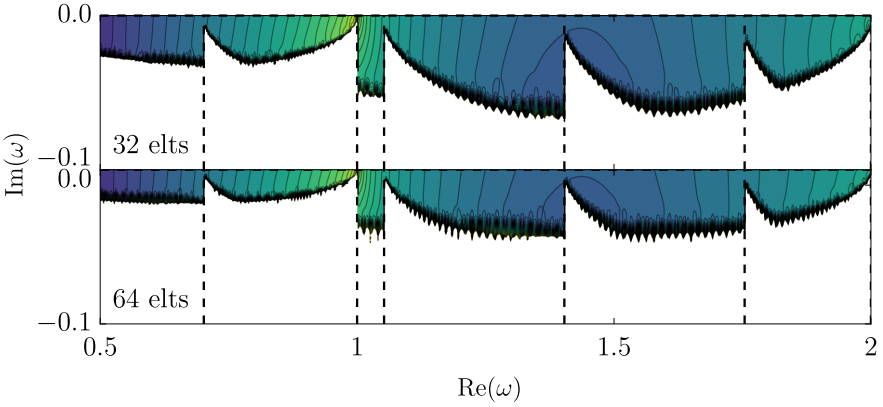

Figure 4.6: Same as figure 4.4 but varying the number of basis elements from 32 to 64. The larger the number of basis elements, the higher the saturation line. Higher order basis elements are more oscillatory and their continuation to complex frequencies is more difficult. If one wants to probe damped frequencies, the number of basis elements should be kept as small as possible.

Conclusion

Some parameters used in Roule et al. (2022) are not the best ones. Indeed, in this article, I use 128 basis elements for the thermal equilibrium and even 1024 for the Plummer one but only 100 Legendre polynomials (and the 100 points for the decomposition). I was later able to reproduce the results from figure 4.3 using only 32 basis elements. Yet, it does not affect nor the linear response results neither the secular one because (i) I was only interested in neutral frequencies, (ii) their overall amplitude is still correct, and (iii) these basis elements are not important for collective effects.

To conclude, probing damped frequencies is an intricate numerical problem. With the current implementation of the method, the number of Legendre polynomials used to expand the G functions should typically not be taken larger than ~ 200 to perform the analytical continuation. Conversely, for growing frequencies, the number of basis elements and the number of Legendre polynomials can be taken as large as the computational resources allow.

4.2 Stability of discs – predictions

Let me now explore the stability of dynamically cold systems such as razor-thin discs, i.e., discs composed mainly of quasi-circular orbits. This section is inspired from Fouvry & Prunet (2022), hereafter FP22, and my work in PR+24.

4.2.1 Bi-orthogonal basis

Owing to the axial invariance of the Newtownian interaction potential from equation (2.3), the linear response of discs (and spheres) can be split in independent harmonics ℓ (historically denoted m for discs). I therefore consider potential basis elements of the form $\psi^{(\mathbf{p})}(r,\phi) = U_p^\ell(r) \mathrm{e}^{\mathrm{i}\ell\phi}$ with $U_p^\ell(r) \in \mathbb{R}$ and associated density basis elements of the same form $\Sigma^{(\mathbf{p})}(r,\phi) = D_p^\ell(r) \mathrm{e}^{\mathrm{i}\ell\phi}$.

In all the computations in this thesis, I use radial basis elements from Clutton-Brock (1972). I reproduce their recurrence relation and provide appropriate normalisation prefactors in appendix 4.A. Similar results could have been obtained using the basis from Kalnajs (1976) (Fouvry et al., 2015; Dootson, 2023) or other bases (e.g., De Rijcke et al., 2019a; Dootson, 2023, using local non-orthogonal Gaussian basis). Advantageously, the Clutton-Brock (1972) basis is (i) global (one only has to set one scale radius), (ii) bi-orthogonal, (iii) has infinite extent and (iv) can be computed

via a numerically-stable recurrence relation. I illustrate the first few basis elements in figure 4.7.

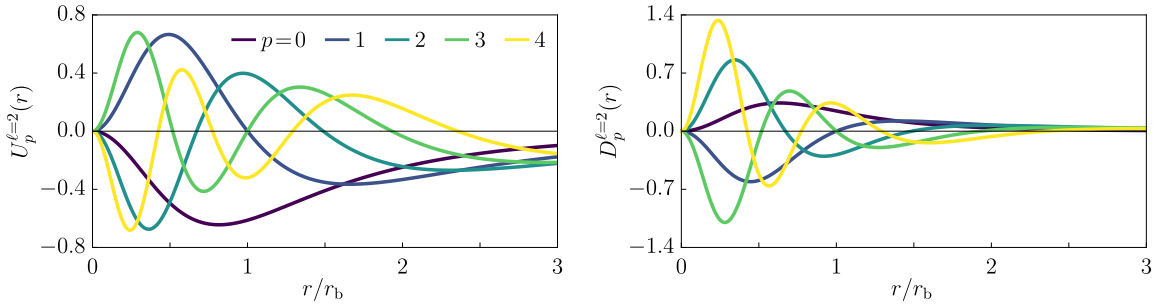

Figure 4.7: Illustration of the first five potential (left) and density (right) basis elements, $U_p^\ell(r)$ and $D_p^\ell(r)$, from Clutton-Brock (1972). The radial basis elements are computed for the azimuthal harmonic $\ell=2$ and are normalised according to equation (3.24) (see appendix 4.A). As expected, the higher the radial number, the more oscillating the basis element. Increasing the number of basis elements resolves finer scales in the system.

4.2.2 Resonant coordinates

Let me now define and discuss the computation of resonance-specific (i.e., dependent on $\mathbf{k}$) coordinates (u, v) for razor-thin discs with central potential, $\psi=\psi(r)$. Their construction from the (dimensionless) frequency ratios, (α, β) from equation (2.16), is concisely presented in appendix B of FP22 which I shortly reproduce and adapt here.

The (dimensionless) resonance frequency,

$$\omega_\mathbf{k} = \mathbf{k}\cdot\mathbf{\Omega}/\Omega_0 = k_r\alpha + k_\phi\alpha\beta, \tag{4.11}$$

is constant along the resonance line. The first resonant coordinate u is then chosen such that (i) $u\propto\omega_\mathbf{k}+\text{cst.}$, and (ii) $u\in[-1,1]$. It reads

$$u = \frac{\omega_\mathbf{k}(\alpha,\beta)-\Sigma_\mathbf{k}}{\Delta_\mathbf{k}}, \tag{4.12}$$

with $\Sigma_\mathbf{k}=\frac{1}{2}(\omega_\mathbf{k}^\mathrm{min}+\omega_\mathbf{k}^\mathrm{max})$, $\Delta_\mathbf{k}=\frac{1}{2}(\omega_\mathbf{k}^\mathrm{max}-\omega_\mathbf{k}^\mathrm{min})$, and $\omega_\mathbf{k}^\mathrm{min}$ (resp. $\omega_\mathbf{k}^\mathrm{max}$) the minimal (resp. maximal) value reached by $\omega_\mathbf{k}$. These extrema can be determined following appendix B of FP22.

The second resonant coordinate v can be arbitrarily chosen as long as it efficiently scans over the resonance line, i.e., as long as it is not proportional to u. One then just needs to provide its boundary values. FP22 typically used $v=\alpha$ for most resonances and $v=\beta$ when u is independent of β, i.e., for $k_\phi=0$. In practice, one would *a priori* want to scan the resonance lines as uniformly as possible. In that respect, choosing $v=\alpha$ proved quite inadequate [especially at inner Lindblad resonance (ILR), $\mathbf{k}=(-1,2)$] and I used instead $v\propto\alpha^n$ (typically with $n=2$). The second resonant coordinate ultimately reads (appendix A4 in PR+24)

$$v = \left[\frac{s - s_\mathbf{k}^\mathrm{min}(u)}{s_\mathbf{k}^\mathrm{max}(u) - s_\mathbf{k}^\mathrm{min}(u)}\right]^n, \tag{4.13}$$

with

$$s = \begin{cases}\beta & \text{if } k_2=0,\\ \alpha & \text{otherwise,}\end{cases} \tag{4.14}$$

and n a free parameter. In equation (4.13), the extremal values of $s\in[s_\mathbf{k}^\mathrm{min}(u), s_\mathbf{k}^\mathrm{max}(u)]$ along the resonance line (set by $\mathbf{k}$ and u) are determined following appendix B of FP22.

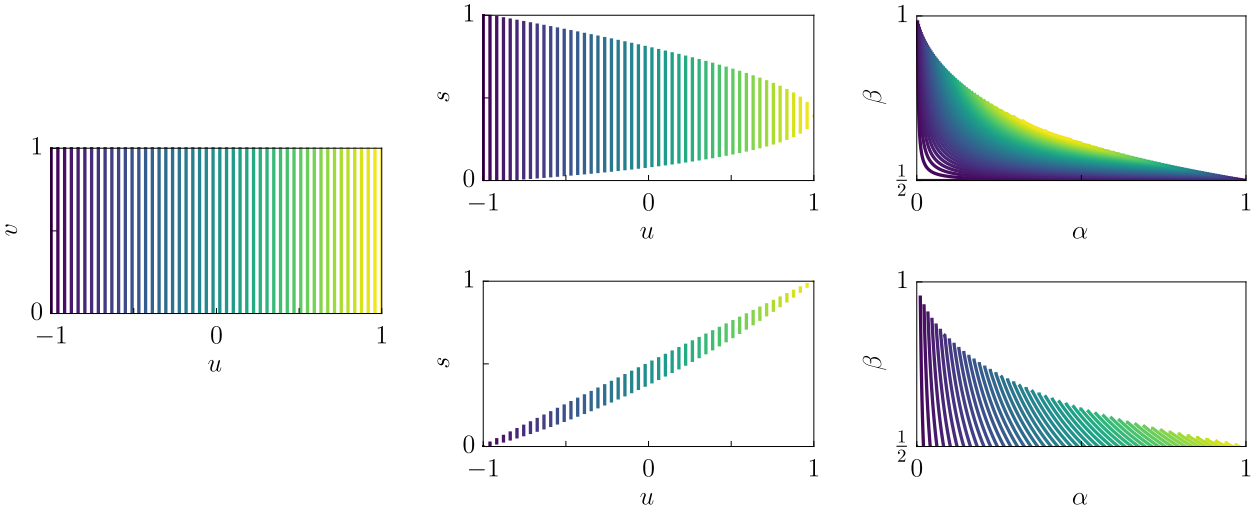

Figure 4.8: Illustration of the resonant mappings $(u, v) \to (\alpha, \beta)$ for the ILR (top) and the corotation (bottom) via the intermediate s coordinate (equation 4.14). Each colour correspond to a resonance line of constant $\mathbf{k}\cdot\mathbf{\Omega}$. For the ILR, the resonance lines go from circular to circular orbits while, for corotation, they go from circular to radial orbits. It illustrates the diversity of resonant mappings to handle.

In figure 4.8, I illustrate the resonant mappings, $(u, v) \to (\alpha, \beta)$, for a few resonance numbers, $\mathbf{k}$, namely the ILR $[\mathbf{k} = (-1, 2)]$ and the corotation resonance $[\mathbf{k} = (0, 2)]$. These change of coordinates are a requirement for the linear response of self-gravitating systems. Indeed, by construction, it involves scanning the full orbital space and dealing appropriately with resonant denominators, as visible in equation (3.38). As mentioned, the ILR resonance lines are not nearly linear in α and the resonance coordinate v needs to be chosen appropriately to ease the integration over the resonance line.

Once this new coordinate system defined, equation (3.28) reduces to equation (3.38) when taking

$$G(u) = \int_0^1 \mathrm{d}v \frac{2}{\Omega_0(\omega_{\mathbf{k}}^{\max} - \omega_{\mathbf{k}}^{\min})} \left| \frac{\partial \mathbf{J}}{\partial(u, v)} \right| G(\mathbf{J}[u, v]), \tag{4.15a}$$

$$\varpi_{\mathbf{k}}(\omega) = \frac{\omega - \Sigma_{\mathbf{k}}}{\Delta_{\mathbf{k}}}, \tag{4.15b}$$

where $\Sigma_{\mathbf{k}}$ and $\Delta_{\mathbf{k}}$ follow from equation (4.12). In equation (4.15a), I also introduce $G(\mathbf{J})$ which, in the case of razor-thin discs, reads

$$G_{pq}^{\ell\mathbf{k}}(\mathbf{J}) = -(2\pi)^2 \, \delta_{k_\phi}^{\ell} \left(\mathbf{k} \cdot \frac{\partial F}{\partial \mathbf{J}} \right) W_p^{\ell\mathbf{k}}(\mathbf{J}) \, W_q^{\ell\mathbf{k}}(\mathbf{J}). \tag{4.16}$$

As expected, they involve the Fourier transform of potential basis elements (equation 3.27). In this case, they read (Tremaine & Weinberg, 1984; Fouvry et al., 2015)

$$W_p^{\ell\mathbf{k}}(\mathbf{J}) = \frac{1}{\pi} \int_{-1}^{1} \mathrm{d}w \, \frac{\mathrm{d}\theta_r}{\mathrm{d}w} \, U_p^{\ell}(r) \, \cos(k_r \theta_r + k_\phi [\theta_\phi - \phi]), \tag{4.17}$$

where the radius, r, and the angles, θ_r and $\theta_\phi - \phi$ (equation 2.22), are implicit functions of the orbit, $\mathbf{J}$, and the Hénon anomaly, w, (equation 2.7). As in the one-dimensional case (section 4.1.2), the integration is performed w.r.t. the Hénon anomaly to cure numerical divergences. Equation (4.17) and the angles are computed simultaneously (see, e.g., appendix B in Rozier et al., 2019), pushing the angles with

$$\frac{\mathrm{d}}{\mathrm{d}w}(\theta_r, \theta_\phi - \phi) = \left(\Omega_r, \Omega_\phi - L/r^2 \right) \Theta(w), \tag{4.18}$$

where Θ follows from equation (2.18).

4.2.3 Software libraries

Computing the linear response of stellar self-gravitating systems is an intricate task. During my PhD, I have developed several libraries with M. Petersen to facilitate it for razor-thin discs and spherical systems. It aims at being a generic framework that could be extended to other systems in the future. These libraries are publicly available at https://github.com/JuliaStellarDynamics. In this section, vastly inspired by PR+24, I briefly present these libraries.

`OrbitalElements.jl`

The library `OrbitalElements.jl` provides computation of the mean-field quantities (e.g, action and frequency from equations 2.15 and 2.16) for (bounded) orbits in a static central potential, $\psi = \psi(r)$. At the heart of the library is the ability, given a central potential and its two first derivatives, to convert nearly seamlessly between different orbital elements, i.e., different constants of motion, namely

- the pericentre and apocentre radii $(r_\mathrm{p}, r_\mathrm{a})$;
- the effective semi-major axis and eccentricity (equation 2.17);
- the energy and angular momentum (equation 2.14);
- the actions (J_r, L) (equation 2.15),
- the orbital frequencies (Ω_r, Ω_ϕ) associated respectively with the radial and azimuthal oscillations (equation 2.21);
- the frequency ratios (α, β) from which the frequencies are computed (equation 2.16);
- the resonance-specific (i.e., dependent on $\mathbf{k}$) coordinates (u, v) (section 4.2.2).

In practice, `OrbitalElements.jl` is centred around the effective semi-major axis and eccentricity (a, e), but straightforward conversions between different orbital labels exist as simple function calls. These change of coordinates are a requirement for the linear response of self-gravitating systems. Indeed, by construction, it involves scanning the full orbital space and dealing appropriately with resonant denominators, as visible in equation (3.28). In FP22, these conversions were performed analytically for the isochrone model. With this library, we provide a generic computation of orbital elements for any central potential.[3]

In figure 4.9, I illustrate the typical conversions required to compute the functions from equation (4.15a): starting from the resonant frequencies, (u, v) (equations 4.12–4.13), up to the energy and angular momentum, (E, L) (equation 2.14), via the frequency ratios, (α, β) (equation 2.16), and the effective anomaly and eccentricity, (a, e) (equation 2.17).

`AstroBasis.jl`

Fundamental to the matrix method are the chosen basis functions. The `AstroBasis.jl` library is an implementation of several bases of radial functions, $r \mapsto U_p^\ell(r)$, with a straightforward interface. At present, `AstroBasis.jl` supports the disc bases from Clutton-Brock (1972) and Kalnajs (1976), and the spherical bases from Clutton-Brock (1973), Fridman & Poliachenko (1984)/Weinberg (1989) (Bessel), and Hernquist & Ostriker (1992). A few basis elements from the basis used in this thesis (Clutton-Brock, 1972) are illustrated in figure 4.7.

`FiniteHilbertTransform.jl`

The library `FiniteHilbertTransform.jl` implements the method from FP22 (section 3.3.3) to compute resonant integrals while complying with Landau's prescription (equation 3.40) in systems

[3] In practice, the library is currently limited to cored potentials, as it assumes $u \in [-1, 1]$.

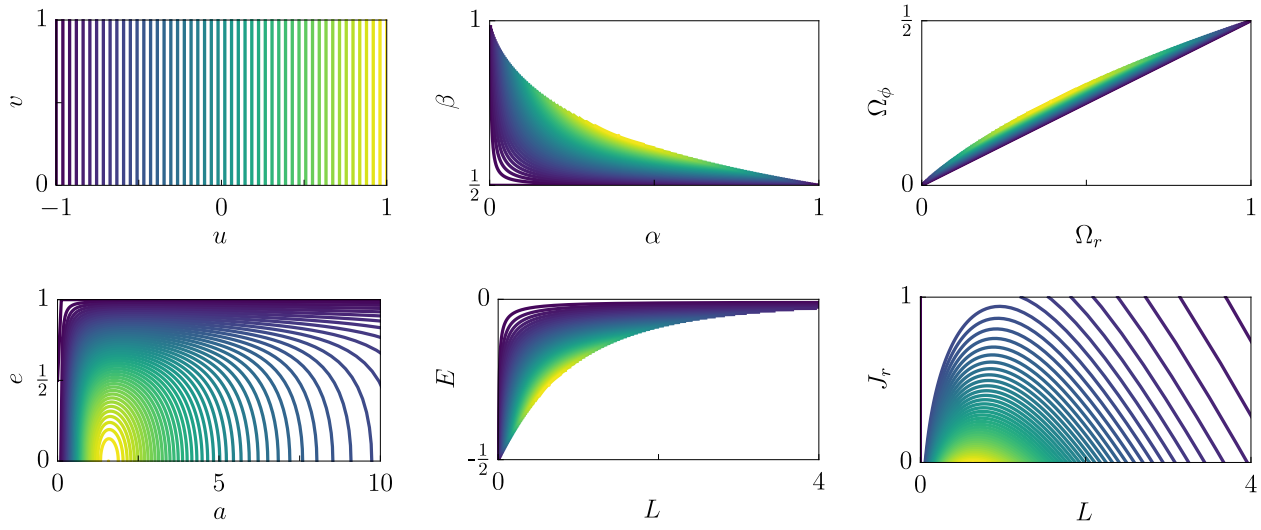

Figure 4.9: Illustration of the typical mappings required to perform linear response computations for razor-thin discs at the ILR. Starting from the resonant coordinates, (u, v) (equations 4.12–4.13), in which the polarisation matrix takes the form of a Hilbert transform (equation 3.38), one needs to convert to the energy and angular momentum (E, L), in which most distribution functions (DFs) are defined, and to the frequencies to ultimately compute the integrand functions G from equation (4.15a).

with finite frequency support. It computes (i) the decomposition coefficients over Legendre polynomials for a given function G, and (ii) the $\omega \mapsto D_k(\omega)$ functions from equation (3.46) at all points in the complex plane.

The present method has mainly been introduced to probe linear response for damped frequencies, i.e., in the lower-half of the complex plane. In this regime, Landau's prescription (equation 3.40) requires to give a meaning to $G(\omega)$ with $\omega \in \mathbb{C}$. Phrased differently, one has to perform an analytical continuation of these G functions, which involve intricate, non-analytically known functions in the present self-gravitating case (equation 4.15a). Given that analytical continuation is intrinsically a (severely) ill-conditioned numerical problem (Trefethen, 2023), for damped frequencies, i.e., $\mathrm{Im}(\omega) < 0$, the effective numerical precision plays an important role in setting the floor for accuracy (section 4.1.4).

`LinearResponse.jl`

The computation of the polarisation matrix (equation 3.28) and associated by-products (equations 4.15a–4.17) is performed by `LinearResponse.jl`. It mainly requires the user to provide (i) the considered gravitational potential (and two derivatives), (ii) the DF (through its directional derivatives $\mathbf{k} \cdot \partial F / \partial \mathbf{J}$), and (iii) a bi-orthogonal basis. Some of these are available via `OrbitalElements.jl` and `AstroBasis.jl`, but the user can also supply its owns.

For a given harmonic ℓ and for each resonance $\mathbf{k}$ and each matrix element (p, q), the calculations proceed in three phases. The first two aim at computing the $u \mapsto G(u)$ functions from equation (4.15a), namely by (i) computing the Fourier transform of basis elements (equation 4.17),[4] and (ii) performing an integral along the resonance line, i.e., over the resonance variable v. The third phase is to decompose these functions over Legendre polynomials, through the computation of the a_k coefficients from equation (3.44) using `FiniteHilbertTransform.jl`. Once these coefficients are known, the polarisation matrix can be efficiently computed at any given complex frequency ω.

[4] The $1/\pi$ prefactor is missing in equation (A15) of PR+24.

4.2.4 Zang's bi-symmetric[5] instabilities

This result has been presented in PR+24 and is reproduced here for completeness.

In order to validate the numerical implementation, I recover well-documented unstable modes in razor-thin discs. In practice, following the work of Zang (1976), I consider the tapered Mestel disc (section 2.3.2), whose scale-invariance allows for some analytical simplifications. Nonetheless, in what follows, I do not use these simplifications and rather use the generic scheme from section 3.2, namely, Kalnajs' matrix method. The DF of the stars is tapered in the central region (section 2.3.2). The presence of this inner cut-off mimics an unresponsive central bulge, hence introducing a reflexive boundary: the sharper this inner cut-out, the stronger the instability (Zang, 1976). The disc's outskirts are also tapered, though this does not impact the disc's stability, provided that this external cut-out is sharp enough and far enough (Evans & Read, 1998b).

Note that the method based on finite Hilbert transform implemented in `LinearResponse.jl` is not perfectly suited here. Indeed, because of its central divergence, the frequency range in the true Mestel disc (section 2.3.2) is not finite. The truncation introduced in equation (2.33) prevents such a divergence. As a result, the truncated Mestel model still supports a wide (but finite) range of frequencies. Yet, the range of interesting frequencies is drastically reduced by the inner taper in the DF (section 2.3.2). Using the full range of possible frequencies would be particularly ill-advised. I deal with this particular issue by limiting the orbital domain probed by the code. This truncation is set by the parameter $r_{\min}$ and illustrated in figure 4.10. The effective domain in (α, β) is restricted

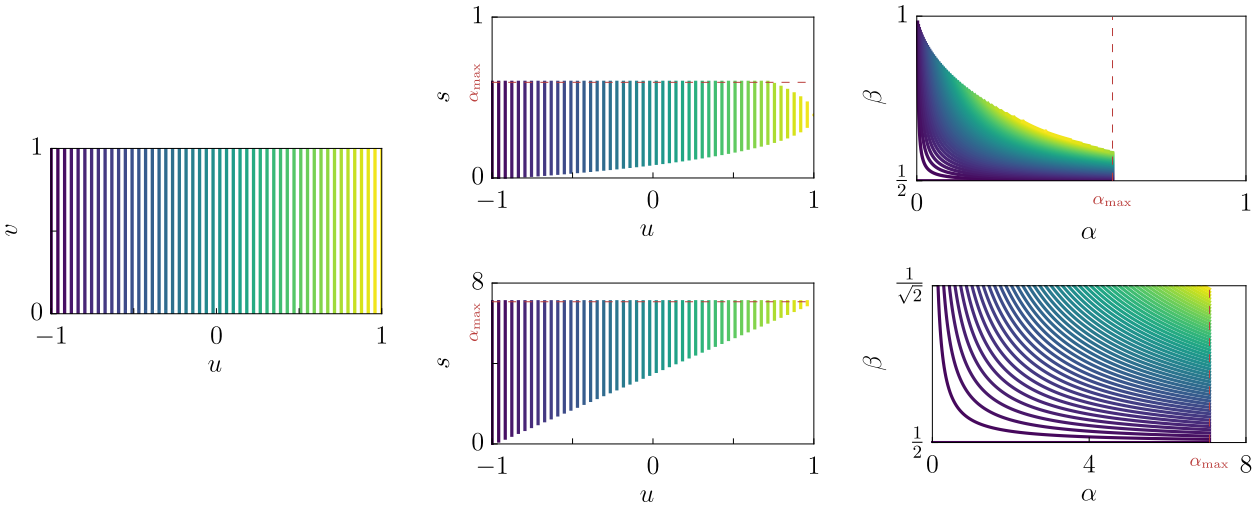

Figure 4.10: Illustration of the truncation of the domain of frequency, (α, β), probed by resonance variables. The top row corresponds to the isochrone mappings from figure 4.8 with truncation parameter $r_{\min} = 1$. This is purely illustrative since there is no particular reason to truncate the domain in this case. The bottom row corresponds to the truncated Mestel potential from equation (2.33). For this potential, the available frequency domain extends far beyond the truncated one. Considering the tapered DFs from equation (2.36), the interesting part of the domain is very limited. Setting $r_{\min} = 0.2 \neq 0$, I focus on the frequencies of interest. Both cases are illustrated for the ILR, $\mathbf{k} = (-1, 2)$. The effective (α, β) domain is restricted to $\alpha \leq \alpha_{\max} = \alpha_c(r_{\min})$ with $\alpha_c(r)$ the circular frequency ratio from equation (2.20).

to the region below $\alpha_{\max} = \alpha_c(r_{\min})$ with $\alpha_c(r)$ the (outward decreasing) circular frequency ratio from equation (2.20). Importantly, this is a linear constraint which is therefore straightforward to take into account. It mainly amounts to tweaking the values of the extrema of the (dimensionless) resonance frequency $\omega_{\mathbf{k}}$ from equation (4.11). Details on taking this new constraint into account

[5] Let me highlight that tapered Mestel discs do suffer from an $\ell = 1$ instability whatever the disc's temperature (Zang, 1976; Toomre, 1981), i.e., whatever q in equation (2.36). As in Sellwood & Evans (2001) and Sellwood (2012), perturbations are therefore always restricted to their bi-symmetric component in all simulations performed in this thesis.

are given in appendix A1 of PR+24. In practice, I set $r_{\rm min}=R_{\rm in}/5$, with $R_{\rm in}$ the radius of the DF inner taper (table 2.1). For fully self-gravitating (core) systems, one would keep the default $r_{\rm min}=0$: this does not introduce any domain restriction.

All these subtleties reflect that the method of FP22 is not perfectly suited to the discs studied in this thesis (section 2.3.2). Its use might prove less cumbersome with more realistic galactic models whose rotation curve do fall in the centre (see, e.g., figure 4 in Reid et al., 2014). In the case of Mestel discs, one might rather want to adapt the method to a resonant coordinate $u\in[0,+\infty)$ by using (orthogonal) functions different from Legendre polynomials. Laguerre's polynomials might be a good candidate for this purpose (Robinson, 1990).

Once this model is set up, I perform stability analysis for two-armed modes, i.e., $\ell=2$ modes, as one varies the properties of the inner taper.[6] As reported in table 2 of PR+24, I find a satisfying agreement between the (semi-analytical) predictions of Zang (1976) and Evans & Read (1998b), and the present linear predictions for the growth rate and oscillation frequency of the most unstable mode. These predictions have already been confirmed using numerical simulations by Sellwood & Evans (2001). I nonetheless performed my own simulations which I present later in section 4.3. Similarly to Sellwood & Evans (2001), the numerical simulation of Zang discs proved particularly challenging.

In figure 4.11, I present a typical map of the complex frequency plane one can obtain using `LinearResponse.jl`. More precisely, figure 4.11 illustrates the determinant of the (gravitational) susceptibility matrix, $\mathbf{N}(\omega)$ from equation (3.18), through its level contours in the complex-frequency plane. This determinant vanishes at the frequency $\omega_{\rm M}/\Omega_0=0.878+0.126{\rm i}$, i.e., the system supports a growing mode. The shape of this unstable mode is reported in figure 4.12, where I compare it with the result from Zang (1976). I find a quantitative match between both approaches. In figure 4.11, the saturation and ringing for damped frequencies are to be expected. As discussed in section 4.1.4, they are a direct consequence of analytical continuation being an ill-conditioned numerical problem.

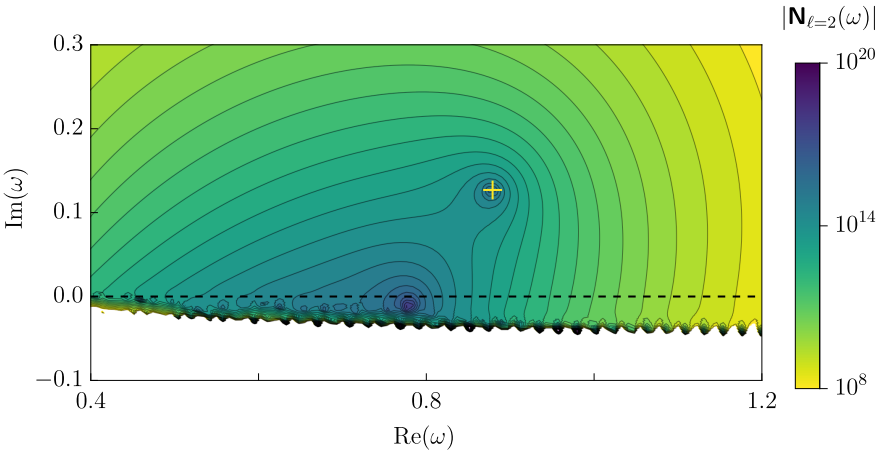

Figure 4.11: Figure adapted from PR+24. Isocontours of the determinant of the $\ell=2$ susceptibility matrix (100 basis elements) from equation (3.18) for Zang's $\nu=4$ disc (section 2.3.2). The dominant mode obtained by Zang (1976) is highlighted with a yellow cross and is recovered within 1% precision.

Let me note that here I used the generic basis from Clutton-Brock (1972), which is not tailored to asymptotically match the disc's underlying potential. Interestingly, this did not impact my ability to recover precisely the underlying modes using linear response theory. Yet, I was not able to consistently measure this mode in N–body simulations using this basis to solve Poisson

[6] The azimuthal harmonic number for discs is historically denoted m. Adapting here from the spherical case, I nonetheless denote it ℓ.

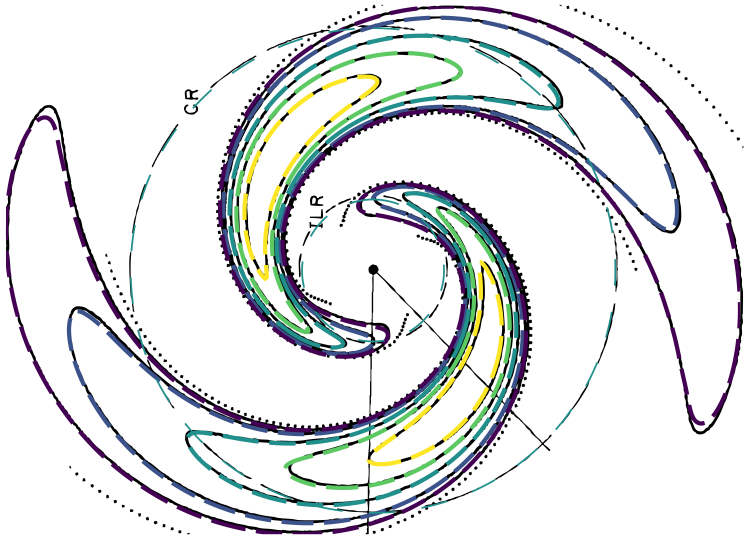

Figure 4.12: Figure from PR+24. Shape of the $\ell=2$ dominant mode of the $N=4$ Zang disc as predicted by `LinearResponse.jl` (coloured dashed lines) overlaid with the shape obtained by Zang (1976) (in black, figure 9 therein). For both shapes, the contours denote the 10, 20, 40, 60 and 80% of the peak density, with only the overdensity being represented. The dotted circles show the corotation (CR) and ILR radii of the mode. Both linear predictions are in very good agreement. This is one of the key results of this thesis.

equation (1.19c) (basis function expansion or self-consistent field method). This is further discussed in section 4.3.1. Expanding `LinearResponse.jl` to accommodate for more generic basis elements should be the topic of future work.

4.2.5 Varying the active fraction

A simple way to stabilise the disc is to decrease the overall active fraction ξ (equation 2.36), i.e., the fraction of the disc that is responsive to the self-gravity (section 2.3.2), while keeping the same underlying potential. It crudely mimics the fact that part of the potential is not generated by the dynamically cold disc of stars but rather by a dynamically hot dark matter halo. The dispersion relation equation (3.22) then becomes

$$\det[\mathbf{I} - \xi\mathbf{M}(\omega)] = 0, \tag{4.19}$$

where $\mathbf{M}$ stands for the polarisation matrix of the fully self-gravitating disc ($\xi=1$).

In figure 4.13, I present the rotation frequency, Ω_M, and the growth rate, γ_M of the most unstable mode in the Zang $\nu=4$ as a function of the active fraction ξ. As expected, the smaller the active

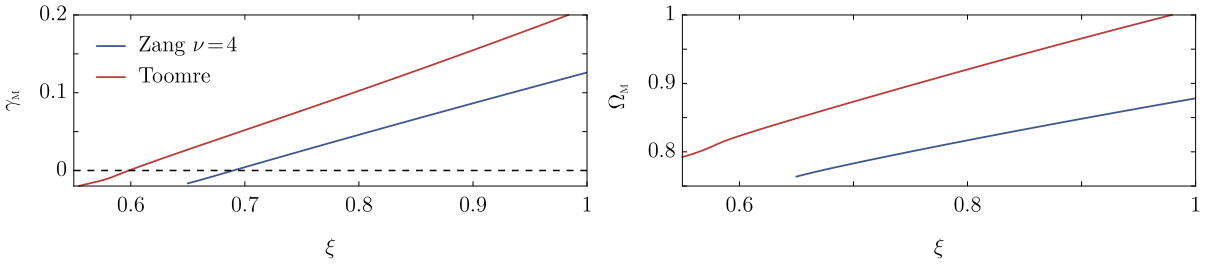

Figure 4.13: Growth rate, γ_M, (left) and rotation frequency, Ω_M, (right) of the most unstable mode in the Zang $\nu=4$ disc and Toomre's disc (table 2.1) as a function of the active fraction ξ. Zang's disc is stabilised at $\xi\approx0.69$. Toomre's disc is colder and therefore requires a smaller active fraction to stabilise.

fraction, the more stable the disc. The pattern speed (or equivalently the rotation frequency) also increases with the active fraction. This should be compared to the results of Dootson (2023) using two different approaches both relying on the linear response in time and not in Laplace frequency ω (section 5.2.4 therein). While perfectly suited for strongly unstable systems, such approaches fail to cross stability and probe the weakly damped modes found in partially self-gravitating (or tepid) discs. Satisfyingly, here, the mode smoothly crosses marginal stability. It proves that the analytical continuation of the susceptibility matrix is performed correctly.

4.2.6 Damped modes in Toomre's disc

While the Zang $\nu=4$ disc with active fraction $\xi\lesssim 0.7$ is stable w.r.t. bisymmetric perturbations, I did not investigate it further. I rather studied Toomre's disc (table 2.1), whose parameters are slightly different but corresponds to the same potential and DF family. Its evolution has been more thoroughly investigated in the literature (Sellwood, 2012; Fouvry et al., 2015; Sellwood & Carlberg, 2019) since the seminal paper of Toomre (1981) who introduced it to illustrate the process of swing amplification. The disc's parameters (table 2.1) are chosen such that the half-mass disc ($\xi=0.5$) is stable with Toomre number $Q=1.5$. This disc is colder than Zang's $\nu=4$ disc studied in the previous sections ($\sigma_r=0.284$ *vs* 0.378). As illustrated in figure 4.13, it therefore requires a smaller active fraction to stabilise the disc.

Yet, as expected from figure 4.13, Toomre's disc seems to support a weakly damped mode. In figure 4.14, I present the determinant of the susceptibility matrix for the $\ell=2$ modes. For this

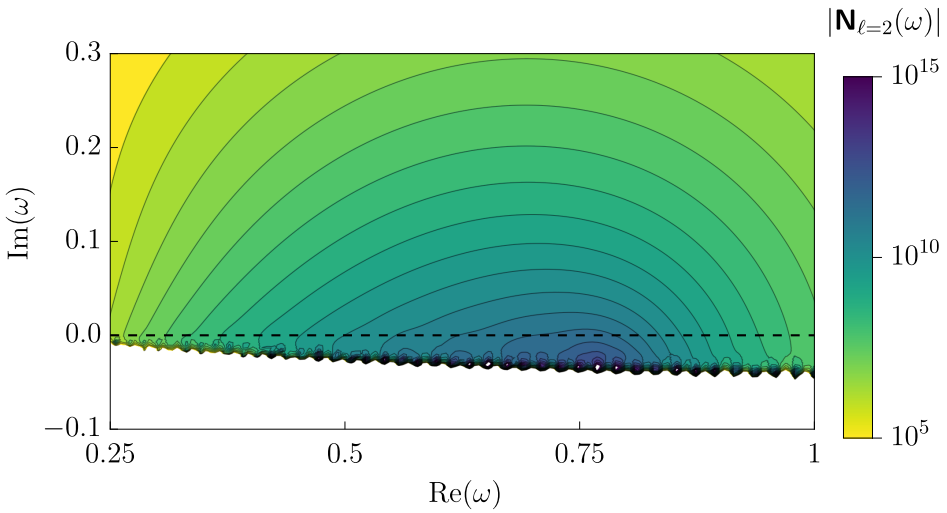

Figure 4.14: Isocontours of the determinant of the $\ell=2$ susceptibility matrix from equation (3.18) for Toomre's disc (section 2.3.2). As expected, the disc is stable, and no growing mode is found. Yet, the shape of the isocontours seemingly reveals the presence of one or more weakly damped modes below the real axis, notably around the rotation frequency $\Omega_{\text{M}}\sim 0.75$.

figure, I used the same parameters (number of basis elements...) as for the Zang $\nu=4$ disc presented in figure 4.11. Unfortunately, for such a set of parameters, the analytical continuation saturates very early and no clear singularity is visible in the lower-half of the complex plane. However, the flatness of the isocontours above the real axis cannot be explained by a single dominant damped mode. It suggests the presence of multiple weakly damped modes around the rotation frequency $\Omega_{\text{M}}\sim[0.6, 0.75]$.

To probe deeper into the damped frequencies, I performed the same analysis as in figure 4.14 but with fewer basis elements and resonances. As discussed in section 4.1.4, reducing the number of basis elements facilitates the continuation as lower basis elements are smoother functions. I also reduced the number of resonances because I empirically found (both in the unstable Zang disc and

this stable one) that using too few basis elements tends to increase the growth rate of the mode and that decreasing the number of resonances has the opposite effect. The computations with 10 basis elements and all resonances $|k_r| \leq 10$ therefore predict an unstable mode, and I do not show it here. In figure 4.15, I present the result of this analysis with 10 basis elements and only 3 resonances [ILR, corotation and outer Lindblad resonance (OLR)]. Let me stress that this result is purposely

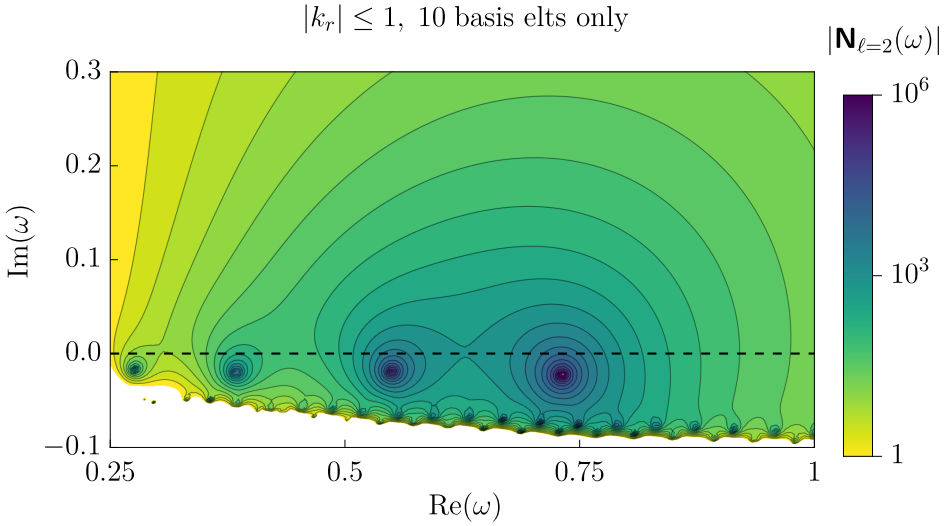

Figure 4.15: Same as figure 4.14 but using fewer basis elements (10 instead of 50) and resonances [ILR, corotation and OLR only] to probe larger damping rates. Interestingly, multiple damped modes with roughly the same damping rate are found. In figure 4.14 the damped modes are either closer to one another or have a larger damping rate, $|\gamma_{\rm M}|$, i.e., are lower down in the complex plane. Indeed, the flatness of the isocontours above the real axis cannot be explained by a single dominant damped mode. This is one of the key results of this thesis.

not converged to illustrate the presence of *weakly* damped modes in tepid Mestel discs and that the exact location of the mode should not be taken as a quantitative result. It would be interesting to investigate this disc using the same method as Zang (1976). Indeed, using the self-similarity of the potential, the functions which need to be evaluated at complex values are known analytically. And (Zang, 1976) already reported on the presence of damped modes in similar discs (namely the full-mass $\nu=2$ disc). This tailored method should give a more precise location of the damped modes.

Even not converged, this prediction is interesting as it confirms the presence of multiple weakly damped modes. Furthermore, it can be used to perform predictions on the long-term evolution of the disc and study the impact of these modes on the secular orbital heating. This is the topic of chapter 6.

4.3 Stability of discs – simulations

In this section, I set out to recover the predicted instabilities (section 4.2.4) in razor-thin Zang discs using numerical simulations. Such an investigation has already been performed by Sellwood & Evans (2001) (hereafter SE01). To that regard, the results presented in this section are not new but rather confirm the analysis of SE01. In particular, I aim to highlight two pitfalls in which I ran while attempting to appropriately simulate and measure the evolution of instabilities of tapered Mestel discs.

4.3.1 Simulation method

As the first necessary step to perform these simulations, I present the method I used to sample the initial conditions of the disc in appendix 4.B.

Basis function expansion

I first attempted to perform the N–body simulations using `EXP` (Petersen et al., 2022), an N–body simulation code using basis function expansion. This self-consistent field method uses the bi-orthogonal basis elements from section 3.2.1 to solve Poisson equation (1.19c) throughout the simulation (see, e.g., Hernquist & Ostriker, 1992). This method is particularly efficient to approximate the collisionless evolution of self-gravitating systems because evaluating the forces only requires $\mathcal{O}(N)$ evaluations and can be straightforwardly parallelised. It is considered to be one of the optimal numerical methods to study the stability of self-gravitating systems in simulations (Earn & Sellwood, 1995). However, the efficiency of this method heavily depends on the appropriate choice of the basis elements. It might behave poorly if the equilibrium state is not well represented by the first few basis elements. To solve this issue, Weinberg (1999) proposed a numerical scheme to tune the basis elements to the equilibrium state by solving the associated Sturm–Liouville equation.

Yet, in the present case, the mean-field potential was externally imposed (and fixed) in the simulations I wished to perform. Only the $\ell=2$ fluctuations did participate in the dynamical evolution. Therefore, I was hoping that the basis only had to be representative of the $\ell=2$ perturbations, i.e., of the growing mode from figure 4.2.4. I used 30 elements of the Clutton-Brock (1972) basis. Here, I might have repeated the mistake of SE01 and used too few basis elements. Unfortunately, performing 16 realisations with $N=2\times10^7$ particles each, the measured instability was (i) varying quite significantly among realisations and (ii) on average, twice stronger than expected. SE01 did try Kalnajs (1976) basis elements, as well as Bessel functions and logarithmic spirals (Kalnajs, 1971). They reported that, in all cases, the measured growth rates were larger than expected up to a factor 10. SE01 associated the failure of the basis function expansion method to aliasing caused by the truncation of the basis. Increasing the number of basis elements might have helped to reduce the aliasing and match the linear predictions, but I did not investigate this method further.

Weinberg (private communication) recently investigated the stability of Zang discs using tailored basis functions from the Sturm–Liouville solver (Weinberg, 1999). He could recover the expected growth rates. This further highlights the importance of a careful choice of the basis elements when performing such self-consistent field simulations.

Particle-mesh code

As SE01, I then turned to a particle-mesh method. I adapted the particle-mesh code used in Fouvry et al. (2015) (courtesy of John Magorrian), a simpler 2D version of the `GROMMET` code (Magorrian, 2007). In particular, this allowed me to test other softening kernels than the Plummer one (section 4.3.2) and to extract relevant summary statistics along the simulation. It is described in section 4.4.1 of Fouvry (2017) and I only give here a brief overview. This code is publicly available at https://github.com/MathieuRoule/mestel2d.git.

As any particle-mesh N–body code, this code uses the fact that the convolution in Poisson equation (1.19c) can be transformed in a simple product using Fourier transform. It reduces the required number of computations compared to a direct N–body code [$O(N\times M\ln M)$ *vs* $O(N^2)$, with M, the number of mesh nodes]. This allows for simulations with a larger number of particles (at the cost of a worse representation of the instantaneous potential). The key steps of the algorithm are then as follows.

First, the (discrete) Fourier transform of the considered (softened) interaction potential, U_ε (equations 4.22 and 4.23), is computed once and for all. It is computed on twice the box size to avoid aliasing ("doubling up"). Then, at each integration time step, the force acting on each particle is computed by (i) projecting the density (particles) on the Cartesian grid, (ii) filtering only the $\ell=2$ fluctuations, (iii) taking the (fast) Fourier transform of these density fluctuations, (iv) multiplying the Fourier transforms of the pairwise interaction potential and the density to get the Fourier transform of the instantaneous potential, (v) inverting it to get the instantaneous

potential fluctuations on the grid, (vi) deriving the associated force field by finite differences, (vii) interpolating the force field at the particle exact location using cloud-in-cell scheme and, (viii) adding the radial contribution of the mean-field Mestel potential.

The projection/filtering step is the trickiest one when working with a Cartesian grid. As explained in section 4.4.1 of Fouvry (2017), the particles are first projected on a much finer polar grid of $n_r \times n_\phi$ cells. This fine grid is used to approximate the bisymmetric density fluctuations

$$\delta\rho_2(r) = \sum_i m_i \delta(r - r_i) \mathrm{e}^{2\mathrm{i}\phi_i}. \tag{4.20}$$

This density is then projected on the Cartesian grid using a cloud-in-cell scheme.

Working within the units $G = R_{\rm in} = V_0 = 1$, the results I present here were obtained with a box which extends up to $\pm R_{\rm max} = 20$, a Cartesian grid of $n_x^2 = 1\,024^2$ cells, and a unique time step $\delta t = 10^{-2}$. The filtering of the $\ell \neq 2$ fluctuations is performed using a polar grid with $n_r = 8\,192$ radial rings and $n_\phi = 2\,048$ angular cells. Once the forces are computed, the leapfrog scheme is used to integrate the equations of motion. Using a higher order integrator would not necessarily improve the integration accuracy (see, e.g., figure 3.23 in Binney & Tremaine, 2008).

4.3.2 Impact of gravitational softening

This section is inspired by the work of De Rijcke et al. (2019b) (hereafter DR+19b). It motivated the numerical investigation I performed.

When performing N–body simulations, using the Newtonian interaction potential, $U(r) = -G/r$ with $r = \|\mathbf{r} - \mathbf{r}'\|$, leads to diverging forces at small separations. This can cause numerical instabilities. To prevent this, the interaction is usually softened. It generically reads (Dehnen, 2001)

$$U_\varepsilon(r) = \frac{-G}{\varepsilon} f\left(\frac{r}{\varepsilon}\right), \tag{4.21}$$

with f the dimensionless softening kernel and ε the softening length.

Such a procedure has known consequences on the stability of self-gravitating systems (see, e.g., Miller, 1971; Salo & Laurikainen, 2000; Sellwood & Evans, 2001; Polyachenko, 2013). Indeed, softening introduces a bias in the gravitational force which can, in turn, impact the simulated evolution of the system. Too much softening introduces a strong gravity bias, too small softening leads to numerical instabilities (Merritt, 1996). This is a classical bias-variance trade-off.

DR+19b investigated the impact of the softening kernel on the instabilities of self-gravitating discs using linear response theory. They considered various softening kernels among which the usual Plummer kernel

$$f_{\rm P}(u) = \frac{1}{\sqrt{1 + u^2}}, \tag{4.22}$$

and the (modified) Kuzmin kernel

$$f_{\rm K}(u) = \frac{3 + \frac{5}{2}u^2 + u^4}{(1 + u^2)^{5/2}}. \tag{4.23}$$

Interestingly, they showed that the Kuzmin kernel should be preferred over the Plummer one as it does not impact the dynamical properties of the disc at first order in ε, the softening length, but only at second order.[7] They compared their theoretical predictions to existing results of N–body simulations, namely the ones from Earn & Sellwood (1995) and SE01. These simulations were performed using the Plummer softening kernel only. They found a good agreement between their theoretical predictions and the numerical results of Earn & Sellwood (1995) on the isochrone disc

[7] Let me note however that using the Plummer kernel can be physically motivated. Indeed, this kernel mimics the effect of finite thickness of the disc (Sellwood, 2014). In this case, the softening length is set accordingly.

and qualitative agreement with those of SE01 on the Mestel disc. Yet, SE01 noted that the N–body measurements were significantly more difficult to perform on Mestel discs than on isochrone discs.

I performed a similar investigation on the Zang $\nu=4$ disc using both the Plummer and Kuzmin softening kernels. For each softening kernel and each softening length, I performed 10 different realisations with $N=2\times10^8$ particles each. The results are presented in figure 4.16. I found that

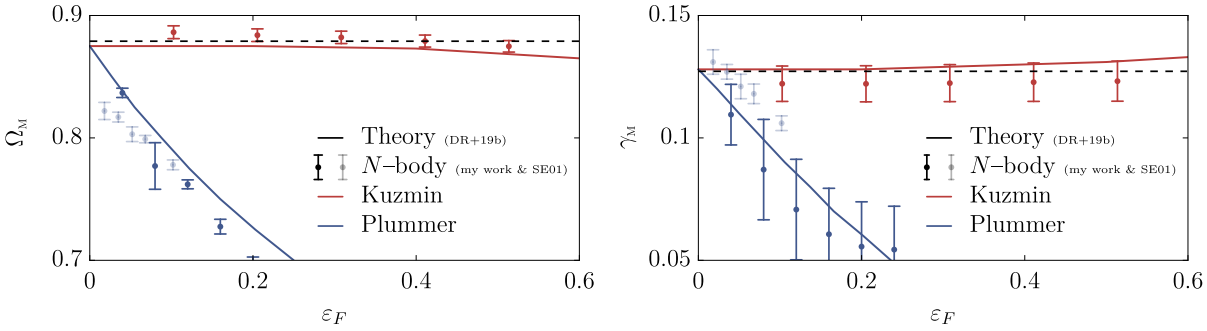

Figure 4.16: Inspired by figure 3 of De Rijcke et al. (2019b). Pattern speed (left) and growth rate (right) of the dominant mode in Zang $\nu=4$ disc, as a function of the softening length for both the Plummer (blue – equation 4.22) and the Kuzmin (blue – equation 4.23) softening kernel. The theoretical predictions (plain lines) are reproduced from DR+19b. I present the results of my numerical investigation (plain dots) and the one from SE01 (faint dots – Plummer softening only). In both cases, the estimated errors are somewhat underestimated. Finally, the dashed line corresponds to the Newtonian (non-softened) prediction from Evans & Read (1998b). Importantly, the numerical simulations recover that the Plummer softening kernel has a strong gravity bias, $\Delta\omega_{\rm M}^{\rm Plummer}\propto\varepsilon$, while the Kuzmin kernel conserves the dynamical properties of the disc at first order in ε, i.e., $\Delta\omega_{\rm M}^{\rm Kuzmin}\propto\varepsilon^2$. This is one of the key results of this thesis.

the mode measurements were indeed less affected by the Kuzmin kernel than the Plummer one. My numerical results are in good agreement with the theoretical predictions of DR+19b and the earlier numerical results of SE01. The estimated errors are however underestimated in both my and SE01's results. SE01 indeed mentioned that they did not take into account the scatter among different realisations. And I did not take into account the uncertainties in the mode measurements (section 4.3.3).

In figure 4.16, the softening length, ε, is rescaled. Indeed, comparing the results for different softening kernels at the same value of ε is not meaningful because the softened potential equation (4.21) is invariant under the transformation (section 2.3 of DR+19b)

$$\varepsilon \to a\varepsilon \quad \text{and} \quad f \to af. \tag{4.24}$$

The two kernels are therefore compared at the same value of maximal interparticle force, i.e., using

$$\varepsilon_F = \frac{\varepsilon}{-f'_{\rm max}}, \tag{4.25}$$

with $f'_{\rm max}$ the maximal value of the derivative of the softening (dimensionless) kernel. Arbitrarily setting $\varepsilon_F/\varepsilon=1$ for the Plummer softening, one has $\varepsilon_F/\varepsilon\approx2.568$ for the Kuzmin softening (table 1 in DR+19b).

4.3.3 Mode measurements

Let me now describe the method I used to measure the frequency and growth rate of the dominant mode in the N–body simulations. This method is similar to the one used in Fouvry et al. (2015) (appendix C therein).

Considering that the system's density fluctuations are well described by a single dominant mode, they read

$$\delta\rho(\mathbf{r},t) = \rho_{\rm M}(\mathbf{r})\exp(\mathrm{i}\omega_{\rm M}t), \tag{4.26}$$

with $\rho_{\rm M}$ the shape of the mode and $\omega_{\rm M}$ its (complex) frequency. Then the density fluctuations can be projected on any spatial function, $f(\mathbf{r}) = f(r)\mathrm{e}^{\mathrm{i}\ell\phi}$. As long as the scalar product of $f(\mathbf{r})$ with the mode shape is not zero, the projection should oscillate and grow at the same frequency as the mode. The projection

$$A_\ell(t) = \int \mathrm{d}\mathbf{r} f(\mathbf{r})\delta\rho(\mathbf{r},t) = m\sum_i f[r_i(t)]\mathrm{e}^{\mathrm{i}\ell\phi_i(t)}, \tag{4.27}$$

offers a single complex time series which can be analysed to extract the frequency and growth rate of the mode. Indeed, one should have

$$|A_\ell(t)| \propto \mathrm{e}^{\gamma_{\rm M} t}; \quad \arg[A_\ell(t)] \propto \Omega_{\rm M} t. \tag{4.28}$$

In practice, the time series of the phase are "unwrapped" to avoid jumps of 2π. This is done by adding 2π to the phase each time the phase jumps by more than $-\pi$. One could use (multiple) basis elements from the linear response theory to project the density fluctuations, as was made in Fouvry et al. (2015). This would also allow one to measure the mode's shape and compare it to the linear predictions. In practice, I used a single log-normal function

$$f(r) = \exp\left[-\frac{\ln(r/r_0)^2}{2\sigma^2}\right], \tag{4.29}$$

with $r_0 = 1.33$ and $\sigma = 0.45$. I chose this particular function to mimic the radial shape of the mode, as predicted by linear response theory. In practice, I could also have performed the measurement using a simpler identity function $f(r) = \mathbb{1}(r_{\rm min} < r < r_{\rm max})$. I used this simpler probe (with $r_{\rm min} = 1.5$ and $r_{\rm min} = 4.5$) for long term simulations in chapter 6. The main point of these functions is to

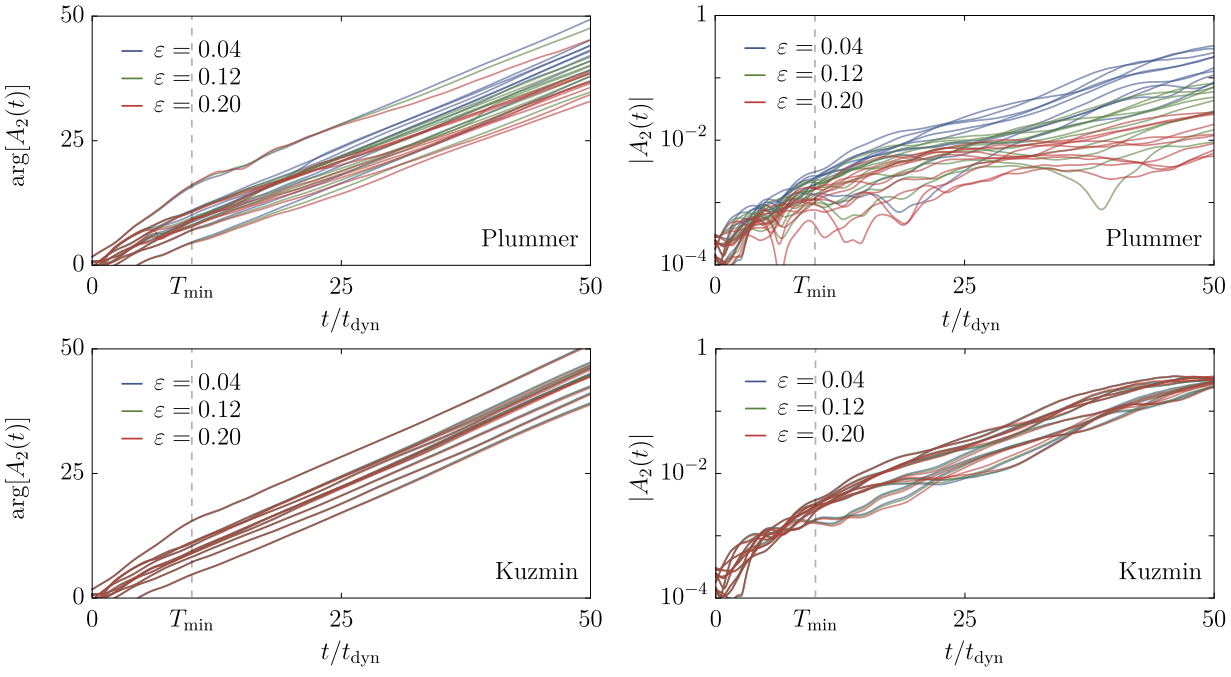

Figure 4.17: Time series of the norm (right) and the (unwrapped) phase (left) of the bisymmetric fluctuations probed by $A_2(t)$ from equation (4.27) using the Plummer (top) and Kuzmin (bottom) softening kernels. For each softening length, the same 10 initial conditions are used and shown in the same colour. The frequency $\Omega_{\rm M}$ (resp. growth rate $\gamma_{\rm M}$) of the mode are estimated by a linear fit of the phase (resp. log of the norm) of such time series, only using $t \geq T_{\rm min} = 10\, t_{\rm dyn}$. The growth of the phase is generically more regular than the growth of the norm. The Plummer softening kernel introduces a strong gravity bias which is not present with the Kuzmin kernel.

neglect the contributions from the central and the outer parts of the disc, where very few particles are present. The corresponding time series are shown in figure 4.17 for various initialisations and

softening kernels. While the phase growth is regular, the norm growth is more erratic. However, both measurements are roughly consistent with the linear predictions as shown in figure 4.16. The time series weakly vary with the softening length, ε, for the Kuzmin softening kernel (equation 4.23). Conversely, the Plummer softening kernel (equation 4.22) introduces a strong gravity bias which is clearly visible in figure 4.17.

4.4 Conclusion

In this chapter, I applied the linear response theory from chapter 3 to study the stability of one-dimensional models and self-gravitating discs.

First, I successfully adapted the method proposed by Fouvry & Prunet (2022) to Zang discs. This allowed me to investigate the specific stability of this disc, providing valuable insights into its behaviour. Furthermore, I developed and published public libraries to compute efficiently the polarisation matrices for arbitrary discs and spherical systems. These libraries serve as valuable resources for researchers interested in studying stability in such systems, facilitating further systematic investigations.

By applying the linear response method to different systems, I was able to demonstrate its effectiveness in recovering known instabilities while also probing their weakly damped modes. This validation of the method's versatility further strengthens its utility and reliability as a generic tool for stability analysis. For instance, colleagues were able to recover the published modes of Kuzmin discs (Miyamoto, 1974) in a matter of less than one hour of uploading the code. However, the counterpoint of this versatility is the difficulty in obtaining converged results for damped frequencies. This difficulty arises from the fact that highly oscillatory basis elements are needed to resolve the shape of eigenmodes, which undermines the analytic continuation.

In addition to these theoretical investigations, I also conducted numerical simulations to explore the impact of two different softening kernels on linear instabilities in Zang's disc. My analysis revealed interesting differences between the Plummer and Kuzmin softening kernels, highlighting the importance of choosing the appropriate softening kernel in stability studies. These differences were predicted by De Rijcke et al. (2019a) and confirmed here by my numerical simulations.

4.5 Perspectives

The work presented in this chapter could be improved and extended in several directions. The main difficulty encountered in this research was the convergence of the linear response method for damped modes and the associated numerical saturation. This was to be expected, as it relies on an analytical continuation which is an ill-conditioned numerical problem (Trefethen, 2020).

I pointed out that optimising the choice of the basis elements is crucial to limit the number of basis elements required for convergence. It would therefore be particularly interesting to implement the method proposed by Weinberg (1999) to tune the basis elements to the equilibrium state by solving a Sturm–Liouville differential equation. One could also investigate the use of non-biorthogonal basis elements (De Rijcke & Voulis, 2016; De Rijcke et al., 2019a; Dootson, 2023). These elements are less oscillatory than the high order elements of global bi-orthogonal basis. The continuation of the matrix to damped frequencies should therefore be easier. However, convergence might be more difficult to assess with such basis elements as they are not ordered by scale-lengths. One should be particularly careful with the representation of the pairwise interaction potential (equation 3.25).

I dealt with the cusp nature of Mestel potential by introducing a cut-off in the resonant frequencies (section 4.2.2) so as to only probe the frequencies of interest in Zang's and Toomre's discs. This tweak was necessary because the method of FP22 is tailored for (core) systems with a finite frequency support. It would be interesting to extend FP22's method to cuspy potentials supporting

infinitely large frequencies. Improving upon equation (3.42), one would then need to compute the integral

$$\int\limits_{\mathcal{L}_0}^{\infty} \mathrm{d}u \, \frac{G(u)}{u-\omega} = \begin{cases} \displaystyle\int_0^{\infty} \mathrm{d}u \, \frac{G(u)}{u-\omega} & \text{if } \mathrm{Im}(\omega) > 0, \\ \mathcal{P}\displaystyle\int_0^{\infty} \mathrm{d}u \, \frac{G(u)}{u-\omega} + \mathrm{i}\pi S(\omega) G(\omega) & \text{if } \mathrm{Im}(\omega) = 0, \\ \displaystyle\int_0^{\infty} \mathrm{d}u \, \frac{G(u)}{u-\omega} + 2\mathrm{i}\pi S[\mathrm{Re}(\omega)] G(\omega) & \text{if } \mathrm{Im}(\omega) < 0, \end{cases} \tag{4.30}$$

with the Heaviside step function

$$S(x) = \begin{cases} 1 & \text{if } x > 0, \\ \frac{1}{2} & \text{if } x = 0, \\ 0 & \text{if } x < 0. \end{cases} \tag{4.31}$$

Following Robinson (1990), the continuation of the G functions could be achieved by using Laguerre polynomials instead of Legendre polynomials. It might also prove useful to implement Zang (1976)'s continuous method (section 3.4) to recover the damped modes in Mestel discs (see also Evans & Read, 1998a). This method would be limited to specific systems but would provide a good benchmark to assess the convergence.

Appendices

4.A Clutton-Brock basis

Following Clutton-Brock (1972), a well-behaved bi-orthogonal basis for thin discs with radial length scale r_b is given by

$$U_p^\ell(r) = -a_\mathbf{p}\sqrt{\frac{G}{r_\mathrm{b}}}\,(r/r_\mathrm{b})^\ell\,\xi^{(\mathbf{p})}(r/r_\mathrm{b}), \quad (4.32a)$$

$$D_p^\ell(r) = \frac{a_\mathbf{p}}{2\pi\sqrt{Gr_\mathrm{b}^3}}\,(r/r_\mathrm{b})^\ell\,\mu^{(\mathbf{p})}(r/r_\mathrm{b}), \quad (4.32b)$$

where $\mathbf{p}=(p,\ell)\in\mathbb{N}^2$ and

$$a_\mathbf{p} = 2^\ell\sqrt{2}\sqrt{\frac{p!}{(p+2\ell)!}}, \quad (4.33)$$

are the normalisation prefactors. In equations (4.32), the dimensionless potential functions, $\xi^{(\mathbf{p})}$, are given by the recurrence relations

$$\xi_0^\ell(x) = \frac{\prod_{i=1}^\ell(2i-1)}{(1+x^2)^{\ell+1/2}}, \quad (4.34a)$$

$$\xi_p^\ell(x) = \left(2+\frac{2\ell-1}{p}\right)\frac{x^2-1}{x^2+1}\xi_{p-1}^\ell(x) - \left(1+\frac{2\ell-1}{p}\right)\xi_{p-2}^\ell(x), \quad (4.34b)$$

and their density counterparts, $\mu^{(\mathbf{p})}$, can be deduced using the relation

$$\mu_p^\ell(x) = \xi_p^{\ell+1}(x) - \xi_{p-2}^{\ell+1}(x), \quad (4.35)$$

for $p\geq 2$ and $\mu_p^\ell(x)=\xi_p^{\ell+1}(x)$ otherwise.

4.B Discs sampling

This section details the sampling procedures of the considered DFs. This is the first necessary step to perform any N–body simulations.

My sampling procedure is based on the one described in appendix E of Fouvry et al. (2015). However, I sampled the integrals of motion in $(r_\mathrm{p}, r_\mathrm{a})$–space rather than in (E, L)–space. Indeed, pericentre and apocentre are easier to sample than energy and angular momentum as the truncation constraint is simpler in this space. In particular, it allows me to avoid the additional rejection method needed to sample the angular momentum in Fouvry et al. (2015). Once the constants of motion are sampled, the additional samplings required for the position and velocity vectors naturally follow.

The distribution (equation 2.36) to sample is

$$F_\mathrm{sp}(E,L) = C_\mathrm{sp}L^q\mathrm{e}^{-E/\sigma_r^2}T_\mathrm{in}(L)T_\mathrm{out}(L), \quad (4.36)$$

together with the truncation[8] constraint

$$r_\mathrm{a}(E,L)\leq R_\mathrm{max} \quad (4.37)$$

and where the normalisation constant C_sp is such that this function is normalised to 1 (w.r.t. integration in $\mathrm{d}\mathbf{x}\mathrm{d}\mathbf{v}=\mathrm{d}\boldsymbol{\theta}\mathrm{d}\mathbf{J}$). Typical values for the distributions explored is this thesis are given in table 4.1.

In the $(r_\mathrm{p}, r_\mathrm{a})$–space, the constraint of no star ever going beyond R_max takes the simple form, $r_\mathrm{a}\leq R_\mathrm{max}$. Hence, the populated (bounded) domain is a simple triangle. It is therefore much easier to perform the rejection in this domain since sampling a uniform distribution on a triangle is trivial. I only need the density of state

[8] This truncation is introduced quite ambiguously in section 2 of Sellwood (2012). As in Fouvry et al. (2015), I interpret it as "no particles with orbits that extend beyond R_max", i.e., $F(E,L)=0$ when $E>\psi_\mathrm{eff}(R_\mathrm{max})$ [and not $\psi(R_\mathrm{max})$].

Distribution Function	Normalisation constant $C_{\rm sp}/C$	Total mass $M_{\rm tot}$	Rejection constant M
Toomre	$\simeq 9.25\times10^{-2}$	$10.8\,(\times\xi)$	15.7
Zang $\nu=4$	$\simeq 9.33\times10^{-2}$	$10.7\,(\times\xi)$	11.8

Table 4.1: Constants used for the sampling of the DFs explored in this thesis. The normalisation constant $C_{\rm sp}$ is such that the DF is normalised to unity in any canonical coordinates space while C is the one from equation (2.35). The total mass $M_{\rm tot}$ is not set to one and corresponds to the mass enclosed within the truncation radius $R_{\rm max}$ (equation 4.37) of the sampled distributions. It sets the individual mass of the particles $m=M_{\rm tot}/N$. The (minimal) rejection constants correspond to the maximal value of the density of state in pericentre and apocentre from equation (4.38).

in $(r_{\rm p}, r_{\rm a})$–space. It reads

$$\begin{aligned} p(r_{\rm p}, r_{\rm a}) &= 4\pi^2 \left|\frac{\partial(J_r, L)}{\partial(r_{\rm p}, r_{\rm a})}\right| F_{\rm sp}(E, L), \\ &= 4\pi^2 \left|\frac{\partial(J_r, L)}{\partial(E, L)}\right| \left|\frac{\partial(E, L)}{\partial(r_{\rm p}, r_{\rm a})}\right| F_{\rm sp}(E, L), \\ &= \frac{4\pi^2}{\Omega_r} \left|\frac{\partial(E, L)}{\partial(r_{\rm p}, r_{\rm a})}\right| F_{\rm sp}(E, L), \end{aligned} \tag{4.38}$$

where the $4\pi^2$–factor comes from integration over the angles and the Jacobian of the $(r_{\rm p}, r_{\rm a})\mapsto(E, L)$ mapping can be deduced from equation (2.14).

The uniform distribution on the $(r_{\rm p}, r_{\rm a})$–triangle is

$$g(r_{\rm p}, r_{\rm a}) = \frac{2}{R_{\rm max}^2} \mathbb{1}_{\{0\leq r_{\rm p}\}} \mathbb{1}_{\{r_{\rm p}\leq r_{\rm a}\}} \mathbb{1}_{\{r_{\rm a}\leq R_{\rm max}\}}.$$

The rejection constant M then has to be chosen such that

$$\forall (r_{\rm p}, r_{\rm a}),\ p_{r_{\rm p}r_{\rm a}}(r_{\rm p}, r_{\rm a}) \leq \frac{2M}{R_{\rm max}^2},$$

depending on the DF parameters.

Once $(r_{\rm p}, r_{\rm a})$ correctly sampled, I have at my disposal any integrals of motion by simple change of variables. Given these integrals, one now has to sample the position and velocity vectors assuming a uniform distribution over canonical angles. In the (r, ϕ)–space, this uniform distribution translates into a uniform distribution over ϕ (axisymmetric) and a probability distribution function (PDF) over r proportional to $1/v_r$. When correctly normalised, it reads (Fouvry et al., 2015)

$$p_r(r) = \frac{\Omega_r/\pi}{\sqrt{2[E-\psi(r)] - L^2/r^2}},$$

for $r\in[r_{\rm p}, r_{\rm a}]$. To cure the divergences of this PDF close to $r_{\rm p}$ and $r_{\rm a}$, I use the same Hénon effective anomaly w as for computing frequencies in equation (2.8). I then want to sample $w\in[-1, 1]$ according to

$$\begin{aligned} p_w(w) &= \frac{\Omega_r}{\pi} \frac{aef'(w)}{\sqrt{2(E-\psi[r(w)]) - L^2/[r(w)]^2}} \\ &= \frac{\Omega_r}{\pi}\Theta(w), \end{aligned}$$

where a, e are the effective semi-major axis and eccentricity (equation 2.17) and Θ is the derivative of the radial angle w.r.t. the anomaly (equation 2.18). I perform this sampling using once again the rejection method with a uniform control PDF, $g_u(u)=\mathbb{1}_{[-1,1]}(u)/2$. The rejection constant, M_u, has to be chosen such that $p_u\leq M_u/2$, the maximal value of p_u being easily determined on the fly as it is reached at the boundary $u=1$. (This is an empirical observation which might be mapping-dependent.)

Chapter 5

Secular theory and Balescu–Lenard equation

Having studied the linear response of self-gravitating systems to perturbations in the previous chapters, let me now turn to the secular evolution of these systems. The slow evolution of the mean-field quantities under the correlated effects of internal fluctuations is captured by equation (1.19a) that I recall here for convenience:

$$\frac{\partial F(\mathbf{J},t)}{\partial t} = -\langle [\delta f, \delta\psi] \rangle. \qquad \text{(recall 1.19a)}$$

In this chapter, I will first introduce the inhomogeneous Balescu–Lenard equation, sketching its derivation while highlighting the main underlying hypotheses. This equation captures the long-term relaxation of stellar systems driven by finite-N effects and (linearly) accounts for the dressing of fluctuations by collective effects. I will then discuss the limit in which collective effects can be neglected, leading to the Landau equation, and the regime where local encounters dominate the relaxation, leading to the Chandrasekhar equation. Finally, I will discuss the limitations of the current state-of-the-art kinetic theory of stellar systems and the regimes in which it is expected to break down.

5.1 Inhomogeneous Balescu–Lenard equation

5.1.1 The master equation

The long-term relaxation of self-gravitating stellar systems driven by finite-N fluctuations is generically governed by the inhomogeneous Balescu–Lenard equation (Heyvaerts, 2010; Chavanis, 2012). It reads

$$\boxed{\frac{\partial F(\mathbf{J},t)}{\partial t} = -\pi(2\pi)^d\, m\, \frac{\partial}{\partial \mathbf{J}} \cdot \Bigg[\sum_{\mathbf{k},\mathbf{k}'} \mathbf{k} \int \mathrm{d}\mathbf{J}' \underbrace{\left| U^{\mathrm{d}}_{\mathbf{k}\mathbf{k}'}(\mathbf{J},\mathbf{J}',\mathbf{k}\cdot\boldsymbol{\Omega}) \right|^2}_{\text{dressed coupling}} \times \underbrace{\delta_{\mathrm{D}}(\mathbf{k}\cdot\boldsymbol{\Omega} - \mathbf{k}'\cdot\boldsymbol{\Omega}')}_{\text{resonance condition}} \underbrace{\left(\mathbf{k}' \cdot \frac{\partial}{\partial \mathbf{J}'} \right)}_{\text{friction}} - \underbrace{\mathbf{k}\cdot\frac{\partial}{\partial \mathbf{J}}}_{\text{diffusion}} \underbrace{F(\mathbf{J},t)\, F(\mathbf{J}',t)}_{\text{orbital population}} \Bigg]. \qquad (5.1)}$$

This is the master equation of self-induced orbital relaxation. It describes how the mean orbital population distribution $F(\mathbf{J})$ evolves through the correlated effect of Poisson noise, i.e., finite-N

effects ($m \propto 1/N$). Importantly, equation (5.1) conserves mass, energy, and satisfies an H-theorem for Boltzmann entropy. It captures the small but cumulative effects of resonant encounters between stars whose efficiency is dressed by collective effects. The sum and the integral in this equation scan over the discrete resonances and over the orbital space looking for all the possible populated resonances. These resonances are selected through the resonance condition, $\mathbf{k}\cdot\boldsymbol{\Omega}-\mathbf{k}'\cdot\boldsymbol{\Omega}'=0$. They are non-local (recurrent) encounters as they involve orbits which are not necessarily close, neither in position nor in action space. The system's propensity to amplify or weaken these resonances is captured in the dressed coupling coefficients, $U^{\mathrm{d}}_{\mathbf{k}\mathbf{k}'}$, as already introduced in equation (3.29). The inhomogeneous Balescu–Lenard equation (5.1) can be re-written as a more compact continuity equation in action space

$$\frac{\partial F(\mathbf{J})}{\partial t} = -\frac{\partial}{\partial \mathbf{J}}\cdot\boldsymbol{\mathcal{F}}(\mathbf{J}), \tag{5.2a}$$

$$= -\frac{\partial}{\partial \mathbf{J}}\cdot\Big[\mathbf{A}(\mathbf{J})F(\mathbf{J}) - \tfrac{1}{2}\,\mathbf{D}(\mathbf{J})\cdot\frac{\partial F}{\partial \mathbf{J}}\Big], \tag{5.2b}$$

where the flux, $\boldsymbol{\mathcal{F}}$, the (polarisation) friction vector $\mathbf{A}$, and the diffusion tensor $\mathbf{D}$ all depend on the mean-field distribution F. This is a Fokker–Planck equation in action space. From equation (5.1), the friction vector and the diffusion tensor are given by

$$\mathbf{A}(\mathbf{J}) = \pi(2\pi)^d\, m \sum_{\mathbf{k},\mathbf{k}'} \mathbf{k} \int \mathrm{d}\mathbf{J}'\, \big|U^{\mathrm{d}}_{\mathbf{k}\mathbf{k}'}(\mathbf{J},\mathbf{J}',\mathbf{k}\cdot\boldsymbol{\Omega})\big|^2\, \delta_{\mathrm{D}}(\mathbf{k}\cdot\boldsymbol{\Omega}-\mathbf{k}'\cdot\boldsymbol{\Omega}')\, \mathbf{k}\cdot\frac{\partial F}{\partial \mathbf{J}'}, \tag{5.3a}$$

$$\mathbf{D}(\mathbf{J}) = (2\pi)^{d+1}\, m \sum_{\mathbf{k},\mathbf{k}'} \mathbf{k}\otimes\mathbf{k} \int \mathrm{d}\mathbf{J}'\, \big|U^{\mathrm{d}}_{\mathbf{k}\mathbf{k}'}(\mathbf{J},\mathbf{J}',\mathbf{k}\cdot\boldsymbol{\Omega})\big|^2\, \delta_{\mathrm{D}}(\mathbf{k}\cdot\boldsymbol{\Omega}-\mathbf{k}'\cdot\boldsymbol{\Omega}')\, F(\mathbf{J}'), \tag{5.3b}$$

with $\mathbf{k}\otimes\mathbf{k}$ the outer product of the resonance vector $\mathbf{k}$ with itself.

Remark: The form of the Fokker–Planck equation (5.2b) determines the interpretation one must make of the friction term. Under this particular form, the friction $\mathbf{A}$ stands for the friction force by polarisation (Chavanis, 2012).

In this self-consistent evolution equation (5.1), both friction and diffusion are proportional to the mass of the particles, m. In practice, when considering the evolution of a test particle of mass m_{t} in a bath of particles of mass m_{b}, the Balescu–Lenard equation reads (Heyvaerts, 2010; Heyvaerts et al., 2017)

$$\frac{\partial P(\mathbf{J},t)}{\partial t} = -\pi(2\pi)^d\, \frac{\partial}{\partial \mathbf{J}}\cdot\Big[\sum_{\mathbf{k},\mathbf{k}'} \mathbf{k} \int \mathrm{d}\mathbf{J}' \big|U^{\mathrm{d}}_{\mathbf{k}\mathbf{k}'}(\mathbf{J},\mathbf{J}',\mathbf{k}\cdot\boldsymbol{\Omega})\big|^2 \times \delta_{\mathrm{D}}(\mathbf{k}\cdot\boldsymbol{\Omega}-\mathbf{k}'\cdot\boldsymbol{\Omega}') \left(m_{\mathrm{t}}\mathbf{k}'\cdot\frac{\partial}{\partial \mathbf{J}'} - m_{\mathrm{b}}\mathbf{k}\cdot\frac{\partial}{\partial \mathbf{J}}\right) P(\mathbf{J},t)\, F(\mathbf{J}',t)\Big]. \tag{5.4}$$

where P is the DF of the test particles and F is the DF of the bath particles. Importantly, the (polarisation) friction is proportional to the test particle's mass while the diffusion is proportional to the bath particles' mass. In equation (5.4), the dressed coupling coefficients only involve the susceptibility of the bath particles. Indeed, the test particles are probes of the potential fluctuations, and do not interact with one another. Friction captures how a heavy particle (statistically) sinks by polarizing the bath particles behind it, while diffusion accounts for the random walk generated by the "kicks" from the bath particles. Let me now illustrate these two processes using my simulations of one-dimensional self-gravitating systems (section 2.1.1).

Friction

To illustrate dynamical friction, I used a massive test particle (100 times more massive than the bath particles) in a bath much more massive overall so that the gravitational effects from the test

particle are not dominant. As such, I have therefore imposed $m \ll m_{\rm t} \ll Nm$. This massive particle, if launched at sufficiently high energy, undergoes a sinking phase: its presence tends to polarise the bath particles on its path. These particles tend to form a small overdensity behind the massive particle and therefore tend to slow the massive particle down. This leads to its irreversible energy decrease as I illustrate in the left panel of figure 5.1. Of course, this sinking is only statistically true: the massive particle's energy is not always decreasing but does decay on average. The sinking continues until the massive particles reaches an equipartition of energy with the bath. The massive particle's energy follows therefore a biased random walk. This is illustrated in figure 5.1.

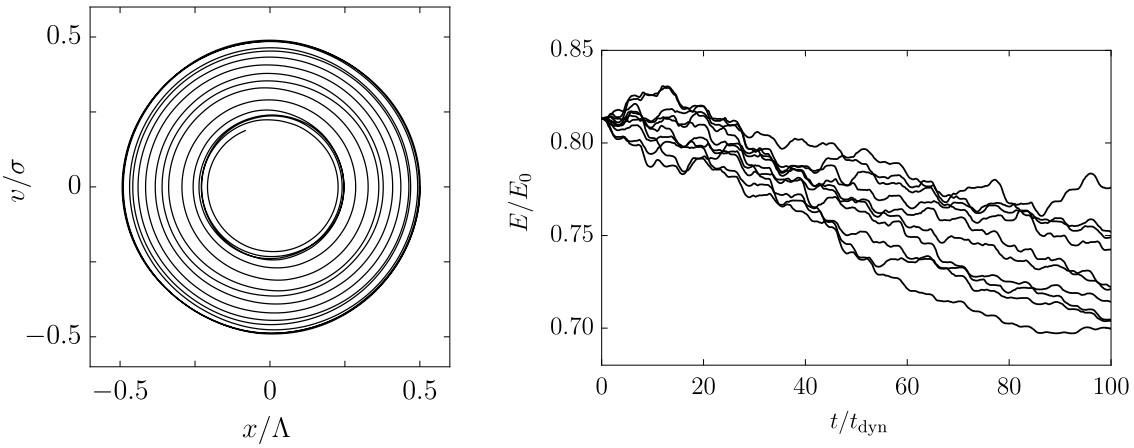

Figure 5.1: Illustration of dynamical friction in the one-dimensional model. A massive test particle (100 times more massive than a bath particle) is placed in a bath of $N = 10^4$ equal mass particles at thermal equilibrium. Overall the test particle's mass is therefore negligible w.r.t. the total mass of the bath. I repeated this experiment over different realisations, always placing the test particle at the same initial location. On the left panel, I represent the trajectory of one test particle (i.e., a single realisation). The particle sinks from its initial orbit towards lower orbits. On the right panel, I represent the time evolution of the energy of the test particles for 10 different initialisations showing how massive particles sink due to dynamical friction. The dynamical time $t_{\rm dyn} = \Lambda/\sigma$ is the characteristic timescale of the orbits in the system.

Diffusion

To illustrate diffusion, I used a massless test particle in a bath of particles at thermal equilibrium. Importantly, the test particle's orbit is not a closed perfect "circle" in phase-space, i.e., what the smooth mean-field potential imposes. Finite-N effects slightly alter the test particle's orbit and its phase-space trajectory appears like a thick circle. Indeed, its (mean-field) constants of motion (e.g., its energy E) are slowly varying over time. This irreversible diffusion cannot be predicted for one particular realisation (i.e., one particular sampling of the bath) as it would imply being able to predict the exact motion of each particle in an N–body system. However, looking at ensemble averages (over bath realisations), one can see a clear diffusion pattern. Placing one test particle at the same phase-space location for 10 different (random) bath initialisations and tracking the evolution of their energy along the simulation, I illustrate in the right panel of figure 5.2 such a diffusion. Each individual particle's energy follows a correlated random walk (Binney & Lacey, 1988).

This stochastic dynamics can be characterised by the time evolution of the energy dispersion between test particles launched at the same energy in different random baths. The dispersion $\langle \Delta E^2 \rangle$ evolves linearly in time on long timescales. As discussed in section 7.4.2 of Binney & Tremaine (2008), the diffusion tensor can therefore be interpreted as

$$D_{ij}(\mathbf{J}) = \lim_{T \to +\infty} \frac{\langle \Delta J_i \Delta J_j \rangle}{T}, \tag{5.5}$$

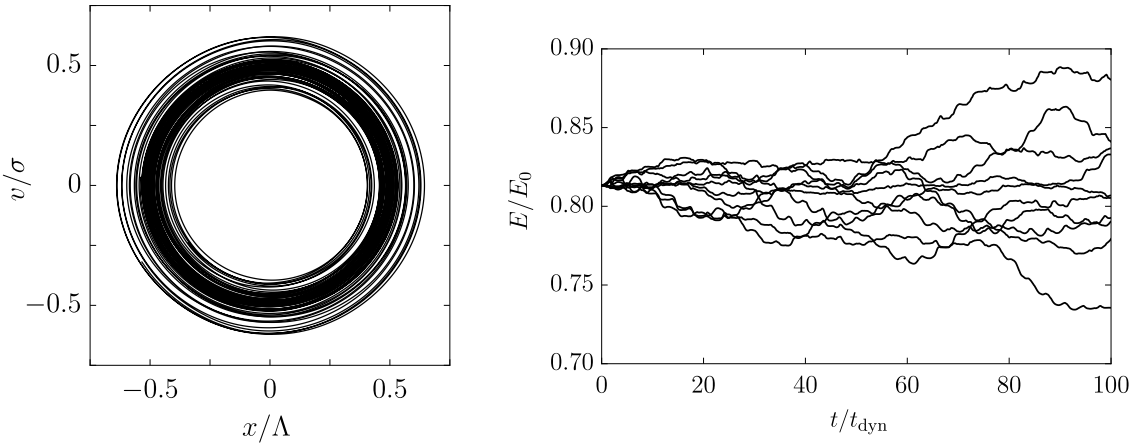

Figure 5.2: Illustration of diffusion in the one-dimensional model. A massless test particle is placed in a bath of $N=10^4$ equal mass particles at thermal equilibrium. I repeated the experiment over different (random) initialisations for the bath (the test particle is always placed at the same phase-space location). On the left panel, I represent the overlap of 3 trajectories of test particles in the (x,v)-plane showing the "widening" of the orbits which are not closed anymore contrary to what would have happened within the smooth mean-field potential. On the right panel, I represent the evolution of the energy of the test particles as a function of time for 10 different initialisations showing the diffusion of energy. The energy of the test particles randomly fluctuates around the initial energy.

with $\Delta\mathbf{J}=\mathbf{J}(t=T)-\mathbf{J}(t=0)$ the change in action of a given particle with initial actions $\mathbf{J}(t=0)=\mathbf{J}$, and $\langle\cdot\rangle$ the ensemble average over realisations.

5.1.2 Heuristic derivation from Klimontovich equation

Let me highlight the key steps of the derivation of the inhomogeneous Balescu–Lenard equation (5.1) from the Klimontovich equation (1.8). Here, I mainly aim to explain the assumptions and the approximations made in the derivation of the Balescu–Lenard equation. Complete derivations can be found in Heyvaerts (2010) from the BBGKY hierarchy, Chavanis (2012) from the Klimontovich equation, Fouvry & Bar-Or (2018) using Novikov's theorem and Hamilton (2021) using Rostoker's principle. This section is inspired by Chavanis (2012) and Hamilton & Fouvry (2024).

In chapter 3, I obtained the linearised evolution of density and potential fluctuations in equations (3.7) and (3.11). I now need to inject these results into the evolution equation of the mean-field distribution, namely equation (1.19a). However, the fluctuations' evolution are given in Fourier–Laplace space, $(\mathbf{k},\omega)$, while the mean-field evolution equation is still in angle, $\boldsymbol{\theta}$, and time, t. To bridge this gap, let me expand the r.h.s. of equation (1.19a). This gives

$$\frac{\partial F(\mathbf{J},t)}{\partial t} = -\sum_{\mathbf{k},\mathbf{k}'}\left\langle \mathrm{i}\mathbf{k}\cdot\frac{\partial\delta\psi_{\mathbf{k}'}}{\partial\mathbf{J}}\delta f_{\mathbf{k}} - \mathrm{i}\mathbf{k}'\cdot\frac{\partial\delta f_{\mathbf{k}}}{\partial\mathbf{J}}\delta\psi_{\mathbf{k}'}\right\rangle \mathrm{e}^{\mathrm{i}(\mathbf{k}+\mathbf{k}')\cdot\boldsymbol{\theta}}, \tag{5.6}$$

where I used the Poisson bracket definition equation (1.3) and where the Fourier coefficients of the fluctuations follow from equations (3.2). Their dependence w.r.t. actions and time is kept implicit. The equilibrium mean-field DF does not depend on the angles (Jeans theorem). It is therefore natural to average the r.h.s. of equation (5.6) over the angles, $\boldsymbol{\theta}$. This imposes $\mathbf{k}'=-\mathbf{k}$. The potential fluctuations are real quantities, so their Fourier coefficients satisfy $\delta\psi^*_{\mathbf{k}}=\delta\psi_{-\mathbf{k}}$. Using these two properties, the angle-averaged mean-field evolution equation reads

$$\frac{\partial F(\mathbf{J},t)}{\partial t} = -\frac{\partial}{\partial\mathbf{J}}\cdot\sum_{\mathbf{k}}\mathrm{i}\mathbf{k}\left\langle\delta f_{\mathbf{k}}(\mathbf{J},t)\delta\psi^*_{\mathbf{k}}(\mathbf{J},t)\right\rangle. \tag{5.7}$$

This is the first key step of this derivation. The fluctuations are averaged along the (unperturbed) orbit. To inject the expressions of the (linearised) fluctuations' evolution from equations (3.7) and (3.11), I first need to bring them back in the time domain via an inverse Laplace transform.

Taking its inverse Laplace transform (equation 3.39), equation (3.11) reads

$$\delta\psi_{\mathbf{k}}(\mathbf{J},t) = (2\pi)^d \sum_{\mathbf{k}'} \int \mathrm{d}\mathbf{J}'\, \delta f_{\mathbf{k}'}(\mathbf{J}',0) \frac{1}{2\pi} \int_{\mathcal{B}} \mathrm{d}\omega \frac{U^{\mathrm{d}}_{\mathbf{k}\mathbf{k}'}(\mathbf{J},\mathbf{J}',\omega)}{\mathrm{i}(\mathbf{k}'\cdot\boldsymbol{\Omega}'-\omega)} \mathrm{e}^{-\mathrm{i}\omega t}, \tag{5.8}$$

where the dressed coupling coefficients $U^{\mathrm{d}}_{\mathbf{k}\mathbf{k}'}(\mathbf{J},\mathbf{J}',\omega)$ are given by equation (3.29) and the Bromwich integration contour, $\mathcal{B}$, is taken above any singularities. In particular, the ballistic pole $1/(\mathbf{k}'\cdot\boldsymbol{\Omega}'-\omega)$ imposes that the integration contour is taken above the real axis.

From now on, I assume that the system is linearly stable so that the dressed coupling coefficients do not have any poles in the upper half-plane. This is a crucial assumption underlying the Balescu–Lenard equation. To perform the integral over ω in equation (5.8), I can bring the Bromwich contour down in the complex plane, as long as I do not cross any singularity. This deformation is illustrated in figure 5.3. By doing so, the contribution along the regular parts of the contour vanishes as $\mathrm{e}^{-\eta t}$ where $\eta = -\mathrm{Im}(\omega)$ and only the singularities remain. It reads

$$\delta\psi_{\mathbf{k}}(\mathbf{J},t) = (2\pi)^d \sum_{\mathbf{k}'} \int \mathrm{d}\mathbf{J}'\, \delta f_{\mathbf{k}'}(\mathbf{J}',0) \Big[U^{\mathrm{d}}_{\mathbf{k}\mathbf{k}'}(\mathbf{J},\mathbf{J}',\mathbf{k}'\cdot\boldsymbol{\Omega}') \mathrm{e}^{-\mathrm{i}\mathbf{k}'\cdot\boldsymbol{\Omega}'t} + \sum_{\mathrm{p}} \mathrm{e}^{-\mathrm{i}\omega_{\mathrm{p}}t} \times (...) + \sum_{\mathrm{b}} t^{\beta_{\mathrm{b}}}\, \mathrm{e}^{\mathrm{i}\Omega_{\mathrm{b}}t} \times (...) \Big], \tag{5.9}$$

where the terms inside the brackets correspond to the contribution from (i) the ballistic pole, and (ii) the damped poles, $\sum_{\mathrm{p}}$, and the branch cuts, $\sum_{\mathrm{b}}$, from the dressed coupling coefficients $\omega \mapsto U^{\mathrm{d}}_{\mathbf{k}\mathbf{k}'}(\mathbf{J},\mathbf{J}',\omega)$, as illustrated in figure 5.3. Of course, it assumes that the dressed coupling coefficients have been properly (analytically) continued to damped frequencies.

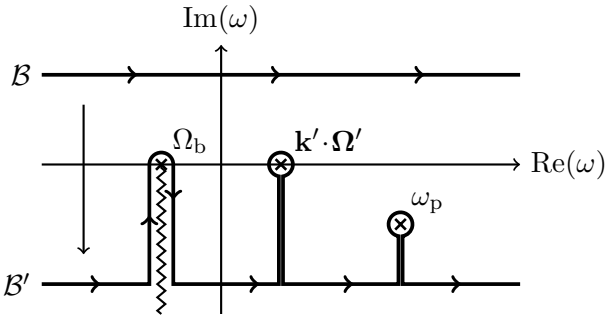

Figure 5.3: Inspired by figure F1 of Fouvry & Bar-Or (2018). Illustration of the computation of the inverse Laplace transform of the potential fluctuations from equation (5.9). By distorting the Bromwich integration contour, $\mathcal{B}$, into the contour, $\mathcal{B}'$, the only remaining contributions are the ones from (i) the ballistic pole, $\omega \mapsto 1/(\mathbf{k}'\cdot\boldsymbol{\Omega}'-\omega)$, and (ii) the damped poles and the branch cuts from the dressed coupling coefficients, $\omega \mapsto U^{\mathrm{d}}_{\mathbf{k}\mathbf{k}'}(\mathbf{J},\mathbf{J}',\omega)$.

The next assumption is to consider that the transient contributions from the damped poles and the branch cuts are small and quickly vanish. Phrased differently, I suppose that the system is sufficiently stable and that I can take t very large. The underlying assumption is that the relaxation of the mean-field quantities is much slower than the relaxation of the fluctuations. In other words, there is a timescale separation between the evolution of the mean-field and the evolution of the fluctuations. This timescale separation allows one to consider t such that $1/|\gamma_{\mathrm{M}}| \ll t \ll T_{\mathrm{relax}}$, with γ_{M} the damping rate of the least damped mode and T_{relax} the relaxation timescale of the mean-field DF.

Ultimately, this line of work leads one to express the fluctuations correlations, $\langle \delta f_{\mathbf{k}}(\mathbf{J},t) \delta\psi^*_{\mathbf{k}}(\mathbf{J},t) \rangle$, in equation (5.7) as a function of the initial DF correlations, $\langle \delta f_{\mathbf{k}}(\mathbf{J},0) \delta f_{\mathbf{k}'}(\mathbf{J}',0) \rangle$. An important assumption is that the initial fluctuations are uncorrelated Poisson noise, i.e., that (see, e.g., appendix C in Chavanis, 2012)

$$\langle \delta f_{\mathbf{k}}(\mathbf{J},0) \delta f_{\mathbf{k}'}(\mathbf{J}',0) \rangle = \frac{1}{(2\pi)^d} \delta^{\mathbf{k}'}_{-\mathbf{k}}\, \delta(\mathbf{J}-\mathbf{J}')\, m\, F(\mathbf{J}). \tag{5.10}$$

This significantly reduces the number of sums over resonances and integrals over actions involved in the fluctuations correlations at time t.

With all these ingredients in hand, one can finally derive the inhomogeneous Balescu–Lenard equation (5.1). I do not attempt to reproduce this intricate derivation here as it would not bring more physical insights beyond the assumptions and approximations I have already highlighted. Let me now summarise and discuss these assumptions.

5.1.3 Assumptions and limitations

Finite-N fluctuations The Balescu–Lenard equation assumes that the relaxation is driven by uncorrelated Poisson shot noise due to finite-N effects and that the particles are identical and have the same mass (equation 5.10). The last constraint can be relaxed. The generalisation to different populations (multi-mass) follows from equation (5.4) and can be found in the original derivation of Heyvaerts (2010).

Non-degenerate system For degenerate systems such as harmonic oscillators or Keplerian systems, the resonance condition is satisfied by sets of non-zero measure and cannot be integrated upon. This is typically the case for isotropic vector resonant relaxation describing the precession of the orbital planes of stars around a central massive black hole in galactic nuclei (Kocsis & Tremaine, 2015; Fouvry et al., 2019b).

Small perturbations The perturbations are small enough for their dynamics to be solved order by order. This notably prevents particles from being trapped in non-linear resonances (Luciani & Pellat, 1987; Hamilton, 2024). This is necessary to ensure that (i) the linearised fluctuations' evolution is a good approximation of their dynamics and (ii) the mean-field relaxes on a timescale much longer than the fluctuations' relaxation.

Stability The system is sufficiently stable so that the transient contributions from the damped modes in the dressed coupling coefficients quickly vanish (equation 5.8). When the system is only weakly stable, transients might live for a particularly long time (see, e.g., D'Onghia et al., 2013). In fact, the Balescu–Lenard prediction unrealistically diverges at phase transition (Weinberg, 1993). Indeed, if the system supports a very weakly damped mode, $\omega_{\rm M} = \Omega_{\rm M} + {\rm i}\gamma_{\rm M}$ with $\gamma_{\rm M} t_{\rm dyn} \ll 1$, one has

$$\frac{\partial F}{\partial t} \propto |U^{\rm d}(\mathbf{k}\cdot\mathbf{\Omega})|^2 \sim \frac{1}{\gamma_{\rm M}^2} \underset{\gamma_{\rm M}\to 0}{\longrightarrow} \infty, \tag{5.11}$$

at resonance with the mode, i.e., for $\mathbf{k}\cdot\mathbf{\Omega} \simeq \Omega_{\rm M}$. This divergence should be regularised by considering the contribution of wave-particle interactions, in the spirit of the so-called quasilinear theory in plasma physics (see, e.g., Rogister & Oberman, 1968). Such a regularisation is an active topic of research (Hamilton & Heinemann, 2020, 2023).

5.2 Two-body *vs* resonant relaxation

5.2.1 Neglecting collective effects

For dynamically hot systems with high velocity dispersion, such as globular clusters, collective effects can be neglected. The Balescu–Lenard equation then reduces to the Landau equation (see Chavanis, 2013c, and references therein). This change amounts to replacing the dressed susceptibility coefficients, $U^{\rm d}_{\mathbf{k}\mathbf{k}'}$, in equation (5.1) with their bare counterpart, $U_{\mathbf{k}\mathbf{k}'}$, as defined in equation (3.4). The inhomogeneous Landau equation then reads (Polyachenko & Shukhman, 1982;

Chavanis, 2013c)

$$\frac{\partial F(\mathbf{J},t)}{\partial t}=-\pi(2\pi)^d\,m\,\frac{\partial}{\partial\mathbf{J}}\cdot\Big[\sum_{\mathbf{k},\mathbf{k}'}\mathbf{k}\int\mathrm{d}\mathbf{J}'\,\underbrace{\left|U_{\mathbf{k}\mathbf{k}'}(\mathbf{J},\mathbf{J}')\right|^2}_{\text{bare coupling}}\times\delta_{\mathrm{D}}(\mathbf{k}\cdot\boldsymbol{\Omega}-\mathbf{k}'\cdot\boldsymbol{\Omega}')\left(\mathbf{k}'\cdot\frac{\partial}{\partial\mathbf{J}'}-\mathbf{k}\cdot\frac{\partial}{\partial\mathbf{J}}\right)F(\mathbf{J},t)\,F(\mathbf{J}',t)\Big]. \quad (5.12)$$

Equations (5.1) and (5.12) are remarkably similar. They both take into account the effects of resonant encounters between stars in driving the relaxation of the mean-field equilibrium. However, the inhomogeneous Landau equation (5.12) neglects the dressing of these resonant encounters by collective effects.

5.2.2 Local encounters

The first historical kinetic theory of stellar systems was developed by Chandrasekhar in the 1940s (see, e.g., Chavanis, 2013a, for a review). Chandrasekhar assumed that the relaxation of a stellar system is driven by local deflections between stars, illustrated in figure 5.4. In this local approximation, the system is considered as infinite and homogeneous and the mean-field motion of stars is a simple straight line. Therefore, this theory does not account for (i) long-range resonant interactions and (ii) collective effects, i.e., the gravitational dressing of stars by their polarisation cloud. Furthermore, it suffers from logarithmic divergences at both small and large scales.

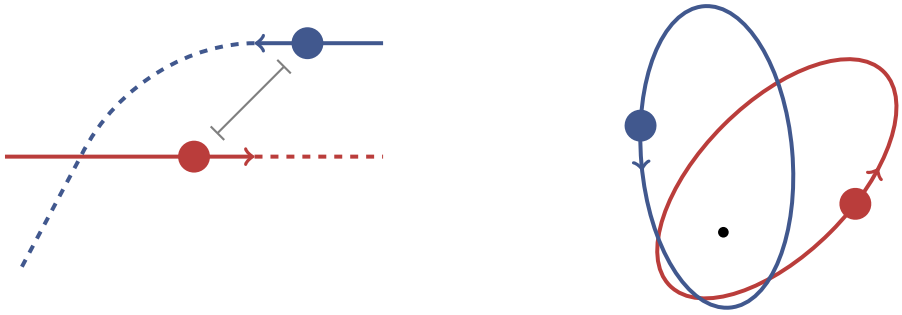

Figure 5.4: Illustration of local pairwise encounters and resonant encounters. Both contribute to the relaxation of the system. The local encounters are captured by the Chandrasekhar theory (Chandrasekhar, 1942). The inhomogeneous Balescu–Lenard equation (5.1) captures both processes but puts the emphasis on the dressed resonant ones.

Homogeneous Landau equation Let me generically consider a homogeneous system with a power-law pairwise interaction potential

$$U(\mathbf{r})\propto\frac{1}{|\mathbf{r}|^\gamma}, \quad (5.13)$$

The usual Coulombian/Newtonian potential corresponds to $\gamma=1$ in dimension $d=3$. Natural variables are position and velocity in the homogeneous case. Therefore, the bare coupling coefficients (equation 3.4) read

$$U_{\mathbf{k}\mathbf{k}'}(\mathbf{v},\mathbf{v}')=U_{\mathbf{k}\mathbf{k}'}\propto\frac{\delta^{\mathbf{k}'}_{\mathbf{k}}}{|\mathbf{k}|^{d-\gamma}}, \quad (5.14)$$

and are independent of the velocity. In this case, Landau equation (5.12) becomes (see, e.g., Chavanis, 2013a)

$$\frac{\partial F(\mathbf{v},t)}{\partial t}=-\pi(2\pi)^d\,m\,\frac{\partial}{\partial\mathbf{v}}\cdot\Big[\int\mathrm{d}\mathbf{k}\mathrm{d}\mathbf{v}'\,\mathbf{k}\,|U_{\mathbf{k}}|^2\,\delta_{\mathrm{D}}[\mathbf{k}\cdot(\mathbf{v}-\mathbf{v}')]\,\mathbf{k}\cdot\left(\frac{\partial}{\partial\mathbf{v}'}-\frac{\partial}{\partial\mathbf{v}}\right)F(\mathbf{v},t)\,F(\mathbf{v}',t)\Big]. \quad (5.15)$$

Focusing on the contribution of the different spatial scales, $k=|\mathbf{k}|$, the relaxation is roughly given by the integral

$$\frac{\partial F}{\partial t} \propto \int_0^\infty \frac{\mathrm{d}k}{k^{d-2\gamma}}, \tag{5.16}$$

where I used equation (5.14) and the δ_{D}-Dirac property $\delta_{\mathrm{D}}(\mathbf{k}\cdot\mathbf{v}')=\delta_{\mathrm{D}}(\mathbf{v}')/|\mathbf{k}|$. This integral diverges at small scales, i.e., for $k\to\infty$, when $d\leq 2\gamma+1$ and at large scales, i.e., for $k\to 0$, when $d\geq 2\gamma+1$ (see also Chavanis, 2013b; Gabrielli et al., 2010; Marcos et al., 2017). For the usual 3D Newtonian gravity, one has $\gamma=1$ and $d=3$, so that the integral diverges logarithmically at both small and large scales. This is the well-known Coulomb logarithm divergence (Landau, 1936).

Small-scale divergence Chandrasekhar (1942) did propose a regularisation of the divergence at small scales without introducing a cut-off in the impact parameter, but taking into account non-linear corrections for hard encounters (see, e.g., Baldwin, 1962; Frieman & Book, 1963; Guernsey, 1964; Weinstock, 1964). Such treatment would need to be revisited in the context of the inhomogeneous resonant interactions involved in the inhomogeneous Landau equation (5.12). Softening the gravitational interaction potential also cures this logarithmic divergence (Weinberg, 1986; Marcos et al., 2017; Fouvry et al., 2021). While somewhat artificial, these softened potentials are ubiquitous in numerical simulations and may therefore have a strong impact on the long-term evolution of these systems (Miller, 1971; Salo & Laurikainen, 2000). In particular, softening can favour the relaxation driven by long-range resonant interactions over local encounters. This might be particularly relevant in dynamically cold systems, such as razor-thin discs, in which long-range interactions are significantly enhanced by collective effects. In the one-dimensional model, there is no divergence at small scales (equation 2.1). This model is therefore more appropriate to study the relaxation driven by long-range resonant interactions.

Large-scale divergence The large-scale divergence is due to the infinite extent of the system and the assumption of a homogeneous distribution of stars. This divergence cannot be regularised in Chandrasekhar's theory without introducing an upper cut-off in the impact parameter. It introduces a free parameter, effectively making the theory less predictive (notably on the overall amplitude of the relaxation rate). This cut-off is usually set to the system's size (e.g., Vasiliev, 2017; Rodriguez et al., 2022). For plasmas, this large-scale divergence is regularised by screening effects: the so-called Debye shielding (Nicholson, 1992). Roughly, the effects of opposite charges cancel out over the Debye length so that the potential is not long-range beyond that scale. This screening mechanism is appropriately captured by collective dressing in the homogeneous Balescu–Lenard equation (Balescu, 1960; Lenard, 1960). In the self-gravitating case, gravity is always attractive and no such screening mechanism can operate. However, it also implies that self-gravitating systems tend to collapse onto finite inhomogeneous structures through Jeans' instability (see, e.g., Magorrian, 2021). For inhomogeneous systems, the integral in equation (5.16) is transformed into a sum over resonances numbers,

$$\frac{\partial F}{\partial t} \propto \sum_{k>0} \frac{1}{k^{d-2\gamma}}, \tag{5.17}$$

regularising *de facto* the large-scale divergence.

Quantifying the relative contributions of local encounters *vs* long-range dressed interactions in various systems is a difficult task because (i) properly accounting for small-scale contributions might require non-linear corrections and (ii) the large-scale contributions have to be regularised by taking into account the inhomogeneity of the system and (iii) collective effects can enhance or suppress the contribution of long-range resonant interactions. In the case of spherical globular clusters, Fouvry et al. (2021) and Tep et al. (2022) showed that, once averaged along the (unperturbed) orbit, Chandrasekhar's theory is able to capture overall the secular evolution of the system, i.e.,

the relaxation is mainly driven by two-body deflections. They also showed that, for large resonance numbers, $|k| \gg 1$, the Landau equation (5.12) indeed recovers the effect of (linearised) local deflections from Chandrasekhar theory (see also Weinberg, 1986).

Chapter 6

Secular response applications

6.1 Long term relaxation of one-dimensional self-gravitating systems

This section reproduces some of the results published in Roule et al. (2022) on the secular evolution of one-dimensional self-gravitating systems.

6.1.1 Collective stiffening

Diffusion predictions

With equations (5.1) and (5.12), I have at my disposal two different predictions taking into account (Balescu–Lenard) or neglecting (Landau) collective effects. For the one dimensional model, the diffusion equation (5.3b) reads

$$D(J) = \sum_{k,k'} \int \mathrm{d}J' \, G^{\mathrm{Diff}}_{kk'}(J,J') \, \delta_{\mathrm{D}}[k\Omega(J) - k'\Omega(J')], \tag{6.1}$$

where, for the Balescu–Lenard case,

$$G^{\mathrm{Diff}}_{kk'}(J,J') = (2\pi)^2 \, m \, k^2 \left|U^{\mathrm{d}}_{kk'}(J,J',k\Omega)\right|^2 F(J'), \tag{6.2}$$

and similarly for the Landau case, with $U^{\mathrm{d}} \to U$. The Balescu–Lenard coupling coefficients can be computed from equation (3.29) using the gravitational susceptibility from section 4.1.3. When neglecting collective effects, the Landau coupling coefficients can be computed more efficiently and independently of any bi-orthogonal basis (appendix 6.B.1).

The integral over action in equation (6.1) can be readily computed using the formula

$$\delta_{\mathrm{D}}[f(J')] = \sum_{J_{\mathrm{res}}} \frac{\delta_{\mathrm{D}}(J' - J_{\mathrm{res}})}{|\partial f / \partial J|_{J_{\mathrm{res}}}}, \tag{6.3}$$

where J_{res} are the solutions of $f(J') = k' \, \Omega(J') - k \, \Omega(J) = 0$. This formula allows me to subsequently get rid of the integral appearing in equation (6.1). Given that the frequency profiles are monotonic (figure 2.7), computing this integral amounts to, for each resonance pair, (k, k'), (i) find the (possible) resonance point using bisection, (ii) compute the integrand value at this point along with the frequency gradient, $\partial\Omega/\partial J$. Finally, the sum over resonances in equation (6.1) can be safely truncated to a few resonances, as the coupling efficiency rapidly drops with the order of the resonance. Typically, I used only the resonances $|k|, |k'| \leq 10$.

Comparison to simulations

In the left panel of figure 6.1, I first present the diffusion coefficients at thermal equilibrium computed with the Balescu–Lenard (section 5.1) and the Landau (section 5.2.1) formalisms, together with the corresponding estimates from numerical simulations. I refer to appendix 6.A for the details

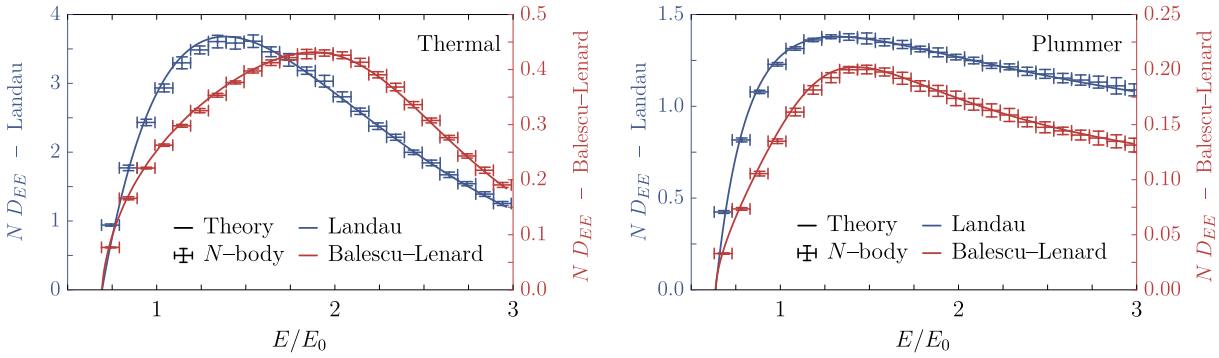

Figure 6.1: Figure from Roule et al. (2022). Left: Diffusion coefficients at thermal equilibrium as a function of energy in both Landau (i.e., without collective effects) and Balescu–Lenard (i.e., with collective effects) cases. Right: Same as the left panel but for the Plummer equilibrium. The kinetic theory shows a very satisfactory match to the numerical measurements. Note that both measurements have their own vertical scales as collective effects slow down diffusion by a factor $\sim$10. This is one of the key results of this thesis.

of the N–body simulations and later in the present section for the associated measurements.

In both the Landau and Balescu–Lenard cases, I recover a very good match ($<5\%$) between the kinetic theory and the numerical measurements. This confirms that, indeed, long-range resonant couplings are responsible for the long-term relaxation of these systems. Given all the assumptions made in the derivation of the kinetic theory (section 5.1.3), this level of agreement was not guaranteed. It validates *a posteriori* the underlying approximations and proves that collective effects and resonant interactions have to be taken into account to accurately describe the long-term evolution of long-range many-body systems.

In the right panel of figure 6.1, I present the same measurements for the Plummer distribution (section 2.3.1). Satisfactorily, this other equilibrium shows the same level of fine agreement. Let me stress that, for both equilibria, the Balescu–Lenard diffusion coefficients are $\sim$10 times smaller than the Landau ones, an effect already noted in the HMF model for highly magnetised thermal equilibria (see figure 9 in Benetti & Marcos, 2017). This is at variance with the low magnetisation HMF result, or the case of self-gravitating stellar disks (Fouvry et al., 2015) where collective effects considerably accelerate the relaxation (section 6.2).

However, this behaviour is not specific to one-dimensional contrived geometries. Indeed, Weinberg (1989) did observe the same phenomenon while studying the torque experienced by a satellite sinking in a spherical halo. The friction force by polarisation exerted by the halo on the satellite is weakened by collective effects. In figure 6.2, I reproduce his figures 6 and 7 to illustrate this stiffening by collective effects in spherical haloes.

Let me now discuss the origin of this collective stiffening in the one-dimensional model.

Resonances contribution

The influence of the gravitational dressing strongly depends on the resonance frequency, $\omega = k\Omega$. It is at these (real) frequencies that the coupling coefficients, $U^{\rm d}(\omega)$, are evaluated in the Balescu–Lenard equation (5.1). It is therefore of interest to pinpoint the individual contributions of reso-

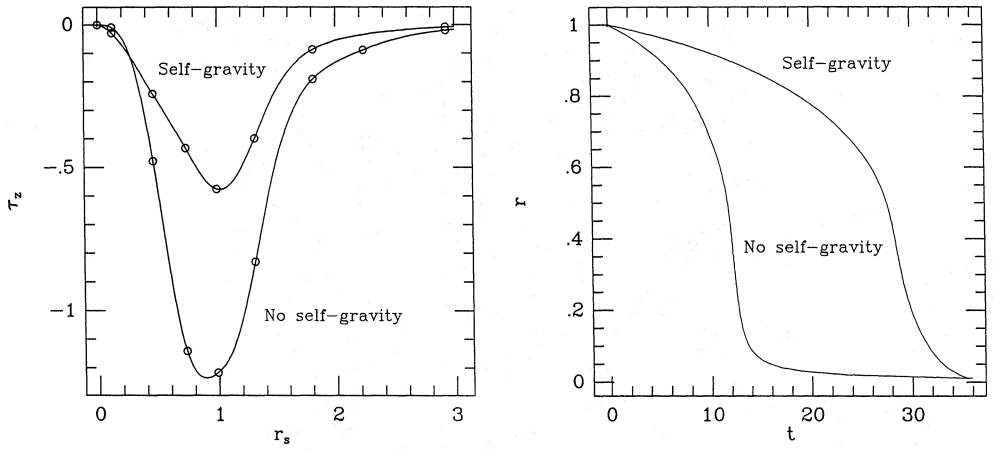

Figure 6.2: Figures from Weinberg (1989) (figures 6 and 7 therein). Sinking satellite in a self-gravitating *vs* non-self-gravitating spherical halo. Left: Torque exerted by the halo on a circular orbit as a function of the distance to the halo's centre. Right: Distance to the halo's centre of the sinking satellite as a function of time. Turning on self-gravity reduces the torque experienced by the satellite and ultimately slows down its inevitable fall. In this instance, the geometry and symmetry of the self-amplified wake is such that the net torque is effectively smaller. The overall amplitude of the wake is nonetheless stronger locally.

nances to the diffusion coefficient

$$D(J) = \sum_{k,k'} D_{kk'}(J). \tag{6.4}$$

First, not all resonances participate in the total diffusion. If k and k' do not share the same parity, the dressed and bare coupling coefficients vanish, since $U^{\mathrm{d}}_{kk'} = U_{kk'} = 0$ (section 4.1.2). Furthermore, the overall frequency range of both profiles is finite (figure 2.7). For a given orbit J, this imposes $k/k' \leq \Omega(J=0)/\Omega(J)$ for the resonance condition from equation (5.1) to be met.

Given that the coupling efficiency rapidly drops with the order of the resonance, figure 6.3 focuses on the contributions of low-order resonances. The left panel of this figure illustrates the

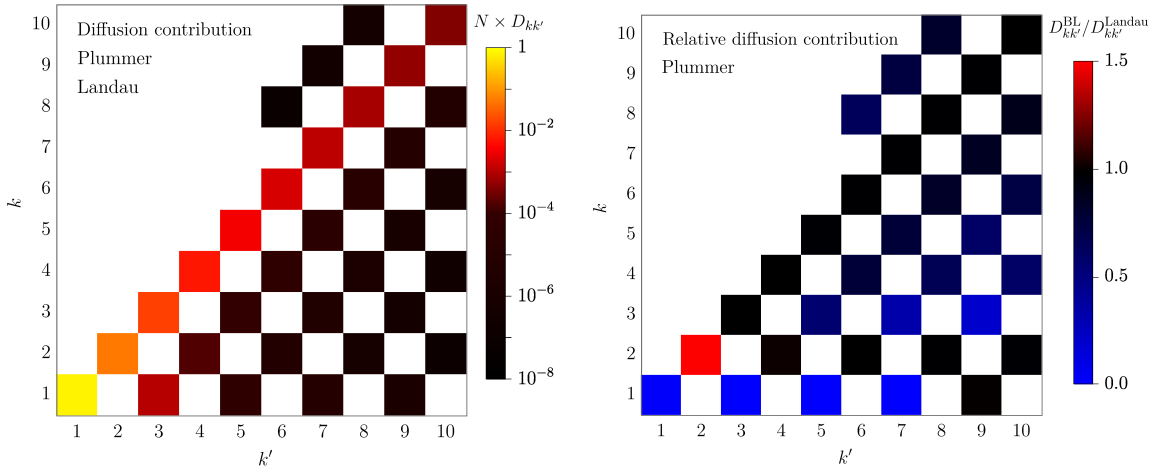

Figure 6.3: Figure from Roule et al. (2022). Left: Individual contributions of the various resonances (k, k') to the Landau diffusion coefficients for the Plummer equilibrium and $E = \psi(2\alpha)$. Right: Relative contributions when collective effects are or are not taken into account, for the same setup. The main contributor to the Landau diffusion, the resonance $(1, 1)$, is severely damped by collective effects, while the amplification of other resonances remains limited.

predominant role of the resonance $(k,k')=(1,1)$ in the Landau orbital diffusion (in yellow), while the right panel shows the extinguishing role of collective effects for any $k=1$ resonances. This is ultimately responsible for the relative inefficiency of the Balescu–Lenard diffusion w.r.t. the Landau one. The determinant of the susceptibility matrix plotted in figure 4.3 allows me to reach the same conclusions. Indeed, the gravitational susceptibility suffers from a drought for any odd resonant couplings with $\omega\sim\Omega_0$. And, the slight amplification of the resonance $(2,2)$ observed in figure 6.3 is equivalently found in figure 4.3 since $2\Omega(2\alpha)\sim1.4\Omega_0$. This amplification still remains too limited to compensate for the strong collective damping of the dominating $(1,1)$ resonance.

Correlation of the perturbations

As emphasised in Binney & Lacey (1988), orbital diffusion is generically sourced by the time correlation of the potential fluctuations, which here stems from Poisson shot noise. Following Fouvry & Bar-Or (2018), I present in figure 6.4 the correlation of the potential fluctuations in simulations with and without collective effects. To estimate this correlation, I use a strategy similar to the one I used for the measurement of unstable modes in section 4.3.3. The instantaneous density, $\rho_{\rm d}(x,t)=\sum_i m\delta_{\rm D}[x-x_i(t)]$, is projected onto the basis elements from section 4.1.1 to write $\rho_{\rm d}(x,t)=\sum_p A_p(t)\rho^{(p)}(x)$ with

$$A_p(t) = -\sum_i m\,\psi^{(p)}[x_i(t)]. \tag{6.5}$$

I use these coefficients to probe the time evolution of the system's finite-N fluctuations. Their spatial dependence have been absorbed in the basis elements. More precisely, I consider

$$\delta A_p(t)=A_p(t)-\langle A_p\rangle_t, \tag{6.6}$$

with $\langle A_p\rangle_t$ the time-average over the simulated duration. Under an assumption of ergodicity, removing the time average amounts to removing the mean-field density, hence having

$$\delta\psi(x,t) = \sum_p \delta A_p(t)\,\psi^{(p)}(x). \tag{6.7}$$

In figure 6.4, I illustrate the measured correlation

$$C(t) = \int_0^{T-t}\frac{{\rm d}\tau}{T-t}\langle\delta A_p(\tau)\,\delta A_p(\tau+t)\rangle, \tag{6.8}$$

where $\langle\cdot\rangle$ stands for the average over realisations, and using the odd basis element $\psi^{(3)}_{\rm odd}$ from equation (4.2).

The gravitational dressing has two main effects: (i) it weakens the overall amplitude of the potential fluctuations; (ii) it reduces the coherence time of these perturbations. Indeed, while the Landau correlations decrease like $1/t^2$, the Balescu–Lenard correlations are found to decay like $1/t^5$, as illustrated in figure 6.5. These decay rates are estimated through linear regressions of the local extrema in log−log scale. It would be interesting to understand analytically the origin of these two algebraic decay rates. The typical coherence time of the fluctuations, a.k.a., $T_{\rm bal}$, the ballistic time, is shorter for the Balescu–Lenard experiments, as (i) the typical amplitude of the Balescu–Lenard correlation is lower than the Landau ones and (ii) correlations decay faster in the presence of collective effects. Naturally, this drives a slower orbital diffusion in the Balescu–Lenard situation compared to the Landau one, as presented in section 6.1.1.

This is fully consistent with figure 6.6 where I equivalently illustrate the diffusion of individual test particles in the presence/absence of collective effects. In that figure, I also recover that the energy diffusion is naturally modulated at the frequency $\sim 2\pi/t_{\rm dyn}$, i.e., the typical frequency of the background thermal equilibrium.

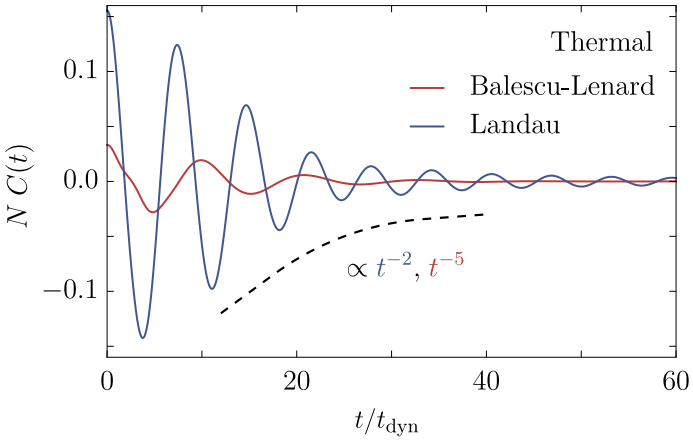

Figure 6.4: Figure from Roule et al. (2022). Time correlation, $C(t)$ (equation 6.8), of the potential fluctuations in N–body simulations for the thermal equilibrium with and without collective effects. In the presence of collective effects, both the amplitude and coherence time of the correlation function are reduced.

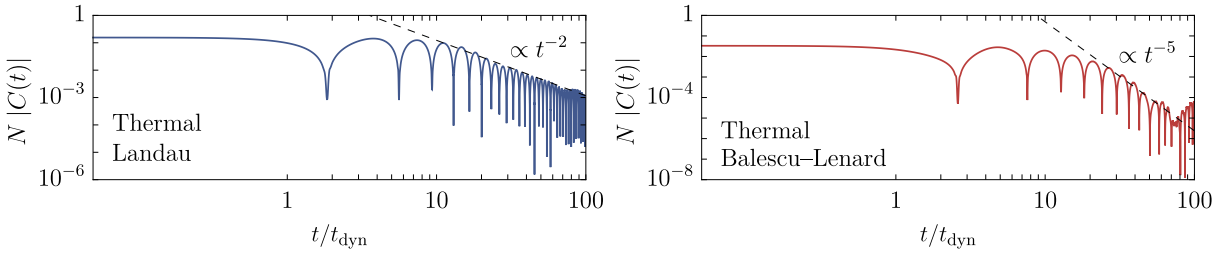

Figure 6.5: Figure from Roule et al. (2022). Fit of the decay rate of the correlation $C(t)$ from figure 6.4 for the Landau (left) and Balescu–Lenard cases (right) using 12 800 realisations. Without collective effects (Landau), the correlations decrease like $C(t) \propto 1/t^2$. In fully self-gravitating experiments (Balescu–Lenard), they decay like $C(t) \propto 1/t^5$. Together with the overall amplitude difference, this results in a slower orbital diffusion in the Balescu–Lenard situation compared to the Landau one.

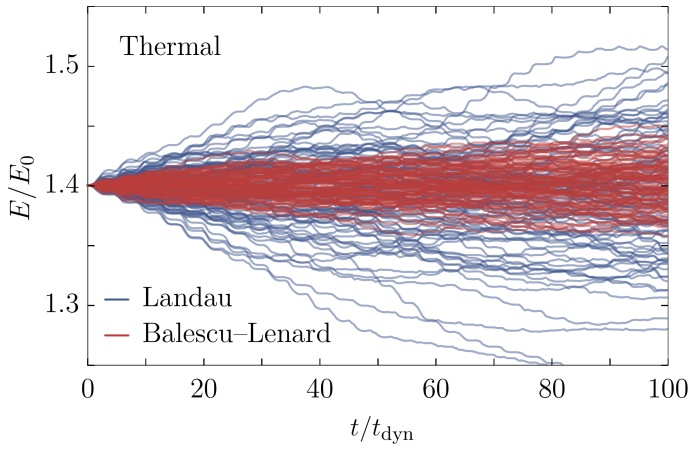

Figure 6.6: Figure from Roule et al. (2022). Typical diffusion of test particles embedded within N–body realisations of the thermal equilibrium with collective effects (Balescu–Lenard) or without (Landau). The massless test particles are all placed at the same initial phase space location in their respective realisations. Collective effects slow down the orbital diffusion.

In practice, I ran 12 800 realisations of the thermal equilibrium with $N=10^5$ particles, with $\delta t=10^{-3}\,t_{\rm dyn}$ up to $T=10^3\,t_{\rm dyn}$. The typical relative error in $E_{\rm tot}$ is of order 10^{-6}, and I dumped values of A_p every $0.05\,t_{\rm dyn}$. For the Balescu–Lenard experiment, I also let the system "warm up" during 200 dynamical times before any measurement, so as to let the initial Poisson shot noise thermalise and get dressed by collective effects (see, e.g., appendix F in Fouvry & Bar-Or, 2018).

Diffusion measurements

For the sake of convenience, I measure diffusion in energy, $E=v^2/2+\psi(x)$, with $\psi(x)$, the system's initial unperturbed potential. To estimate diffusion coefficients in N–body simulations, I follow equation (5.5) and write

$$D_{EE}=\lim_{t\to+\infty}\frac{\langle\Delta E^2(t)\rangle}{t}. \tag{6.9}$$

In practice, this limit has to be understood as considering the changes of orbit on a timescale much longer than the ballistic time, $T_{\rm bal}$, but much shorter than the diffusion time.

Bias at small times If one does not wait long enough, the dispersion will first evolve quadratically with time before reaching a linear regime. Indeed, one has

$$\Big\langle\Delta E^2(t)\Big\rangle=\int_0^t{\rm d}t'\int_0^t{\rm d}t''\,\langle\delta E(t')\delta E(t'')\rangle\,. \tag{6.10}$$

The correlation of the energy fluctuations corresponds to the function

$$C(t''-t')=\langle\delta E(t')\delta E(t'')\rangle \tag{6.11}$$

introduced in equation (6.8) and illustrated in figure 6.4. Importantly, these fluctuations are *not* δ-correlated in time. Very roughly accounting for this correlation during the ballistic time, one has

$$\Big\langle\Delta E^2(t)\Big\rangle\sim\begin{cases}C_0t^2 & \text{if } t\lesssim T_{\rm bal},\\ C_0T_{\rm bal}t & \text{if } t\gg T_{\rm bal},\end{cases} \tag{6.12}$$

with $C_0=C(t=0)$. To prevent this initial quadratic growth from biasing the measurement, I must (i) wait long enough so that the system has reached the linear regime and (ii) throw away the initial growth in the time series, $t\to\langle\Delta E^2(t)\rangle$, and fit the linear regime only.

Bias at large times Conversely, if one waits too long, the measurement will suffer from another bias. Indeed, if one waits infinitely long, the test particle will explore the whole orbital phase. The diffusion rate effectively measured would then correspond to an average of the diffusion rates (over phase space) and not to its value for the initial actions. Therefore, I truncate the time series at a time $T_{\rm max}$ so that the test particles have not diffused too much, i.e., such that $\langle\Delta E^2(T_{\rm max})\rangle\leq\delta E_{\rm bin}^2$, with $\delta E_{\rm bin}$ the width of the energy bin.

Anomalous long-term diffusion A final caveat stems from the fact that at large time, the Balescu–Lenard time series become sublinear, a phenomenon already noted in the HMF model (see figure 8 in Benetti & Marcos, 2017). This is not due to particles exploring too different energies as the dispersion is still far below the bin width. I do not have a clear physical explanation for this long-term behaviour. In practice, I accounted for this effect by appropriately reducing the series' maximal time, $T_{\rm max}$, so as not to enter this regime.

These subtleties are particularly important to allow for an accurate measurement of the diffusion coefficients and ultimately reach the agreement between the kinetic theory and the numerical simulations presented in figure 6.1. Once the domain $T_{\rm bal}\leq t\leq T_{\rm max}$ is determined, the diffusion coefficient is estimated with a linear fit (least squares method) on that timespan. This is illustrated in figure 6.7 for both Landau and Balescu–Lenard measurements.

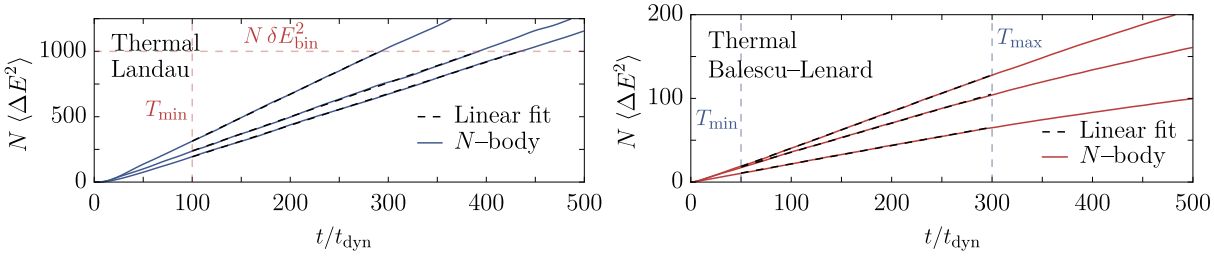

Figure 6.7: Figure from Roule et al. (2022). Typical time series of energy dispersion averaged over a given energy bin and 1 280 realisations for Landau (left) and Balescu–Lenard (right) measurements, together with the associated linear fits. Here, $\langle\Delta E^2\rangle$ first evolves quadratically in time (ballistic regime) and then linearly (diffusive regime). For the Balescu–Lenard experiments, the time series ultimately becomes sublinear, as already noted in the HMF model (Benetti & Marcos, 2017).

Numerical details For a given realisation, particles are initially binned in 25 bins of width $\delta E_{\rm bin} = 0.1\,E_0$, starting at the minimal energy, $\psi(0)$. For every bin and every time dump, I compute $\langle\Delta E^2(t)\rangle = \langle[E(t) - E(t=0)]^2\rangle$, averaged over all the particles initially in the bin and all the available realisations.

For the Balescu–Lenard measurements in figure 6.1, I ran 10 independent groups of 1 280 realisations with $N = 10^5$ particles, $\delta t = 10^{-3}\,t_{\rm dyn}$ and up to $T = 500\,t_{\rm dyn}$. The typical relative error in $E_{\rm tot}$ is of order 10^{-6}, and I dumped ΔE^2 values every $t_{\rm dyn}$. As illustrated in the right panel of figure 6.7, I performed the linear fit within the domain $[T_{\rm bal}, T_{\rm max}] = [50\,t_{\rm dyn}, 300\,t_{\rm dyn}]$. In figure 6.1, I reported the mean value and standard deviation of the 10 independent batches of realisations.

For the Landau experiments, I used the exact same parameters, except that the $N = 10^5$ massive background particles follow the smooth mean potential, and I injected 2×10^4 massless test particles sampled initially according to $F(E)$. As highlighted by equation (5.4), these massless test particles only experience diffusion and no friction. Their diffusion is driven by the massive bath particles and therefore is proportional to $1/N$ with N the number of bath particles (not test particles). Because Landau simulations exhibit longer correlation times (see figure 6.4), I used $T_{\rm bal} = 100\,t_{\rm dyn}$. Furthermore, the diffusion is stronger in these experiments. Consequently, I adjusted $T_{\rm max}$ for every bin so that $\langle\Delta E^2(T_{\rm max})\rangle \leq \delta E^2_{\rm bin}$, as illustrated in figure 6.7. This prevents averaging the diffusion over multiple bins.

6.1.2 Quasi-kinetic blocking

Let me now investigate the initial flux, $\mathcal{F}(J, t=0)$, as given by equation (5.2a). Of course, this flux vanishes at thermodynamical equilibrium. Indeed, at thermal equilibrium, diffusion and friction obey the so-called detailed balance (see, e.g., appendix B in Binney & Lacey, 1988). Their contribution cancel out, and the equilibrium is preserved. This is however not the case for the Plummer quasi-stationary state (QSS) (section 2.3.1) which is not the state of maximum entropy. In figure 6.8, I illustrate its initial flux. Once again, the kinetic theory and numerical simulations are found to be in a good agreement, and both recover the (slow) relaxation of the Plummer distribution towards the thermal one. The predictions naturally follow from section 6.1.1. The details of the flux measurements can be found in appendix B of Roule et al. (2022). They are computationally more expensive than the diffusion measurements. Indeed, using appropriate dimensionless units, the flux is typically $\sim10^5$ times smaller than the diffusion coefficients, i.e., the efficiency of the relaxation is drastically hampered by a "quasi kinetic blocking" (chapter 7). It highlights the system's difficulty to populate resonances driving an efficient relaxation.

Contrary to the diffusion figure 6.1, there is no measured Landau flux in figure 6.8. Indeed, Landau diffusion measurements are made using massless test particles. Such particles do not experience any friction (equation 5.4) and cannot be used as probes for the whole flux, but solely for

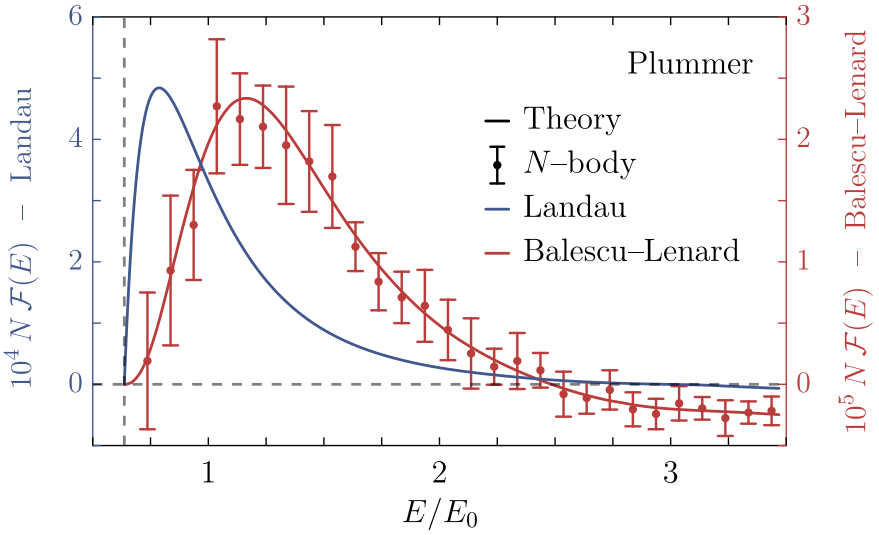

Figure 6.8: Initial flux in the Plummer equilibrium as a function of energy predicted by kinetic theory (line) in both Landau (i.e., without collective effects) and Balescu–Lenard (i.e., with collective effects) cases, together with the measurement in N–body simulations (points). The redistribution of orbits is only measured in self-consistent simulations where collective effects are, by design, present. The Balescu–Lenard prediction satisfyingly recovers the measurements. Let me stress that the amplitude of $N\mathcal{F}(E)$ has been rescaled by 10^5. Phrased differently, the overall relaxation is far less efficient than diffusion. Both predictions have their own vertical scales. Collective effects slow down the orbital reshuffling by a factor $\sim$20. This is one of the key results of this thesis.

diffusion. However, I computed the expected flux when neglecting collective effects through Landau equation (5.12). It amounts to replacing the dressed coupling coefficients, $U^{\mathrm{d}}_{kk'}$ (equation 3.12), by their bare counterpart $U_{kk'}$ (equation 3.4). As for diffusion, the Landau flux is about 20 times larger than the Balescu–Lenard one. Once again, collective effects restrain the evolution of the system.

To understand the origin of the quasi kinetic blocking, I now look at the individual contribution of the different resonances.

Resonances contribution

As put forward in equation (5.1), the system's long-term diffusion is sourced by resonant interactions. For a given resonant pair (k, k'), one has to ensure that the resonance condition, $k\Omega - k'\Omega' = 0$, is met, while the overall efficiency of this coupling is governed by the susceptibility coefficients, $U^{\mathrm{d}}_{kk'}(J, J', \omega)$, for that pair. In practice, a couple of important "conspiracies" are responsible for the small flux observed in figure 6.8:

(i) The Plummer frequency profile is monotonic (see figure 2.7). Any resonance $k = k'$ systematically imposes $J = J'$, leading to an exactly vanishing flux in equation (5.1).

(ii) Symmetry imposes $U^{\mathrm{d}}_{kk'} = 0$, for all k, k' of different parity (see the discussion after equation 4.7). As a consequence, one must have $|k - k'| \geq 2$ for a resonance to contribute to the flux. Similarly, k and k' must also have the same sign.

(iii) Despite its denser core, the overall frequency range of the Plummer profile is still finite (see figure 2.7). As for the diffusion, this imposes $k/k' \leq \Omega(J=0)/\Omega(J)$ for the resonance condition to be met.

(iv) For k large enough, the bare susceptibility coefficients asymptotically scale as $U_{kk}(J, J) \propto 1/k^2$. The higher the order of the resonance, the less efficient the coupling, and hence the (drastically) smaller the contribution to the flux.

I highlight these different effects in figure 6.9, by isolating the contributions, $\mathcal{F}_{kk'}$, of the different

resonances (k, k') to the Landau flux $\mathcal{F} = \sum_{k,k'>0} \mathcal{F}_{kk'}$. I emphasise in particular the rapid decay of the flux contributions as k, k' increase and as one moves away from the diagonal $k = k'$ (which only contributes to the diffusion coefficient and not the flux). These different effects are jointly responsible for the small flux reported in figure 6.8.

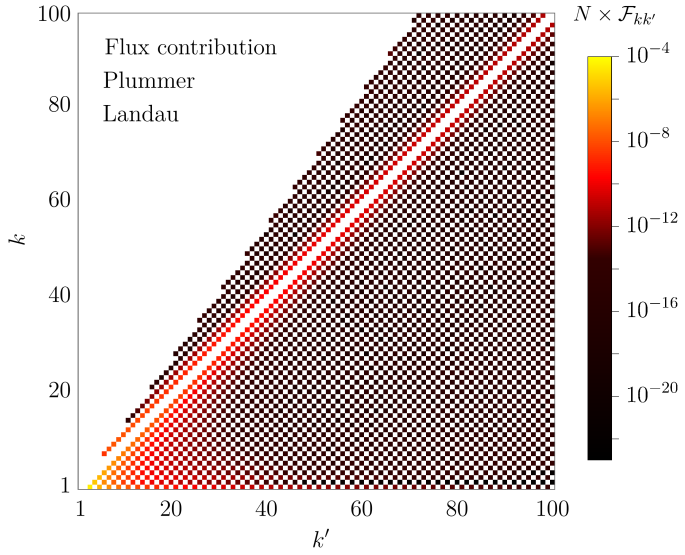

Figure 6.9: Figure from Roule et al. (2022). Individual contributions of the various resonances (k, k') to the initial Landau flux, $\mathcal{F}(E, t=0)$, for the Plummer equilibrium at $E = \psi(2\alpha)$. By symmetry, only $k, k' \geq 0$ resonances are considered. Note the logarithmic colour coding. The flux is dominated by low order resonances and suffers from many annihilating conspiracies (see main text).

Figure 6.9 is essentially left unchanged when taking into account collective effects. The only significant difference in the Balescu–Lenard case is the reduced contribution from the resonances with $k = 1$ for which gravitational dressing weakens the amplitude of the orbital coupling as detailed in section 6.1.1. Taking collective effects into account therefore further reduces the flux as they notably damp contribution from the resonance $(k, k') = (1, 3)$, the main contributor to the Landau flux (see figure 6.9).

Despite this relative inefficiency, I stress that the Plummer equilibrium still relaxes through $1/N$ two-body resonant effects. This is in stark contrast with homogeneous one-dimensional systems which are generically kinetically blocked at order $1/N$ (see, e.g., Chavanis, 2012) and require the derivation of appropriate kinetic equations at order $1/N^2$ sourced by three-body effects (Fouvry et al., 2020). This is also the case for inhomogeneous one-dimensional systems with monotonic frequency profile and only subject to 1:1 resonances. In this case, the resonance condition in equation (5.1) is only met for $J = J'$ and the flux vanishes. These *full* kinetic blockings are discussed in more details in chapter 7.

6.2 Long term relaxation of discs

In this section, I discuss the secular evolution of stable Mestel discs (section 2.3.2). I first present the context of this study, i.e., the results of Sellwood (2012) and Fouvry et al. (2015). I then present the expected flux computed from equation (5.1) together with N–body measurements and discuss the impact of damped modes presented in section 4.2.6. Using numerical simulations, I then study the effect of gravitational softening and the intrinsic stochasticity among different realisations.

6.2.1 Context

This study is motivated by the work of Sellwood (2012) (hereafter S12) and Fouvry et al. (2015) (hereafter F+15) who investigated the long term evolution of the stable Toomre disc (half-mass Mestel disc) from section 2.3.2. S12 investigated the long-term evolution of the disc using N–body simulations. F+15 then analysed this evolution implementing, for the first time, the inhomogeneous Balescu–Lenard equation (5.1). I first present and discuss their results to give the context of this study.

Sellwood (2012)'s N–body results

The first long-term simulation of a stable isolated Mestel disc was conducted by Sellwood (2012). He focused on the effect of $\ell=2$ fluctuations only (filtering out the other harmonics as I did to measure the instability in Zang's disc in section 4.3.1). S12 found that, albeit initially stable, the disc becomes linearly unstable after a slow growth of the potential/density fluctuations. The time at which the instability sets in depends on the number of particles, N, as illustrated in figure 6.10 adapted from S12. To prove that the system was indeed linearly unstable after a certain time,

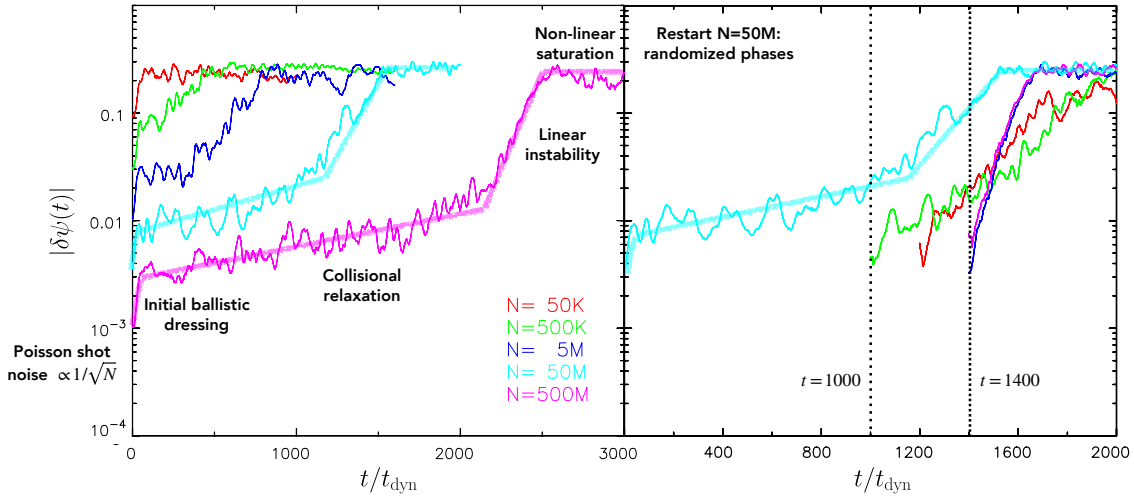

Figure 6.10: Figures adapted from Sellwood (2012), with additional annotations. Evolution of the $\ell=2$ fluctuations in N–body simulations of the Toomre disc for different number of particles, N. Starting from uncorrelated Poisson shot noise, the fluctuations quickly get dressed by collective effects on a ballistic time, $T_{\rm bal}$ (equation 6.12). The amplitude of the fluctuations then slowly grows until a clear instability sets in. The larger the number of particles, the lower the initial Poisson noise and the slower the secular growth, hence the later the dynamical phase transition. The instability ultimately possibly saturates under non-linear resonance-trapping effects (see, e.g., Hamilton, 2024).

S12 stopped the simulation at different times and restarted it after randomising the phases of the particles. Doing so, he killed *de facto* any prior bisymmetric coherent features, ruling out a possible non-linear effect. As reproduced in the right panel of figure 6.10, S12 found that the later the simulation was stopped, the stronger was the instability.

Such a change, from a stable to an unstable state, cannot be explained by the linear theory. It necessarily involves changes in the mean-field DF. Similar dynamical phase transitions, driven by collisional secular evolution, occur in the HMF model (Campa et al., 2008). S12 therefore looked at the distribution of orbits in action space. He reported on (i) a localised depletion of circular orbits (or groove) before the instability kicks in ($t/t_{\rm dyn}=1000$) and (ii) the presence of a strong, sharp ridge at resonance with the instability before it saturates ($t/t_{\rm dyn}=1400$). Both measurements are reproduced in figure 6.11. This groove generated in the inner part of the disc is responsible for the nascent instability. Sellwood & Kahn (1991) already noted that such a localised feature can

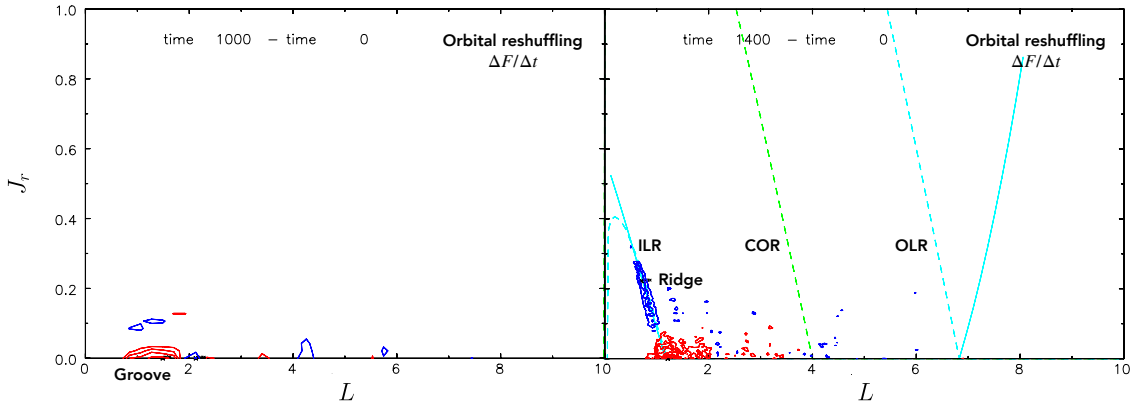

Figure 6.11: Figures adapted from Sellwood (2012), with additional annotations. Distribution of orbits in action space in N–body simulations of the Toomre disc for $N = 50\times10^6$ particles. *Left:* At $t/t_{\rm dyn} = 1000$, one observes a localised small depletion of circular orbits before the instability sets in. *Right:* At $t/t_{\rm dyn} = 1400$, one observes a strong, sharp ridge at resonance (ILR) with the nascent instability ($\Omega_{\rm M} t_{\rm dyn} = 0.5$). Note that, in these figures, red contours correspond to a depletion of the number of particles while blue contours correspond to an excess.

generate an instability in N–body simulations. This result was later confirmed by De Rijcke et al. (2019a) and Dootson (2023) using linear response theory.

Let me note that the author later confirmed that his results were consistent with changing the simulation method from a polar to a Cartesian grid (Sellwood, 2020). He also tried a different sampling of the initial conditions and recovered similar growth curves of the fluctuations. On this last point, I stress that, in both cases, the initial conditions were not pure Poisson noise. Indeed, the disc was sampled using a so-called "quiet start" procedure (Debattista & Sellwood, 2000; Sellwood, 2024), i.e., with a reduced randomness on the initial conditions.[1] Finally, the author did not show the equivalent of figure 6.11 for this new realisation. It would be interesting to see if, despite similar growth curves of the fluctuations, the changes in the DF could be different.

Fouvry et al. (2015)'s results

The slow growth of the fluctuations and the subsequent changes in the mean-field DF were still to be explained. Predicting such a change in the mean-field DF arising from fluctuations is exactly the purpose of the kinetic theories presented in chapter 5.

F+15 investigated the same disc as S12 using their own numerical simulations and implementing predictions from different kinetic theories. With their simulations, they showed (i) that the changes in the mean-field DF happened on timescales proportional to the number of particles, i.e., $\partial F/\partial t \propto 1/N$, and (ii) that slightly increasing the active fraction, ξ, of the disc enhanced the relaxation. More precisely, they measured the overall flux difference when varying the active fraction and reported that $|\boldsymbol{\mathcal{F}}(\xi=0.6)|/|\boldsymbol{\mathcal{F}}(\xi=0.5)| \sim 30$, with $\boldsymbol{\mathcal{F}}$ the measured flux (equation 5.2a). Implementing, for the first time, the inhomogeneous Balescu–Lenard equation (5.1), they found that the predicted changes in the mean-field DF were qualitatively consistent with the N–body results. Importantly, they proved that accounting for collective effects considerably modified and enhanced the relaxation, as illustrated in figure 6.12.

Taken together, S12 and F+15's results offer a convincing picture for the long-term evolution of the isolated Toomre disc. Initially stable, the disc first evolves under the collisional effects of swing amplified finite-N fluctuations. This secular relaxation is characterised by a strong heating and

[1] The "quiet start" initial conditions are not pure Poisson noise. This sampling procedure is designed to mimic the smooth mean-field DF. While this is particularly useful for collisionless simulations, here one might be worried that it could bias the collisional relaxation.

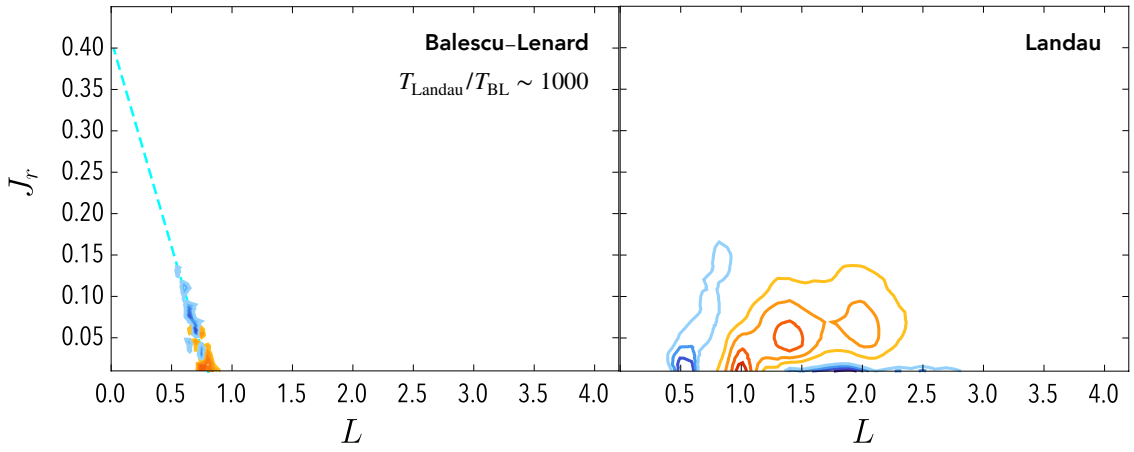

Figure 6.12: Figures adapted from Fouvry et al. (2015), with additional annotations. Predicted changes in the mean-field DF from the inhomogeneous Balescu–Lenard equation (5.1) (left) and Landau equation (5.12) for the long-term evolution of the Toomre disc. The Balescu–Lenard flux displays a sharp ridge, depopulating the circular orbits and diffusing along the direction associated with the ILR in action space, $\mathbf{k}\cdot\mathbf{J} = J_r - 2L$. The overall amplitude (not shown) of this ridge is consistent with S12's N–body results. Importantly, taking collective effects into account (Balescu–Lenard) drastically enhances the relaxation compared to the "naive" bare relaxation rate. The relaxation time predicted by the Balescu–Lenard theory, $T_{\rm BL}$, is three orders of magnitude shorter than the one predicted by the Landau theory, $T_{\rm Landau}$. Any kinetic theory who does not take them into account, either Chandrasekhar's two-body encounters (section 5.2.2) or Landau bare resonant interactions (section 5.2.1), would fail to predict even roughly the correct relaxation timescale.

churning (Sellwood & Binney, 2002) of circular orbits sharply localised in action space. The new DF is then linearly unstable allowing for an exponential growth of the potential/density fluctuations.

Yet, a few potential caveats in the early phase of this story can be raised and deserve further investigation.

(i) The ridge presented in S12's simulation is measured when the instability is already present. This ridge might not correspond to the initial change in the DF but rather be induced by the new instability. Earlier measurements (left panel of figure 6.11) mainly show a localised depletion of circular orbits. Note however that this measurement is more challenging as the changes are smaller.

(ii) The Balescu–Lenard equation (5.1) predicts the average evolution of the DF among different realisations with initial Poisson shot noise. It does not predict the evolution of a single (quiet start) N–body realisation.

(iii) The agreement between the prediction and the N–body measurement is more qualitative than quantitative. The predicted ridge and the measured one are not at the same location. The overall amplitude is claimed to be consistent, but the exact values are not given.

In the following, I address these points by investigating my own suite of N–body simulations and providing a new, more quantitative comparison with improved kinetic predictions.

6.2.2 Predictions *vs* average measurements

Computing the flux

The flux from equations (5.1) and (5.12) generically reads

$$\mathcal{F}(\mathbf{J}) = \sum_{\mathbf{k},\mathbf{k}'} \int \mathrm{d}\mathbf{J}'\, G_{\mathbf{k}\mathbf{k}'}(\mathbf{J},\mathbf{J}')\, \delta_{\rm D}[\mathbf{k}\cdot\mathbf{\Omega}(\mathbf{J}) - \mathbf{k}'\cdot\mathbf{\Omega}(\mathbf{J}')], \tag{6.13}$$

and similarly for the friction vector and diffusion tensor. For the Balescu–Lenard flux, the integrand function, $G_{\mathbf{k}\mathbf{k}'}$, reads

$$G^{\rm Flux}_{\mathbf{k}\mathbf{k}'}(\mathbf{J},\mathbf{J}') = \pi(2\pi)^d\, m\,\mathbf{k}\left|U^{\rm d}_{\mathbf{k}\mathbf{k}'}(\mathbf{J},\mathbf{J}',\mathbf{k}\cdot\boldsymbol{\Omega})\right|^2\left[\mathbf{k}'\cdot\frac{\partial F}{\partial\mathbf{J}'}\,F(\mathbf{J})-\mathbf{k}\cdot\frac{\partial F}{\partial\mathbf{J}}\,F(\mathbf{J}')\right], \tag{6.14}$$

and similarly for the Landau flux, with $U^{\rm d}\to U$. When neglecting collective effects, the Landau coupling coefficients can be computed independently of any bi-orthogonal basis (appendix 6.B.2). The friction vector and diffusion tensor take the same form with

$$G^{\rm Fric}_{\mathbf{k}\mathbf{k}'}(\mathbf{J},\mathbf{J}') = \pi(2\pi)^d\, m\,\mathbf{k}\left|U^{\rm d}_{\mathbf{k}\mathbf{k}'}(\mathbf{J},\mathbf{J}',\mathbf{k}\cdot\boldsymbol{\Omega})\right|^2\mathbf{k}'\cdot\frac{\partial F}{\partial\mathbf{J}'} \tag{6.15a}$$

$$G^{\rm Diff}_{\mathbf{k}\mathbf{k}'}(\mathbf{J},\mathbf{J}') = (2\pi)^{d+1}\, m\,\mathbf{k}\otimes\mathbf{k}\left|U^{\rm d}_{\mathbf{k}\mathbf{k}'}(\mathbf{J},\mathbf{J}',\mathbf{k}\cdot\boldsymbol{\Omega})\right|^2 F(\mathbf{J}') \tag{6.15b}$$

Each resonance contribution then corresponds to an integral of the form

$$\boldsymbol{\mathcal{F}}_{\mathbf{k}\mathbf{k}'}(\mathbf{J}) = \int\mathrm{d}\mathbf{J}'\,G(\mathbf{J}')\,\delta_{\rm D}[f(\mathbf{J}')], \tag{6.16}$$

where $f(\mathbf{J}')=\mathbf{k}\cdot\boldsymbol{\Omega}(\mathbf{J})-\mathbf{k}'\cdot\boldsymbol{\Omega}(\mathbf{J}')$. One has to perform integral along the resonance line $f(\mathbf{J}')=0$. In section 4.2.2, I have defined some resonance coordinates, (u,v), such that $u\propto\mathbf{k}\cdot\boldsymbol{\Omega}$ is constant along these resonance lines. Using these resonance coordinates, the resonance condition then reads

$$f(u',v') = \Omega_0\,\Delta_{\mathbf{k}'}\left(u_{\rm res}-u'\right), \tag{6.17}$$

with Ω_0 the frequency scale and $\Delta_{\mathbf{k}'}$ the half-range of the (dimensionless) resonant frequency (equation 4.11). In equation (6.17), I also introduced the resonant line

$$u_{\rm res} = \varpi_{\mathbf{k}'}(\mathbf{k}\cdot\boldsymbol{\Omega}/\Omega_0) \tag{6.18}$$

where $\varpi_{\mathbf{k}'}(\omega)$ follows from equation (4.15b). Performing the change of variables $\mathbf{J}'\to(u',v')$ in equation (6.16) and using the property $\delta_{\rm D}(\alpha x)=\delta_{\rm D}(x)/|\alpha|$, the flux ultimately reads

$$\boldsymbol{\mathcal{F}}_{\mathbf{k}\mathbf{k}'}(\mathbf{J}) = H(u_{\rm res})\int_{-1}^{1}\frac{\mathrm{d}v'}{\Omega_0\Delta_{\mathbf{k}'}}\left|\frac{\partial\mathbf{J}'}{\partial(u',v')}\right|G^{\rm Flux}_{\mathbf{k}\mathbf{k}'}[\mathbf{J},\mathbf{J}'(u_{\rm res},v')]. \tag{6.19}$$

In this equation, the rectangular Heaviside function, H, from equation (3.43), ensures that the resonance condition is satisfied. The friction and diffusion naturally follow using the G functions from equations (6.15).

I then need to sum over the pairs of resonance numbers, $\mathbf{k},\mathbf{k}'$. For discs, the coupling coefficients impose $k_\phi=k'_\phi=\ell$, with ℓ the considered harmonic number. Following Fouvry et al. (2015), I only consider the pairs of ILR, OLR and corotation resonances. In practice, I added both the contribution from the harmonics $\ell=2$ and $\ell=-2$. The rate of change of the DF, $\partial F/\partial t$, is the divergence w.r.t. actions of the flux (equation 5.2a). I compute this divergence using naive finite differences with the step distance, $\delta J_r=\delta L=10^{-3}$.

Small scale contribution Given the discussion in section 5.2.2, one might be worried by the contribution of the small-scale resonances. Indeed, from equation (5.17), the contributions should scale as

$$\frac{\partial F}{\partial t}\propto\sum_{k>0}\frac{1}{k^{d-2\gamma}}, \qquad \text{(recall 5.17)}$$

with $\gamma=1$ and $d=2$. This is algebraically divergent. It was already pointed out in Rybicki (1971) that the relaxation in razor-thin discs is of the order of the dynamical time, independently of the number of particles. Yet, in the experiments I considered, the disc is not fully self-gravitating:

part of the mean-field potential is given by a static halo. Furthermore, only the contributions from $\ell=2$ fluctuations are participating in the evolution of the system. Therefore, only the resonances with $k_\phi=k'_\phi=\ell$ contribute to the flux, which ultimately scales as $\partial F/\partial t\propto\sum_k 1/k$. This is still logarithmically divergent, as in the usual 3D Newtonian case (section 5.2.2). This divergence should be regularised properly and is not physical: it is a consequence of the linearisation of the fluctuations' evolution (equation 1.19b). In what follows, I focus on the low-order resonances only. This will be heuristically justified by the fact that, contrary to the 3D case, collective effects strongly enhance these long-range (resonant) interactions.

Results In figure 6.13, I present the results of my computations of the expected flux[2] from the inhomogeneous Balescu–Lenard equation (5.1) and Landau equation (5.12). As already pointed

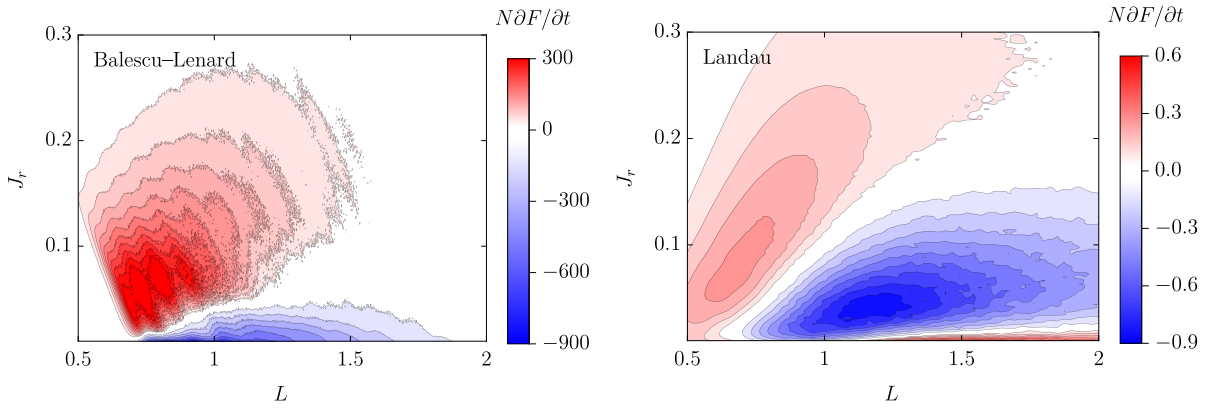

Figure 6.13: Predictions of the mean-field changes, $\partial F/\partial t$, from the inhomogeneous Balescu–Lenard equation (5.1) (left) and Landau equation (5.12) (right) for the long-term evolution of the Toomre disc (section 2.3.2) in action space. In this figure (and hereafter), the colour scheme is inverted compared to figures 6.11 and 6.12: red contours represent an increase in the number of particles, while blue contours indicate a depletion. Both predictions have their own scale as collective effects strongly enhance the orbital reshuffling. Indeed, the relaxation time predicted by the Balescu–Lenard theory, $T_{\rm BL}$, is three orders of magnitude shorter than the one predicted by the Landau theory, $T_{\rm Landau}$, i.e., $T_{\rm Landau}/T_{\rm BL}\sim1000$. Undoubtedly, collective effects can drastically alter the secular evolution of discs. Properly evaluating this collective dressing remains a particularly challenging task, as discussed in section 4.2.6.

out by F+15, the Balescu–Lenard flux is larger than the Landau one by three orders of magnitude. This collective amplification is at variance with the one-dimensional case (figure 6.1) and the highly magnetised HMF model (Benetti & Marcos, 2017) where collective effects considerably decelerate the relaxation. From equation (5.1), the secular flux involves the square of the dressed coupling coefficients and thus of the gravitational susceptibility, $\partial F/\partial t\sim|U^{\rm d}|^2\sim|\mathbf{N}(\mathbf{k}\cdot\boldsymbol{\Omega})|^2$ (equations 3.29 and 5.1). For this specific disc (half-mass Mestel $Q=1.5$), Toomre (1981) showed that collective effects are able to swing amplify the perturbations by a factor $|\mathbf{N}|\sim30$ (figure 7 therein). This is reassuringly consistent with the ratio of the dressed *vs* bare fluxes, $|\boldsymbol{\mathcal{F}}^{\rm BL}|/|\boldsymbol{\mathcal{F}}^{\rm Landau}|\sim10^3\sim|\mathbf{N}|^2$, in figure 6.13. It has been long known that cold discs are particularly prone to collective amplification (Goldreich & Lynden-Bell, 1965; Julian & Toomre, 1966). This amplification is even more striking here in the context of the collisional relaxation as it involves the square of the susceptibility.

Measuring the flux in simulations

I now set out to measure this flux in simulations. To do so, I used the same N–body code and sampling procedures as for the linear response of Zang discs (section 4.3). I performed 100 realisations of the Toomre disc, each with $N=25\times10^6$ particles. Each simulation was run for $t/t_{\rm dyn}=500$ with

[2]From now on, I abusively refer to the rate of change of the mean-field DF as the "flux", $\partial F/\partial t=-\nabla_{\mathbf{J}}\cdot\boldsymbol{\mathcal{F}}$.

a Plummer softening of $\varepsilon = 0.04$ (equation 4.22). A full snapshot is recorded every $t/t_{\rm dyn} = 100$. Each snapshot is post-processed using `OrbitalElements.jl` (section 4.2.3) to compute the particles' actions (J_r, L) and I simply count their number, $n(J_i, L_j)$, in bins of width $\delta J_r = \delta L = 0.01$. From these bin counts, the DF and its changes are obtained through

$$\begin{aligned} n(J_i, L_j) &= 4\pi^2 \frac{N}{M_{\rm tot}} \int_{J_i}^{J_i+\delta J_r} \int_{L_j}^{L_j+\delta L} \mathrm{d}J_r \, \mathrm{d}L \, F(J_r, L) \\ &\simeq 4\pi^2 \frac{N}{M_{\rm tot}} \delta J_r \delta L \, F(J_i, L_j), \end{aligned} \tag{6.20}$$

where the $4\pi^2$ prefactor comes from the integration over the angles (θ_r, θ_ϕ).

In figure 6.14, I present the flux averaged over the 100 N–body simulations I performed along with the Balescu–Lenard prediction from figure 6.13. The amplitude and the overall shape of

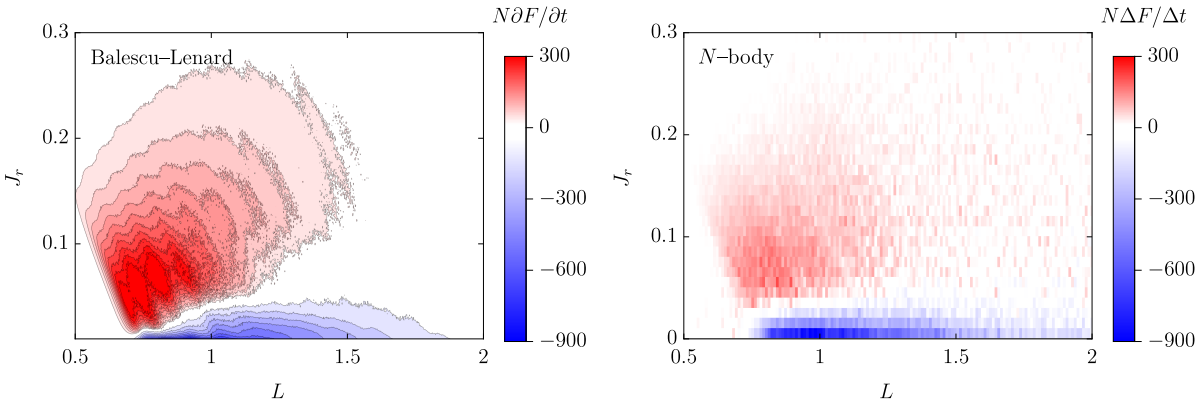

Figure 6.14: *Left:* Prediction of the mean-field changes, $\partial F/\partial t$, accounting for collective amplification (figure 6.13). *Right:* Flux measured in N–body simulations of the Toomre disc, averaged over 100 realisations with $N = 25\times10^6$ particles each. The changes in the DF are computed at $t/t_{\rm dyn} = 200$, before the phase transition to an unstable state. The prediction and measurement are found to be in good agreement, both in shape and most importantly in amplitude. Collective effects play a major role in the secular evolution of these simulations and accounting for them, albeit being a difficult task, is necessary to correctly describe their dynamical long-term evolution. This is one of the key results of this thesis.

the flux in the Balescu–Lenard case are consistent with the N–body measurements. The changes in the mean-field DF are computed as the difference between the initial bin counts and those at $t/t_{\rm dyn} = 200$. As illustrated in figure 6.15, this time is chosen so that the disc has not yet reached the phase transition to an unstable state.

Let me stress that such an agreement between the Balescu–Lenard theory and the N–body simulation was definitely not a given. The system is only marginally stable and supports weakly damped modes (section 4.2.6). This is typically a regime where one could expect some discrepancy between the Balescu–Lenard prediction and the measured relaxation rate (section 5.1.3).

With the results presented in this section, one could be tempted to conclude that the Balescu–Lenard theory works perfectly for the initial evolution of this disc and call it a closed case. Yet, a few questions remain.

(i) One may wonder why the flux is so much larger in the Balescu–Lenard case compared to the Landau one. Beyond the statement that collective effects enhance the fluctuations through swing amplification (Toomre, 1981), I wish to offer a new perspective on this question in section 6.2.3.

(ii) Comparing figures 6.10 and 6.15, one may notice that the instability develops earlier in my N–body simulations of $N = 25\times10^6$ particles than in S12's with $N = 5\times10^6$ particles. This

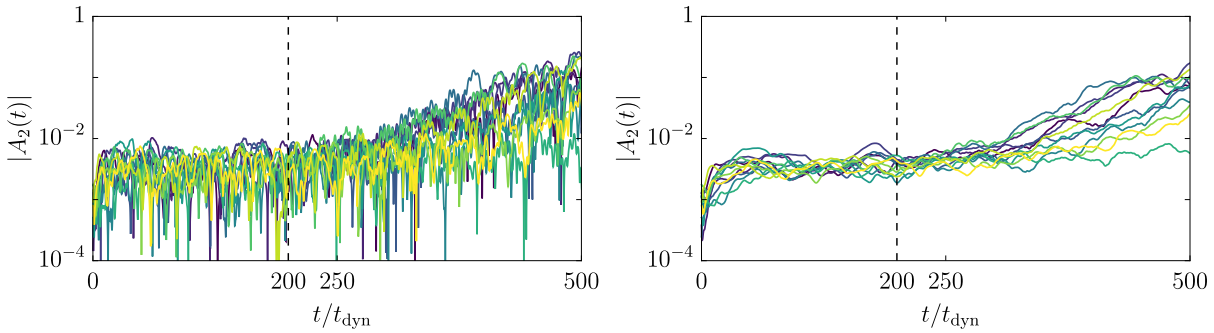

Figure 6.15: *Left:* Time evolution of the bisymmetric fluctuations (equation 4.27) in 12 different N–body realisations of the Toomre disc with same parameters ($N=25\times10^6$ particles, Plummer softening $\varepsilon=0.04$). *Right:* Same with a running average over 30 dynamical times. Similarly to figure 6.10, the system is initially stable and undergoes a slow relaxation towards an unstable state. The dashed line at $t/t_{\rm dyn}=200$ indicates the time at which the changes in the DF are recorded in figures 6.14 and 6.19.

seems inconsistent with the claim that the relaxation time is proportional to the number of particles, N. I will discuss this discrepancy in section 6.2.4.

(iii) The overall shape of the flux in my (averaged) N–body simulations and my Balescu–Lenard prediction do not look at all the same as the measurements of Sellwood (2012) in a single realisation and the prediction of Fouvry et al. (2015). This is the topic of section 6.2.5 below.

6.2.3 Damped modes and ridges

The collective amplification of the flux in Balescu–Lenard equation (5.1) is the direct consequence of the gravitational susceptibility, $\mathbf{N}$, from equation (3.18) through its contribution to the dressed coupling coefficients, $U^{\rm d}$ (equation 3.12). Phrased differently, the Balescu–Lenard kinetic theory accounts for the linear swing amplification of the fluctuations. To better understand the Balescu–Lenard flux from figure 6.13, it is therefore enlightening to analyse it together with the results from section 4.2.6 on damped modes in Toomre's disc.

In figure 6.16 I illustrate the expected flux from the Balescu–Lenard equation (5.1) on top of the associated linear susceptibility from section 4.2.6. To highlight the close link between damped modes and ridges, I present both the converged and partially converged susceptibilities and the associated fluxes. Degrading the convergence of the linear predictions, I showed in figure 4.15 that Toomre's disc has (at least) three weakly damped modes. Using this partially converged susceptibility, one can clearly see that each of these modes is at the origin of a sharp resonant ridge in the long-term evolution of the mean-field DF.

In this figure, the susceptibility contour plots are represented as a function of the angular momentum, L. The conversion between the pattern frequency, $\mathrm{Re}(\omega)$, and the angular momentum, L, is performed using the circular angular momentum corresponding to ILR frequency, i.e., $2\Omega_\phi(L)-\Omega_r(L)=\mathrm{Re}(\omega)$. At resonance with these modes' frequencies, stars are heated and move from circular orbits to more eccentric orbits and to different guiding centre. At ILR, this heating/churning does not change (much) the resonant frequency of the orbit which flows along the resonance line. Such a configuration is therefore particularly efficient at heating the disc. The flux presented in figure 6.13 did not show such clear ridges. As illustrated in the right panel of figure 6.16, this is consistent with the associated linear response from figure 4.14.

Interestingly, Sellwood (2012) observed the power-spectra of fluctuations as a function of the radius during his long-term simulation. In the resulting figure 4, reproduced here in figure 6.17, he highlighted the presence of three peaks in the power-spectra, in the early stage of the simulation, i.e., before the appearance of any instability. These peaks are localised at their respective ILR

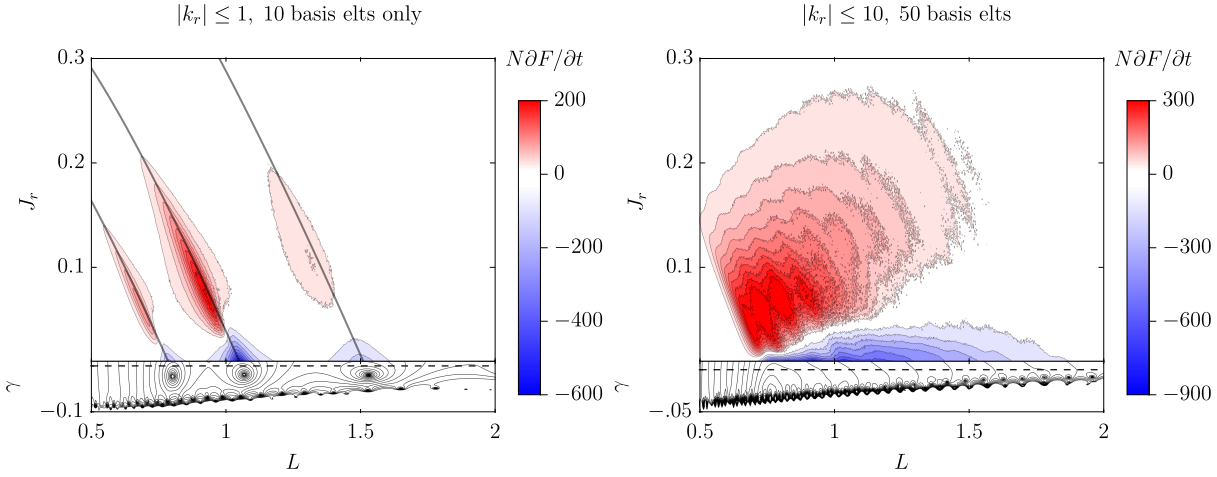

Figure 6.16: *Left:* Illustration of the link between linear damped modes (bottom) and secular ridges (top) in the long-term evolution of discs. The damped modes obtained in figure 4.15 are represented at the circular angular momentum corresponding to their ILR, $2\Omega_\phi(L)-\Omega_r(L)=\Omega_{\rm M}$. *Right:* Same as the left panel but with the susceptibility from figure 4.14 using more basis elements and resonances to ensure numerical convergence. The accuracy of the Balescu–Lenard prediction is directly linked to the (slow) convergence of the linear susceptibility. The damped modes are fully responsible for the ridges observed in the predicted flux. Near marginal stability, the secular heating of the disc is strongly enhanced at resonance with the underlying weakly damped modes. This is particularly strong at the ILR because (i) the pattern speed corresponds to populated locations in the disc and (ii) the flux direction is aligned with the resonance line (black line), i.e., stars stay at resonance with the mode albeit being pushed away on more eccentric orbits. This figure is one of the key results of this thesis.

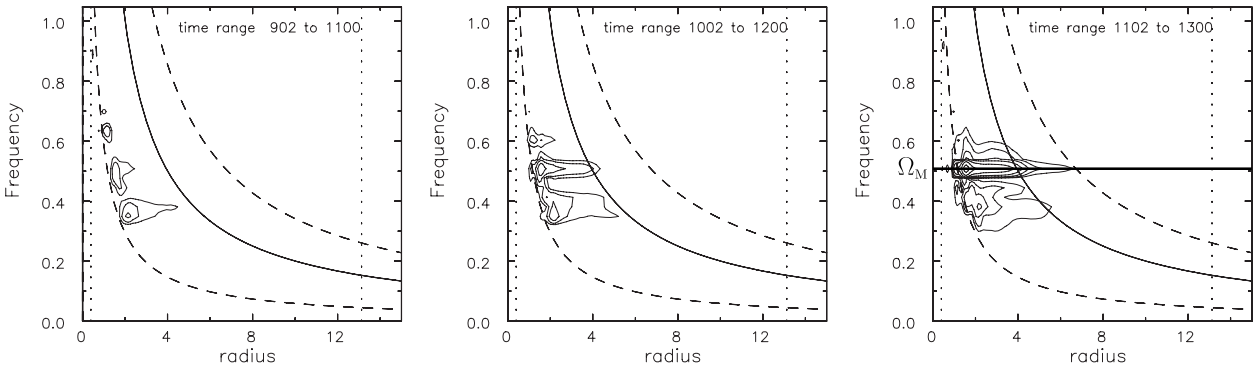

Figure 6.17: Figure from Sellwood (2012). Illustration of the presence of weakly damped modes in N–body simulations of Toomre's disc. Power-spectra of the $\ell=2$ fluctuations as a function of radius. The presence of 3 peaks in the early power-spectra, localised at their respective ILR radius, might be the signature of the presence of weakly damped modes. Later, the DF has been destabilised by the groove/ridge created at resonance with one of these modes and the power-spectra is dominated by the instability.

radius. They might be the signature of weakly damped modes. While their number is tentatively comparable to my results from figure 4.15, I do not claim that they should be quantitatively compared. Indeed, my predictions in the left panel of figure 6.16 have been purposely degraded to illustrate the presence of these modes. Improving the generic linear computations (section 4.5) would be necessary to perform a more quantitative comparison. One could also investigate the method used by Heggie et al. (2020) to probe the damped mode predicted by Weinberg (1994) in spherical King's models.

6.2.4 Impact of softening

I have shown in section 4.3.2, that softening the gravitational interaction affects the location of (unstable) modes. In the previous section 6.2.3, I discussed the close link between (weakly) damped modes and the secular evolution of the DF. It is therefore natural to investigate the impact of softening on this long-term evolution. In particular, as Plummer softening tends to shift modes towards lower pattern speed and growth rate (figure 4.16), I would expect the ridge(s) to (i) appear later and (ii) move towards higher angular momentum in simulations with a larger softening length. I set out to investigate these hypotheses in numerical simulations. I ran long-term simulations of Toomre's disc with Plummer softening (equation 4.22) for different softening lengths. The results presented in the previous sections were all obtained using the smallest softening length, $\varepsilon = 0.04$.

In figure 6.18, I illustrate the long-term evolution of bisymmetric fluctuations using the projection coefficient, $|A_2(t)|$, from equation (4.27). It is clear that softening weakens the secular

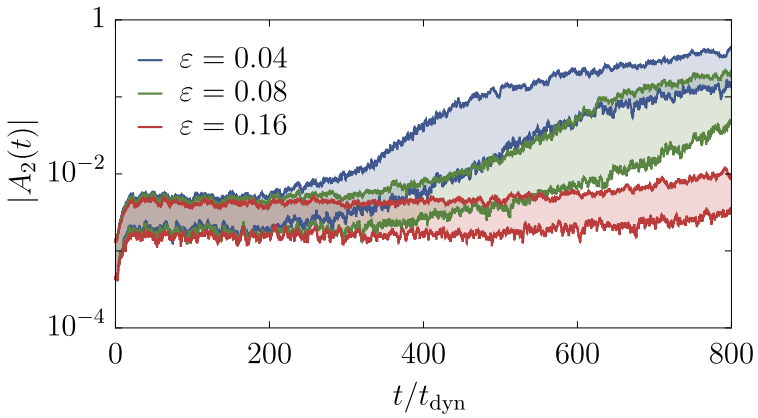

Figure 6.18: Illustration of the impact of Plummer softening on the simulated long-term evolution of discs. Power in the bisymmetric fluctuations (section 4.3.3) as a function of time. For each softening value (colour) the bottom (resp. top) line corresponds to the lowest 20% (resp. largest 80%) instantaneous values of the bisymmetric coefficient, $|A_2(t)|$ from equation (4.28). The statistics are performed among 100 different realisations of $N = 25\times10^6$ particles (same initialisations for different softening values). As expected from Sellwood (2012)'s results, the disc first undergoes a slow relaxation before entering a linearly unstable regime. The larger the softening length, the slower the relaxation, and the more delayed the phase transition. This is one of the key results of this thesis.

relaxation and delays phase transition. Note that it would also happen if the relaxation was driven by two-body local encounters (Theis, 1998). However, local encounters are ruled out in these experiments as I only considered global, $\ell = 2$, fluctuations. I claim that, here, the phase transition is delayed because the softening affect the collisionless properties of the disc and consequently its (collisional) dressed resonant relaxation. Phrased differently, the softening makes the disc more (linearly) stable than it should be. Consequently, softening reduces swing amplification and ultimately delays the relaxation of the disc towards an unstable configuration.

In particular, this explains the discrepancy in the time of phase transition between S12's simulations (figure 6.10) and mine (figure 6.15). Indeed, S12 used a larger softening length, $\varepsilon = 0.125$, than mine, $\varepsilon = 0.04$. In his simulation of $N = 5\times10^7$ particles, the instability sets in at $t/t_{\rm dyn} \sim 1200$. This is consistent with my results (figure 6.18) where the instability sets in at $t/t_{\rm dyn} \sim 400$ (resp. 800) for $\varepsilon = 0.8$ (resp. 0.16) using $N = 25\times10^6$ particles.

To further substantiate my claim, it would be enlightening to simulate this long-term evolution using Kuzmin softening kernel (equation 4.23). In section 4.3.2, I showed that this softening was able to preserve the collisionless properties of the unstable Zang disc. I therefore expect it not to affect the long-term simulations of razor-thin disc for a wide range of softening lengths. Let me finally note that, as already mentioned in footnote 7, the Plummer softening kernel has a physical interpretation in razor-thin disc simulations (Sellwood, 2014). The associated softening length can

be set to mimic the finite thickness of the realistic disc. Yet, to compare quantitatively N–body simulations and theoretical predictions, either from linear response or kinetic theory, one should be aware of the bias that softening introduces.

6.2.5 Stochastic ridges

The last point I raised in section 6.2.2 is the discrepancy between on one side the average flux measured in my kinetic predictions and simulation results and on the other side the predictions of F+15 and the simulations of S12.

Predictions First, let me start with the kinetic predictions. Following section 6.2.3, the source of the discrepancy between my Balescu–Lenard prediction and that from F+15 obviously lies in the computation of the polarisation matrix. The computation of the associated Balescu–Lenard flux was performed very similarly in the two cases, summing over the same pairs of resonances (pairs of ILR, corotation and OLR only). Beyond the care one should take on the overall prefactor, these computations are intensive but are not specifically challenging. The only fundamentally difficult part is the computation of the dressed coupling coefficients, U^{d}, and more precisely the computation of the polarisation matrix, $\mathbf{M}$ (equation 3.28). As visible in figure 6.16, the shape and amplitude of the Balescu–Lenard flux is closely linked to the shape and amplitude of the linear susceptibility. F+15 used a different bi-orthogonal basis (Kalnajs, 1976) to compute the polarisation matrix. This basis is defined through relatively unstable recurrence relations so that they only used 9 basis functions. Furthermore, they computed the resonant integral from equation (3.28) directly in apocentre and pericentre coordinates. They were therefore unable to evaluate the polarisation matrix at real frequencies and used values slightly above the real axis. All these elements together lead me to believe that their polarisation matrix was not converged.[3]

Simulations On the other hand, the discrepancy between my N–body simulations and S12's is more interesting to address. There are two important differences between our simulations. The first one is the softening length, $\varepsilon = 0.04$ for me and $\varepsilon = 0.125$ for S12 (same Plummer softening kernel from equation 4.22). The second one is that my N–body figure 6.14 is an average over 100 realisations randomly sampled while S12's N–body result (figure 6.11) is a single realisation with quiet start initial conditions.

The Balescu–Lenard equation (5.1) provides a prediction for the average evolution among different realisations, i.e., different initial conditions drawn from the same mean-field DF. This is the reason why I performed multiple realisations as was done for the one-dimensional system (section 6.1). From figure 6.15, one can already spot that the evolution of the fluctuations significantly varies from one realisation to another.[4] It is therefore of interest to investigate the impact of the intrinsic stochasticity among different realisations on the secular evolution of discs. To do so, I represent in figure 6.19 the flux measured in 12 different realisations of the Toomre disc. These realisations are those whose fluctuations are represented in figure 6.15. The time at which the changes in the DF are recorded is the same as in figure 6.14, i.e., $t/t_{\mathrm{dyn}} = 200$.

The first thing to notice is that individual realisations are very different from the averaged one. In the averaged flux (figure 6.14), all the circular orbits with $0.75 \lesssim L \lesssim 1.5$ are depopulated in profit of more eccentric orbits. In each individual realisation, the changes in the DF are much more localised. The changes are concentrated along one or multiple sharp ridges. These ridges

[3] I did compute the polarisation matrix using the same parameters as F+15 but using the Legendre method presented in section 3.3.3. I found that Toomre's disc was predicted to be unstable. This is also a problem I encountered when using too few Clutton-Brock (1972)'s basis functions without reducing the number of resonances.

[4] These variations are larger than the ones reported by Sellwood (2020). However, he did perform only two different realisations and used a quiet start sampling procedure.

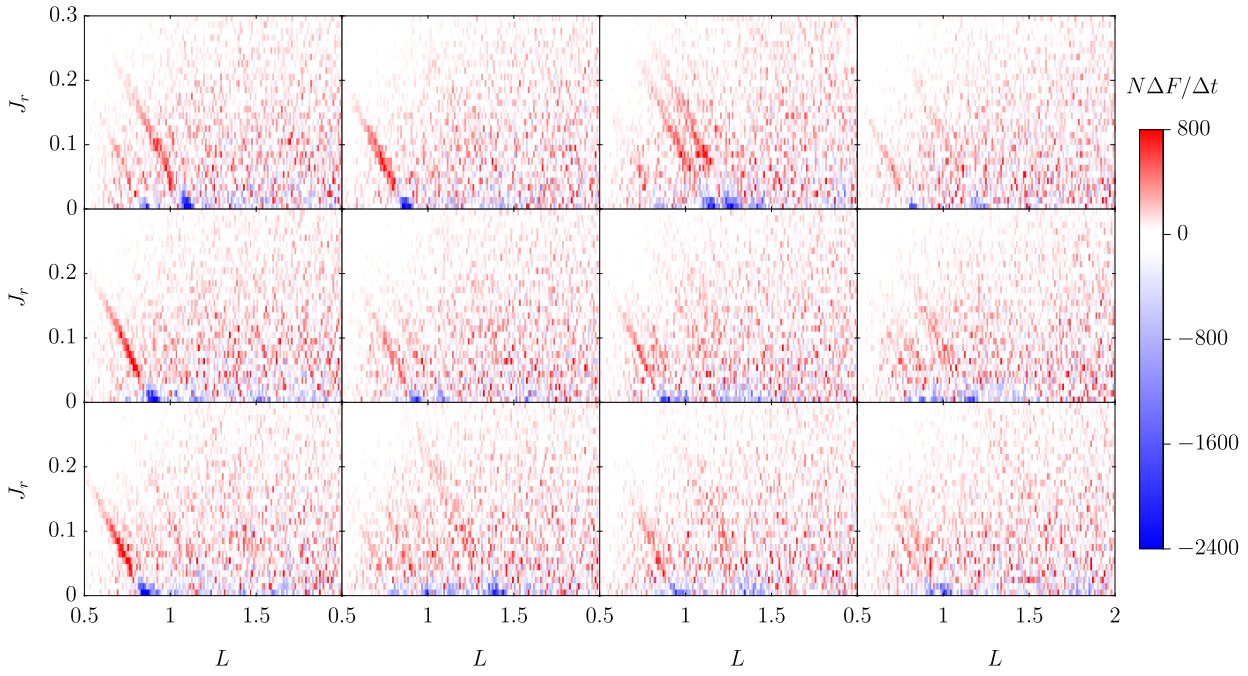

Figure 6.19: Illustration of the stochasticity of the long-term evolution of marginally stable discs. Flux measured in 12 individual realisations of the Toomre disc, with $N = 25 \times 10^6$ particles each. As for the averaged flux in figure 6.14, the changes in the DF are measured at $t/t_{\rm dyn} = 200$, i.e., before the phase transition to an unstable state. The number and location of the ridges strongly varies from one initialisation to another, and they do not appear simultaneously. This is one of the key results of this thesis.

come in different number, locations and at different time/amplitude in each realisation. Note that their individual intensity is up to 2-3 times larger than the averaged one.

The inhomogeneous Balescu–Lenard equation (5.1) is, by design, unable to predict such a diversity as it is an average prediction. Predicting the scatter among different realisations is the purpose of the large deviation theory (Bouchet, 2020; Feliachi & Bouchet, 2021). Recent advances have been made in this direction for inhomogeneous systems while neglecting collective effects (Feliachi & Fouvry, 2023). Self-gravity has been taken into account in the large deviation theory of homogeneous systems (Feliachi & Bouchet, 2022). However, the inclusion of collective effects in the large deviation theory of inhomogeneous systems is still an open question.

On a more speculative note, it is interesting to notice that the scatter in results from different initial conditions is particularly large in this system near marginal stability. From the right panel of figure 6.15, it seems to increase as the disc approaches the phase transition. This highlights the importance of averaging over many realisations to study reliably the secular evolution of marginally stable discs. The origin of this stochasticity is still to be understood.

6.3 Conclusion

In this chapter, I presented applications of the Balescu–Lenard kinetic theory from chapter 5 to the secular evolution of the one-dimensional and razor-thin self-gravitating systems. I showed that the inhomogeneous Balescu–Lenard equation (5.1) is able to quantitatively predict the mean long-term evolution of these systems. The kinetic predictions were compared with N–body simulations once averaged over many realisations in action space. Doing so, I highlighted the importance of resonant encounters and collective effects in driving the relaxation of stellar systems.

The consequences of self-gravity proved to be particularly diverse and would have been difficult to predict *a priori* without the valuable insights provided by the Balescu–Lenard kinetic theory. In the one-dimensional system, I showed in figure 6.1 that collective effects can drastically slow down the diffusion. Self-gravity stiffens the system making it less responsive to perturbations. Furthermore, even out of (thermal) equilibrium, the system suffers from a quasi kinetic blocking, further delaying its relaxation (figure 6.8). This at variance with the situation for cold razor-thin discs (figure 6.13) where collective effects strongly enhance the orbital reshuffling.

In such marginally stable systems, fluctuations get strongly swing amplified at resonance with the underlying weakly damped modes (figure 6.16). The secular evolution therefore is particularly sensitive to the collisionless linear response of the disc. By stabilizing the disc, I showed that softening delays the phase transition to an unstable state (figure 6.18). Finally, I noted that, in this regime, the average flux is not representative of the individual realisations (figure 6.19): the variance among different initial conditions get increasingly large as the disc approaches the phase transition.

6.4 Perspectives

Among the most pressing improvements to the work presented in this chapter, I would like to highlight (i) the need for a regularised treatment of marginal stability and small scales in the Balescu–Lenard kinetic theory and (ii) the importance of accounting for the intrinsic stochasticity of the secular evolution of weakly stable systems.

On the first point, the kinetic predictions diverge at small scales (section 5.2.2) and at phase transition (section 5.1.3). Chandrasekhar did regularise the deflections at small scales taking hard encounters into account. This regularisation should be adapted to the resonant (inhomogeneous) Landau and Balescu–Lenard kinetic theory. Ultimately, this regularisation would enable the appropriate comparison of the impact of small *vs* large scales on the secular relaxation of self-gravitating systems. Of course, the respective contributions would vary depending on the geometry and the kinematics. In the one-dimensional (section 6.1) and HMF (Benetti & Marcos, 2017) models, the pairwise interaction potential favours the latter. The usual 3D Newtonian potential (equation 2.3) favours the former in dynamically hot systems such as globular clusters (Fouvry et al., 2021). In colder configurations such as thin galactic discs, the dressing of the long-range interactions by collective effects could dominate, but this remains to be accurately quantified.

Similarly, the divergence of the Balescu–Lenard at marginal stability is particularly worrying as (isolated) discs are driven towards phase transition by collisional relaxation (section 6.2.1). This divergence should be regularised by considering the contribution of wave-particle interactions, in the spirit of the so-called quasilinear theory in plasma physics (see, e.g., Rogister & Oberman, 1968; Hamilton & Heinemann, 2020).

On the second point, individual realisations do evolve very differently (figure 6.19). This large variance among different initial conditions is particularly striking near marginal stability. Capturing this intrinsic stochasticity is beyond the scope of the Balescu–Lenard kinetic theory. The large deviation theory is a promising avenue to estimate this variance (Bouchet, 2020; Feliachi & Bouchet, 2021). However, the inclusion of collective effects in the large deviation theory of inhomogeneous systems and its effective computation are still open questions.

Beyond these deep theoretical challenges, a few more practical improvements and investigations could be performed. In particular, it would be rewarding to transpose Zang's method to the computation of dressed coupling coefficients for a more accurate secular prediction in discs. This would notably allow one to accurately quantify the convergence of the present generic method. It could also be interesting to investigate the impact of the softening kernel on the secular evolution of weakly stable discs (section 6.2.4).

Appendices

6.A One-dimensional simulations

This appendix is reproduced from Roule et al. (2022). It details the numerical methods I used to perform the N–body simulations of the one-dimensional systems studied in this thesis.

The system's total Hamiltonian is

$$H_{\rm tot} = \sum_{i=1}^{N} \tfrac{1}{2} m_i v_i^2 + \sum_{i<j} m_i m_j \, U(x_i, x_j), \quad (6.21)$$

so that the equations of motion for particle i read

$$\dot{x}_i = v_i, \quad \dot{v}_i = G\left(M_i^{\rm r} - M_i^{\rm l}\right), \quad (6.22)$$

with $M_i^{\rm r}$ (resp. $M_i^{\rm l}$) the total mass on the right (resp. on the left) of particle i. Importantly, by sorting the set $\{x_i\}$, one can compute these cumulative masses in a single pass. Determining the (exact) instantaneous forces on all particles requires therefore $\mathcal{O}(N \ln N)$ operations.

The present one-dimensional system can be integrated exactly using a collision-driven scheme (Noullez et al., 2003). However, this approach requires $\mathcal{O}(N^2 \ln N)$ operations per dynamical time, making long-time integrations of large-N systems too challenging. As such, I rather settle on using an approximate time integrator (with exact forces). Because equation (6.21) is separable, one can use standard splitting methods (see, e.g., Hairer et al., 2006) to devise integration schemes. The main source of error comes from the abrupt force changes every time particles cross, making it wiser to limit oneself to low-order schemes. I use the standard leapfrog scheme (see, e.g., Sec. 3.4.1 in Binney & Tremaine, 2008) which requires a single (costly) force evaluation per timestep, δt, and an overall $\mathcal{O}(N \ln N \, t_{\rm dyn}/\delta t)$ operations per dynamical time.

In figure 6.20, I check the sanity of the integration algorithm, by illustrating the conservation of the total energy, $E_{\rm tot}$, as one varies the timestep δt, the number of particles, N, and the overall number of integration time steps, $t/\delta t$.

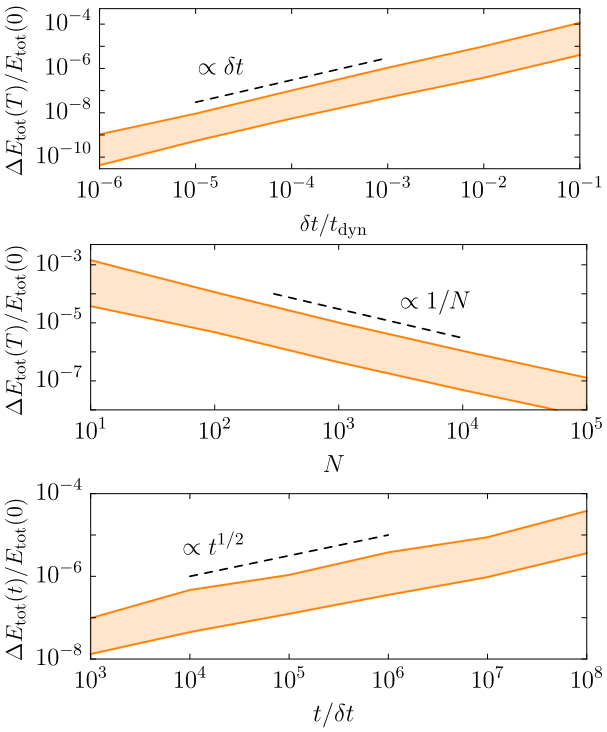

Figure 6.20: Relative error in the system's total energy, $E_{\rm tot}$, as a function of (i) the timestep δt (with $N = 10^4$, $T/t_{\rm dyn} = 100$), (ii) the number of particles N (with $\delta t/t_{\rm dyn} = 10^{-3}$, $T/t_{\rm dyn} = 100$), (iii) the total number of integration steps $t/\delta t$ (with $N = 10^4$, $\delta t/t_{\rm dyn} = 10^{-3}$).

Because the pairwise interaction, $U(x, x')$ from equation (2.1), does not have a continuous derivative, the leapfrog scheme is only first-order accurate, i.e., its error scales like $\mathcal{O}(\delta t)$ after a fixed finite time (top panel). As one increases N, these discontinuities weaken, so that the error at finite time scales like $\mathcal{O}(1/N)$ (central panel).

Finally, for the present explicit scheme, I empirically find that the error in $E_{\rm tot}$ grows like $\sqrt{t}$ as a function of time (bottom panel).

To prevent the N–body realisations from drifting away, I systematically perform the operation $v_i \leftarrow v_i - \sum_{i=1}^{N} m_i v_i / M_{\rm tot}$ at the simulation's onset, hence setting the system's total momentum to zero. Such a recentring slightly blurs the effective DF in velocity space (and therefore in energy) by an amount proportional to $1/\sqrt{N}$. To mitigate this effect, I always chose values of N large enough, typically $N = 10^5$.

In the Landau simulations (chapter 6), I introduce two types of particles: (i) massive background particles that follow the smooth mean potential, and (ii) massless test particles driven by the instantaneous (noisy) potential generated by the background particles. While the background particles follow the unperturbed mean-field orbits, the orbits of the test particles are slightly altered by the bare potential fluctuations in which they are embedded. The orbital diffusion undergone by these test particles corresponds to the (undressed) Landau diffusion. Such simulations only keep track of the Landau diffusion. They do not mimic the Landau flux as massless test particles do not undergo any friction (Nelson & Tremaine, 1999).

6.B Bare coupling coefficients

Only considering the initial Poisson noise (finite-N) effects, not dressed by collective effects, there is a much easier way to compute the diffusion coefficients. The bare susceptibility coefficients from equation (3.4) can notably be computed independently of any basis element.

6.B.1 One-dimensional model

In the 1D case, using the effective anomaly w introduced for angle-action computation (equation 2.7), they take the simple form

$$U_{kk'}(J, J') \propto \int_{-1}^{1} \mathrm{d}w \mathrm{d}w' g(x) g(x') U(x, x'), \quad (6.23)$$

with $g(x) = \frac{\mathrm{d}\theta}{\mathrm{d}w} \cos(k\theta)$. Note that symmetry imposes $U_{kk'}(J, J') = 0$ for any k, k' of different parity, as illustrated in figure 6.3. Sampling uniformly the anomalies w, w' using K nodes (per anomaly) and following the mid-point rule, equation (6.23) becomes

$$U_{kk'}(J, J') \propto \frac{1}{K^2} \sum_{i,j=1}^{K} g_i g'_j U(x_i, x'_j), \quad (6.24)$$

where the $g_i = g(x_i)$ and $g'_j = g(x'_j)$ are precomputed using direct integration of $\mathrm{d}\theta/\mathrm{d}w$. This computation only has to be made once, and can be made in $\mathcal{O}(K)$ steps.

A naive reading of equation (6.24) could lead us to believe that the computation of $U_{kk'}(J, J')$ requires $\mathcal{O}(K^2)$ steps. Fortunately, this can be made in $\mathcal{O}(K)$ steps, owing to the (almost separable) form of the pairwise interaction potential

$$\begin{aligned} U(x, x') &\propto |x - x'| \\ &= \begin{cases} (x - x') & \text{if } x > x', \\ (x' - x) & \text{if } x < x'. \end{cases} \end{aligned} \quad (6.25)$$

This allows me to expand equation (6.24) and rewrite the sums over i and j into a unique sum of cumulative terms to be computed on the fly. It reads

$$U_{kk'}(J, J') = \frac{4G}{\pi^2 K^2} \sum_{j=1}^{K} g'_j \left(P_j + Q_j\right), \quad (6.26)$$

with the cumulative sums

$$P_j = \sum_{i=1}^{w_j} g_i \left(x'_j - x_i\right), \; Q_j = \sum_{i=w_j+1}^{K} g_i \left(x_i - x'_j\right), \quad (6.27)$$

and $w_j = \mathrm{Card}\{i \in [\![1, K]\!] \,|\, x_i \leq x'_j\}$. Importantly, P_j and Q_j can both be computed in a single pass, requiring overall $\mathcal{O}(K)$ operations to estimate $U_{kk'}(J, J')$. Such algorithmic technicalities are key to provide efficient and trustworthy predictions of the bare coupling coefficients.

Therefore, I now have an easy and precise way to compute the bare susceptibility coefficients without resorting to any biorthogonal basis. This has also been useful as an element of comparison for the bare susceptibility coefficients computation using the bi-orthogonal basis through equation (3.26) allowing me to validate *a posteriori* my methods.

6.B.2 Razor-thin discs

Similarly, for the razor-thin discs, the bare susceptibility coefficients can be computed directly

from equation (3.4) without any need for a basis. For a given harmonic number ℓ, they read

$$U^{\ell}_{\mathbf{k}\mathbf{k}'}(\mathbf{J},\mathbf{J}') = \frac{\delta^{\ell}_{k_\phi}\delta^{\ell}_{k'_\phi}}{\pi^2}\int_0^\pi \mathrm{d}\theta_r \int_0^\pi \mathrm{d}\theta'_r\, U^{\ell}(r,r') \times \cos[k_r\theta_r + k_\phi(\theta_\phi - \phi)] \times \cos\left[k'_r\theta'_r + k'_\phi(\theta'_\phi - \phi')\right], \quad (6.28)$$

where $U^{\ell}(r,r')$ stands for the Fourier transform w.r.t. the configuration angle difference $\Delta\phi = \phi - \phi'$ of the interaction potential. Using the parity of the interaction potential

$$U(r,r',\Delta\phi) = \frac{-G}{\sqrt{r^2 + r'^2 - 2rr'\cos\Delta\phi}}. \quad (6.29)$$

w.r.t. this angle difference, it reads,

$$U^{\ell}(r,r') = \frac{1}{\pi}\int_0^\pi \mathrm{d}\gamma\, U(r,r',\gamma)\cos(\ell\gamma), \quad (6.30a)$$

$$= \frac{-G}{\overline{r}}\frac{{}_3\tilde{F}_2\left[(\frac{1}{2},\frac{1}{2},1),(1-\ell,1+\ell),2a/(1+a)\right]}{\sqrt{1+a}}, \quad (6.30b)$$

where $\overline{r} = \sqrt{r^2 + r'^2}$, $a = 2rr'/\overline{r}^2$ and ${}_3\tilde{F}_2$ is the regularised (generalised) hypergeometric function. This integral diverges for $r = r'$. In practice, this divergence is to be integrated over through equation (6.28). However, to avoid numerical instabilities, I regularise the potential by using the Plummer softened potential, U_ε from equation (3.30), with $\varepsilon = 10^{-5}$. For this softening kernel, the expression of $U^{\ell}_{\varepsilon}(r,r')$ is still given by equation (6.30b), with $\overline{r} = \sqrt{r^2 + r'^2 + \varepsilon^2}$.

The double integral in equation (6.28) can be computed using a simple middle point rule and the computation of the bare susceptibility coefficients can be made in $\mathcal{O}(K^2)$ steps, where K is the number of nodes per angle. Unfortunately in this case, the separability of the interaction potential is lost. As a sidenote, this is because $1/r$ is not a "harmonic" interaction in 2D, i.e., it is not a solution of Laplace equation. The computation of the bare susceptibility coefficients is therefore more costly than in the 1D case. However, it still provides a good benchmark for the computation of the bare susceptibility coefficients using the biorthogonal basis (equation 3.26).

The analytic expression in equation (6.30b) could also prove useful for the computation of softened basis elements for razor-thin discs. To design softened basis elements, following section 3.2.4, one mainly has to compute the cross-product matrix from equation (3.32). For razor-thin bases, different azimuthal harmonics are decoupled. For a given harmonic number, ℓ, the cross-product matrix reads

$$C^{\ell}_{pq} = -(2\pi)^2 \int \mathrm{d}r\mathrm{d}r'\, rr'\, U^{\ell}_{\varepsilon}(r,r') \times D^{p\ell}(r)\, D^{q\ell}(r'), \quad (6.31)$$

with U^{ℓ}_{ε} the Fourier transform of the softened potential from equation (6.30a).

Chapter 7

Kinetic blockings

In this chapter, I revisit the results we published in Fouvry & Roule (2023), hereafter FR23. For this article, I contributed to the interpretation of the results, i.e., the understanding of the relaxation scalings, the plan and the writing of the paper. The numerical simulations were performed by the first author. Their detailed description is not reproduced here but can be found in appendix E of FR23.

In some particularly contrived set-ups, the inhomogeneous Balescu–Lenard equation (5.1) can exactly vanish, i.e., predict no evolution for the mean-field distribution F. This is a *kinetic blocking* (Eldridge & Feix, 1963; Chavanis, 2001; Dubin, 2003; Bouchet & Dauxois, 2005; Chavanis & Lemou, 2007; Gupta & Mukamel, 2011; Barré & Gupta, 2014; Lourenço & Rocha Filho, 2015). For these systems, a higher-order kinetic equation needs to be derived to capture the evolution of the mean-field distribution. Such an equation has recently been derived and tested by Fouvry (2022), in the dynamically hot limit where collective effects can be neglected. While the Landau and Balescu–Lenard equations presented in chapter 5 capture (linearised) two-body interactions and scale as $1/N$, this second-order equation involves three-body interactions and scales as $1/N^2$. I will therefore refer to it as the (inhomogeneous) $1/N^2$ Landau equation. Taking collective effects into account in this regime, i.e., deriving the $1/N^2$ Balescu–Lenard equation, is yet to be achieved (even in the homogeneous regime).

Interestingly, Fouvry (2022) pointed out the existence of a class of interaction potentials for which the inhomogeneous $1/N^2$ Landau equation also exactly vanishes – whatever the considered mean DF. It is a second-order *bare* kinetic blocking, where *bare* emphasises here that this blocking only holds in the limit where collective effects are neglected.

In this chapter, I will first present a specific set up in which these various blockings can occur. I will then sketch the kinetic equations at play and discuss the implications of these blockings on the system's evolution. Finally, I will present numerical investigations of these regimes, highlighting the impossibility of a second-order *full* kinetic blocking. Hence, I will claim that the evolution of self-gravitating systems is at most driven by three-body interactions, and that the $1/N^2$ Balescu–Lenard equation is the highest-order kinetic equation which still needs be derived.

7.1 Blocked systems

For the two-body collision operator, i.e., the r.h.s., to vanish in equation (5.1) whatever the considered DF, the system must:

- live in a one-dimensional position space (two-dimensional phase space),
- have a monotonic frequency profile,
- only support 1:1 resonances, i.e., impose $k = k'$ in the Fourier expansion of the interaction

potential,

$$U(\theta, J, \theta', J') = \sum_{k,k'} \delta_k^{k'} U_k(J, J')\, \mathrm{e}^{\mathrm{i}(k\theta - k'\theta')}. \tag{7.1}$$

Taken together, these conditions ensure that the only orbit satisfying the resonance condition in equation (5.1) is the considered orbit itself. Such a local resonant coupling cannot contribute to any change in the DF, as already highlighted in section 6.1.2.

For this chapter, I will directly use angle-actions as the base 1D canonical (specific) phase space coordinates, $\mathbf{w}=(\theta, J)$, without reference to the usual position-velocity configuration space. The angle θ is to be considered as a 2π-periodic position and the associated action J as a momentum. They are not "instantaneous" angle-action coordinates self-consistently constructed from the current DF. Indeed, these coordinates are rather defined initially, once and for all, from the mean external potential.

Let me consider that the system's evolution is driven by the total specific Hamiltonian

$$H = \sum_{i=1}^{N} U_{\mathrm{ext}}(\mathbf{w}_i) + \sum_{i<j}^{N} \mu\, U(\mathbf{w}_i, \mathbf{w}_j), \tag{7.2}$$

with $U_{\mathrm{ext}}(\mathbf{w})$ some given external potential and $U(\mathbf{w}, \mathbf{w}')$ some pairwise interaction potential, whose typical amplitude is denoted G. In practice, the symmetry $U(\mathbf{w}, \mathbf{w}')=U(|\theta-\theta'|, \{J, J'\})$ is assumed. This choice also ensures the usual conservation laws (see appendix E1 in FR23), namely of the total energy and total momentum. Furthermore, the pairwise interaction potential is taken to have no mean-field contribution whatever the angle-independent DF, i.e., it vanishes once averaged over the angles. Phrased differently, $U_{00}(J, J')=0$ in equation (3.4). Therefore, the mean-field potential is fully imposed by the external potential, $U_{\mathrm{ext}}(\mathbf{w})$. Setting a mean-field equilibrium then amounts to choosing an external potential, or equivalently a frequency profile, $J \mapsto \Omega(J)$.

This system is said to be inhomogeneous because the pairwise interaction does depend on the particles' actions.[1] In addition, the Fourier expansion of the pairwise interaction is assumed to be $U(\mathbf{w}, \mathbf{w}')=\sum_{k,k'} \delta_k^{k'} U_k(J, J')\mathrm{e}^{\mathrm{i}k(\theta-\theta')}$. Here, the Kronecker symbol, $\delta_k^{k'}$, imposes $k=k'$. The system only sustains 1:1 resonances; this is a necessary condition for the first-order full kinetic blocking to occur. The shortened notation for the Fourier coefficients is to be understood as $U_k(J, J')=U_{kk}(J, J')$ from the usual notations introduced in equation (3.4).

In FR23, we focused on one particular interaction potential, namely equation (D6) in Fouvry (2022). This interaction potential reads[2]

$$U(\mathbf{w}, \mathbf{w}') = G\,(J-J')^2\, \mathcal{B}_2[\theta-\theta'], \tag{7.3}$$

with $\mathcal{B}_2(\theta)=B_2[\frac{1}{2\pi} w_{2\pi}(\theta)]$, $B_2(x)=x^2-x+\frac{1}{6}$, the second Bernoulli polynomial, and the angle "wrapping function"

$$0 \leq w_{2\pi}(\theta) < 2\pi; \quad w_{2\pi}(\theta) \equiv \theta\ [2\pi]. \tag{7.4}$$

The function $\mathcal{B}_2(\theta)$ is illustrated in figure 7.1. As discussed, the interaction potential averages to zero over angles, i.e., $\int \mathrm{d}\theta \mathcal{B}_2[\theta]=0$, so that $F(J)$ never generates any mean potential. Mean field quantities such as the frequency profile are therefore fully determined by the external potential $U_{\mathrm{ext}}(\mathbf{w})$.

We focused on this specific interaction potential because it allows all kinetic regimes to be reviewed by varying the mean-field potential. Other known systems with more standard interaction potential exhibiting a first-order *full* kinetic blocking include one-dimensional plasmas (Chavanis,

[1] It is as if in a homogeneous plasma, the electrostatic force between two electrons would not only depend on their distance but also on their velocities.

[2] The interaction potential from Eq. (7.3) was devised in Fouvry (2022) from theoretical considerations. Unfortunately, as far as we know, this potential does not directly correspond to any physical system.

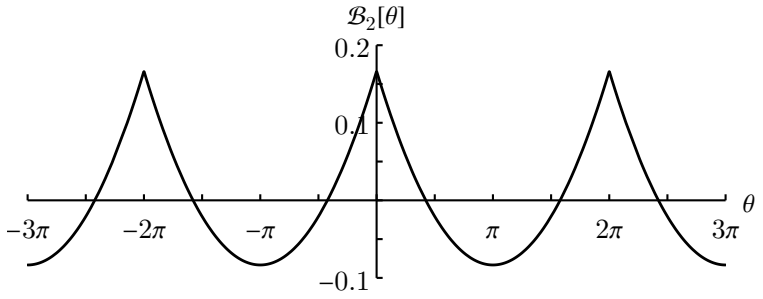

Figure 7.1: Figure from Fouvry & Roule (2023). Angular dependence, $\mathcal{B}_2(\theta)$, from the interaction potential of equation (7.3).

2013a), axisymmetric vector resonant relaxation (Fouvry et al., 2019b) and vortices (Chavanis & Lemou, 2007). However, none of these classical systems exhibit a second-order *bare* kinetic blocking.

Let me investigate the long-term evolution of systems driven by equation (7.3) in the dynamically hot limit. In that context, it corresponds to the limit $G \ll G_{\rm crit}$ (abusively denoted $G \to 0$) where $G_{\rm crit}$ stands for the critical value of G above which the system becomes linearly unstable.

In order to highlight various regimes of relaxation, let me consider three different external potentials, i.e., three different frequency profiles. More precisely, fixing the prefactors to unity, these profiles are given by

$$\text{Profile 1:} \quad \Omega(J) = |J|; \tag{7.5a}$$

$$\text{Profile 2:} \quad \Omega(J) = J\,|J|; \tag{7.5b}$$

$$\text{Profile 3:} \quad \Omega(J) = J. \tag{7.5c}$$

And for each case, the same initial DF, $F(J) \propto \exp(-J^4)$, is used. This DF does not correspond to the thermal equilibrium of these profiles.

7.2 Kinetic equations

Given some interaction and external potentials, kinetic theory aims at predicting $\partial F(J,t)/\partial t$, i.e., the rate of orbital redistribution, in the statistical limit $N \gg 1$. Let me now sketch the equations describing the evolution of the previous systems at successive orders in $1/N$, highlighting in particular how kinetic blockings may occur.

7.2.1 First-order kinetic equation

Accounting only for two-body correlations, assuming linear stability, and neglecting collective effects, the system's relaxation is described by the inhomogeneous Landau equation (section 5.2.1). Limiting ourselves to 1:1 resonances, it reads

$$\frac{\partial F(J)}{\partial t} \propto \mu \frac{\partial}{\partial J} \Big[\sum_{k_1} k_1 \int \mathrm{d}J_1 \, \big|U_{k_1}(\mathbf{J})\big|^2 \, \delta_{\rm D}(\mathbf{k}\cdot\mathbf{\Omega}) \, \mathbf{k}\cdot \frac{\partial}{\partial \mathbf{J}} F_2(\mathbf{J}) \Big], \tag{7.6}$$

where the time dependence was omitted for clarity. Recalling that $\mu = M_{\rm tot}/N$, this relaxation is driven by $1/N$ effects. In equation (7.6), the notations are shortened using the 2-vectors $\mathbf{J} = (J, J_1)$, $\mathbf{\Omega} = (\Omega[J], \Omega[J_1])$ and $\mathbf{k} = (k_1, -k_1)$, and $F_2(\mathbf{J}) = F(J)F(J_1)$. These 2-vectors should not be confused with multidimensional actions, frequency and resonance numbers. They do correspond to multiple interacting orbits and are used to highlight the similarities with the following second-order equation. This equation also involves the bare coupling coefficients, $U_{k_1}(\mathbf{J})$, namely the Fourier transform

in angles of the pairwise interaction potential. When taking collective effects into account, equation (7.6) becomes the inhomogeneous Balescu–Lenard equation (Heyvaerts, 2010; Chavanis, 2012). It follows from equation (7.6) with the substitution $|U_{k_1}(\mathbf{J})|^2 \to |U^{\rm d}_{k_1}[F](\mathbf{J})|^2$, with the dressed coupling coefficients $U^{\rm d}_{k_1}[F](\mathbf{J}) = U^{\rm d}_{k_1 k_1}(J, J_1)$ given by equation (3.29).

On long timescales, two particles can efficiently couple to one another and drive relaxation only if they share commensurate orbital frequencies. This is visible in equation (7.6) through the presence of the Dirac delta, $\delta_{\rm D}(\mathbf{k}\cdot\boldsymbol{\Omega})$. For a system with a monotonic frequency profile, $J \mapsto \Omega(J)$, the resonance condition $\delta_{\rm D}(\mathbf{k}\cdot\boldsymbol{\Omega})$ imposes $J_1 = J$ (a so-called local resonance), so that the cross term, $\mathbf{k}\cdot\partial F_2/\partial\mathbf{J}$, in equation (7.6) exactly vanishes. Ultimately, this leads to $\partial F(J)/\partial t = 0$, i.e., the kinetic equation predicts no relaxation. Importantly, for a monotonic frequency profile, this cancellation holds (i) whatever the considered interaction potential, $U(\mathbf{w}, \mathbf{w}')$; (ii) whatever the considered (stable) DF, $F(J)$; (iii) and for both the Landau and Balescu–Lenard equations, i.e., independently of whether collective effects are or are not accounted for. This is a first-order *full* kinetic blocking: such systems cannot relax via two-body correlations ($1/N$ effects). In that case, the relaxation is greatly delayed and can only occur through three-body correlations ($1/N^2$ effects).

7.2.2 Second-order kinetic equation

Placing themselves within this regime and neglecting collective effects, Fouvry (2022) derived a closed kinetic equation describing relaxation driven by $1/N^2$ effects. This inhomogeneous $1/N^2$ Landau equation is of the form

$$\frac{\partial F(J)}{\partial t} \propto \mu^2 \frac{\partial}{\partial J}\Big[\sum_{k_1,k_2} (k_1+k_2) \int {\rm d}J_1 {\rm d}J_2 \, |\Lambda_{k_1 k_2}(\mathbf{J})|^2 \delta_{\rm D}(\mathbf{k}\cdot\boldsymbol{\Omega}) \, \mathbf{k}\cdot\frac{\partial}{\partial\mathbf{J}} F_3(\mathbf{J}) \Big], \tag{7.7}$$

and I refer to appendix C in FR23 for the full expression of the equation and the coupling coefficients, $\Lambda_{k_1 k_2}(\mathbf{J})$. In equation (7.7), notations are shortened using here the 3-vectors $\mathbf{J} = (J, J_1, J_2)$, $\boldsymbol{\Omega} = (\Omega[J], \Omega[J_1], \Omega[J_2])$ and $\mathbf{k} = (k_1+k_2, -k_1, -k_2)$, and $F_3(\mathbf{J}) = F(J)F(J_1)F(J_2)$. Since collective effects have been neglected, it is crucial to note that the coupling coefficients, $\Lambda_{k_1 k_2}(\mathbf{J})$, only depend on the pairwise interaction potential: they do *not* involve the system's DF, $F(J)$. In equation (7.7), the resonance condition on orbital frequencies, $\delta_{\rm D}(\mathbf{k}\cdot\boldsymbol{\Omega})$, becomes more intricate than the one in equation (7.6). Indeed, it now involves three particles with commensurate orbital frequencies. This allows for non-local resonances, i.e., triplet of actions, $\mathbf{J}$, which are not all identical.

The generalisation of equation (7.7) to account for collective effects, i.e., the inhomogeneous $1/N^2$ Balescu–Lenard equation, is currently unknown. In particular, at order $1/N^2$, one may expect for collective effects to be more involved than a simple dressing of the pairwise interaction potential (see, e.g., footnote 5 in Hamilton, 2021). Nonetheless, in equation (7.7), the cross term, $\mathbf{k}\cdot\partial F_3/\partial\mathbf{J}$, does not explicitly involve the interaction potential and its precise form is key to ensure all the conservation laws and H-theorem of the kinetic equation (Fouvry, 2022). As a consequence, one could expect that the inhomogeneous $1/N^2$ Balescu–Lenard equation can be obtained from Eq. (7.7) through some intricate substitution $|\Lambda_{k_1 k_2}(\mathbf{J})|^2 \to |\Lambda^{\rm d}_{k_1 k_2}[F](\mathbf{J})|^2$, which is still unknown.

In equation (7.7), the three-body cross term, $\mathbf{k}\cdot\partial F_3/\partial\mathbf{J}$, never vanishes at resonance except for the thermodynamical equilibrium (see section IV.C in Fouvry, 2022). In that sense, three-body collisions always involve non-trivial resonances and cannot generically vanish whatever the DF: this is in sharp contrast with the first-order kinetic blocking of equation (7.6).

The goal of further delaying the relaxation described by equation (7.7),was investigated in §IV.D of Fouvry (2022). Therein, they showed that the pairwise potential from equation (7.3) in conjunction with the profile (3) from Eq. (7.5c) ensures that $\Lambda_{k_1 k_2}(\mathbf{J}) = 0$ at resonance. Phrased differently, the vanishing condition obtained in Fouvry (2022) amounted to devising $\Omega(J)$ and $U(\mathbf{w}, \mathbf{w}')$ so that $\delta_{\rm D}(\mathbf{k}\cdot\boldsymbol{\Omega})\,\Lambda_{k_1 k_2}(\mathbf{J}) = 0$. In that case, one gets $\partial F(J)/\partial t = 0$ in equation (7.7), i.e., this kinetic equation predicts no relaxation whatever the considered (stable) $F(J)$. This is a second-order *bare* kinetic blocking.

Let me emphasise that the first-order blocking of equation (7.6) relies on the vanishing, at resonance, of the crossed term $\mathbf{k}\cdot\partial F_2/\mathbf{J}=0$, while the second-order blocking of equation (7.7) relies on the vanishing, at resonance, of the coupling coefficients $\Lambda_{k_1k_2}(\mathbf{J})=0$. This is a fundamental difference. Indeed, the vanishing of the bare coefficients, $\Lambda_{k_1k_2}(\mathbf{J})$, does not imply the vanishing of the dressed coefficients, $\Lambda^{\mathrm{d}}_{k_1k_2}[F](\mathbf{J})$, because dressing depends on the considered DF. Since $\Lambda^{\mathrm{d}}_{k_1k_2}[F](\mathbf{J})$ will generically be non-zero at resonance, the inhomogeneous $1/N^2$ Balescu–Lenard equation is not expected to vanish. I claim that this prevents any system from ever undergoing a second-order *full* kinetic blocking.

7.2.3 Scalings of the relaxation

Let me now detail the expected scaling of the relaxation time w.r.t. the total number of particles N and the amplitude of the pairwise interaction, G, in these various regimes.

In equations (7.6) and (7.7), the scaling w.r.t. N is straightforwardly read from the dependence w.r.t. the individual mass $\mu=M_{\mathrm{tot}}/N$. One has $\partial F/\partial t\propto 1/N$ [resp. $\propto 1/N^2$] in equation (7.6) [resp. equation (7.7)]. In the present dynamically hot limit, the scaling w.r.t. G stems from the scaling of the coupling coefficients. In equation (7.6), one has $U_k\propto G$, so that $\partial F/\partial t\propto G^2$. As for equation (7.7), the bare coupling coefficients, $\Lambda(\mathbf{J})$, are quadratic in the interaction potential, i.e., $\Lambda(\mathbf{J})\propto G^2$ (see appendix C in FR23). As a consequence, equation (7.7), leads to $\partial F/\partial t\propto G^4$. To summarise, in the dynamically hot limit, the $1/N$ Landau equation (7.6) predicts a relaxation timescale of order $T_{\mathrm{relax}}/t_{\mathrm{dyn}}\propto N/G^2$. And, in the same hot limit, the $1/N^2$ Landau equation (7.7) predicts a relaxation on the (slower) timescale $T_{\mathrm{relax}}/t_{\mathrm{dyn}}\propto N^2/G^4$. In both cases, the larger the number of particles, the slower the evolution; the stronger the interaction, the faster the evolution.

Now, let me consider the case of systems subject to a second-order bare kinetic blocking. In the dynamically hot limit, i.e., for $G\to 0$, one expects for the $1/N^2$ dressed coefficients, $\Lambda^{\mathrm{d}}[F](\mathbf{J})$, to converge to the bare ones, $\Lambda(\mathbf{J})$. Since $\Lambda(\mathbf{J})\propto G^2$, this leads to an expansion of the form

$$\Lambda^{\mathrm{d}}[F](\mathbf{J}) \underset{G\to 0}{=} \Lambda(\mathbf{J}) + G^3\Lambda^{\mathrm{d}}_{(3)}[F](\mathbf{J}) + \mathcal{O}(G^4). \tag{7.8}$$

For systems undergoing a second-order bare kinetic blocking, one has $\Lambda(\mathbf{J})=0$ at resonance. As a consequence, in the hot limit, one finds the asymptotic scaling $\Lambda^{\mathrm{d}}[F](\mathbf{J})\propto G^3$. Given that $\partial F/\partial t\propto|\Lambda^{\mathrm{d}}[F](\mathbf{J})|^2$, systems subject to a second-order bare kinetic blocking are therefore expected to relax on a timescale of order $T_{\mathrm{relax}}/t_{\mathrm{dyn}}\propto N^2/G^6$. In that limit, relaxation is driven by "leaks" from dressed three-body interactions. Phrased differently, $1/N^2$ effects, albeit made less efficient by a second-order bare kinetic blocking, are always driving some non-zero relaxation in the present long-range interacting inhomogeneous one-dimensional systems. I claim that one cannot design a system in which three-body correlations would systematically drive no dynamics, whatever the considered DF.

One could be worried that four-body correlations, i.e., $1/N^3$ effects, could drive relaxation more efficiently than the previous leaks from three-body collective effects. In appendix D of FR23, placing ourselves in the hot limit, we justified that $1/N^3$ effects drive relaxation on a timescale of order $T_{\mathrm{relax}}/t_{\mathrm{dyn}}\propto N^3/G^6$, i.e., a subdominant process. As a conclusion, even if it was derived, an inhomogeneous $1/N^3$ Landau equation can never be the main driver of relaxation in the asymptotic limit $N\gg 1$. This is one of the main results of the present investigation.

7.3 Numerical measurements

7.3.1 Scalings

Let me now recap for each of the frequency profiles considered in equation (7.5), the scaling of the relaxation time expected as one varies the total number of particles, N, and the amplitude of the pairwise coupling, G, within the limit of a dynamically hot system, i.e., $G\to 0$.

- **Profile (1)**. This profile is non-monotonic. This allows for non-local resonances, $J_1 \neq J$, in the $1/N$ Landau equation (7.6). The system is not subject to any kinetic blocking. It is then expected that $T_{\rm relax}/t_{\rm dyn} \propto N/G^2$.
- **Profile (2)**. This profile is monotonic, so that the $1/N$ Landau and Balescu–Lenard operators both vanish. The $1/N$ dynamics is *fully* blocked. The system can only relax through $1/N^2$ effects, as governed by equation (7.7) in the hot regime. The profile (2) is not submitted to any second-order bare kinetic blocking, i.e., equation (7.7) gives a non-vanishing contribution. The expected scaling is then $T_{\rm relax}/t_{\rm dyn} \propto N^2/G^4$.
- **Profile (3)**. This profile is monotonic, hence the $1/N$ dynamics is fully blocked. In addition, following Fouvry (2022), this profile is also submitted to a second-order bare kinetic blocking, i.e., the $1/N^2$ equation (7.7) vanishes. Yet, even though the $1/N^2$ Landau equation is zero whatever the considered DF, I argued in section 7.2.3 that leaks from the (yet unknown) $1/N^2$ Balescu–Lenard equation will lead to a relaxation time scaling like $T_{\rm relax}/t_{\rm dyn} \propto N^2/G^6$ and not like $T_{\rm relax}/t_{\rm dyn} \propto N^3/G^6$ as one could have (wrongly) guessed from four-body correlations contribution (see appendix D of FR23).

To summarise, the profiles from equation (7.5) are predicted to be associated with relaxation times scaling like

$$\text{Profile 1:} \quad T_{\rm relax}/t_{\rm dyn} \propto N/G^2; \tag{7.9a}$$

$$\text{Profile 2:} \quad T_{\rm relax}/t_{\rm dyn} \propto N^2/G^4; \tag{7.9b}$$

$$\text{Profile 3:} \quad T_{\rm relax}/t_{\rm dyn} \propto N^2/G^6. \tag{7.9c}$$

In FR23, we set out to recover numerically the scalings predicted in equation (7.9). In practice, we searched for a power-law dependence of the form

$$T_{\rm relax}/t_{\rm dyn} \propto N^{\gamma_N}/G^{\gamma_G}, \tag{7.10}$$

and constraints on the power indices (γ_N, γ_G). A handful of reasons made these measurements challenging. These important numerical details are discussed in section IV of FR23.

In figure 7.2, I report our main result, namely the measurement of the power indices (γ_N, γ_G) from equation (7.10) as one varies the considered frequency profiles. In this figure, all profiles

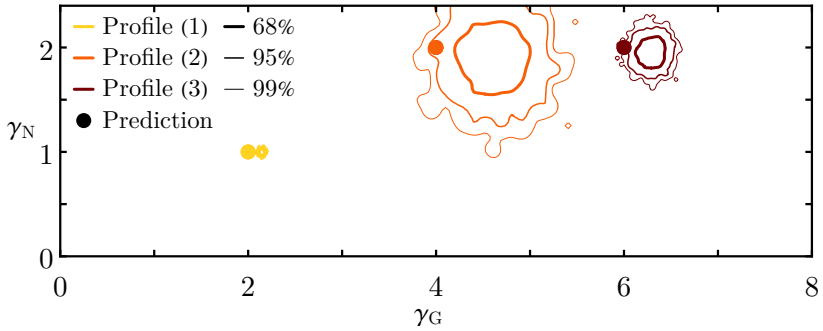

Figure 7.2: Figure from Fouvry & Roule (2023). Dependence of the relaxation time, via the power-law indices (γ_N, γ_G) from equation (7.10), as a function of the total number of particles, N, and the strength of the pairwise interaction, G, for the various frequency profiles from equation (7.5) (represented with different colours). Points correspond to the kinetic prediction from equation (7.9), while contours are obtained from N–body measurements (see appendix E in FR23). A contour labelled x% contains x% of the measured power indices: the thinner the contour, the larger the fraction of measurements it encompasses. As explained in section 7.3.2, a systematic bias towards higher γ_G is to be expected.

exhibit their expected scaling w.r.t. N, i.e., the value of γ_N. In particular, even though the profile (3) is submitted to a second-order bare kinetic blocking, i.e., equation (7.7) exactly vanishes, its

relaxation is still driven by $1/N^2$ effects, i.e., three-body correlations. Once again, I emphasise that this particularly slow relaxation is sourced by leaks from dressed three-body correlations and not by four-body correlations.

In figure 7.2, all profiles also show scalings w.r.t. G, i.e., the value of γ_G, in agreement with the predictions. Though, one could be suspicious about the systematic bias in the value of γ_G, which is always measured to be larger than the predicted one. I argue in the next section that this was to be expected since the measurements were made for a finite value of G, while the predictions correspond to the limit $G\to 0$. In particular, given the difficulty of integrating the motion driven by the potential from equation (7.3), we had to limit ourselves to considering not so dynamically hot systems (see appendix E 5 in FR23). In section 7.3.2, I show that the bias observed in figure 7.2 is well within the limits that could be expected from the effective use of finite values of G.

Ultimately, figure 7.2 clearly confirms numerically the scaling of the relaxation times predicted in equation (7.9), along with all the signatures associated with these various kinetic blockings.

7.3.2 Bias in γ_G

In figure 7.2, the kinetic prediction for γ_G corresponds to the limit $G\to 0$, while the measurements are performed for finite values of G. This leads to a biased overestimation of γ_G, once again associated with leaks from collective effects. In this section, I briefly estimate the maximum extent of that pollution.

For a fixed value of N the scaling of the $1/N$ Balescu–Lenard equation w.r.t. G is, roughly,

$$\frac{\partial F}{\partial t} \propto \left(\frac{G}{1-G/G_{\mathrm{crit}}}\right)^2. \tag{7.11}$$

Here, following equation (3.13) and abruptly neglecting the frequency dependence of the polarisation matrix, $\mathbf{M}(\omega)$, from equation (3.28), the dressed coupling coefficient could be roughly written as $U^{\mathrm{d}} \propto U/|\mathbf{I}-\mathbf{M}| \propto G/(1-G/G_{\mathrm{crit}})$.

Similarly, within the same limits and following equation (7.7), the $1/N^2$ Balescu–Lenard equation is expected to scale w.r.t. G roughly like

$$\frac{\partial F}{\partial t} \propto \left(\frac{G}{1-G/G_{\mathrm{crit}}}\right)^4. \tag{7.12}$$

In order to estimate the maximum bias in γ_G associated with this particular choice, one can compute $\partial F/\partial t$ as given by equations (7.11) and (7.12), and then perform the linear fit $\ln(\partial F/\partial t) \simeq \widetilde{\gamma}_G \ln G + \mathrm{cst}$. In that case, $\widetilde{\gamma}_G$ is an estimate of the maximum value of γ_G that could stem from our use of finite values of G. In practice, for the $1/N$ [resp. $1/N^2$] dynamics from equation (7.11) [resp. equation (7.12)], and with the considered values of G, we found $\widetilde{\gamma}_G \simeq 2.64$ [resp. $\widetilde{\gamma}_G \simeq 5.28$]. For the third profile, the same qualitative analysis could be made to estimate the bias in γ_G. Roughly assuming a power-law dependence of the form $\partial F/\partial t \propto G^6/(1-G/G_{\mathrm{crit}})^4$, one would estimate the maximum value of γ_G that could stem from the use of finite values of G to be $\widetilde{\gamma}_G \simeq 7.28$. Fortunately, these values of $\widetilde{\gamma}_G$ are larger than the mean values obtained in figure 7.2. This strengthens my confidence in the sanity of the numerical measurements.

7.4 Conclusion

In this chapter, I investigated the long-term evolution of long-range interacting inhomogeneous one-dimensional systems. In particular, I highlighted the existence of two types of kinetic blockings: (i) a first-order *full* kinetic blocking in systems with a monotonic frequency profile and subject to 1:1 resonances only, associated with the vanishing of the inhomogeneous $1/N$ Balescu–Lenard

equation (5.1); (ii) a second-order *bare* kinetic blocking associated with the vanishing of the inhomogeneous $1/N^2$ Landau equation.

Considering a particular interaction potential (equation 7.3), I presented a large numerical exploration to confirm the existence of these various blockings. I showed that dynamically hot systems submitted to a second-order bare kinetic blocking still relax via $1/N^2$ effects, as a result of "leaks" from collective effects. I argued that the (still unknown) $1/N^2$ Balescu–Lenard collision operator would never vanish since the cancellation of the $1/N^2$ Landau operator arises from very specific condition on the coupling terms. These conditions should not be met when taking collective effects into account since the resulting coupling coefficients will depend on the considered DF. Hence, four-body correlations, i.e., $1/N^3$ effects, can never be the main driver of the relaxation of long-range interacting inhomogeneous systems, even in the present contrived one-dimensional geometry. As such, no system will ever suffer from a second-order *full* kinetic blocking, and I claim that the $1/N^3$ Landau equation does not need further investigation.

7.5 Perspectives

A few assumptions have been made in this analysis and could deserve further investigation.

- The action coordinate has been assumed to have an infinite support, as well as the kinetically-blocked frequency profiles (2) and (3) in equation (7.5). This is not generically true for inhomogeneous systems, where the action domain may be semi-infinite or even finite. For such setups, it has been shown that the presence of a minimum/maximum action/frequency drastically slows down the decay of perturbations, which only vanish algebraically with time (Smereka, 1998; Barré et al., 2011; Barré & Yamaguchi, 2013; Faou et al., 2021). This algebraic decay and its link with the presence of branch cuts in the susceptibility was shortly discussed in section 3.3.3.
- The system has been assumed to remain linearly stable throughout its whole evolution. However, there exist cases for which the system's global thermodynamical equilibrium is "magnetised", i.e., its DF, $F = F_{\rm eq}(\theta, J)$, has a non-trivial angular dependence (see, e.g., Campa et al., 2008; Gupta & Mukamel, 2011; Barré & Gupta, 2014; Das & Gupta, 2019). In that case, although the kinetically-blocked DF, $F = F(J, t)$, initially evolves slowly on a timescale of order $N^2 t_{\rm dyn}$, it unavoidably becomes linearly unstable at some point. This triggers a dynamical phase transition, and the DF (rapidly) "magnetises" to become $F = F(\theta, J, t)$. The relaxation towards the thermodynamical equilibrium, $F_{\rm eq}(\theta, J)$, then keeps proceeding. Yet, this dynamics does not suffer from a first-order kinetic blocking because non-local resonances are now permitted. As a result, in this second stage of evolution, the relaxation occurs on a timescale of order $N t_{\rm dyn}$. Therefore, the overall dependence w.r.t. N of the total relaxation time towards the thermodynamical equilibrium must exhibit an intermediate scaling between N and N^2. Interestingly, this agrees with the scaling $N^{3/2}$ reported in figure 6 of Das & Gupta (2019) which considered long-range coupled classical spins undergoing this dynamical phase transition.

The present numerical work is only one more step towards a finer understanding of (very) long-term dynamics and high-order correlations. Naturally, it would be worthwhile and rewarding to derive the $1/N^2$ Balescu–Lenard equation, hence generalising equation (7.7). This is no easy task. A realistic roadmap to perform such a delicate calculation would be to follow the development of the $1/N^2$ Landau equation: first tackling the (single-harmonic) homogeneous HMF model (Rocha Filho et al., 2014; Fouvry et al., 2019a), then homogeneous systems with an arbitrary potential of interaction (Fouvry et al., 2020), and finally the present inhomogeneous regime (Fouvry, 2022). Ultimately, this line of work would convincingly show that second-order kinetic blockings can never lead to the full vanishing of $1/N^2$ effects.

Chapter 8

Conclusion

Let me conclude this PhD by an overview of the main results and highlight some perspectives it provides. To summarise the ingredients involved in the evolution of isolated self-gravitating systems, I have illustrated the major causes of this evolution in figure 8.1. At first, an out-of-equilibrium

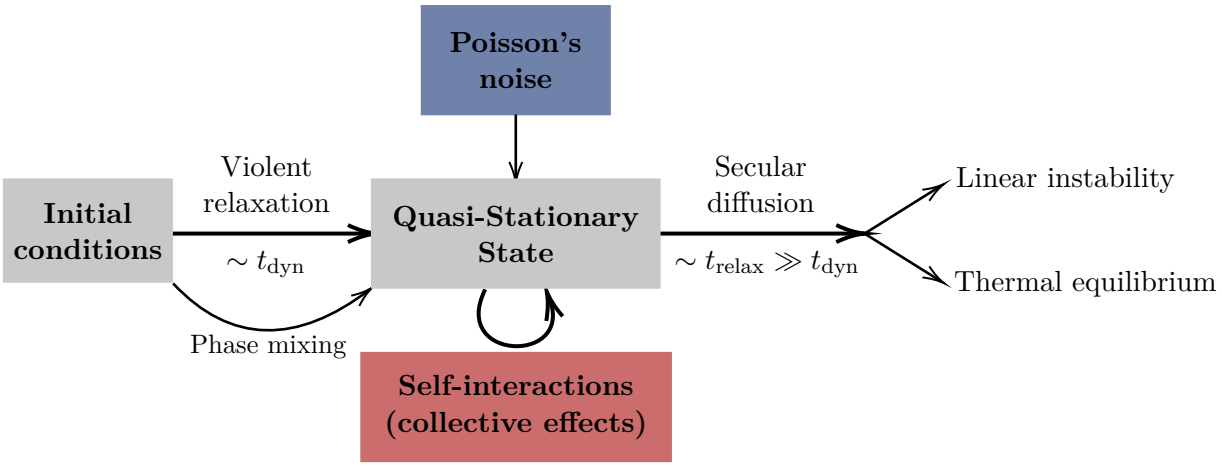

Figure 8.1: Courtesy of J.-B. Fouvry. Schematics of the typical fate of an isolated stellar self-gravitating system. During the first few dynamical times, the system undergoes violent relaxation (Lynden-Bell, 1967) and phase mixing. It quickly settles into a quasi-stationary state (QSS), i.e., an equilibrium state of the collisionless dynamics. When stable, the system then evolves on much longer timescales through the correlated effects of internal fluctuations. Collective effects might heighten or weaken these fluctuations and therefore accelerate or delay the system's secular relaxation towards a new equilibrium.

state undergoes a violent relaxation (Lynden-Bell, 1967) during which its mean distribution evolves quickly towards an angle-independent QSS through phase mixing and highly non-linear processes. From this QSS, the system's evolution is driven by fluctuations. Even when isolated, the system undergoes such internal fluctuations through finite-N effects which get amplified by collective effects, and can resonantly couple to one another. If this state is unstable, the system supports a mode which will first grow exponentially and eventually saturate. For stable isolated systems, over long timescales small but cumulative effects build up and these internal couplings ultimately drive the system towards its thermal equilibrium (when it exists). This secular relaxation could also drive adiabatically the system towards a new unstable quasi-stationary state.

8.1 Overview

In this thesis, I studied this long-term reshuffling of orbits. I focused on the role of resonant interactions and collective effects in shaping this secular relaxation. The cross-analysis of the one-

dimensional model and razor-thin discs allowed me to highlight the diverse consequences these effects might have on the evolution of self-gravitating systems. This diversity raised multiple questions: When do collective effects enhance or dampen the long-term orbital reshuffling in self-gravitating systems? What kind of systems are least subject to orbital diffusions? What is the relationship between damped modes and orbital diffusion in galactic discs? What are the limitations of the current state-of-the-art kinetic theory?

Linear response theory To tackle these questions, it was first necessary to properly capture the response of stellar systems to perturbations and its amplification by the so-called collective effects. In chapter 3, I sketched the necessary tools and the method I used to do so. While probing instabilities can be numerically challenging, the generic response of stable systems to perturbations is intrinsically much more difficult. It is an ill-conditioned problem (Trefethen, 2020) and therefore requires a careful treatment. Beyond specific analytical models (Zang, 1976; Olivetti, 2011), there is very few general methods to tackle this problem (Weinberg, 1994; Fouvry & Prunet, 2022) and their predictive power is quite limited.

In chapter 4, I applied the generic method presented in chapter 3 to the one-dimensional model and razor-thin stellar disc. I illustrated the versatility of this method and its ability to capture documented instabilities as well as to unveil the presence of multiple weakly damped modes in marginally stable discs (figure 4.15). By releasing adaptable public libraries (PR+24), I hope to foster the systematic study of the linear response of stellar systems to perturbations. As later discussed in chapter 6, this is not only relevant to study the (linear) stability of self-gravitating systems, but also to properly understand their long-term evolution. While studying instabilities in razor-thin discs, I highlighted the impact of gravitational softening on their collisionless properties. More precisely, I confirmed the theoretical predictions of De Rijcke et al. (2019b) on two different softening kernels (figure 4.16). The gravitational bias (Dehnen, 2001) strongly depends on the choice of this softening kernel. I also presented a new method to take softening into account in theoretical predictions (section 3.2.4).

Kinetic theory and long-term evolution Once the linear response of self-gravitating systems to perturbations is properly captured, it is possible to study their long-term evolution using the Balescu–Lenard kinetic theory. The associated equation (5.1) is the result of decades of efforts, incrementally extending the original Landau and Chandrasekhar theories to take into account the spatial inhomogeneity of stellar systems together with collective effects. Since its derivation, it has been successfully applied to a variety of systems, from razor-thin discs (Fouvry et al., 2015) to galactic nuclei (Bar-Or & Fouvry, 2018), the Hamiltonian mean-field (HMF) model (Benetti & Marcos, 2017) and the periodic cube (Weinberg, 1993; Magorrian, 2021). I described its underlying assumptions and limitations in chapter 5.

In chapter 6, I applied kinetic theories to the one-dimensional model and razor-thin disc and compared the predictions to numerical simulations. By comparing side by side the predictions of the Balescu–Lenard equation to Landau's, I was able to pinpoint the contribution of collective effects. This is precisely the missing contribution in most kinetic estimates of the relaxation rate such as the Chandrasekhar theory of local two-body deflections. I showed that, indeed, a self-gravitating system could evolve very differently from particles embedded in an external potential and scattered around by fluctuations. Furthermore, the consequences of self-gravity vary depending on the system's configuration and kinematics. This variety would have been impossible to predict without the valuable insights provided by the Balescu–Lenard kinetic theory. In the one-dimensional case, self-gravity leads to a collective stiffening: particles diffuse slower from their initial orbits than Landau theory would predict (figure 6.1). As a proxy model for the vertical motion of stars in the galactic plane, this result suggests that the disc would thicken slower than expected. I also showed that this one-dimensional system often suffers from a quasi-kinetic blocking. The relaxation rate is far

smaller than the typical diffusion rate: even not at thermal equilibrium, it almost obeys detailed balance (figure 6.8). Yet, it still relaxes towards its thermal equilibrium under the effect of two-body correlations.

This slow relaxation and this collective stiffening is at variance with the behaviour of dynamically cold razor-thin discs. In chapter 6, I revisited the numerical simulations of Sellwood (2012) and its interpretation by Fouvry et al. (2015). I confirmed that for this marginally stable disc, swing amplification (Toomre, 1981) drastically enhances the relaxation rate of the disc. With the results obtained in chapter 4, I showed that the resonant coupling between the (collisionless) damped modes and the stars is the main driver of this localised swing amplified reshuffling (figure 6.16). By stabilizing the disc, softening therefore significantly reduces the relaxation rate of the disc (figure 6.18). A direct consequence is that the quality of the quasi-linear Balescu–Lenard prediction is entirely set by the quality of the linear response computations. Let me stress that beyond the question of computational resources, the computation of the Landau (equation 5.1) and Balescu–Lenard (equation 5.12) collision operators is, by far, less technically challenging than the computation of the linear polarisation matrix alone (equation 3.28) at neutral and damped frequencies (section 3.3.2). If progress should be made in the secular computation, it is primarily in the linear response theory. To this end, I hope that the generic public libraries I contributed to develop in this thesis (section 4.2.3) will offer a valuable playground to test, improve and extend the current numerical methods for linear response. All in all, the Balescu–Lenard equation (5.1) provides a quantitative estimate for the relaxation rate of stellar systems. We have reached the time of precise kinetic predictions.

Beyond Balescu–Lenard While the Balescu–Lenard theory proved accurate when compared to averaged N–body simulations in the regime I explored, I also highlighted some of its limitations. In particular, individual simulations can evolve very differently from one another. This stochasticity is widely enhanced in the vicinity of marginal stability such as in the razor-thin disc I studied (figure 6.19). Predicting the scatter among different realisations is a challenging task which lies beyond the scope of the Balescu–Lenard theory. Beyond the marginally stable regime, it is an important question on its own as it would allow one to quantify the likelihood of a single realisation. Promising theories have been recently developed in this direction using large deviations (Bouchet, 2020; Feliachi & Bouchet, 2022; Feliachi & Fouvry, 2023).

Another limitation of the Balescu–Lenard theory involves one-dimensional homogeneous systems and inhomogeneous systems limited to 1:1 resonances. In chapter 7, I investigated these systems which suffer from a full first-order kinetic blocking. Any estimate based on two-body encounters, either Chandrasekhar, Landau or Balescu–Lenard, would predict no relaxation. The relaxation is further delayed and is driven by three-body encounters. In this case, a kinetic equation has recently been derived to take into account the effect of three-body encounters while neglecting collective effects (Fouvry et al., 2019a, 2020; Fouvry, 2022). Yet, some specific systems can also be blocked for this dynamics. I showed that collective effects again play a crucial role in the relaxation of these systems. Using numerical simulations, I proved that they notably enable three-body encounters to drive an evolution, thereby disrupting the second-order (bare) kinetic blocking. Hence, four-body correlations will never be the leading contributors to the relaxation of any self-interacting system.

The main purpose of my PhD was to validate quantitatively the (inhomogeneous) Balescu–Lenard theory against ensemble average sets of simulation. In complement with Fouvry et al. (2021) my work establishes that this theory correctly captures the secular evolution of self gravitating systems in geometries of one to three dimensions. The task has proven technically challenging and has led to a few unexpected results while highlighting new complexities, such as quasi kinetic blocking and increased variance near marginal stability. Yet, a decade after its publication, my results

establishes the Balescu–Lenard theory as the pillar of self-consistent heating in collisionless stellar systems. This, in turn, allows us to start and capture their long term evolution while accounting for fluctuations beyond the mean field.

8.2 Perspectives

Let me conclude with a few prospects which I believe would be worth exploring to further our theoretical understanding of self-gravitating systems.

Time evolution A direct follow-up of this work would involve integrating the Balescu–Lenard equation (5.1) forward in time to estimate the system's diffusion flux at a later stage. The predictions presented in this manuscript (chapter 6) only hold for the initial stellar distribution. Yet, integrating the relevant evolution equation forward in time is challenging, as highlighted by Weinberg (2001). The primary difficulty lies in computing the diffusion coefficients, which already is a challenging task as we have seen in this thesis. Additionally, the evolution of the distribution function (DF) implies changes in the self-consistent potential (Poisson equation 1.11), hence requiring new angle-action coordinates. Numerically, this presents a challenge due to the substantial computational resources required to determine the diffusion rate. One potential approach is to integrate the corresponding stochastic Langevin equation using a Monte Carlo method (Hénon, 1971; Cohn, 1979; Giersz, 1998), which could ultimately serve to validate N–body codes on secular timescales.

Crossing marginal stability As discussed in section 5.1.3, the Balescu–Lenard theory unrealistically diverges at marginal stability (Weinberg, 1993). In chapter 6, I showed that the Balescu–Lenard theory is still accurate in a relatively close vicinity of phase transition in the razor-thin disc. Yet, if one was to evolve the Balescu–Lenard equation in time, it would break down at some point. This divergence should be regularised by considering the contribution of wave-particle interactions, in the spirit of the so-called quasilinear theory in plasma physics (see, e.g., Rogister & Oberman, 1968; Hamilton & Heinemann, 2020, 2023).

Non-linear regime After phase transition, the evolution is dominated by the emerging unstable mode. As this mode grows, non-linear contributions in equation (1.13b) become increasingly important. There is growing interest in this non perturbative regime of saturation via the non-linear trapping of stars at resonances (see, e.g., Hamilton, 2024). Such a regime cannot be captured by quasi-linear theories by design, even when taking into account wave-particle interactions. This should offer key insights in the saturation amplitude of bars in galaxies.

Beyond average predictions Beyond this divergence in the mean evolution, I also pointed out the increased variance among different initial conditions near phase transition (figure 6.19). Predicting this scatter becomes a crucial question to properly assess the likelihood of a given realisation and hence to compare theoretical predictions to observations or cosmological simulations. To this end, the recent developments in large deviation theory (Bouchet, 2020; Feliachi & Bouchet, 2022; Feliachi & Fouvry, 2023) offer promising perspectives and should be further explored to take collective effects (both wake-particle and dressed particle-particle interactions) into account in inhomogeneous systems.

Three-body dressed kinetic theory In chapter 7, I heuristically showed that three-body interactions necessarily drive a relaxation in long-range self-interacting systems, whatever the interaction potential. Naturally, it would be worthwhile and rewarding to derive the three-body $(1/N^2)$

Balescu–Lenard equation, hence generalising equation (7.7). Ultimately, this derivation would convincingly show that second-order kinetic blockings can never lead to the full vanishing of $1/N^2$ effects.

Thick discs Of course, the models studied in this thesis are not perfect representation of the motion of stars in galactic discs. While the case of spherically symmetric systems is also well captured (Rozier et al., 2019; Fouvry et al., 2021; Tep et al., 2022), the extension to thick discs or flattened spheres is yet to be achieved, beyond the WKB approximation (Fouvry et al., 2016). One of the potential issue in these systems is the existence of angle-actions coordinates: the system may lack integrability (Weinberg, 2015) or the actions may not be analytically defined.

Coupled halo-disc evolution Through the ansatz of equation (4.19), I have assumed and simulated the evolution of the disc in a static, rigid dark matter halo. Yet, the dark matter halo, albeit dynamically hotter, is also subject to fluctuations. Accounting for the coupling between the disc and the halo would be a natural extension of this work and would provide a more realistic picture of the secular evolution of galaxies (see, e.g., Johnson et al., 2023).

Open dissipative systems Finally, let me address the elephant in the room: galaxies are not isolated objects. The Milky Way is continuously perturbed by external sources triggering various response features (see, e.g., Grion Filho et al., 2021, for a review). Firstly, it is important to differentiate between systems that are adiabatically relaxing and those undergoing resonant, non-resonant, or violent relaxation. The former do not resonate with any relevant frequencies, whereas the latter do not even maintain their mean field. In practice, these processes often operate concurrently in open systems. Moreover, dissipative processes within a (potentially subordinate) baryonic component can drive unlikely evolutionary pathways and may lead to self-regulation.

Taken together, these prospects would significantly deepen our understanding of the long-term evolution of self-gravitating systems and enable us to move beyond the current closed-box perspective in stellar dynamics. At a time when *ab initio* cosmological simulations of large volume of our Universe reach sufficient resolution to characterise the intricate resonant dynamics of stellar clusters, the linear and secular response theory presented in this thesis should prove enlightening to fully grasp the complex interplay between nature and nurture in the evolution of galaxies over a Hubble time.

Synthèse

Cette thèse explore l'évolution à long terme des ensembles de masses, liés par la force de gravité. C'est le célèbre problème à N corps. L'étude de l'évolution de tels systèmes est communément appelé la dynamique stellaire (Binney & Tremaine, 2008). Elle englobe un large ensemble de systèmes astrophysiques de tailles et de masses variées, allant des amas d'étoiles en orbite autour de Sagittarius A*, le trou noir supermassif au centre de notre galaxie, jusqu'à la Voie Lactée elle-même, son halo de matière noire et les réseaux d'amas de galaxies.

Leur étude est à la fois difficile et particulièrement intéressante car la gravité est une force attractive à longue portée. Ainsi, les systèmes stellaires forment généralement des structures inhomogènes et leur évolution est fondamentalement une histoire collective. Les étoiles dans un amas globulaire ou une galaxie ne se déplacent pas en ligne droite. Elles orbitent autour du centre de masse du système. Mais contrairement aux systèmes planétaires, ce mouvement n'est pas dicté par un seul objet central massif. Il résulte du potentiel gravitationnel collectif généré par toutes les étoiles du système. En tant que tel, les étoiles ne peuvent pas être considérées comme des particules tests traçant un potentiel imposé de l'extérieur. Ces interactions collectives peuvent jouer un rôle majeur dans la réponse du système aux perturbations externes et dans son évolution à long terme via la formation de structures telles que des bras spiraux ou des barres.

Le domaine de la formation et de l'évolution des galaxies implique divers phénomènes physiques multi-échelles interagissant de manière non linéaire. Par conséquent, ce domaine s'appuie principalement sur des simulations numériques pour comprendre l'interaction complexe de ces processus. Malgré leurs nombreux succès, ces simulations rencontrent des défis importants. Elles sont limitées par la puissance de calcul, ce qui contraint leur résolution et la complexité des modèles physiques qu'elles peuvent simuler avec précision. Les processus à l'échelle dite sous-grille, tels que la formation des étoiles et l'accrétion des trous noirs, doivent être traités avec des prescriptions phénoménologiques qui approximent les physiques non résolues. Ces limitations, combinées à leur nature intrinsèquement non linéaire, introduisent des incertitudes qui peuvent affecter le pouvoir prédictif et la précision des simulations (Scannapieco et al., 2012). En tant qu'approche complémentaire, il est donc intéressant de développer un cadre théorique générique capable d'expliquer l'évolution à long terme de ces systèmes sous l'effet de la gravité, en s'appuyant sur une approche perturbative déterministe. Un tel cadre pourrait fournir des éclairages sur la physique sous-jacente de ces systèmes et aider à interpréter et tester les résultats et limitations des simulations numériques. La dynamique à N corps se concentre sur la seule physique de la gravité tout en perdant de vue d'autres phénomènes physiques. Cette approximation grossière est motivé par le fait que la gravité est, le plus souvent, la force dominante.

Dans la limite d'un grand nombre de particules, $N \gg 1$, la longue portée de la gravité permet d'introduire une approximation de champ moyen. A l'ordre zéro, tout se passe comme si la distribution de particules et le potentiel qu'elles génèrent étaient des quantités lisses. Un système à N particules peut alors être vu comme une réalisation particulière d'un champ moyen que l'on aurait échantillonné. Formulé différemment, les orbites des étoiles dans une galaxie sont principalement influencées par le potentiel gravitationnel collectif de l'ensemble de la galaxie, plutôt que par les interactions immédiates avec les étoiles voisines. Cela contraste fortement avec le mouvement des

molécules dans un gaz, qui est principalement dicté par leurs interactions violentes et de courte durée avec leurs plus proches voisines.

L'évolution dynamique d'un système auto-gravitant peut alors être divisée en deux régimes distincts. Tout d'abord, un état hors équilibre subit une relaxation violente (Lynden-Bell, 1967) au cours de laquelle sa distribution moyenne évolue rapidement vers un état dit quasi-stationnaire. C'est le régime typique dans lequel se trouvent deux galaxies en train de fusionner. Les orbites des étoiles changent sur des temps courts, proche de leur durée typique, à travers un mélange de phase et des processus hautement non linéaires. Très peu de résultats analytiques ont été obtenus (voir, par exemple, Chavanis, 2006b, pour une revue) et la compréhension complète de l'aboutissement de cette phase reste une question ouverte et un domaine de recherche actif (Ewart et al., 2022; Chavanis, 2022; Teles et al., 2023; Worrakitpoonpon, 2024). Il est important de noter que cet équilibre de champ moyen n'est généralement pas l'équilibre thermodynamique du système. Sauf dans des cas très spécifiques, il n'existe pas d'état d'équilibre thermique pour les systèmes auto-gravitants, c'est-à-dire qu'il n'existe pas d'état de maximum d'entropie (Campa et al., 2014). Un état quasi-stationnaire est un état d'équilibre de la dynamique non-collisionnelle, i.e., de la dynamique dictée par le champ moyen lisse.

Le second régime est celui de la relaxation dite séculaire. Cette évolution peut-être sourcée par des changements lents comme l'accrétion cohérente de gaz froid ou de petits satellites pour des systèmes ouverts. Dans le cas des systèmes isolés que je considère ici, cette évolution à long terme est sourcée par des processus dit collisionels ou effets de N fini. Le système considéré (N corps) n'est pas parfaitement décrit par le champ moyen. En conséquence, les orbites des étoiles ne sont pas parfaitement régulières, elle diffusent lentement ce qui peut amener à une réorganisation globale du système. Ces fluctuations gravitationelles peuvent être fortement amplifiés par les effets collectifs : les perturbations de potentiel sont sourcées par les perturbations de densités sur lesquelles elles agissent. C'est une boucle de rétroaction qui peut conduire à des instabilités collectives. L'état quasi-stationnaire peut être instable, le système supporte alors un mode qui va croître exponentiellement avant de finalement saturer sous l'effet de processus non linéaires. Les barres présentes dans de nombreuses galaxies spirales sont un exemple de telles instabilités. Pour les systèmes stables, sur de longues échelles de temps, des effets petits mais cumulatifs finissent par conduire le système vers son équilibre thermique (quand il existe) ou d'autres états quasi-stationnaires. Les développements récents de la théorie cinétique des systèmes auto-gravitants offrent un cadre théorique pour comprendre les résultats statistiques de ces processus d'évolution non linéaires.

Dans cette thèse, j'ai étudié ce réarrangement à long terme des orbites. Je me suis concentré sur le rôle des interactions résonnantes et des effets collectifs sur cette relaxation séculaire. L'analyse croisée d'un modèle unidimensionnel et de disques infiniment fins m'a permis de mettre en évidence les conséquences diverses que ces effets peuvent avoir sur l'évolution des systèmes auto-gravitants. Cette diversité soulèvent plusieurs questions : Quand les effets collectifs amplifient-ils ou atténuent-ils le réarrangement orbital à long terme dans les systèmes auto-gravitants ? Quels types de systèmes sont les moins sujets à la diffusion orbitale ? Quelle est la relation entre les modes amortis et la diffusion orbitale dans les disques galactiques ? Quelles sont les limitations de l'état de l'art en théorie cinétique ?

Théorie de la réponse linéaire Pour aborder ces questions, il était d'abord nécessaire de bien capturer la réponse des systèmes stellaires aux différentes perturbations, i.e., les effets collectifs. Dans le chapitre 3, j'ai esquissé les outils nécessaires et la méthode que j'ai utilisée pour ce faire. Bien que sonder les instabilités puisse être numériquement difficile, la réponse générique des systèmes stables aux perturbations est intrinsèquement beaucoup plus complexe. C'est un problème mal conditionné (Trefethen, 2020) qui nécessite donc un traitement minutieux. Au-delà des modèles analytiques spécifiques (Zang, 1976; Olivetti, 2011), il existe très peu de méthodes générales pour

aborder ce problème (Weinberg, 1994; Fouvry & Prunet, 2022) et leur pouvoir prédictif est assez limité.

Dans le chapitre 4, j'ai appliqué la méthode générique présentée dans le chapitre 3 au modèle unidimensionnel et au disque. J'ai illustré la polyvalence de cette méthode et sa capacité à retrouver des instabilités documentées ainsi qu'à révéler la présence de multiples modes faiblement amortis dans des disques marginalement stables (figure 4.15). En publiant des librairies versatiles (PR+24), j'espère encourager l'étude systématique de la réponse linéaire des systèmes stellaires. Comme discuté plus tard dans le chapitre 6, cela n'est pas seulement pertinent pour étudier la stabilité (linéaire) des systèmes auto-gravitants, mais aussi pour bien comprendre leur évolution à long terme. En étudiant les instabilités dans les disques, j'ai également mis en évidence l'impact du "softening" gravitationnel sur leurs propriétés non collisionnelles. Ce softening est une approximation numérique courante qui consiste à lisser le potentiel d'interaction gravitationnel dans les simulations numériques pour éviter des forces trop singulières et les instabilités numériques associées. Plus précisément, j'ai confirmé les prédictions théoriques de De Rijcke et al. (2019b) sur deux noyaux de softening différents (figure 4.16). Ce biais gravitationnel (Dehnen, 2001) dépend fortement du choix de ce noyau de softening. J'ai également présenté une nouvelle méthode pour prendre en compte ces effets dans les prédictions théoriques (section 3.2.4).

Théorie cinétique et évolution à long terme Une fois la réponse linéaire des systèmes auto-gravitants correctement capturée, il est possible d'étudier leur évolution à long terme en utilisant la théorie cinétique de Balescu–Lenard. L'équation associée (5.1) est le résultat de décennies d'efforts, prolongeant progressivement les théories originales de Landau et Chandrasekhar pour prendre en compte l'inhomogénéité spatiale des systèmes stellaires ainsi que les effets collectifs. Lorsque les effets collectifs sont négligés, l'équation associée est l'équation dite de Landau. Depuis sa dérivation, elle a été appliquée avec succès à une variété de systèmes, allant des disques infiniment fins (Fouvry et al., 2015) aux noyaux galactiques (Bar-Or & Fouvry, 2018), en passant par le modèle HMF (Benetti & Marcos, 2017) et le cube périodique (Magorrian, 2021). J'ai décrit ses hypothèses sous-jacentes et ses limitations dans le chapitre 5.

Dans le chapitre 6, j'ai appliqué les théories cinétiques de Landau et Balescu–Lenard au modèle unidimensionnel et au disque, et j'ai comparé les prédictions à des simulations numériques. En comparant les prédictions de l'équation de Balescu–Lenard à celles de l'équation de Landau, j'ai pu identifier la contribution des effets collectifs. C'est précisément cette contribution qui manque dans la plupart des estimations cinétiques du taux de relaxation telles que la théorie de Chandrasekhar des déviations locales à deux corps. J'ai montré qu'effectivement, un système auto-gravitant pouvait évoluer très différemment d'un système de particules plongées dans un potentiel externe et non couplées. Les conséquences de l'auto-gravité varient en fonction de la configuration et de la cinématique du système. Cette diversité aurait été impossible à prédire sans les précieux renseignements fournis par la théorie cinétique de Balescu–Lenard. Dans le cas unidimensionnel, l'auto-gravité conduit à un raidissement collectif : les particules diffusent plus lentement à partir de leurs orbites initiales que ne le prédirait la théorie de Landau (figure 6.1). Ce modèle approximant le mouvement vertical des étoiles dans le plan galactique, ce résultat suggère que le disque s'épaissirait plus lentement que prévu grâce aux effets collectifs. J'ai également montré que ce système unidimensionnel souffre souvent d'un quasi-blocage cinétique. Le taux de relaxation est bien inférieur au taux typique de diffusion : même sans être à l'équilibre thermique, les effets de diffusion et de friction dynamique se compensent presque (figure 6.8). Cependant, il y a tout de même bien une relaxation vers l'équilibre thermique sous l'effet des corrélations à deux corps.

Cette relaxation très lente et ce raidissement collectif différent avec le comportement des disques dynamiquement froids. Dans le chapitre 6, j'ai revisité les simulations numériques de Sellwood (2012) et leur interprétation par Fouvry et al. (2015). J'ai confirmé que pour ce disque marginalement stable, l'amplification "swing" (Toomre, 1981) augmente drastiquement la relax-

ation du disque. Avec les résultats obtenus dans le chapitre 4, j'ai montré que le couplage résonant entre les modes amortis (non collisionels) et les étoiles est le principal moteur de ce réarrangement amplifié et localisé (figure 6.16). En stabilisant le disque, le "softening" gravitationel ralenti donc de manière significative la relaxation du disque (figure 6.18). Une conséquence directe est que la qualité de la prédiction quasi-linéaire de Balescu–Lenard est entièrement déterminée par la qualité des calculs de réponse linéaire. Il faut souligner que, au-delà de la question du coût de calcul, le calcul des opérateurs de collision de Landau (equation 5.12) et de Balescu–Lenard (equation 5.1) est, de loin, techniquement moins difficile que le calcul de la matrice de polarisation linéaire (equation 3.28) à des fréquences neutres et amorties (section 3.3.2). Si des progrès doivent être réalisés dans les prédictions séculaires, c'est principalement dans le calcul de la réponse linéaire. À cette fin, j'espère que les librairies publiques génériques que j'ai contribué à développer dans cette thèse (section 4.2.3) permettront de tester, améliorer et étendre les méthodes numériques actuelles. En conclusion, l'équation de Balescu–Lenard (5.1) fournit une estimation quantitative de la relaxation des systèmes stellaires.

Au-delà de Balescu–Lenard Dans les régimes que j'ai exploré, la théorie de Balescu–Lenard fonctionne très précisement lorsqu'elle est comparée à un ensemble de simulations à N corps. Cependant, j'ai également mis en évidence certaines de ses limitations. En particulier, des simulations individuelles peuvent évoluer de manière très différente les unes des autres. Cette stochasticité est largement amplifiée à la proximité de la stabilité marginale, comme dans le disque que j'ai étudié (figure 6.19). Prévoir la dispersion entre différentes réalisations est une tâche difficile qui dépasse le cadre de la théorie cinétique de Balescu–Lenard. Au-delà du régime marginalement stable, il s'agit d'une question importante en soi car cela permettrait de quantifier la probabilité d'une seule réalisation/observation. Des théories prometteuses ont été récemment développées dans cette direction en utilisant les théories de grandes déviations (Bouchet, 2020; Feliachi & Bouchet, 2022; Feliachi & Fouvry, 2023).

Une autre limitation de la théorie de Balescu–Lenard est le cas des systèmes homogènes unidimensionnels et des systèmes inhomogènes limités aux résonances 1:1. Dans le chapitre 7, j'ai étudié ces systèmes qui souffrent d'un blocage cinétique complet de premier ordre. Toute estimation basée sur des rencontres à deux corps, que ce soit Chandrasekhar, Landau ou Balescu–Lenard, ne prévoirait aucune relaxation. La relaxation est encore retardée et est entraînée par des rencontres à trois corps. Dans ce cas, une équation cinétique a récemment été dérivée pour prendre en compte l'effet des rencontres à trois corps tout en négligeant les effets collectifs (Fouvry et al., 2019a, 2020; Fouvry, 2022). Pourtant, certains systèmes spécifiques peuvent également être bloqués pour cette dynamique. J'ai montré que les effets collectifs jouent à nouveau un rôle crucial dans la relaxation de ces systèmes. En utilisant des simulations numériques, j'ai prouvé qu'ils permettent notamment aux rencontres à trois corps d'entraîner une évolution, empêchant ainsi le blocage cinétique complet au second ordre. Ainsi, il ne sera jamais nécessaire de prendre en compte les rencontres à quatre corps pour décrire la relaxation de ces systèmes car elles joueront toujours un rôle négligeable.

L'objectif principal de ma thèse était de valider quantitativement la théorie (inhomogène) de Balescu–Lenard par rapport à des ensembles de simulations moyennées. En complément de Fouvry et al. (2021), mon travail établit que cette théorie capture correctement l'évolution séculaire des systèmes auto-gravitants dans des géométries allant d'une à trois dimensions. Cette tâche s'est avérée techniquement difficile et a conduit à quelques résultats inattendus tout en mettant en lumière de nouvelles complexités, telles qu'un quasi-blocage cinétique dans le système unidimensionel et une variance accrue près de la stabilité marginale. Pourtant, une décennie après sa publication, mes résultats établissent la théorie de Balescu–Lenard comme le pilier du chauffage auto-cohérent dans les systèmes stellaires collisionnels. Cela nous permet ainsi de commencer à capturer leur évolution à long terme en tenant compte des fluctuations au-delà du champ moyen.

Bibliography

Aarseth S. J., 1963, MNRAS, 126, 223

Antoja T., et al., 2018, Nature, 561, 360

Arnold V. I., 1978, Mathematical methods of classical mechanics. Springer

Baldwin D. E., 1962, Phys. Fluids, 5, 1523

Balescu R., 1960, Phys. Fluids, 3, 52

Bar-Or B., Fouvry J.-B., 2018, ApJ, 860, L23

Barré J., Gupta S., 2014, J. Stat. Mech., 2014, 02017

Barré J., Yamaguchi Y. Y., 2013, J. Phys. A, 46, 225501

Barré J., Olivetti A., Yamaguchi Y. Y., 2010, J. Stat. Mech., 2010, 08002

Barré J., Olivetti A., Yamaguchi Y. Y., 2011, J. Phys. A, 44, 405502

Barré J., Olivetti A., Yamaguchi Y. Y., 2015, Comptes Rendus Physique, 16, 723

Benetti F. P. C., Marcos B., 2017, Phys. Rev. E, 95, 022111

Binney J., Lacey C., 1988, MNRAS, 230, 597

Binney J., Tremaine S., 2008, Galactic Dynamics: Second Edition. Princeton University Press

Blumenthal G. R., Faber S. M., Primack J. R., Rees M. J., 1984, Nature, 311, 517

Bonaca A., Price-Whelan A. M., 2024, arXiv, 2405.19410

Bouchet F., 2020, J. Stat. Phys., 181, 515

Bouchet F., Dauxois T., 2005, Phys. Rev. E, 72, 045103

Bovy J., Rix H.-W., 2013, ApJ, 779, 115

Camm G. L., 1950, MNRAS, 110, 305

Campa A., Chavanis P.-H., Giansanti A., Morelli G., 2008, Phys. Rev. E, 78, 040102

Campa A., Dauxois T., Fanelli D., Ruffo S., 2014, Physics of long-range interacting systems. Oxford University Press

Case K. M., 1959, Annals Phys., 7, 349

Chandrasekhar S., 1942, Principles of stellar dynamics. University of Chicago Press

Chandrasekhar S., 1943, ApJ, 97, 255

Chavanis P.-H., 2001, Phys. Rev. E, 64, 026309

Chavanis P.-H., 2006a, IJMPB, 20, 3113

Chavanis P.-H., 2006b, Physica A, 365, 102

Chavanis P.-H., 2012, Physica A, 391, 3680

Chavanis P.-H., 2013a, Eur. Phys. J. P., 128, 126

Chavanis P.-H., 2013b, Eur. Phys. J. P., 128, 128

Chavanis P.-H., 2013c, A&A, 556, A93

Chavanis P.-H., 2022, Physica A, 606, 128089

Chavanis P.-H., 2024, Eur. Phys. J. P., 139, 51

Chavanis P.-H., Lemou M., 2007, Eur. Phys. J. B, 59, 217

Clutton-Brock M., 1972, Ap&SS, 16, 101

Clutton-Brock M., 1973, Ap&SS, 23, 55

Cohn H., 1979, ApJ, 234, 1036

D'Onghia E., Vogelsberger M., Hernquist L., 2013, ApJ, 766, 34

Das D., Gupta S., 2019, J. Stat. Mech., 8, 084007

Dauxois T., Latora V., Rapisarda A., Ruffo S., Torcini A., 2002, Lecture Notes in Physics, Springer, 602, 458

De Rijcke S., Voulis I., 2016, MNRAS, 456, 2024

De Rijcke S., Fouvry J.-B., Pichon C., 2019a, MNRAS, 484, 3198

De Rijcke S., Fouvry J.-B., Dehnen W., 2019b, MNRAS, 485, 150

Debattista V. P., Sellwood J. A., 2000, ApJ, 543, 704

Dehnen W., 2001, MNRAS, 324, 273

Dootson D., 2023, PhD thesis, Oxford University

Dubin D. H. E., 2003, Phys. Plasmas, 10, 1338

Dubois Y., et al., 2021, A&A, 651, A109

Duval C., Cherroret N., 2024, arXiv, 2405.08606

Earn D. J. D., Sellwood J. A., 1995, ApJ, 451, 533

Eddington A. S., 1916, MNRAS, 76, 572

Eilers A.-C., Hogg D. W., Rix H.-W., Ness M. K., 2019, ApJ, 871, 120

Eldridge O. C., Feix M., 1963, Phys. Fluids, 6, 398

Elmegreen B. G., Elmegreen D. M., Vollbach D. R., Foster E. R., Ferguson T. E., 2005, ApJ, 634, 101

Evans N. W., Read J. C. A., 1998a, MNRAS, 300, 83

Evans N. W., Read J. C. A., 1998b, MNRAS, 300, 106

Ewart R. J., Brown A., Adkins T., Schekochihin A. A., 2022, J. Plasma Phys., 88, 925880501

Faou E., Horsin R., Rousset F., 2021, J. Dyn. Differ. Equ., 33, 1531

Feliachi O., Bouchet F., 2021, J. Stat. Phys., 183, 42

Feliachi O., Bouchet F., 2022, J. Stat. Phys., 186, 22

Feliachi O., Fouvry J.-B., 2023, arXiv, 2308.08308

Fouvry J.-B., 2017, Secular Evolution of Self-Gravitating Systems Over Cosmic Age. Springer

Fouvry J.-B., 2022, Phys. Rev. E, 106, 054123

Fouvry J.-B., Bar-Or B., 2018, MNRAS, 481, 4566

Fouvry J.-B., Prunet S., 2022, MNRAS, 509, 2443

Fouvry J.-B., Roule M., 2023, Phys. Rev. E, 108, 054108
Fouvry J.-B., Pichon C., Magorrian J., Chavanis P.-H., 2015, A&A, 584, A129
Fouvry J.-B., Pichon C., Chavanis P.-H., 2016, arXiv, 1605.03384
Fouvry J.-B., Bar-Or B., Chavanis P.-H., 2019a, Phys. Rev. E, 100, 052142
Fouvry J.-B., Bar-Or B., Chavanis P.-H., 2019b, ApJ, 883, 161
Fouvry J.-B., Chavanis P.-H., Pichon C., 2020, Phys. Rev. E, 102, 052110
Fouvry J.-B., Hamilton C., Rozier S., Pichon C., 2021, MNRAS, 508, 2210
Freeman K. C., 1970, ApJ, 160, 811
Frenk C. S., White S. D. M., 2012, Annalen der Physik, 524, 507
Fridman A. M., Poliachenko V. L., 1984, Physics of gravitating systems. I. Springer
Frieman E. A., Book D. L., 1963, Phys. Fluids, 6, 1700
Gabrielli A., Joyce M., Marcos B., 2010, Phys. Rev. Lett., 105, 210602
Giersz M., 1998, MNRAS, 298, 1239
Goldreich P., Lynden-Bell D., 1965, MNRAS, 130, 125
Goldstein H., 1950, Classical mechanics. Addison-Wesley
Grion Filho D., Johnston K. V., Poggio E., Laporte C. F. P., Drimmel R., D'Onghia E., 2021, MNRAS, 507, 2825
Guernsey R. L., 1964, Phys. Fluids, 7, 1600
Gupta S., Mukamel D., 2011, J. Stat. Mech., 2011, 03015
Guth A. H., 1981, Phys. Rev. D, 23, 347
Hairer E., Lubich C., Wanner G., 2006, Geometric numerical integration: Second Edition. Springer
Hamilton C., 2021, MNRAS, 501, 3371
Hamilton C., 2024, MNRAS, 528, 5286
Hamilton C., Fouvry J.-B., 2024, arXiv, 2402.13322
Hamilton C., Heinemann T., 2020, arXiv, 2011.14812
Hamilton C., Heinemann T., 2023, MNRAS, 525, 4161
Heggie D. C., Breen P. G., Varri A. L., 2020, MNRAS, 492, 6019
Hénon M., 1959, Annales d'Astrophysique, 22, 126
Hénon M., 1971, Ap&SS, 14, 151
Hénon M., 1973, A&A, 24, 229
Hernquist L., Ostriker J. P., 1992, ApJ, 386, 375
Heyvaerts J., 2010, MNRAS, 407, 355
Heyvaerts J., Fouvry J.-B., Chavanis P.-H., Pichon C., 2017, MNRAS, 469, 4193
Hohl F., Campbell J. W., 1968, AJ, 73, 611
Horedt G. P., 2004, Polytropes. Kluwer Acad. Publ.
Hunt J. A. S., Price-Whelan A. M., Johnston K. V., Darragh-Ford E., 2022, MNRAS, 516, L7
Jalali M. A., 2007, ApJ, 669, 218
Jalali M. A., 2010, MNRAS, 404, 1519
Jalali M. A., Hunter C., 2005, ApJ, 630, 804
Jeans J. H., 1929, The universe around us. Cambridge University Press
Johnson A. C., Petersen M. S., Johnston K. V., Weinberg M. D., 2023, MNRAS, 521, 1757
Johnston K. V., Spergel D. N., Hernquist L., 1995, ApJ, 451, 598
Johnston K. V., et al., 2017, Galaxies, 5, 44
Joyce M., Worrakitpoonpon T., 2010, J. Stat. Mech., 2010, 10012
Julian W. H., Toomre A., 1966, ApJ, 146, 810
Kalnajs A. J., 1971, ApJ, 166, 275
Kalnajs A. J., 1976, ApJ, 205, 745
Kalnajs A. J., 1977, ApJ, 212, 637
Klimontovich Y. L., 1967, The Statistical Theory of Non-Equilibrium Processes in a Plasma. Elsevier
Kocsis B., Tremaine S., 2015, MNRAS, 448, 3265
Krommes J. A., 2002, Phys. Rep., 360, 1
Landau L. D., 1936, Phys. Z. Sowjetunion, 10, 154
Lau J. Y., Binney J., 2021, MNRAS, 507, 2241
Laughlin G., Korchagin V., Adams F. C., 1997, ApJ, 477, 410
Lenard A., 1960, Annals of Physics, 10, 390
Lourenço C. R., Rocha Filho T. M., 2015, Phys. Rev. E, 92, 012117
Luciani J. F., Pellat R., 1987, J. Phys., 48, 591
Lynden-Bell D., 1967, MNRAS, 136, 101
Lynden-Bell D., 1979, MNRAS, 187, 101
Lynden-Bell D., Kalnajs A. J., 1972, MNRAS, 157, 1
Magorrian J., 2007, MNRAS, 381, 1663
Magorrian J., 2021, MNRAS, 507, 4840
Marcos B., Gabrielli A., Joyce M., 2017, Phys. Rev. E, 96, 032102
Merritt D., 1996, AJ, 111, 2462
Miller R. H., 1971, Ap&SS, 14, 73
Miller B. N., Youngkins P., 1998, Phys. Rev. Lett., 81, 4794
Miyamoto M., 1974, A&A, 30, 441
Mouhot C., Villani C., 2011, Acta Mathematica, 207, 29
Murali C., 1999, ApJ, 519, 580
Nelson R. W., Tremaine S., 1999, MNRAS, 306, 1
Nicholson D. R., 1992, Introduction to Plasma Theory. Krieger
Noullez A., Fanelli D., Aurell E., 2003, J. Comp. Phys., 186, 697
Olivetti A., 2011, PhD thesis, Université Nice Sophia Antipolis
Omurkanov T. Z., Polyachenko E. V., 2014, Astro. Lett., 40, 724
Padmanabhan T., 1990, Phys. Rep., 188, 285
Palmer P. L., 1994, Stability of Collisionless Stellar Systems: Mechanisms for the Dynamical Structure of Galaxies. Springer Netherlands
Peebles P. J. E., 1980, The large-scale structure of the universe. Princeton University Press
Petersen M. S., Weinberg M. D., Katz N., 2022, MNRAS, 510, 6201
Petersen M. S., Roule M., Fouvry J.-B., Pichon C., Tep

K., 2024, MNRAS,
Pichon C., 1994, PhD thesis, University of Cambridge
Pichon C., Aubert D., 2006, MNRAS, 368, 1657
Pichon C., Cannon R. C., 1997, MNRAS, 291, 616
Planck Collaboration 2020, A&A, 641, A6
Plummer H. C., 1911, MNRAS, 71, 460
Pohlen M., Trujillo I., 2006, A&A, 454, 759
Polyachenko E. V., 2005, MNRAS, 357, 559
Polyachenko E. V., 2013, Astro. Lett., 39, 72
Polyachenko V. L., Shukhman I. G., 1982, Soviet Ast., 26, 140
Polyachenko E. V., Shukhman I. G., Borodina O. I., 2021, MNRAS, 503, 660
Press W., et al., 2007, Numerical Recipes 3rd Edition. Cambridge Univ. Press
Reid M. J., et al., 2014, ApJ, 783, 130
Reidl C. J. J., Miller B. N., 1988, ApJ, 332, 619
Robinson P. A., 1990, J. Comp. Phys., 88, 381
Rocha Filho T. M., Santana A. E., Amato M. A., Figueiredo A., 2014, Phys. Rev. E, 90, 032133
Rodriguez C. L., et al., 2022, ApJS, 258, 22
Rogister A., Oberman C., 1968, J. Plasma Phys., 2, 33
Rostoker N., 1964, Physics of Fluids, 7, 479
Roule M., Fouvry J.-B., Pichon C., Chavanis P.-H., 2022, Phys. Rev. E, 106, 044118
Rozier S., Fouvry J. B., Breen P. G., Varri A. L., Pichon C., Heggie D. C., 2019, MNRAS, 487, 711
Rozier S., Famaey B., Siebert A., Monari G., Pichon C., Ibata R., 2022, ApJ, 933, 113
Rubin V. C., Ford W. K. J., Thonnard N., 1980, ApJ, 238, 471
Rybicki G. B., 1971, Ap&SS, 14, 56
Saha P., 1991, MNRAS, 248, 494
Salo H., Laurikainen E., 2000, MNRAS, 319, 393
Scannapieco C., et al., 2012, MNRAS, 423, 1726
Sellwood J. A., 2012, ApJ, 751, 44
Sellwood J. A., 2014, Reviews of Modern Physics, 86, 1
Sellwood J. A., 2020, MNRAS, 492, 3103
Sellwood J. A., 2024, MNRAS, 529, 3035
Sellwood J. A., Binney J. J., 2002, MNRAS, 336, 785
Sellwood J. A., Carlberg R. G., 2019, MNRAS, 489, 116
Sellwood J. A., Evans N. W., 2001, ApJ, 546, 176
Sellwood J. A., Kahn F. D., 1991, MNRAS, 250, 278
Silk J., Rees M. J., 1998, A&A, 331, L1
Smereka P., 1998, Physica D, 124, 104
Souza L. F., Rocha Filho T. M., 2023, Phys. Rev. E, 107, 014114
Spitzer L. J., 1942, ApJ, 95, 329
Spitzer Lyman J., Schwarzschild M., 1951, ApJ, 114, 385
Springel V., Frenk C. S., White S. D. M., 2006, Nature, 440, 1137
Teles T. N., Levin Y., Pakter R., 2011, MNRAS, 417, L21
Teles T. N., Farias C. A. F., Pakter R., Levin Y., 2023, Entropy, 25, 1379
Tep K., Fouvry J.-B., Pichon C., 2022, MNRAS, 514, 875
Theis C., 1998, A&A, 330, 1180
Toomre A., 1964, ApJ, 139, 1217
Toomre A., 1981, in Structure and Evolution of Normal Galaxies. p. 111
Trefethen L. N., 2020, BIT Numer. Math., 60, 901
Trefethen L. N., 2023, JJIAM, 40, 1587
Tremaine S., Weinberg M. D., 1984, MNRAS, 209, 729
Tremaine S., Frankel N., Bovy J., 2023, MNRAS, 521, 114
Van Kampen N. G., 1955, Physica, 21, 949
Vasiliev E., 2017, ApJ, 848, 10
Vauterin P., Dejonghe H., 1996, A&A, 313, 465
Vlasov A. A., 1968, Sov. Phys. Usp., 10, 721
Vogelsberger M., Marinacci F., Torrey P., Puchwein E., 2020, Nature Rev. Phys., 2, 42
Weinberg M. D., 1986, ApJ, 300, 93
Weinberg M. D., 1989, MNRAS, 239, 549
Weinberg M. D., 1993, ApJ, 410, 543
Weinberg M. D., 1994, ApJ, 421, 481
Weinberg M. D., 1999, AJ, 117, 629
Weinberg M. D., 2001, MNRAS, 328, 311
Weinberg M. D., 2015, arXiv, 1508.06855
Weinstock J., 1964, Phys. Rev., 133, 673
Worrakitpoonpon T., 2024, Phys. Rev. E, 109, 054118
Wright H. L., Miller B. N., Stein W. E., 1982, Ap&SS, 84, 421
Yawn K. R., Miller B. N., 1997, Phys. Rev. E, 56, 2429
Zang T. A., 1976, PhD thesis, Massachusetts Institute of Technology